University of Tennessee, Knoxville

TRACE: Tennessee Research and Creative Exchange

Doctoral Dissertations

Graduate School

5-2006

Development of a Potentially Accurate and Efficient LES CFD Algorithm to Predict Heat and Mass Transport in Inhabited Spaces

Marcel Andre Grubert
University of Tennessee - Knoxville

Follow this and additional works at: https://trace.tennessee.edu/utk_graddiss

Part of the Mechanical Engineering Commons

Recommended Citation

Grubert, Marcel Andre, "Development of a Potentially Accurate and Efficient LES CFD Algorithm to Predict Heat and Mass Transport in Inhabited Spaces. " PhD diss., University of Tennessee, 2006.
https://trace.tennessee.edu/utk_graddiss/1672

This Dissertation is brought to you for free and open access by the Graduate School at TRACE: Tennessee Research and Creative Exchange. It has been accepted for inclusion in Doctoral Dissertations by an authorized administrator of TRACE: Tennessee Research and Creative Exchange. For more information, please contact trace@utk.edu.

To the Graduate Council:

I am submitting herewith a dissertation written by Marcel Andre Grubert entitled "Development of a Potentially Accurate and Efficient LES CFD Algorithm to Predict Heat and Mass Transport in Inhabited Spaces." I have examined the final electronic copy of this dissertation for form and content and recommend that it be accepted in partial fulfillment of the requirements for the degree of Doctor of Philosophy, with a major in Mechanical Engineering.

A. J. Baker, Major Professor

We have read this dissertation and recommend its acceptance:

Suzanne Lenhart, Arthur Ruggles, Mohamed Mahfouz

Accepted for the Council:

Carolyn R. Hodges

Vice Provost and Dean of the Graduate School

(Original signatures are on file with official student records.)

To the Graduate Council:

I am submitting herewith a dissertation written by Marcel Andre Grubert entitled "Development of a Potentially Accurate and Efficient LES CFD Algorithm to Predict Heat and Mass Transport in Inhabited Spaces." I have examined the final electronic copy of this dissertation for form and content and recommend that it be accepted in partial fulfillment of the requirements for the degree of Doctor of Philosophy, with a major in Mechanical Engineering.

A.J. Baker

Major Professor

We have read this dissertation
and recommend its acceptance:

Suzanne Lenhart

Arthur Ruggles

Mohamed Mahfouz

Accepted for the Council:

Anne Mayhew

Vice Chancellor and Dean of
Graduate Studies

(Original signatures are on file with official student records.)

Development of a Potentially Accurate and Efficient LES CFD Algorithm to Predict Heat and Mass Transport in Inhabited Spaces

A dissertation for

Presented for the

Doctor of Philosophy

Degree

The University of Tennessee, Knoxville

Marcel A. Grubert

May, 2006

Copyright © 2006 by Marcel A. Grubert
All rights reserved.

This work is dedicated to my loving parents, Maria and Heinz, and my wonderful wife Rebecca, who all sacrificed so much to get me where I am today.

Acknowledgments

I would like to thank my major professor Dr. Allen J. Baker for his help, advice, encouragement and financial support that was rendered during my studies. Without him this dissertation would have never become reality. I would also like to thank my dissertation committee, Profs. Suzanne Lenhart, Arthur Ruggles and Mohamed Mahfouz for their assistance rendered during my dissertation writing. In addition I would like to thank my colleagues Sunil Sahu, Shawn Ericson and Joe Orzechowski for their countless hours of valuable discussion and technical help.

I am deeply in dept to my loving parents, who supported me for so many decades, who's affection and care molded me into the person I am today, as well as to my wonderful wife Rebecca, who sacrificed beyond measure during this difficult time of our lives. Her understanding and support kept me going, even when the possibility of success seemed unreachable.

Abstract

During the last decades many advances have been made in the prediction of turbulent flow behavior, due largely to new achievements in the field of computational fluid dynamics (CFD). For many years the Reynolds-averaged Navier-Stokes (RaNS) approach, which employs time-averaging, has been the work-horse of the industry in predicting turbulent flow in real-world applications. Although the accuracy of those turbulent flows and the details in flow structure are mostly limited due to its empirical modeling approach, the RaNS based algorithms are able to achieve solutions in relative short amounts of computational time using relatively coarse meshes.

But with increased computational capacities, utilizing faster chips and more memory, a different group of theories are getting more attention, one of which is Large-Eddy-Simulation (LES) theory. Able to deliver increased detail in turbulent flow structures and better accuracy due to the fact that a significant range of flow structures are predicted resolvable while only the unresolved, small scale structures are modeled, they are still restricted in use. This comes from the need to resolve the flow details in wall-bounded domains, which unfortunately makes up most of the real-world applications. This need leads to a very fine mesh requirement in the wall region, rivaling direct numerical simulation (DNS) approaches. Since the mesh requirement for LES resolution is a function of Reynolds (Re) and Rayleigh (Ra) numbers, computations are in general limited to relatively modest values of Re and Ra.

This dissertation examines several possible improvements to the class of LES formulations. It develops the basic formulation for the unsteady 3-dimensional, incompressible thermal Navier-Stokes equation system, focused on prediction of mixed convection flows in ventilated domains characterized by human habitation. This is accomplished by extending the rational LES theory, developed by Volker John, to the heat and/or mass transport problem class, with focus on boundary conditions suitable for bounded domain implementations. A new sub-grid scale (SGS) model based on the Taylor Weak Statement beta term is introduced, which models the dissipation of mechanical energy by the smallest eddies via artificial (numerical) diffusion. This model is compared to established SGS models, including that due to Smagornisky and several formulations developed by Layton and Illiescu. Numerical results for a range of benchmark and validation problems are generated to access accuracy and utility of the new LES formulation.

TABLE OF CONTENTS

1. INTRODUCTION …….. …. 1
   1.1 A BRIEF LES HISTORY ……. 2
   1.2 THIS DISSERTATION ……. 3
2. LARGE EDDY SIMULATION THEORY …… 6
   2.1 CONSERVATION PRINCIPLES ……. 6
   2.2 SPATIAL FILTERING …….. 8
   2.3 LES CLOSURE FOR MOMENTUM …… 10
   2.4 LES FOR SCALAR TRANSPORT …….. 16
   2.5 CLOSURE FOR THE SGS REYNOLDS TENSOR …… 17
   2.6 SUBGRID SCALE CLOSURE ……. 18
   2.7 AN ALTERNATIVE SGS FORMULATION ……...…….. 21
   2.8 RATIONAL LES FLUX VECTOR REPRESENTATION ….. 23
   2.9 BOUNDARY AND INITIAL CONDITIONS …… 26
3. LES THEORY CFD ALGORITHM …… 32
   3.1 CONTINUITY CONSTRAINT ALGORITHM ……..…… 32
   3.2 CONTINUITY ERROR ……... 32
   3.3 POTENTIAL FUNCTION …….. 36
   3.4 PRESSURE POISSON EQUATION …….. 38
4. CFD ALGORITHM WEAK FORM FE IMPLEMENTATION …… 41
   4.1 GALERKIN WEAK STATEMENT FORMULATION …….…. 42
   4.2 TAYLOR WEAK STATEMENT FORMULATION ……. 45
   4.3 FINITE ELEMENT FLUX VECTOR COMPUTATIONS …….. 48
   4.4 ACCURACY AND CONVERGENCE ……... 52
5. DISCUSSION AND RESULTS …… 56
   5.1 TURBULENT DUCT FLOW …… 56
   5.2 LAMINAR FLOW IN DRIVEN CAVITY ……...… 59
   5.3 THERMAL CAVITY, LAMINAR TO TURBULENT FLOW … 62

5.3.1 ABOUT SYMMETRIES IN THERMAL CAVITY FLOWFIELDS ……..… 64
5.3.2 THERMAL CAVITY AT RA = $3.4x10^5$ ……. 66
5.3.3 THERMAL CAVITY AT RA = $3.4x10^6$ …….. 68
5.3.4 THERMAL CAVITY AT RA = $3.4x10^7$ ……. 69
5.3.5 THERMAL CAVITY AT RA = $3.4x10^8$ …… 71
6. CONCLUSIONS AND RECOMMENDATIONS ……...……. 76
6.1 CONCLUSIONS …….…….. 76
6.2 RECOMMENDATIONS …….. 77
BIBLIOGRAPHY ……..…… 78
APPENDIX …….. 84
TABLES …….. 85
FIGURES …….. 88
TURBULENT DUCT …… 98
DRIVEN CAVITY …… 105
THERMAL CAVITY …… 111
CODE TEMPLATE …….. 148
VITA ……..……..... 169

List of Tables

Table		Page
2.1	Filter functions and transfer function	85
5.1	Compilation of temperature difference between hot and cold wall, Rayleigh, Reynolds, Grashof and Archimedes numbers for the thermal cavity test case	86
5.2	Comparison of symmetry between square cavity and 5:1 aspect ratio thermal cavity using Omega-Psi algorithm	87

List of Figures

Figure		Page
2.1	Filter functions in physical space; solid line: Gaussian filter, dashed line: box filter, dashed-dotted line: sharp spectral filter	88
2.2	Filter functions in wave number space; solid line: Gaussian filter, dashed line: box filter, dashed-dotted line: sharp spectral filter	89
2.3.	Second order Taylor series approximation for the Gaussian filter	90
2.4.	Second order Pade approximation for the Gaussian filter	90
2.5.	Filtering at the wall	91
4.1	Phase velocity error distribution for a range of CFD algorithm	92
4.2	Amplification factor error distribution for a range of CFD algorithm	93
4.3a	Analytical solution for rotating cone problem	94
4.3b	Crank-Nicolson solution for rotating cone problem	95
4.3c	GWS solution for rotating cone problem	96
4.3d	TWS solution for rotating cone problem	97
5.1.1	33x25 non-uniform meshing for turbulent duct flow case; distorted plot; original dimensions are 0.5 inch height to 3 feet length	98
5.1.2	Validation of turbulent duct velocity profile along centerline of duct versus turbulent boundary layer theory	99
5.1.3	Y+ at first node of the wall distribution along the length of	99

the duct

5.1.4. Axial-velocity profile for turbulent duct flow 100

5.1.5. Turbulent duct turbulence kinetic energy 100

5.1.6. Turbulent duct dissipation rate 101

5.1.7. Turbulent duct turbulent Reynolds number 101

5.1.8. Comparison of Stokes shear stress FD12 and TWS shear stress FB12 102

5.1.9. Comparison of Smagorinsky FS12 and Reynolds shear stresses T12 102

5.1.10. Laminar diffusion flux vector component FD11 103

5.1.11. Modified TWS flux vector component FB11 103

5.1.12. Smagorinsky flux vector component FS11 103

5.1.13. Reynolds stress tensor component T11 103

5.1.14. Laminar diffusion flux vector component FD12 104

5.1.15. Modified TWS flux vector component FB12 104

5.1.16. Smagorinsky flux vector component FS12 104

5.1.17. Reynolds stress tensor component T12 104

5.2.1 Driven cavity setup 105

5.2.2 Optimized meshing for Re = 2000 laminar execution 105

5.2.3 Energy norm comparison versus mesh progression ratio for driven cavity at Re = 2000 106

5.2.4 Reference solution by [Eri01], showing the velocity field of the laminar driven cavity for Re = 2000 on an optimized mesh, 106

	featuring TWS beta stabilization	
5.2.5.	Velocity vector distribution	107
5.2.6.	Pressure distribution	107
5.2.7.	Laminar diffusion flux vector component FD11	108
5.2.8.	Modified TWS flux vector component FB11	108
5.2.9.	Laminar diffusion flux vector component FD12	109
5.2.10.	Modified TWS flux vector component FB12	109
5.2.11.	Laminar diffusion flux vector component FD22	110
5.2.12.	Modified TWS flux vector component FB22	110
5.3.1	Comparison of stream function on an 8x1 thermal cavity at Ra = 1.0E5 (left), 1.0E6 (middle) and 3.4E6 (right)	111
5.3.2	8:1 thermal cavity problem	112
5.3.3	8:1 ration non-uniform mesh featuring 41x281 nodes. This figure shows the upper 12.5% of the mesh	113
5.3.1.1	Un-symmetric stream-function (left) and temperature (right) distribution at t = 88 sec for a laminar LES algorithm computation using TWS SGS model, Re = 2186, Ra = 3.4E6	114
5.3.1.2	Vorticity (upper) and symmetry variable TAU2 (lower) distribution for a laminar, square thermal cavity at Ra = 1E3	115
5.3.1.3	Vorticity (upper) and symmetry variable TAU2 (lower) distribution for a laminar, square thermal cavity at Ra = 1E4	116
5.3.1.4	Vorticity (upper) and symmetry variable TAU2 (lower) distribution for a laminar, square thermal cavity at Ra = 1E5	117

5.3.1.5 Vorticity (left) and symmetry variable TAU2 (right) distribution for a laminar, 5:1 aspect ratio, thermal cavity at Ra = 1E3 118

5.3.1.6 Vorticity (left) and symmetry variable TAU2 (right) distribution for a laminar, 5:1 aspect ratio, thermal cavity at Ra = 1E4 119

5.3.1.7 Vorticity (left) and symmetry variable TAU2 (right) distribution for a laminar, 5:1 aspect ratio, thermal cavity at Ra = 1E5 120

5.3.2.1 Temperature distribution at t = 54, 194 and 294 sec for a laminar flow LES algorithm computation using TWS SGS model, Ra = 3.4xE5, Re = 680 121

5.3.2.2 Stream-function distribution at t = 54, 194 and 294 sec for a laminar flow LES algorithm computation using TWS SGS model, Ra = 3.4xE5, Re = 680 122

5.3.2.3 Comparison of Stokes (STOKES11), Reynolds (R11) and TWS SGS (TWS11) normal stresses for a laminar flow LES algorithm computation using TWS SGS model, Ra = 3.4xE5, Re = 680 at t = 296 sec. 123

5.3.2.4 Comparison of Stokes (STOKES12), Reynolds (R12) and TWS SGS (TWS12) shear stresses for a laminar flow LES algorithm computation using TWS SGS model, Ra = 3.4xE5, Re = 680 at t = 296 sec. 124

5.3.3.1 Temperature distribution at t = 11.5, 49.8 and 96.8 sec for the rational LES algorithm computation using TWS SGS 125

model, Ra = 3.4xE6, transitional Re = 2186

5.3.3.2 Stream-function distribution at t = 11.5, 49.8 and 96.8 sec for the rational LES algorithm computation using TWS SGS model, Ra = 3.4xE6, transitional Re = 2186 126

5.3.3.3 Comparison of Stokes (STOKES11), Reynolds (R11) and TWS SGS (TWS11) normal stresses for a transitional flow LES algorithm computation using TWS SGS model, Ra = 3.4xE6, Re = 2186 at t = 96.8 sec. 127

5.3.3.4 Comparison of Stokes (STOKES12), Reynolds (R12) and TWS SGS (TWS12) shear stresses for a laminar flow LES algorithm computation using TWS SGS model, Ra = 3.4xE6, Re = 2186 at t = 96.8 sec. 128

5.3.4.1 Temperature distribution at t = 7.03, 49.5 and 104 sec for a LES algorithm computation using TWS SGS model, Ra = 3.4xE7, Re = 6850. 129

5.3.4.2 Stream-function distribution at t = 7.03, 49.5 and 104 sec for a LES algorithm computation using TWS SGS model, Ra = 3.4xE7, Re = 6850 130

5.3.4.3 Comparison of Stokes (STOKES12), Reynolds (R12) and TWS SGS (TWS12) shear stresses for a LES algorithm computation using TWS SGS model, Ra = 3.4xE7, Re = 6850 at t = 104 sec 131

5.3.4.4 Comparison of Stokes (STOKES12), Reynolds (R12) and 132

TWS SGS (TWS12) shear stresses for a transitional flow LES algorithm computation using TWS SGS model, Ra = 3.4xE7, Re = 6850 at t = 104 sec; close-up at upper left corner

5.3.4.5 Auxiliary variable tensor of the momentum equations, RS11, RS12 and RS22 for a LES algorithm computation using TWS SGS model, Ra = 3.4xE7, Re = 6850 at t = 104 sec. 133

5.3.4.6 Comparison of shear TWS SGS stress (TWS12), Smagorinsky (SMAG12) and SGS stress based on Eqn. (2.57), (SGS12), for a transitional flow LES algorithm computation using TWS SGS model, Ra = 3.4xE7, Re = 6850 at t = 104 sec. 134

5.3.4.7 Energy norm based on temperature for a rational LES algorithm computation using TWS SGS model, Ra = 3.4xE7, Re = 6850 at t = 104 sec. 135

5.3.5.1 Temperature distribution at t = 1.83, 9.86 and 22.8 sec for a turbulent flow LES algorithm computation using TWS SGS model, Ra = 3.4xE8, Re = 19932. 136

5.3.5.2 Stream-function distribution at t = 1.83, 9.86 and 22.8 sec for a rational LES algorithm computation using TWS SGS model, Ra = 3.4xE8, Re = 19932 137

5.3.5.3 Comparison of Stokes (STOKES12), Reynolds (R12) and TWS SGS (TWS12) shear stresses for a turbulent flow LES algorithm computation using TWS SGS model, Ra = 3.4xE8, Re = 19932 at t = 22.8 sec 138

5.3.5.4 Comparison of Stokes (STOKES12), Reynolds (R12) and TWS SGS (TWS12) shear stresses for a turbulent flow LES algorithm computation using TWS SGS model, Ra = 3.4xE8, Re = 19932 at t = 22.8 sec; close-up of upper left corner of domain 139

5.3.5.5 Comparison of shear TWS SGS stress (TWS12), Smagorinsky (SMAG12) and SGS stress based on Eqn. (2.57), (SGS12), for a rational LES algorithm computation using TWS SGS model, Ra = 3.4xE8, Re = 19932 at t = 22.8 sec. 140

5.3.5.6 Temperature distribution at t = 9.87, 12.7 and 15.7 sec for a turbulent flow LES algorithm computation using Smagorinsky SGS model, Ra = 3.4xE8, Re = 19932. This execution is a continuation of the TWS result at t = 9.6 for the same Rayleigh number 141

5.3.5.7 Stream-function distribution at t = 9.87, 12.7 and 15.7 sec for a turbulent flow LES algorithm computation using Smagorinsky SGS model, Ra = 3.4xE8, Re = 19932. This execution is a continuation of the TWS result at t = 9.6 for the same Rayleigh number 142

5.3.5.8 Temperature distribution at t = 10.4, 15.6 and 19 sec for a turbulent flow LES algorithm computation using SGS model based on (2.57), Ra = 3.4xE8, Re = 19932. This execution is a continuation of the TWS result at t = 9.6 for the same 143

Rayleigh number

5.3.5.9 Stream-function comparison at t = 14.7, 15.6 for turbulent flow LES algorithm computations using TWS, Smagorinsky and SGS model based on (2.57), Ra = 3.4xE8, Re = 19932. This execution is a continuation of the TWS result at t = 9.6 for the same Rayleigh number 144

5.3.5.10 Comparison of stream-function distributions at t = 14.7 sec for turbulent flow LES algorithm computations using the TWS, Smagorinsky and SGS model based on (2.57), Ra = 3.4xE8, Re = 19932 145

5.3.5.11 Comparison of driving SGS shear stress distribution at t = 14.7 sec for turbulent flow LES algorithm computations using the TWS, Smagorinsky and SGS model based on (2.57), Ra = 3.4xE8, Re = 19932 146

5.3.5.12 Comparison of temperature energy norm distribution at t = 14.7 sec for turbulent flow LES algorithm computations using the TWS, Smagorinsky and SGS model based on (2.57), Ra = 3.4xE8, Re = 19932 147

List of Symbols

A	inverse operator
c_ε	concentration
c_p	mass-specific heat capacity
C_s	Smagorinsky constant
F	Fourier transform
f_j	convective flux vector
f_j^v	diffusive flux vector
g	acceleration of gravity
$\hat{g}_i$	gravity vector
g_δ	Gaussian filter
h	mesh size
k	conductivity
L_r	reference length
l_m	mixing length
$\hat{n}$	normal unit vector
P	pressure

R_{ij}	Reynolds tensor
S_{ij}	strain rate tensor
S_T	source term of energy equation
S_ε	source term of mass transport equation
SGS_{ij}	sub-grid scale tensor (depends on used model)
t	time
T	temperature
T_r	reference temperature
u_i	velocity vector
U_r	reference velocity
x_i	spatial coordinate
Y_j	auxiliary variable for energy equation
Z_j	auxiliary variable for mass transport equation

Greek symbols

α	thermal diffusivity
β	coefficient of volume expansion, TWS beta term coefficient
δ	filter width
δ_{ij}	delta function
υ	kinematic viscosity

ρ_0	constant reference density
Φ	thermal dissipation function
θ	implicitness factor
Θ	non-dimensional temperature
τ_{ij}^{R}	residual stress tensor
τ_{ij}^{r}	residual stress tensor (anisotropic part)
τ_{kk}^{R}	residual stress tensor (isotropic part)
τ_w	wall stress
Ψ	trail space

1. Introduction

Over the past decades the continuous development of better and faster computer technology has given computational mechanics a permanent and important place as a tool in engineering design and analysis methodology. The field has matured from scientific examination of simple test cases to industrial size design and real-time control simulations. In today's world we compute airflow around whole aircraft, heat flow in microprocessors, blood circulation in human bodies, even whole weather pattern predictions for our planet.

But not only hardware improvements have advanced the field of CFD. During the years, mathematicians and engineers have developed new formulations and algorithms to better model the real-world physics in increasingly accurate ways. One of the fields of current interest, and one of the greatest challenges of our times, is the simulation of turbulent flows. Since most real-life applications are comprised of turbulent motion, much research thought has been given to that area, although understanding the exact physics behind the phenomena is still a challenge.

Theories describe turbulent fluid motions as erratic, chaotic in nature, hence impossible to predict exactly. Nevertheless, from experiments we know that turbulence shows a predictable average behavior, underlying the erratic motion [Wil00]. This observation promotes a CFD attempt to calculate the average movement directly, with the action of superimposed oscillations modeled through diverse algorithmic approaches. The averaging can be done in time, resulting in Reynolds-averaged Navier-Stokes (RaNS)

schemes, or spatially, resulting in a theoretical approach termed Large Eddy Simulation (LES) theory.

1.1 A Brief LES History

Large Eddy Simulation theory, specifically the idea of spatially filtering the Navier-Stokes equations to identify the resolvable scales, while the unresolved scale effects are modeled, has existed for more than four decades. The first successful implementation of this concept was due to Smagorinsky in 1963 [Sma63]. He suggested to model the action of filtering through an eddy viscosity, which he defined as a function of the filter width, the magnitude of the resolved velocity gradient and a global constant. This model proved adequate only for simple problems employing only one global flow pattern. Through its inability to be calibrated for locally changing flow phenomena, e.g. flow over a wing with a wake region, it is an insufficient formulation for simulation of multi-scale flow problems.

Improvements on the Smagorinsky model have been made, with the most successful implementation developed by Germano at al. in 1991 [GPMC91]. Its dynamic-subgrid scale approach replaces the global constant with a local constant, which is computed through a code-internal multi-meshing scheme. In this way, the constant becomes an internal variable dependent on local flow conditions. Other researchers have built on this success, e.g. Lilly in 1992 [Lil92].

A new approach to LES theory, called rational LES, was developed by Layton et al. in 2003 [IJL+03]. By formally filtering the Navier-Stokes equations via a physically

meaningful and mathematically exact process, they developed analytical expressions for three of the four LES theory-defined (Reynolds) stress tensors. This theory admits increased accuracy in the prediction of the energy distribution in the resolved scales, while reducing the modeling requirement to only the sub-grid scale Reynolds stress tensor. Details about its implementation using a finite element discretization, as well as a comparison of sub-grid scale closure models, are given by John [Joh04].

1.2 This Dissertation

The most common tool to tackle real-world CFD problems is currently still the RaNS approach, while LES and Direct Numerical Simulations (DNS) are used mainly in academic and research environments due to mesh resolution requirements, hence their limited applicability at larger Reynolds numbers. Furthermore, implementations of LES theory via a finite element discretization are rare, since the CFD community started with finite difference approximations, and then adapted finite volume formulations for geometric improvement. The reasons for applying a finite element implementation in CFD include at least the mathematical elegance of a process, purely defined in calculus, and the ability of its theory to precisely qualify approximation error in intrinsic norms.

The first challenge in this dissertation is the derivation of an equation system usable on a real-world applicable problem. Therefore an LES formulation for the 3-dimensional, incompressible thermal Navier-Stokes equation system, focused on prediction of mixed convection flows ventilated domains characterized by human habitation is constructed.

As second point, the rational LES theory is extended from previous publications to the heat and/or mass transport problem class, with focus on suitable boundary conditions for bounded domains. Additional terms are created for the influence of the filtering process onto the Navier-Stokes equation system, as well as expressions for an appropriate sub-grid scale (SGS) model.

The main issue in LES is the accurate representation of the energy cascade from resolved scales towards scales unresolved, the action of which must be modeled. Perhaps the most implemented sub-grid scale model remains that of Smagorinsky, [Smag63]. This work examines alternatives to the Smagorinsky sub-grid scale (SGS) model, recently proven to be of inappropriate order in filter measure, [Joh04]. The proposed alternative is via TWS, proven in the past as a scale-sensitive stabilization (numerical diffusion) process dominant at the smallest mesh scales. It examines the general feasibility of this approach, as well as the efficiency with which the mechanical energy dissipation induces algorithm stability.

A comparison to verification and benchmarking results for pertinent multi-dimensional mixed convection problem statements examines the accuracy of the new method. In particularly, the TWS SGS model energy dissipation behavior is examined on a turbulent duct flow, as well as on a laminar driven cavity. The 8x1 thermal cavity test case is employed to detail differences between the TWS SGS model approach and several established SGS models in a laminar to turbulent flow simulation.

In summary, the specific goals of this dissertation project were

- the derivation of an LES formulation for the 3-dimensional, incompressible thermal Navier-Stokes equation system, focused on prediction of mixed convection flows in ventilated domains characterized by human habitation,
- the extension of the rational LES formulation to the heat and/or mass transport problem class, with focus on boundary conditions suitable to bounded domain implementation,
- the assessment of the use of the TWS beta term to dissipate energy at the smallest resolved scales, compared to published rational and other LES sub-grid scale models,
- and the generation of benchmark and validation class solutions pertinent to multi-dimensional mixed convection problem statements.

This dissertation documents the successful derivation of a 3-dimensional LES formulation for mass, momentum, energy and mass transport based on the rational LES approach, with the filtering extended to heat and mass transport expressions. Several boundary condition options for LES are examined. Particularly novel is the use of a dual theory LES approach, developed in this project to overcome rational LES theory restrictions on meshing regularity at boundaries. The TWS beta term was compared to SGS models from Smagorinsky, Layton and Illiescu and showed improved behavior regarding location and magnitude of energy dissipation, as well as positive influence on the stability of the algorithm. The benchmarking and validation results on the turbulent duct, driven cavity and the thermal cavity prove the potential usefulness of the newly developed TWS SGS model.

2. Large Eddy Simulation Theory

2.1 Conservation Principles

The partial differential equation system describing the Eulerian conservation principles for viscous, thermal, incompressible Newtonian fluid is termed the Navier-Stokes (NS) equations, complemented with a temperature-driven body force term, the energy equation and a mass transport equation. The NS partial differential equation (PDE) system dimensional form for mass, momentum, energy and mass transport contains

$$\mathcal{L}\left(\rho_0\right) = \frac{\partial u_i}{\partial x_i} = 0 \tag{2.1}$$

$$\begin{aligned}\mathcal{L}\left(u_i\right) = \frac{\partial u_i}{\partial t} + \frac{\partial}{\partial x_j}\left[u_j u_i - \upsilon\left(\frac{\partial u_i}{\partial x_j} + \frac{\partial u_j}{\partial x_i}\right) + \frac{p}{\rho_0}\delta_{ij}\right] \\ + \left[\beta\left(T - T_r\right)g\right]\hat{\mathbf{g}}_{\mathbf{i}} = 0\end{aligned} \tag{2.2}$$

$$\mathcal{L}\left(T\right) = \frac{\partial T}{\partial t} + \frac{\partial}{\partial x_j}\left[u_j T - \alpha\frac{\partial T}{\partial x_j}\right] - \frac{\upsilon}{c_p}\Phi - \frac{1}{\rho_0 c_p}S_T = 0 \tag{2.3}$$

$$\mathcal{L}\left(c_\varepsilon\right) = \frac{\partial c_\varepsilon}{\partial t} + \frac{\partial}{\partial x_j}\left[u_j c - D_\varepsilon\frac{\partial c_\varepsilon}{\partial x_j}\right] - S_\varepsilon = 0 \tag{2.4}$$

The tensor index range $1 \le i, j \le n = 3$, and the Boussinesq approximation [Bou03] is employed to expresses the thermal body force in the momentum equation, (2.2).

This PDE system can be non-dimensionalized with the following scalings,

$$x_j^* = \frac{x_j}{L_r} \qquad u_j^* = \frac{u_j}{U_r} \qquad t^* = \frac{t}{L_r / U_r}$$

$$\Theta^* = \frac{T - T_r}{\Delta T_r} \qquad P^* = \frac{p / \rho_0}{U_r^2} \qquad c_\varepsilon^* = \frac{c_\varepsilon}{U_r L^3}$$

generating the fundamental dimensionless groups

$$\mathrm{Re} \equiv \frac{U_r L_r}{\upsilon} \qquad \mathrm{Pr} \equiv \frac{\upsilon}{\alpha} \qquad \mathrm{St} \equiv \frac{\omega_r L_r}{U_r}$$

$$\mathrm{Gr} \equiv \frac{\beta g \Delta T_r L_r^3}{\upsilon^2} \qquad \mathrm{Ec} \equiv \frac{U_r^2}{c_p \Delta T_r} \qquad \mathrm{Ar} \equiv \frac{\mathrm{Gr}}{\mathrm{Re}^2} \qquad \mathrm{Sc} \equiv \frac{\upsilon}{D_\varepsilon}$$

for ω_r being a frequency (traditionally associated with vortex shedding) and $\alpha = k / \rho c_p$.

The resulting NS conservation principles in preferred non-dimensional PDE form are

$$\mathcal{L}(\rho_0) = \frac{\partial u_j}{\partial x_j} = 0 \tag{2.5}$$

$$\begin{aligned} \mathcal{L}(u_i) = \mathrm{St}\frac{\partial u_i}{\partial t} + \frac{\partial}{\partial x_j}\left[u_j u_i - \frac{1}{\mathrm{Re}}\left(\frac{\partial u_i}{\partial x_j} + \frac{\partial u_j}{\partial x_i} \right) + p\delta_{ij} \right] \\ + Ar\Theta \hat{\mathbf{g}}_\mathbf{i} = 0 \end{aligned} \tag{2.6}$$

$$\mathcal{L}(\Theta) = \mathrm{St}\frac{\partial \Theta}{\partial t} + \frac{\partial}{\partial x_j}\left[u_j \Theta - \frac{1}{\mathrm{Re}\,\mathrm{Pr}}\frac{\partial \Theta}{\partial x_j} \right] - \frac{\mathrm{Ec}}{\mathrm{Re}}\Phi - s_\Theta = 0 \tag{2.7}$$

$$\mathcal{L}\left(c_\varepsilon\right) = \mathrm{St}\frac{\partial c}{\partial t} + \frac{\partial}{\partial x_j}\left[u_j c_\varepsilon - \frac{1}{\mathrm{Re}\,\mathrm{Sc}}\frac{\partial c_\varepsilon}{\partial x_j}\right] - s_\varepsilon = 0 \tag{2.8}$$

Note the second term multiplied by Re^{-1} in (2.6) vanishes identically, via (2.5). It is retained for future reference in the LES theory formulation.

2.2 Spatial Filtering

The goal in LES is to accurately resolve all flow scales ranging from that of the container to the limit of resolvability enforced by computer (mesh density) limitations. Appropriate spatial filtering operations need to be identified, resulting in the time-dependent, space-filtered velocity vector $\overline{u}_i$, pressure $\overline{p}$, temperature $\overline{\Theta}$ and mass fractions $\overline{c}_\varepsilon$, respectively. This spatial operation is called filtering, and filtered variables are symbolized via an over-bar. Thus, each NS state variable member is divided into resolved and unresolved scales as

$$\begin{aligned} u_i\left(x_j,t\right) &= \overline{u}_i\left(x_j,t\right) + u_i'\left(x_j,t\right) \\ \Theta\left(x_j,t\right) &= \overline{\Theta}\left(x_j,t\right) + \Theta'\left(x_j,t\right) \\ c_\varepsilon\left(x_j,t\right) &= \overline{c}_\varepsilon\left(x_j,t\right) + c_\varepsilon'\left(x_j,t\right) \end{aligned} \tag{2.9}$$

The resolved (computable) components in (2.9) are $\left(\overline{u}_i, \overline{\Theta}, \overline{c}_\varepsilon\right)$, while $\left(u_i', \Theta', c_\varepsilon'\right)$ exist at the unresolved or subgrid scales. The filter operation must fulfill two distinct requirements; first the filter has to be a linear operator, e.g.

$$\overline{u_i + \lambda v_i} = \overline{u}_i + \lambda \overline{v}_i \tag{2.10}$$

and second, differentiation and filtering operations must commute, i.e.

$$\overline{\left(\frac{\partial u_i}{\partial x_j}\right)} = \left(\frac{\partial \overline{u}_i}{\partial x_j}\right), \quad \overline{\left(\frac{\partial u_i}{\partial t}\right)} = \left(\frac{\partial \overline{u}_i}{\partial t}\right), \; i, j = 1, \ldots, d \tag{2.11}$$

If the NS state variable describes a flow field that is adequately smooth in space and time, then filtering and differentiation generally commute.

The filtering operation employs the mathematical convolution of each state variable member with a filter function g, e.g., in one dimension

$$\overline{u}\left(x,t\right) \equiv \int_{-\infty}^{\infty} g\left(y\right)\, u\left(x-y,t\right) dy \tag{2.12}$$

In the following sections the convolution (2.12) is multi-dimensional symbolized as

$$\overline{u}_i\left(x_j,t\right) = g_\delta * u_i\left(x_j,t\right) \tag{2.13}$$

where δ signifies the (constant) scale (measure) of the filter.

The commonly applied filter functions for LES formulations to date are the box filter, the sharp spectral filter, and the Gaussian filter (see Table 2.1)[*]. Figure 2.1 shows these filter functions in one-dimensional physical space, while Figure 2.2 shows their transfer functions in wave number or Fourier space. The filtering Fourier transform process is formed in wave number space, since it is often possible to find simpler approximations to complex functions in Fourier space, which then can be transferred back into physical space.

Without definition of a specific filter function, filtering (2.5) – (2.8) results in the Navier-Stokes LES theory PDE system

[*] All tables and figures are compiled in the appendix.

$$\mathcal{L}\left(\rho_0\right)=\frac{\partial \overline{u}_j}{\partial x_j}=0 \tag{2.14}$$

$$\begin{aligned}\mathcal{L}\left(\overline{u}_i\right)=&\,\mathrm{St}\frac{\partial \overline{u}_i}{\partial t}+\frac{\partial}{\partial x_j}\left[\overline{u_j u_i}-\frac{1}{\mathrm{Re}}\left(\frac{\partial \overline{u}_i}{\partial x_j}+\frac{\partial \overline{u}_j}{\partial x_i}\right)+\frac{\overline{p}}{\rho_0}\delta_{ij}\right]\\&+Ar\overline{\Theta}\hat{\mathbf{g}}_{\mathbf{i}}=0\end{aligned} \tag{2.15}$$

$$\mathcal{L}\left(\overline{\Theta}\right)=\mathrm{St}\frac{\partial \overline{\Theta}}{\partial t}+\frac{\partial}{\partial x_j}\left[\overline{u_j\Theta}-\frac{1}{\mathrm{Re}\,\mathrm{Pr}}\frac{\partial \overline{\Theta}}{\partial x_j}\right]-\frac{\mathrm{Ec}}{\mathrm{Re}}\overline{\Phi}+\mathrm{source}=0 \tag{2.16}$$

$$\mathcal{L}\left(\overline{c}_\varepsilon\right)=\mathrm{St}\frac{\partial \overline{c}_\varepsilon}{\partial t}+\frac{\partial}{\partial x_j}\left[\overline{u_j c_\varepsilon}-\frac{1}{\mathrm{Re}\,\mathrm{Sc}}\frac{\partial \overline{c}_\varepsilon}{\partial x_j}\right]=0 \tag{2.17}$$

2.3 LES Closure for Momentum

The LES theory-created non-linear convection terms in equations (2.15) to (2.17) lead to the LES closure requirement. For the momentum equation (2.15), this term has historically [Pop00] been expressed as

$$\begin{aligned}\overline{u_j u_i}&=\overline{u}_j\overline{u}_i+\underbrace{\left(\overline{\overline{u}_j\overline{u}_i}-\overline{u}_j\overline{u}_i\right)}_{L_{ij}}+\underbrace{\left(\overline{\overline{u}_j u'_i}+\overline{u'_j\overline{u}_i}\right)}_{C_{ij}}+\underbrace{\overline{u'_j u'_i}}_{R_{ij}}\\&=\overline{u}_j\overline{u}_i+\tau_{ij}^{R}=\overline{u}_j\overline{u}_i+\tau_{ij}^{r}+\frac{1}{3}\tau_{kk}^{R}\delta_{ij}\end{aligned} \tag{2.18}$$

where L_{ij}, C_{ij} and R_{ij} are termed the Leonard, Cross and subgrid scale (SGS) Reynolds stresses, respectively. The isotropic part τ_{kk}^{R} of the residual LES stress tensor τ_{ij}^{R} can be included in a modified pressure. The remaining anisotropic stress tensor requires

determination, which to date has generally been accomplished via an eddy viscosity model in the form

$$\tau_{ij}^{r} \equiv -2\upsilon_t \bar{S}_{ij} \tag{2.19}$$

This thus requires definition of a "turbulent eddy viscosity" υ_t, while the strain rate tensor definition is

$$\bar{S}_{ij} = \frac{1}{2}\left(\frac{\partial \bar{u}_i}{\partial x_j} + \frac{\partial \bar{u}_j}{\partial x_i}\right) \tag{2.20}$$

This historical modeling process has met with some success, [Pop00]. Its principle limitation is that it is only a model. In this research, this requirement for a "total model" is replaced via the rational LES theory [IJL+03], [Joh04]. The mathematically, i.e., unmodified, classic definition of the filtered convection term in (2.15) is

$$\overline{u_j u_i} = \overline{\bar{u}_j \bar{u}}_i + \overline{u'_j \bar{u}}_i + \overline{\bar{u}_j u'}_i + \overline{u'_j u'}_i \tag{2.21}$$

The first tensor in (2.21) signifies the convection influence of the large scale flow structures, called eddies, onto themselves. The second and third tensors describe the convection interaction between the resolved and unresolved (SGS) eddies. The last term is termed the sub-grid scale (SGS) tensor, the action of which is mechanical energy dissipation at the top of the unresolved scales of the flow.

To minimize modeling requirements, the goal is to mathematically formalize the convolution process leading to (2.21). Via the convolution, the Fourier transform of the first three terms on the right side of (2.21) are

$$F\left(\overline{\bar{u}_j \bar{u}}_i\right) = F\left(g_\delta\right) F\left(\bar{u}_j \bar{u}_i\right) \tag{2.22}$$

$$F\left(\overline{\bar{u}_j u'_i}\right) = F\left(g_\delta\right)\left(F\left(\bar{u}_j\right) * F\left(u'_i\right)\right)$$
$$F\left(\overline{u'_j \bar{u}_i}\right) = F\left(g_\delta\right)\left(F\left(u'_j\right) * F\left(\bar{u}_i\right)\right) \tag{2.23}$$

For $F\left(g_\delta\right) \neq 0$ the Fourier transform of u_i is

$$F\left(u_i\right) = \frac{F\left(g_\delta\right) F\left(u_i\right)}{F\left(g_\delta\right)} = \frac{F\left(\bar{u}_i\right)}{F\left(g_\delta\right)} \tag{2.24}$$

Using the decomposition $u_i = \bar{u}_i + u'_i$ one determines

$$F\left(u'_i\right) = \left(\frac{1}{F\left(g_\delta\right)} - 1\right) F\left(\bar{u}_i\right) \tag{2.25}$$

Inserting (2.25) into (2.23) results in

$$F\left(\overline{\bar{u}_j \bar{u}_i}\right) = F\left(g_\delta\right) F\left(\bar{u}_j \bar{u}_i\right)$$
$$F\left(\overline{\bar{u}_j u'_i}\right) = F\left(g_\delta\right)\left(F\left(\bar{u}_j\right) * \left(\frac{1}{F\left(g_\delta\right)} - 1\right) F\left(\bar{u}_i\right)\right) \tag{2.26}$$
$$F\left(\overline{u'_j \bar{u}_i}\right) = F\left(g_\delta\right)\left(\left(\frac{1}{F\left(g_\delta\right)} - 1\right) F\left(\bar{u}_j\right) * F\left(\bar{u}_i\right)\right)$$

Since the Fourier transform of the resolved scales is available, an approximation has to be found for $F\left(g_\delta\right)$ and $\frac{1}{F\left(g_\delta\right)}$ to determine (2.26).

One approach used quite often in the past, is via a second order Taylor series approximation to the Gaussian. For the filter measure δ, the result is

$$F\left(g_\delta\right)\left(\delta, y_i\right) = 1 - \frac{\left\|y_i\right\|_2^2}{4\gamma} \delta^2 + O\left(\delta^4\right)$$
$$\frac{1}{F\left(g_\delta\right)\left(\delta, y_i\right)} = 1 + \frac{\left\|y_i\right\|_2^2}{4\gamma} \delta^2 + O\left(\delta^4\right) \tag{2.27}$$

Inserting (2.27) into (2.26) and employing certain properties of Fourier transforms results in

$$
\begin{aligned}
F\left(\overline{\overline{u}_j\overline{u}_i}\right) &= F\left(\overline{u}_j\overline{u}_i\right) + \frac{\delta^2}{4\gamma}F\left(\frac{\partial^2\left(\overline{u}_j\overline{u}_i\right)}{\partial x_k \partial x_k}\right) + O\left(\delta^4\right) \\
F\left(\overline{\overline{u}_j u'_i}\right) &= -\frac{\delta^2}{4\gamma}F\left(\overline{u}_j\frac{\partial^2\overline{u}_i}{\partial x_k \partial x_k}\right) + O\left(\delta^4\right) \\
F\left(\overline{u'_j\overline{u}_i}\right) &= -\frac{\delta^2}{4\gamma}F\left(\frac{\partial^2\overline{u}_j}{\partial x_k \partial x_k}u_i\right) + O\left(\delta^4\right)
\end{aligned}
\tag{2.28}
$$

Applying the inverse Fourier transform gives the filtered approximations in physical space

$$
\begin{aligned}
\overline{\overline{u}_j\overline{u}_i} &= \overline{u}_j\overline{u}_i + \frac{\delta^2}{4\gamma}\frac{\partial^2\left(\overline{u}_j\overline{u}_i\right)}{\partial x_k \partial x_k} + O\left(\delta^4\right) \\
\overline{\overline{u}_j u'_i} &= -\frac{\delta^2}{4\gamma}\overline{u}_j\frac{\partial^2\overline{u}_i}{\partial x_k \partial x_k} + O\left(\delta^4\right) \\
\overline{u'_j\overline{u}_i} &= -\frac{\delta^2}{4\gamma}\frac{\partial^2\overline{u}_j}{\partial x_k \partial x_k}\overline{u}_i + O\left(\delta^4\right)
\end{aligned}
\tag{2.29}
$$

Then, using kinematics relations and omitting all terms $O\left(\delta^4\right)$ or higher, the final expression for the sum is

$$
\overline{\overline{u}_j\overline{u}_i} + \overline{\overline{u}_j u'_i} + \overline{u'_j\overline{u}_i} = \overline{u}_j\overline{u}_i + \frac{\delta^2}{2\gamma}\frac{\partial\overline{u}_j}{\partial x_k}\frac{\partial\overline{u}_i}{\partial x_k} \tag{2.30}
$$

The problem with the second order Taylor series polynomial approximation of the Gaussian filter is that it is accurate only in a very small wave number range, and completely wrong for large wave numbers (see Figure 2.3). Since the task of the Gaussian filter is to render negligible the small eddies, which corresponds to large wave numbers in Fourier space, this approximation is quite unsatisfactory.

Thereby, a more accurate approximation for the Gaussian filter is needed. The lowest order rational approximation of the exponential in the Gaussian filter [GL00] is

$$e^{ax} = \frac{1}{1+ax} + O\left(a^2 x^2\right) \tag{2.31}$$

which leads to the following Pade approximations for $F\left(g_\delta\right)$ and $\frac{1}{F\left(g_\delta\right)}$

$$\begin{aligned} F\left(g_\delta\right)\left(\delta, y_i\right) &= \frac{1}{1+\frac{\left\|y_i\right\|_2^2}{4\gamma}} + O\left(\delta^4\right) \\ \frac{1}{F\left(g_\delta\right)\left(\delta, y_i\right)} &= 1 + \frac{\left\|y_i\right\|_2^2}{4\gamma}\delta^2 + O\left(\delta^4\right) \end{aligned} \tag{2.32}$$

From Figure 2.4 it is clear that the Pade form much better approximates the behavior of the Gaussian filter in Fourier space. Further, this approximation is monotone, non-negative, an important contribution for realization of the LES stress tensor formulation, [Joh04].

Using (2.32) in (2.26) and taking the inverse Fourier transform yields

$$\begin{aligned} \overline{\overline{u}_j \overline{u}_i} &= \left(\delta_{ij} - \frac{\delta^2}{4\gamma}\frac{\partial^2}{\partial x_k \partial x_k}\right)^{-1}\left(\overline{u}_j \overline{u}_i\right) + O\left(\delta^4\right) \\ \overline{\overline{u}_j u'_i} &= -\frac{\delta^2}{4\gamma}\left(\delta_{ij} - \frac{\delta^2}{4\gamma}\frac{\partial^2}{\partial x_k \partial x_k}\right)^{-1}\left(\overline{u}_j \frac{\partial^2 \overline{u}_i}{\partial x_k \partial x_k}\right) + O\left(\delta^4\right) \\ \overline{u'_j \overline{u}_i} &= -\frac{\delta^2}{4\gamma}\left(\delta_{ij} - \frac{\delta^2}{4\gamma}\frac{\partial^2}{\partial x_k \partial x_k}\right)^{-1}\left(\frac{\partial^2 \overline{u}_j}{\partial x_k \partial x_k}\overline{u}_i\right) + O\left(\delta^4\right) \end{aligned} \tag{2.33}$$

which, when omitting all term $O\left(\delta^4\right)$ or higher, leads to

$$\overline{\overline{u}_j\overline{u}_i} + \overline{\overline{u}_j u_i'} + \overline{u_j'\overline{u}_i} = \overline{u}_j\overline{u}_i + \frac{\delta^2}{2\gamma}\left(\delta_{ij} - \frac{\delta^2}{4\gamma}\frac{\partial^2}{\partial x_k \partial x_k}\right)^{-1}\left(\frac{\partial \overline{u}_j}{\partial x_k}\frac{\partial \overline{u}_i}{\partial x_k}\right) \tag{2.34}$$

where δ_{ij} is the Kronecker delta.

In the following, the inverse operator in (2.34) is defined as

$$A \equiv \left(\delta_{ij} - \frac{\delta^2}{4\gamma}\frac{\partial^2}{\partial x_k \partial x_k}\right)^{-1} \tag{2.35}$$

hence the matrix operator A defines an elliptic, second order boundary value problem, generating a harmonic PDE which John terms the "auxiliary problem." For the momentum equation, the rational Pade formulation results in an analytical form for the first three LES theory-generated Reynolds stress tensors as

$$R_{ij} = A\left(\frac{\partial \overline{u}_j}{\partial x_l}\frac{\partial \overline{u}_i}{\partial x_l}\right) \tag{2.36}$$

hence

$$\mathcal{L}\left(R_{ij}\right) = -\frac{\delta^2}{4\gamma}\frac{\partial^2 R_{ij}}{\partial x_k \partial x_k} + R_{ij} - \frac{\partial \overline{u}_j}{\partial x_l}\frac{\partial \overline{u}_i}{\partial x_l} = 0 \tag{2.37}$$

Since this represents an elliptic boundary value problem, boundary conditions (BCs) on the entire domain closure are required. For previous studies on unbounded domains, Layton et al, [IJL+03], have employed the homogeneous Neumann condition

$$\left(\frac{\partial R_{ij}}{\partial x_k}\right)\hat{n}_k = 0 \tag{2.38}$$

2.4 LES for Scalar Transport

One of the original contributions in this dissertation is to extend the theory of the previous section to the energy and mass transport PDEs, (2.16) and (2.17).

The filtering of the energy equation produces the advection vector

$$\overline{u_j\Theta} = \overline{\bar{u}_j\bar{\Theta}} + \overline{u'_j\bar{\Theta}} + \overline{\bar{u}_j\Theta'} + \overline{u'_j\Theta'} \tag{2.39}$$

Following the same derivations as for the momentum equation yields

$$\overline{\bar{u}_j\bar{\Theta}} + \overline{\bar{u}_j\Theta'} + \overline{u'_j\bar{\Theta}} = \bar{u}_j\bar{\Theta} + A\left(\frac{\partial\bar{u}_j}{\partial x_k}\frac{\partial\bar{\Theta}}{\partial x_k}\right) \tag{2.40}$$

with the auxiliary problem

$$Y_j = A\left(\frac{\partial\bar{u}_j}{\partial x_l}\frac{\partial\bar{\Theta}}{\partial x_l}\right)$$

hence

$$\mathcal{L}\left(Y_j\right) = -\frac{\delta^2}{4\gamma}\frac{\partial^2 Y_j}{\partial x_k\partial x_k} + Y_j - \frac{\partial\bar{u}_j}{\partial x_l}\frac{\partial\bar{\Theta}}{\partial x_l} = 0 \tag{2.41}$$

For each species a separate transport equation is required, see (2.17), which has a mass advection vector of the form

$$\overline{u_j c_\varepsilon} = \overline{\bar{u}_j\bar{c}_\varepsilon} + \overline{u'_j\bar{c}_\varepsilon} + \overline{\bar{u}_j c'_\varepsilon} + \overline{u'_j c'_\varepsilon} \tag{2.42}$$

The Fourier analysis leads to

$$\overline{\bar{u}_j\bar{c}_\varepsilon} + \overline{\bar{u}_j c'_\varepsilon} + \overline{u'_j\bar{c}_\varepsilon} = \bar{u}_j\bar{c}_\varepsilon + A\left(\frac{\partial\bar{u}_j}{\partial x_k}\frac{\partial\bar{c}_\varepsilon}{\partial x_k}\right) \tag{2.43}$$

with

$$Z_j = A\left(\frac{\partial \overline{u}_j}{\partial x_l}\frac{\partial \overline{c}_\varepsilon}{\partial x_l}\right)$$

hence

$$\mathcal{L}\left(Z_j\right) = -\frac{\delta^2}{4\gamma}\frac{\partial^2 Z_j}{\partial x_k \partial x_k} + Z_j - \frac{\partial \overline{u}_j}{\partial x_l}\frac{\partial \overline{c}_\varepsilon}{\partial x_l} = 0 \tag{2.44}$$

2.5 Closure for the SGS Reynolds Tensor

The last term of Eqn. (2.21) to be analyzed in Fourier space is the SGS Reynolds stress tensor. Using the second order Taylor series polynomial to approximate the Gaussian filter results in, [Joh04]

$$\overline{u_j' u_i'} = \frac{\delta^4}{16\gamma^2}\frac{\partial^2 \overline{u}_j}{\partial x_k \partial x_k}\frac{\partial^2 \overline{u}_i}{\partial x_l \partial x_l} + O\left(\delta^6\right) \tag{2.45}$$

and for the second order Pade approximation

$$\overline{u_j' u_i'} = \frac{\delta^4}{16\gamma^2} A\left(\frac{\partial^2 \overline{u}_j}{\partial x_k \partial x_k}\frac{\partial^2 \overline{u}_i}{\partial x_l \partial x_l}\right) + O\left(\delta^6\right) \tag{2.46}$$

Since the lead terms in both (2.45) and (2.46) are of order $O\left(\delta^4\right)$, they are negligible in context of the order of terms retained in (2.33). Hence, to the significant order, the developed LES theory for the approximation to the Gaussian filter is not capable of generating a useful expression for $\overline{u_j' u'}_i$. The same conclusion applies to $\overline{u_j' \Theta'}$ and $\overline{u_j' c_\varepsilon'}$. Therefore, the SGS Reynolds stress and heat/mass flux vectors must be modeled. A detailed examination of the options available is given in section 2.7.

2.6 Sub-grid Scale Closure

LES theory characterizes turbulent motion as consisting of flow structures called eddies possessing a wide range of scales. The largest eddies are of enclosure dimension scale, are the most energy rich structures, and cascade their energy to progressively smaller scales, until at the smallest scale the mechanical energy is dissipated into heat by the action of viscosity for genuine NS. This phenomena is termed the energy cascade. The LES filter size δ determines the eddy scales that are resolved. All scales that are smaller than this so-called cut-off scale have to be modeled. Hence enters the LES sub-grid scale (SGS) model, the purpose of which is to emulate the action of viscosity in dissipating energy at the smallest resolvable scale.

The theoretically simplest LES SGS model for momentum, developed by Smagorinsky [Sma63], defines a turbulent eddy viscosity. Based on classical mixing-length hypotheses, the Smagorinsky SGS model is

$$\overline{u'_j u'_i} \equiv -\upsilon_t \overline{S}_{ij} \tag{2.47}$$

$$\upsilon_t = C_s \delta^2 \left\| \overline{S} \right\|_F = C_s \delta^2 \hat{S} \tag{2.48}$$

for the Frobenius norm definition

$$\left\| \overline{S} \right\|_F \equiv \hat{S} = \left(2\overline{S}_{ij}\overline{S}_{ij} \right)^{1/2} \tag{2.49}$$

C_s is the “Smagorinsky constant,” a global constant that has to be adjusted for each applied flow problem [ZSK93]. Furthermore, for wall-bounded problems it is necessary to adjust the filter width closer to the wall, or develop a wall-function expression to

reduce the influence of the sub-grid scale term when approaching the wall. The filter for the Smagorinsky SGS closure model is the simple box filter, see Figure 2.1. Adjusting the Smagorinsky model with a van-Driest damping function, [Cut01], has show acceptable performance for select benchmark problems.

However, recent numerical studies, [Joh04], confirm that the Smagorinsky formulation is overly diffusive, confirming that (2.48) being only second-order in filter scale δ is theoretically inconsistent with the rational LES theory. Alternative eddy-viscosity type SGS closure models were proposed by Illiescu-Layton [IL98], based on the physical reasoning that the turbulent diffusion parameters should depend on the kinetic energy of the small eddies. Using an expression developed by Kolmogorov and Prandtl leads to

$$\upsilon_t = c l_m \sqrt{\frac{1}{2}\rho \left\| u_i' \right\|_2^2} \tag{2.50}$$

with l_m the mixing length, usually set to $l_m = \delta$. Note that $\|\bullet\|_2$ is the L2 norm. Neglecting terms of $O\left(\delta^4\right)$, and using Eqn. (2.25) and (2.32), gives an approximation for u_i' as

$$u_i' \approx -\frac{\delta^2}{4\gamma}\frac{\partial^2 \overline{u}_i}{\partial x_k \partial x_k} \tag{2.51}$$

Inserting (2.51) into (2.50) gives

$$\upsilon_t = C_s \frac{\delta^3}{\gamma}\left\| \frac{\partial^2 \overline{u}_i}{\partial x_k \partial x_k} \right\|_2 + O\left(\delta^4\right) \tag{2.52}$$

which approximates more closely the rational LES order requirement.

A second possibility is to base the diffusion parameter on the averaged kinetic energy, which results in

$$\upsilon_t = C_s \frac{\delta^3}{\gamma} \left\| g_\delta * \frac{\partial^2 \overline{u}_i}{\partial x_k \partial x_k} \right\|_2 \tag{2.53}$$

With

$$\begin{aligned} F\left(\overline{u}_i - g_\delta * \overline{u}_i\right) &= F\left(g_\delta\right)\left(\frac{1}{F\left(g_\delta\right)} - 1\right) F\left(\overline{u}_i\right) \\ &\approx F\left(g_\delta\right)\left(\frac{\left\|y_i\right\|_2^2}{4\gamma}\delta^2\right) F\left(\overline{u}_i\right) = -\frac{\delta^2}{4\gamma} F\left(g_\delta * \frac{\partial^2 \overline{u}_i}{\partial x_k \partial x_k}\right) \end{aligned} \tag{2.54}$$

a third model is derived as, [Joh04], [IL98],

$$\upsilon_t = C_s \frac{\delta^3}{\gamma} \left\| \overline{u}_j - g_\delta * \frac{\partial^2 \overline{u}_i}{\partial x_k \partial x_k} \right\|_2 \tag{2.55}$$

which is also third order in filter scale δ. Approximating the convolution operation on g_δ, similar to Eqn. (2.32) in terms of the inverse operator A, leads to the alternatives for (2.52) and (2.55) as

$$\upsilon_t = C_s \frac{\delta^3}{\gamma} \left\| A\left(\overline{u}_i\right) \right\|_2 \tag{2.56}$$

$$\upsilon_t = C_s \frac{\delta^3}{\gamma} \left\| \overline{u}_j - A\left(\overline{u}_i\right) \right\|_2 \tag{2.57}$$

2.7 An Alternative SGS Formulation

As an alternative to strictly "modeling" the SGS tensor, Boris et al. [BGO+92] conjectured that, since an LES SGS model in principle adds diffusion, it should be possible to directly use the numerical diffusion supplied by a CFD algorithm, hence their "Monotone Integrated LES" model. Various implementations of this thought can be found, [RF99], [SCC01], [JC02]. Using their flux-corrected transport algorithm, this numerical diffusion operator indeed provided the mechanical energy drainage required to create dissipation at the sub-grid level.

At the UT CFD Laboratory extensive research has been completed on development of a NS conservation principle modification process, [Kol00], [Kim88], [Cha97], via Taylor series manipulations. Analytical expressions result from this theory that, properly chosen, can increase stability and error control of finite element CFD algorithms. Following the idea of the direct use of algorithm numerical diffusion, the same effect should be provided by the Taylor Weak Statement (TWS) algorithm "beta" term modification to Navier-Stokes PDE systems. The analytical theory is established for both steady and time-accurate unsteady NS, and in both cases the TWS beta term theory confirms diffusion is limited to the smallest mesh scales.

A unique aspect of finite element implementations of the TWS theory is that precise *a priori* error estimates exist for asymptotic convergence under mesh refinement in the

intrinsic energy semi-norm, identical to the square of the L2 norm. Specifically, the TWS formulation for unsteady NS solution possesses asymptotic error estimates of the forms

$$\left\| e^h\left(u^h,t\right)\right\|_E \le Ch^{2\gamma}\left\| data\right\|_{\Omega,\partial\Omega} + C_t \Delta t^{f(\theta)}\left\| u^h\left(t_0\right)\right\|_E$$
$$\gamma = \begin{cases} \min\left(k, r-1\right) & \text{for } \mathrm{Re}^{-1} > 0 \\ \min\left(1, r-1\right) & \text{for } \mathrm{Re}^{-1} = 0 \end{cases} \tag{2.58}$$

where k symbolizes the finite element basis degree, r is the smoothness measure of the exact solution, and h is the measure of the mesh. For steady flow and smooth initial data the error estimate for the $k=1$ basis implementation is

$$\left\| e^h\left(u^h\right)\right\|_E \le Ch^4\left\| data\right\|_{\Omega,\partial\Omega} \tag{2.59}$$

The accuracy of (2.58) – (2.59) has been thoroughly validated. The beta term derivation is originally based on a Taylor series expansion of the NS time term [Kim88], resulting in the analytically modified momentum conservation equation

$$\mathcal{L}^m\left(u_i\right) = \mathcal{L}\left(u_i\right) - \frac{\Delta t}{2}\frac{\partial}{\partial x_j}\left(\beta u_j u_k \frac{\partial u_i}{\partial x_k}\right) + \text{additional terms} \tag{2.60}$$

Further research by Kolesnikov, [Kol00], for steady NS flow eliminates the arbitrary coefficient β in (2.60) leading to

$$\mathcal{L}^m\left(u_i\right) = \mathcal{L}\left(u_i\right) - \frac{\partial}{\partial x_j}\left(\frac{\mathrm{Re}\, h^2}{12} u_j u_k \frac{\partial u_i}{\partial x_k}\right) \tag{2.61}$$

For adequate capture of the energy in the resolved scales, the relation between filter scale and mesh measure is, [Pop00],

$$\frac{\delta}{h} \ge 2 \tag{2.62}$$

Using (2.62) in the theory of the error estimate, I expect that the FE implementation of the rational LES theory should approximate a fourth-order formulation in δ for the $k=2$ quadratic basis unsteady theory, or the $k=1$ linear basis steady flow theory. Based on these options, the TWS beta diffusive flux vector set may prove appropriate for meeting the SGS dissipation tensor scale requirement. Selecting the later, and realizing the SGS tensor must be symmetric at the minimum, hence recalling [NoB89], the proposed model is

$$-\overline{u'_j u'}_i = \frac{\beta \operatorname{Re} h^2}{24}\left(\bar{u}_j \bar{u}_k \bar{S}_{ik} + \bar{u}_i \bar{u}_k \bar{S}_{jk}\right) + O\left(\delta^4\right) \tag{2.63}$$

where β is an adjustable factor (for debug). The companion expressions, theoretically derived for the energy and mass transport PDEs, are the vectors

$$-\overline{u'_j \Theta'} = \frac{\beta_t \operatorname{Re} \operatorname{Pr} h^2}{12} \bar{u}_k \bar{u}_j \frac{\partial \bar{\Theta}}{\partial x_k} + O\left(\delta^4\right) \tag{2.64}$$

$$-\overline{u'_j c'_\varepsilon} = \frac{\beta_c \operatorname{Re} \operatorname{Sc} h^2}{12} \bar{u}_k \bar{u}_j \frac{\partial \bar{c}_\varepsilon}{\partial x_k} + O\left(\delta^4\right) \tag{2.65}$$

2.8 Rational LES Flux Vector Representation

This dissertation project approach is to develop the rational LES Navier-Stokes PDE system in flux vector form. Leaving the SGS tensor model general, the established LES NS PDE system is

$$\mathcal{L}\left(\rho_0\right) = \frac{\partial \bar{u}_j}{\partial x_j} = 0 \tag{2.66}$$

$$\mathcal{L}\left(\bar{u}_i\right) = \mathrm{St}\frac{\partial \bar{u}_i}{\partial t} + \frac{\partial}{\partial x_j}\left[\bar{u}_j\bar{u}_i - \frac{2}{\mathrm{Re}}\bar{S}_{ij} + \frac{\delta^2}{2\gamma}R_{ij} + \overline{u'_j u'}_i + \bar{P}\delta_{ij}\right] + \mathrm{Ar}\bar{\Theta}\hat{\mathbf{g}}_{\mathbf{i}} = 0 \tag{2.67}$$

$$\mathcal{L}\left(\bar{\Theta}\right) = \mathrm{St}\frac{\partial \bar{\Theta}}{\partial t} + \frac{\partial}{\partial x_j}\left[\bar{u}_j\bar{\Theta} - \frac{1}{\mathrm{Re}\,\mathrm{Pr}}\frac{\partial \bar{\Theta}}{\partial x_j} + \frac{\delta^2}{2\gamma}Y_j + \overline{u'_j\Theta'}\right] - \frac{\mathrm{Ec}}{\mathrm{Re}}\bar{\Phi} = 0 \tag{2.68}$$

$$\mathcal{L}\left(\bar{c}_\varepsilon\right) = \mathrm{St}\frac{\partial \bar{c}}{\partial t} + \frac{\partial}{\partial x_j}\left[\bar{u}_j\bar{c}_\varepsilon - \frac{1}{\mathrm{Re}\,\mathrm{Sc}}\frac{\partial \bar{c}_\varepsilon}{\partial x_j} + \frac{\delta^2}{2\gamma}Z_j + \overline{u'_j c'_\varepsilon}\right] = 0 \tag{2.69}$$

where $\bar{P} \equiv \bar{p}/\rho_0$ is the kinematic pressure. This system is conveniently coalesced in the flux vector form

$$\mathcal{L}\left(q_\alpha\right) = \frac{\partial q_\alpha}{\partial t} + \frac{\partial}{\partial x_j}\left(f_j - f_j^v\right)_\alpha - s_\alpha = 0 \tag{2.70}$$

with the set of companion Poisson equations of the form

$$\mathcal{L}\left(q_A\right) = -\frac{\partial^2 q_A}{\partial x_k \partial x_k} - s_A\left(q_\alpha, q_A\right) = 0 \tag{2.71}$$

where q_α contains the NS state variable members, q_A the auxiliary state variable members, f_j and f_j^υ are the convective and diffusive flux vectors, respectively, and s_α and s_A stand for the appropriate source term array. Applied to Eqn. (2.66) – (2.69) the following equalities are assigned:

$$q_\alpha = \begin{Bmatrix} \bar{u}_i \\ \bar{\Theta} \\ \bar{c}_\varepsilon \end{Bmatrix} \tag{2.72}$$

$$f_j\left(q_\alpha\right) = \begin{Bmatrix} \bar{u}_j \bar{u}_i + \bar{P}\delta_{ij} \\ \bar{u}_j \bar{\Theta} \\ \bar{u}_j \bar{c}_\varepsilon \end{Bmatrix} \tag{2.73}$$

$$f_j^v\left(q_\alpha\right) = \begin{Bmatrix} \dfrac{2}{\mathrm{Re}}\bar{S}_{ij} - \dfrac{\delta^2}{2\gamma}R_{ij} - \overline{u'_j u'}_i \\ \dfrac{1}{\mathrm{Re}\,\mathrm{Pr}}\dfrac{\partial\bar{\Theta}}{\partial x_j} - \dfrac{\delta^2}{2\gamma}Y_j - \overline{u'_j\Theta'} \\ \dfrac{1}{\mathrm{Re}\,\mathrm{Sc}}\dfrac{\partial\bar{c}_\varepsilon}{\partial x_j} - \dfrac{\delta^2}{2\gamma}Z_j - \overline{u'_j c'_\varepsilon} \end{Bmatrix} \tag{2.74}$$

$$s_\alpha = \begin{Bmatrix} -\mathrm{Ar}\bar{\Theta}\hat{\mathbf{g}}_i \\ \dfrac{\mathrm{Ec}}{\mathrm{Re}}\bar{\Phi} \\ S_\varepsilon \end{Bmatrix} \tag{2.75}$$

In the instance of the SGS tensor selected from the TWS stability theory, then

$$f_j^\upsilon\left(q_\alpha\right) = \begin{Bmatrix} \dfrac{2}{\mathrm{Re}}\bar{S}_{ij} - \dfrac{\delta^2}{2\gamma}R_{ij} + \dfrac{\beta\,\mathrm{Re}\,h^2}{24}\left(\bar{u}_j\bar{u}_k\bar{S}_{ik} + \bar{u}_i\bar{u}_k\bar{S}_{jk}\right) \\ \dfrac{1}{\mathrm{Re}\,\mathrm{Pr}}\dfrac{\partial\bar{\Theta}}{\partial x_j} - \dfrac{\delta^2}{2\gamma}Y_j + \dfrac{\beta_t\,\mathrm{Re}\,\mathrm{Pr}\,h^2}{12}\bar{u}_k\bar{u}_j\dfrac{\partial\bar{\Theta}}{\partial x_j} \\ \dfrac{1}{\mathrm{Re}\,Sc}\dfrac{\partial\bar{c}_\varepsilon}{\partial x_j} - \dfrac{\delta^2}{2\gamma}Z_j + \dfrac{\beta_c\,\mathrm{Re}\,\mathrm{Sc}h^2}{12}\bar{u}_k\bar{u}_j\dfrac{\partial\bar{c}_\varepsilon}{\partial x_j} \end{Bmatrix} \tag{2.76}$$

with the sole model constants β scaling the SGS tensor model for all variables. For the auxiliary problems, Eqns. (2.22), (2.24) and (2.25), Eqn. (2.71) results for the definitions

$$q_A = \begin{Bmatrix} R_{ij} \\ Y_j \\ Z_j \end{Bmatrix} \tag{2.77}$$

$$s_A = \begin{Bmatrix} \frac{4\gamma}{\delta^2}\left(R_{ij} - \frac{\partial \overline{u}_j}{\partial x_l}\frac{\partial \overline{u}_i}{\partial x_l} \right) \\ \frac{4\gamma}{\delta^2}\left(Y_j - \frac{\partial \overline{u}_j}{\partial x_l}\frac{\partial \overline{\Theta}}{\partial x_l} \right) \\ \frac{4\gamma}{\delta^2}\left(Z_j - \frac{\partial \overline{u}_j}{\partial x_l}\frac{\partial \overline{c}_\varepsilon}{\partial x_l} \right) \end{Bmatrix} \tag{2.78}$$

Notice that (2.71) – (2.75) do not include the mass conservation constraint (2.66), as well as an equation for kinematic pressure. Both will be handled by a “pressure projection” CFD algorithm formulation, developed in completeness in the next chapter.

2.9 Boundary and Initial Conditions

The established LES equation system (2.70) – (2.78) is a coupled set of elliptic nonlinear PDEs, hence requires definition of initial and boundary conditions for well-posedness. It is assumed that the PDE set is defined within a domain Ω with a boundary closure Γ. Furthermore, the boundary can be subdivided into Γ_D and Γ_N. This leads to the following generalized boundary condition statements

$$\bar{u}_i\left(x_j,t\right)=w_i\left(x_{j,t}\right) \qquad \mathrm{x_j}\in\Gamma_D$$

$$\left.\begin{aligned}-P+\left(\left(\frac{2}{\mathrm{Re}}\bar{S}_{ij}-\frac{\delta^2}{2\gamma}R_{ij}-\overline{u'_j u'_i}\right)n_\Gamma\right)n_\Gamma=F_n\left(x_j,t\right)\\ \left(\left(\frac{2}{\mathrm{Re}}\bar{S}_{ij}-\frac{\delta^2}{2\gamma}R_{ij}-\overline{u'_j u'_i}\right)\tau_\Gamma\right)n_\Gamma=F_\tau\left(x_j,t\right)\end{aligned}\right\} \qquad \mathrm{x_j}\in\Gamma_N \tag{2.79}$$

$$\bar{\Theta}\left(x_j,t\right)=\Theta_0\left(x_j.t\right) \qquad \mathrm{x_j}\in\Gamma_D^\Theta$$

$$\left(\frac{1}{\mathrm{Re}\,\mathrm{Pr}}\frac{\partial\bar{\Theta}}{\partial x_j}-\frac{\delta^2}{2\gamma}Y_j-\overline{u'_j\Theta'}\right)n_\Gamma=G_0\left(x_j,t\right) \qquad \mathrm{x_j}\in\Gamma_N^\Theta \tag{2.80}$$

$$\bar{\mathrm{c}}_\varepsilon\left(x_j,t\right)=c_{\varepsilon 0}\left(x_j.t\right) \qquad \mathrm{x_j}\in\Gamma_D^{c_\varepsilon}$$

$$\left(\frac{1}{\mathrm{Re}\,Sc}\frac{\partial\bar{c}_\varepsilon}{\partial x_j}-\frac{\delta^2}{2\gamma}Z_j-\overline{u'_j c'_\varepsilon}\right)n_\Gamma=E_0\left(x_j,t\right) \qquad \mathrm{x_j}\in\Gamma_N^{c_\varepsilon} \tag{2.81}$$

The given boundary data include $w_i, F_n, F_\tau, \Theta_0, G_0, c_{\varepsilon 0},$ and E_0. The initial conditions are

$$\begin{aligned}\bar{u}_i\left(x_j,0\right)&=w_i\left(x_j,0\right) \quad \mathrm{x_j}\in\Omega\cup\Gamma\\ \bar{\Theta}\left(x_j,0\right)&=\Theta_0\left(x_j,0\right) \quad \mathrm{x_j}\in\Omega\cup\Gamma^\Theta\\ \bar{c}_\varepsilon\left(x_j,0\right)&=c_{\varepsilon 0}\left(x_j,0\right) \quad \mathrm{x_j}\in\Omega\cup\Gamma^{c_\varepsilon}\end{aligned} \tag{2.82}$$

The generalized boundary conditions must then be translated into various physical conditions. The simplest, and most often used boundary condition is Dirichlet, which occurs when a fixed value of a variable is assigned, e.g. a given wall temperature or a velocity at a surface. For $u_i=0$ on Γ, the condition is termed “no-slip”, since the fluid sticks to the wall. The no-slip BC is generally required for viscous flow simulations. However, for the LES theory the no-slip boundary condition is quite inappropriate. Note that the velocity has been convolved with a filter of scale δ. Hence, the velocity at a certain point has been averaged from values within a spherical neighborhood of radius δ.

From Figure 2.5 it is obvious that for the wall velocity $u = 0$, the filtered mean velocity is $\bar{u} \neq 0$.

Hence, the proposed more appropriate boundary condition for LES theory at walls is slip with a friction condition, [JA06], [JLS04]. The slip boundary condition with friction has the form of

$$\begin{aligned} &\bar{u}_i\left(x_j, t\right) n_\Gamma = w \\ &-P + \left(\left(\frac{2}{\mathrm{Re}}\bar{S}_{ij} - \frac{\delta^2}{2\gamma}R_{ij} - \overline{u'_j u'_i}\right)\tau_\Gamma\right) n_\Gamma = 0 \end{aligned} \tag{2.83}$$

where no penetration through the wall occurs for $w = 0$. The slip with linear friction and no penetration boundary condition is expressed through

$$\begin{aligned} &\bar{u}_i\left(x_j, t\right) n_\Gamma = 0 \\ &\bar{u}_i\left(x_j, t\right)\tau_\Gamma + \beta^{-1}\left(\delta, \upsilon\right)\left[\left(\left(\frac{2}{\mathrm{Re}}\bar{S}_{ij} - \frac{\delta^2}{2\gamma}R_{ij} - \overline{u'_j u'_i}\right)\tau_\Gamma\right) n_\Gamma\right] = 0 \end{aligned} \tag{2.84}$$

If it is assumed that the value of a variable doesn't change spatially, hence $\frac{\partial u}{\partial n} = 0$ at Γ, then a homogeneous Neumann BC is given, which is also called the "outflow" BC.

In terms of (2.79) this implies

$$\left(\left(\frac{2}{\mathrm{Re}}\bar{S}_{ij} - \frac{\delta^2}{2\gamma}R_{ij} - \overline{u'_j u'_i}\right)\tau_\Gamma\right) n_\Gamma = 0 \tag{2.85}$$

Another approach to theorizing a wall boundary condition is through adaptations on turbulent boundary layer models. For this approach, the LES theory is implemented only down to Y, the first node off the no-slip wall. In a wall-layer model, the LES simulation

supplies a velocity at Y, which is then used to determine the local wall stress. This is then fed back to the LES simulation in form of proper momentum flux at the wall due to normal diffusion.

An example is the implementation of Schumann [Sch75], who directly related the shear stresses at the wall to the velocity at the node off the wall via

$$\tau_{xy,w}(x) = \frac{\langle \tau_w \rangle}{\langle \bar{u}(x,Y) \rangle} \bar{u}(x,Y) = \left(\left(\frac{2}{\mathrm{Re}} \bar{S}_{ij} - \frac{\delta^2}{2\gamma} R_{ij} - \overline{u'_j u'_i} \right) \tau_\Gamma \right) n_\Gamma = 0 \tag{2.86}$$

where $\langle \bullet \rangle$ denotes averaging over a plane parallel to the wall. The mean wall stress $\langle \tau_w \rangle$ has to be computed iteratively using the averaged velocity at point Y, $\langle \bar{u}(x,Y) \rangle$, in the law-of-the-wall correlation, [Wil00]

$$\begin{aligned} u^+ &= \frac{u}{u_\tau} = \frac{1}{\kappa} \log\left(y^+\right) + B \\ y^+ &= \frac{u_\tau y}{\upsilon} \\ \tau_w &= \rho u_\tau^2 \end{aligned} \tag{2.87}$$

with $B = 5.0$ and $\kappa = 0.41$.

A third way of implementing appropriate boundary conditions is via the zonal approach, which is based on solving a separate explicit set of equations for the inner layer, while the LES theory PDE set is limited to the core region of the domain. An example of this approach is the Two-Layer Model (TLM), [BBP96], which uses two separate meshes. On the inner layer mesh the turbulent boundary layer equations are solved according to

$$\frac{\partial \overline{u}_i}{\partial t} + \left(\overline{u}_n \overline{u}_i\right) + \frac{\partial \overline{p}}{\partial x_i} - \frac{\partial}{\partial x_n}\left(\left(\upsilon + \upsilon_t\right)\frac{\partial \overline{u}_i}{\partial x_n}\right) = 0 \tag{2.88}$$

where n indicates the normal direction from the wall. The normal velocity u_n is calculated based on mass conservation in the inner layer. The wall is equipped with no-slip condition, while the velocity at the interface between the meshes is provided by the LES simulation of the core mesh. Integration of (2.88) results in a wall-stress, which supplies the boundary condition for the LES model.

A second example of the zonal approach is Detached Eddy Simulation (DES), [SJSA97], which uses only one mesh. The boundary layer region is under the control of a RaNS set of PDEs, while a LES PDE system is used in the core region. Since no zonal interface exist, the velocity is smooth everywhere.

In this dissertation, an alternative theory for circumventing the problem with wall boundary conditions is to use a dual-LES theory, in principle similar to the DES approach by Spalart. The computational domain is divided into non-overlapping domains, $\Omega = \Omega_{LES} \cup \Omega_{Wall}$. Within Ω_{LES}, which is the unbounded interior of Ω, the developed LES theory according to Eqn. (2.70) – (2.78) is appropriate. In Ω_{Wall}, which constitutes regions near the walls of Ω, the rational LES theory solutions for R_{ij}, Y_j and Z_j are disabled in favor of a lower order LES theory, generated via the box filter for example, whence the SGS closure model constitutes a turbulent eddy viscosity model analogous to Smagorinsky. The mathematically rigorous rational LES theory requires the filter scale δ to be a constant, hence limits implementations to uniform meshes. No such restriction

exists for convolution with the box filter. Therefore, a non-uniform mesh can be used in the wall region, which allows the application of the no-slip boundary condition assuming that the mesh is sufficiently refined in the wall regions.

3. LES Theory CFD Algorithm

3.1 Continuity Constraint Algorithm

The Continuity Constraint Method (CCM), developed at the UT CFD Laboratory by Williams, [Wil93], belongs to the class of "pressure relaxation" CFD algorithms, [AH70], [SRY78]. For incompressible Navier-Stokes, pressure has two tasks: to enforce the constraint of mass conservation (2.1), and to be a balance force in the momentum equations. This theory directly addresses both requirements, hence is selected for generating the derived LES theory CFD algorithm.

3.2 Continuity Error

An explicit Taylor series expansion expresses the divergence-free, analytically exact velocity field at time step t^{n+1} as a function of the velocity at time step t^n via

$$u_i^{n+1} = u_i^n + \Delta t \left.\frac{\partial u_i}{\partial t}\right|_n + \frac{\Delta t^2}{2}\left.\frac{\partial^2 u_i}{\partial t^2}\right|_n + O\left(\Delta t^3\right) \tag{3.1}$$

Assuming that any approximated velocity field u_i^* can be calculated from a guessed pressure field, P^*, an equation for u_i^* at time t^{n+1} is

$$u_i^{*n+1} = u_i^n + \Delta t \left.\frac{\partial u_i}{\partial t}\right|_{*n} + \frac{\Delta t^2}{2}\left.\frac{\partial^2 u_i}{\partial t^2}\right|_{*n} + O\left(\Delta t^3\right) \tag{3.2}$$

At $t = t_n$, the guessed velocity field is the same as the old velocity field, hence

$$u_i^{*n} = u_i^n \Rightarrow \left.\frac{\partial u_i^*}{\partial t}\right|_n = \left.\frac{\partial u_i}{\partial t}\right|_n =$$
$$-\left[u_j \frac{\partial u_i}{\partial x_j} - \frac{1}{\mathrm{Re}}\frac{\partial^2 u_i}{\partial x_j^2} + \frac{\partial P}{\partial x_i} - \frac{\partial}{\partial x_j}\left(R_{ij} + SGS_{ij}\right) + Ar\Theta\hat{g}_i\right]_n \tag{3.3}$$

where SGS_{ij} is the placeholder for the sub-grid scale model, e.g. in the case of the TWS SGS model, it is Eqn. (2.63). The following second temporal derivatives can be formed

$$\left.\frac{\partial^2 u_i}{\partial t^2}\right|_n = -\frac{\partial}{\partial t}\left[u_j \frac{\partial u_i}{\partial x_j} - \frac{1}{\mathrm{Re}}\frac{\partial^2 u_i}{\partial x_j^2} + \frac{\partial P}{\partial x_i} - \frac{\partial}{\partial x_j}\left(R_{ij} + SGS_{ij}\right) + Ar\Theta\hat{g}_i\right]_n$$
$$\left.\frac{\partial^2 u_i^*}{\partial t^2}\right|_{*n} = -\frac{\partial}{\partial t}\left[u_j \frac{\partial u_i}{\partial x_j} - \frac{1}{\mathrm{Re}}\frac{\partial^2 u_i}{\partial x_j^2} - \frac{\partial}{\partial x_j}\left(R_{ij} + SGS_{ij}\right) + Ar\Theta\hat{g}_i\right]_{*n} \tag{3.4}$$

Subtracting Eq. (3.1) from (3.2) leads to the error in the velocity field

$$u_i^{n+1} - u_i^* = \frac{\Delta t^2}{2}\left(\frac{\partial^2 u_i}{\partial t^2} - \frac{\partial^2 u_i^*}{\partial t^2}\right)_n + O\left(\Delta t^3\right) = -\frac{\Delta t^2}{2}\frac{\partial}{\partial t}\left(\frac{\partial P}{\partial x_i}\right)$$
$$= -\frac{\Delta t^2}{2}\frac{\partial}{\partial x_i}\left(\frac{\partial P}{\partial t}\right)_n + O\left(\Delta t^3\right) \tag{3.5}$$

Since the curl of (3.5) is identically zero, the difference between the exact and any CFD approximate velocity field must correspond mathematically to the gradient of a potential function, hence

$$u_i^{n+1} - u_i^* = \frac{\partial \phi}{\partial x_i} \tag{3.6}$$

The LES theory implementation must be time-accurate, which implies an implicit Taylor series (TS) approach. A theta-implicit time Taylor series yields

$$u_i^{n+1-\theta} = u_i^n + \left(1-\theta\right)\Delta t \left.\frac{\partial u_i}{\partial t}\right|_n + \frac{\left(1-\theta\right)^2 \Delta t^2}{2}\left.\frac{\partial^2 u_i}{\partial t^2}\right|_n + O\left(\Delta t^3\right) \tag{3.7}$$

$$u_i^{n+1-\theta} = u_i^{n+1} - \theta\Delta t \left.\frac{\partial u_i}{\partial t}\right|_{n+1} + \frac{\theta^2 \Delta t^2}{2} \left.\frac{\partial^2 u_i}{\partial t^2}\right|_{n+1} + O\left(\Delta t^3\right) \tag{3.8}$$

Subtracting (3.8) from (3.7) leads to

$$u_i^{n+1} - u_i^n = \Delta t \left(\theta \left.\frac{\partial u_i}{\partial t}\right|_{n+1} + \left(1-\theta\right) \left.\frac{\partial u_i}{\partial t}\right|_{n} \right) + O\left(\Delta t^2\right) \tag{3.9}$$

Using the momentum equation to replace the time derivative, (3.9) becomes

$$\begin{aligned} & u_i\big|_{n+1} - u_i\big|_n = \\ & -\theta\Delta t \left[\frac{\partial\left(u_j u_i\right)}{\partial x_j} + \frac{\partial P}{\partial x_i} - \frac{\partial}{\partial x_j}\left\{ \frac{1}{\mathrm{Re}}\left(\frac{\partial u_i}{\partial x_j} + \frac{\partial u_j}{\partial x_i} \right) + R_{ij} + SGS_{ij} \right\} + Ar\theta \hat{g}_i \right]_{n+1} \\ & -\left(1-\theta\right)\Delta t \left[\frac{\partial\left(u_j u_i\right)}{\partial x_j} + \frac{\partial P}{\partial x_i} - \frac{\partial}{\partial x_j}\left\{ \frac{1}{\mathrm{Re}}\left(\frac{\partial u_i}{\partial x_j} + \frac{\partial u_j}{\partial x_i} \right) + R_{ij} + SGS_{ij} \right\} + Ar\theta \hat{g}_i \right]_{n} \\ & +O\left(\Delta t^2\right) \end{aligned} \tag{3.10}$$

For a guessed pressure P^* at time t^{n+1}, the velocity field u_i^* does not satisfy the mass conservation constraint, hence

$$\frac{\partial u_i^*}{\partial x_i} \neq 0 \Rightarrow u_j^* \frac{\partial u_i^*}{\partial x_j} \neq \frac{\partial}{\partial x_j}\left(u_j^* u_i^*\right) \tag{3.11}$$

Therefore, for a suitable guessed pressure P^* at time t^{n+1}, Eq. (3.10) becomes

$$\begin{aligned} & u_i^*\big|_{n+1} - u_i^*\big|_n = \\ & -\theta\Delta t \left[u_j^* \frac{\partial u_i^*}{\partial x_j} + \frac{\partial P^*}{\partial x_i} - \frac{\partial}{\partial x_j}\left\{ \frac{1}{\mathrm{Re}}\left(\frac{\partial u_i^*}{\partial x_j} + \frac{\partial u_j^*}{\partial x_i} \right) + R_{ij}^* + SGS_{ij}^* \right\} + Ar\theta^* \hat{g}_i \right]_{n+1} \\ & -\left(1-\theta\right)\Delta t \left[\frac{\partial\left(u_j u_i\right)}{\partial x_j} + \frac{\partial P}{\partial x_i} - \frac{\partial}{\partial x_j}\left\{ \frac{1}{\mathrm{Re}}\left(\frac{\partial u_i}{\partial x_j} + \frac{\partial u_j}{\partial x_i} \right) + R_{ij} + SGS_{ij} \right\} + Ar\theta \hat{g}_i \right]_{n} \\ & +O\left(\Delta t^2\right) \end{aligned} \tag{3.12}$$

The theta-implicit divergence error is expressed through subtraction of Eq. (3.12) from (3.10)

$$
\begin{aligned}
\left(u_i - u_i^*\right)_{n+1} &= \theta\Delta t\left[u_j^*\frac{\partial u_i^*}{\partial x_j} - \frac{\partial\left(u_j^* u_i^*\right)}{\partial x_j}\right]_{n+1} \\
&+\theta\Delta t\frac{\partial}{\partial x_j}\left[\frac{1}{\mathrm{Re}}\left(\frac{\partial u_i}{\partial x_j}+\frac{\partial u_j}{\partial x_i}\right)-\frac{1}{\mathrm{Re}}\left(\frac{\partial u_i^*}{\partial x_j}+\frac{\partial u_j^*}{\partial x_i}\right)\right]_{n+1} \\
&+\theta\Delta t\frac{\partial}{\partial x_j}\left[R_{ij}-R_{ij}^*\right]_{n+1}+\theta\Delta t\frac{\partial}{\partial x_j}\left[SGS_{ij}-SGS_{ij}^*\right]_{n+1} \\
&+\theta\Delta t\left.\frac{\partial\left(P^*-P\right)}{\partial x_j}\right|_{n+1}+Ar\left(\theta^*-\theta\right)_{n+1}\hat{g}_i+O\left(\Delta t^2\right)
\end{aligned}
\tag{3.13}
$$

This equation has six modes of error generation for the velocity field at t^{n+1}, namely due to advection, laminar diffusion, Reynolds and SGS stress tensor, pressure and the buoyancy body force. Since only the pressure term can be expressed through a potential function, all other terms are considered mathematically intractable, in the manner of the original theory, [Wil93]. That means that the error generated by the remaining terms must be reduced through an iterative process guaranteeing that $u_i^* \to u_i^{n+1}$ as the iteration proceeds. With *p* the iteration parameter, the error at iteration *p*+1 between the exact velocity vector at time step t^{n+1} and a CFD-generated velocity vector is assumed of the form

$$
\left(u_i^* - u_i\right)_{n+1}^{p+1} = -\left.\frac{\partial\phi}{\partial x_i}\right|_{n+1}^{p+1} \tag{3.14}
$$

Using Eq. (3.14), and neglecting the intractable terms in Eq. (3.13), yields

$$\left.\frac{\partial \phi}{\partial x_i}\right|_{n+1}^{p+1} \approx \theta \Delta t \left.\frac{\partial\left(P^* - P\right)}{\partial x_i}\right|_{n+1}^{p} \tag{3.15}$$

Integrating this expression, with integration constant set to zero leads to an expression for the genuine pressure at time t^{n+1} as

$$P\big|_{n+1}^{p} = P^*\big|_{n+1}^{p} + \frac{1}{\theta \Delta t}\phi\big|_{n+1}^{p+1} \tag{3.16}$$

The problem in this expression is the fact that the pressure at iteration *p* requires the yet unknown potential function at iteration *p*+1. A solution to this dilemma is to accumulate the solutions for ϕ over the iterative sequence yielding

$$P^*\big|_{n+1}^{p} = P\big|_{n} + \frac{1}{\theta \Delta t}\sum_{\alpha=1}^{p}\phi_{n+1}^{\alpha} \tag{3.17}$$

where P_n is the known, mass-conserving kinematic pressure at the original time station.

3.3 Potential Function

Constraint theory completion requires an equation to solve for the identified potential function ϕ. From (3.14), the definition for the potential function is

$$\frac{\partial \phi}{\partial x_i} = \left(u_i^* - u_i\right) \tag{3.18}$$

with u_i the constraint fulfilling velocity vector field and u_i^* any other velocity vector which is assumed not solenoidal. Applying the divergence operator to Eqn. (3.18) yields

$$\frac{\partial}{\partial x_i}\left(\frac{\partial \phi}{\partial x_i}\right) = \frac{\partial}{\partial x_i}\left(u_i^* - u_i\right) = \frac{\partial u_i^*}{\partial x_i} - \frac{\partial u_i}{\partial x_i} = \frac{\partial u_i^*}{\partial x_i} \tag{3.19}$$

Hence, the continuity constraint function ϕ is the solution to an elliptic boundary value problem of Poisson type

$$\mathcal{L}(\phi) = \frac{\partial^2 \phi}{\partial x_i \partial x_i} - \frac{\partial u_i^*}{\partial x_i} = 0 \tag{3.20}$$

The natural boundary condition for (3.20) is the projection of the gradient of ϕ onto the outward-pointing normal of the boundary. From Eqn. (3.18), this projection is related to the velocity vector error at the boundary as

$$\frac{\partial \phi}{\partial x_i} \hat{n}_i = \left(u_i^* - u_i\right) \hat{n}_i \tag{3.21}$$

The required determinations for (3.21) are inflow, outflow, symmetry plane and no-slip or slip at a solid surface. At an inflow plane the typical BC is velocity vector fixed, i.e., Dirichlet BC, hence $u_i^* = u_i$, resulting in (3.21) as homogeneous Neumann

$$\frac{\partial \phi}{\partial x_i} \hat{n}_i = 0 \tag{3.22}$$

At an outflow plane it is assumed that a sufficiently long flow straightening section exists such that the velocity vector is essentially aligned with the outward pointing normal. With this assumption it can be argued that the continuity error in the tangential direction is negligible, via the iterative process, hence

$$\begin{aligned} \frac{\partial \phi}{\partial n} &= \left(u_n^* - u_n\right) \neq 0 \\ \frac{\partial \phi}{\partial s} &= \left(u_s^* - u_s\right) \approx 0 \end{aligned} \tag{3.23}$$

This results in the potential function being a constant along this boundary, which for mathematical convenience is chosen as zero, hence at outflow

$$\phi = \text{constant}=0 \tag{3.24}$$

On a symmetry plane, the normal velocity component is zero, hence the homogeneous Neumann condition is valid.

The velocity boundary condition at walls is typically no-slip for NS, which states that the velocity vector is zero. This results in the homogeneous Neumann BC being appropriate. Alternatively, a slip boundary condition requires that the velocity vector is tangent to the wall, hence

$$u_i \hat{n}_i = 0 \tag{3.25}$$

Therefore

$$\frac{\partial \phi}{\partial x_i} \hat{n}_i = \left(u_i^* - u_i \right) \hat{n}_i = u_i^* \hat{n}_i - u_i \hat{n}_i = u_i^* \hat{n}_i \tag{3.26}$$

which is a non-homogeneous Neumann boundary condition. This is automatically enforced upon forming the weak statement expression for (3.21), as developed in the next chapter.

3.4 Pressure Poisson Equation

The pressure Poisson equation for the LES theory CFD algorithm is a generalization of the form in [Wil93]. Starting with the divergence of (2.67)

$$
\begin{aligned}
\mathcal{L}(P) &= \frac{\partial}{\partial x_i}\left(\mathcal{L}\left(u_i\right)\right) \\
&= \frac{\partial}{\partial x_i}\left(\frac{\partial u_i}{\partial t} - \frac{1}{\mathrm{Re}}\frac{\partial^2 u_i}{\partial x_j \partial x_j}\right) + \\
&\frac{\partial}{\partial x_i}\left\{\frac{\partial P}{\partial x_i} + u_j \frac{\partial u_i}{\partial u_j} - \frac{\partial}{\partial x_j}\left[SGS_{ij} - \frac{\delta^2}{2\gamma}R_{ij}\right] + Ar\Theta\hat{g}_i\right\} = 0
\end{aligned}
\tag{3.27}
$$

where SGS_{ij} stands for the sub-grid scale model. In the case of the TWS SGS, SGS_{ij} is replaced by Eqn. (2.61).

Since the constraint theory requires only P at time t_n, (3.27) can be simplified by imposing the continuity constraint. Assuming that the temporal derivative commutes with the divergence operation, which is applicable for flow fields with smooth changes in time, the acceleration is solenoidal, hence

$$
\frac{\partial}{\partial x_i}\left(\frac{\partial u_i}{\partial t}\right) = \frac{\partial}{\partial t}\left(\frac{\partial u_i}{\partial x_i}\right) = 0 \tag{3.28}
$$

Similarly, for sufficient smoothness in spatial derivatives, they also commute. The Reynolds number, Re, is a constant, hence

$$
\frac{\partial}{\partial x_i}\left(\frac{1}{\mathrm{Re}}\frac{\partial^2 u_i}{\partial x_j \partial x_j}\right) = \frac{1}{\mathrm{Re}}\frac{\partial^2}{\partial x_j^2}\left(\frac{\partial u_i}{\partial x_i}\right) = 0 \tag{3.29}
$$

Therefore the pressure Poisson equation for a divergence-free LES theory velocity vector field is

$$
\begin{aligned}
\mathcal{L}(P) &= \frac{\partial}{\partial x_i}\left(\mathcal{L}^*\left(u_i\right)\right) \\
&= \frac{\partial}{\partial x_i}\left\{\frac{\partial P}{\partial x_i} + u_j \frac{\partial u_i}{\partial x_j} - \frac{\partial}{\partial x_j}\left[SGS_{ij} - \frac{\delta^2}{2\gamma}R_{ij}\right] + Ar\Theta\hat{g}_i\right\} = 0
\end{aligned}
\tag{3.30}
$$

Being an elliptic boundary value PDE, the BC for (3.30) is of non-homogeneous Neumann form, as derived by projecting the momentum equation onto the boundary, which yields

$$\frac{\partial P}{\partial x_i}\hat{n}_i = \frac{\partial}{\partial x_j}\left[SGS_{ij} + \frac{\delta^2}{2\gamma}R_{ij}\right]\hat{n}_i - \frac{\partial u_i}{\partial t}\hat{n}_i + \frac{1}{\mathrm{Re}}\frac{\partial^2}{\partial x_j^2}\left(u_i\hat{n}_i\right) \tag{3.31}$$

4. CFD Algorithm Weak Form FE Implementation

Including the two Poisson PDEs generated by the continuity constraint algorithm into the set of LES theory PDEs, the LES state variable representation from Chapter 2.9 is augmented as

$$\mathcal{L}\left(q_A\right) = -\frac{\partial^2 q_A}{\partial x_k \partial x_k} - s_A\left(q_\alpha, q_A\right) = 0 \tag{4.1}$$

With the definitions

$$q_A = \begin{Bmatrix} \phi \\ P \\ R_{ij} \\ Y_j \\ Z_j \end{Bmatrix} \tag{4.2}$$

$$s_A = \begin{Bmatrix} \dfrac{\partial u_i}{\partial x_i} \\ -\dfrac{\partial}{\partial x_i}\left(\mathcal{L}\left(u_i\right) - \dfrac{\partial P}{\partial x_i}\right) \\ \dfrac{4\gamma}{\delta^2}\left(R_{ij} - \dfrac{\partial \overline{u}_j}{\partial x_l}\dfrac{\partial \overline{u}_i}{\partial x_l}\right) \\ \dfrac{4\gamma}{\delta^2}\left(Y_j - \dfrac{\partial \overline{u}_j}{\partial x_l}\dfrac{\partial \overline{\Theta}}{\partial x_l}\right) \\ \dfrac{4\gamma}{\delta^2}\left(Z_j - \dfrac{\partial \overline{u}_j}{\partial x_l}\dfrac{\partial \overline{c}_\varepsilon}{\partial x_l}\right) \end{Bmatrix} \tag{4.3}$$

4.1 Galerkin Weak Statement Formulation

The implementation of the derived LES CFD algorithm is via a finite element spatial discretization [Bak83, Bak05] of a Galerkin weak statement for the LES theory-identified PDE systems. For q_α the NS state variable, any approximation continuous in space and time is assumed as

$$q_\alpha\left(x_i,t\right) \approx q_\alpha^N\left(x_i,t\right) \equiv \sum_{k=1}^{N} \Psi_k\left(x_j\right) Q_k\left(t\right) \tag{4.4}$$

Similarly, for the quasi-linear harmonic PDE system (4.1)

$$q_A\left(x_i,t\right) \approx q_A^N\left(x_i,t\right) \equiv \sum_{k=1}^{N} \Psi_k\left(x_j\right) Q_k^A\left(t\right) \tag{4.5}$$

where the set of known functions $\Psi_k\left(x_i\right)$ is called the approximation trialspace. The extremization of the approximation error is obtained via forming a Galerkin weak statement, [Bak05], on the LES theory PDE systems as

$$\text{GWS}=\int_\Omega \Psi_\beta\left(x_j\right)\mathcal{L}\left(q_\alpha^N\right)d\tau = 0, \quad \text{for } 1 \le \beta \le N \tag{4.6}$$

and

$$\text{GWS}=\int_\Omega \Psi_\beta\left(x_j\right)\mathcal{L}\left(q_A^N\right)d\tau = 0, \quad \text{for } 1 \le \beta \le N \tag{4.7}$$

where Ω symbolizes the domain of definition of the PDEs.

Substitution of $\mathcal{L}\left(q_\alpha^N\right)$ and $\mathcal{L}\left(q_A^N\right)$ results in the requirement to form the following integrals

$$GWS\left(q_\alpha^N\right)=\int_\Omega \Psi_\beta\left(\frac{\partial q_\alpha^N}{\partial t}+\frac{\partial}{\partial x_j}\left(f_j-f_j^\upsilon\right)^N-s_\alpha^N\right)d\tau \tag{4.8}$$

$$GWS\left(q_A^N\right)=\int_\Omega \Psi_\beta\left(-\frac{\partial q_A^N}{\partial x_i \partial x_i}-s_A^N\right)d\tau \tag{4.9}$$

Applying a Green-Gauss theorem to (4.8) and (4.9) yields

$$\begin{aligned} GWS\left(q_\alpha^N\right)=&\int_\Omega \Psi_\beta\left(\frac{\partial q_\alpha^N}{\partial t}-s_\alpha^N\right)d\tau-\int_\Omega \frac{\partial \Psi_\beta}{\partial x_j}\left(f_j-f_j^\upsilon\right)^N d\tau \\ &+\oint_{\partial\Omega}\Psi_\beta\left(f_j-f_j^\upsilon\right)^N \hat{n}_j d\sigma=0 \end{aligned} \tag{4.10a}$$

$$\begin{aligned} GWS\left(q_A^N\right)=&\int_\Omega \frac{\partial \Psi_\beta}{\partial x_i}\frac{\partial q_A^N}{\partial x_i}d\tau-\int_\Omega \Psi_\beta s_A^N d\tau \\ &-\oint_{\partial\Omega}\Psi_\beta \frac{\partial q_A^N}{\partial x_i}\hat{n}_i d\sigma \end{aligned} \tag{4.10b}$$

and the generated surface integrals are the mathematical placeholder for all natural boundary conditions.

A finite element implementation of (4.10) utilizes a spatial semi-discretization Ω^h of the PDE domain Ω, which is the union of a set of non-overlapping sub-domains, or finite elements Ω_e, hence

$$\Omega \approx \Omega^h=\bigcup_e \Omega_e \tag{4.11}$$

The approximation (4.4) is then formed as the union over all finite elements of

$$q_\alpha\left(x_j,t\right)\approx q_\alpha^N\left(x_j,t\right)\equiv q_\alpha^h\left(x_j,t\right)=\bigcup_e q_e\left(x_j,t\right) \tag{4.12}$$

with an identical expression for $q_A^N\left(x_j,t\right)$. For any finite element, the generic form for q_e is

$$q_e\left(x_j,t\right)\equiv\left\{N_k\left(\eta_j\right)\right\}^T\left\{Q\left(t\right)\right\}_e \tag{4.13}$$

where the row matrix $\left\{N_k\right\}^T$ is termed the finite element basis function containing a set of polynomials complete to degree k.

Equation (2.11) is evaluated for each element of the discretization, and the resulting element-level expressions are then assembled into a global matrix statement of the form

$$GWS\left(q_\alpha^N\right)\Rightarrow GWS\left(q_\alpha^h\right)=\left[\mathrm{MASS}\right]\frac{d\left\{Q\right\}}{dt}+\left\{\mathrm{RES}\left(Q,Q_A\right)\right\}=\left\{0\right\} \tag{4.14}$$

with $\left[MASS\right]$ and $\left\{RES\right\}$ being global size square and column matrices, and $\left\{Q\right\}\equiv\left\{Q\left(t\right)\right\}$ a column matrix of the state-variable approximation coefficients at the nodes of the mesh. The residual $\left\{RES\right\}$ is a non-linear function of $\left\{Q,Q_A\right\}$ and contains contributions from all terms in Eqn. (4.10a) except the time term.

The remaining time derivative is then discretized using a θ-implicit, one-step algorithm, resulting in the algebraic statement

$$\left\{FQ\right\}=\left[MASS\right]\left\{Q_{n+1}-Q_n\right\}+\Delta t\left(\theta\left\{RES\right\}_{n+1}+\left(1+\theta\right)\left\{RES\right\}_n\right)=\left\{0\right\} \tag{4.15}$$

where $t_{n+1}=t_n+\Delta t$, and $0.5\le\theta\le1$.

The finite element implementation of Eqn. (4.9) directly produces an algebraic system

$$\left\{FQ_A\right\}=\left[DIFF+MASS\right]\left\{Q_A\right\}-\left\{S_A\left(Q\left(t\right)\right)\right\}=\left\{0\right\} \tag{4.16}$$

where $[MASS]$ results only from the harmonic terms in the auxiliary problems, since the PDE systems for ϕ and P are pure Poisson equations.

The solution for the algebraic matrix expression (4.15) - (4.16) must be found iteratively, since it represents a coupled, non-linear system of equations. Following the theoretical Newton scheme, the iterative cycle is

$$\{Q\}_{n+1}^{0} = \{Q\}_{n}, \quad \{FQ\}_{n+1}^{0} = \{FQ\}_{n}$$

for $p = 0,1,2,\ldots$ until convergence

$$\left[MASS + \theta \Delta t \frac{\partial \{RES\}}{\partial \{Q\}} \right]_{n+1}^{p} \{\delta Q\}_{n+1}^{p+1} = -\{FQ\}_{n+1}^{p} \tag{4.17}$$

$$\{Q\}_{n+1}^{p+1} = \{Q\}_{n+1}^{p} + \{\delta Q\}_{n+1}^{p+1}$$

For (4.16) the solution can be found directly via the matrix statement

$$[DIFF + MASS]\{Q_A\} = \{S_A(Q(t))\} \tag{4.18}$$

4.2 Taylor Weak Statement Formulation

One of the main issues in the development of CFD algorithm is numerical stability, in particular for flows with large Reynolds number Re, as all CFD algorithms show an inability to handle the dispersive error mode solely by the use of the physical diffusion mechanism. This dispersion error is introduced through spatial discretization, and manifests itself in the appearance of mesh-scale oscillations in the velocity and temperature fields, see [Bak05].

To effectively dissipate this dispersion error mode is the central thesis of the Taylor Weak Statement (TWS) theory, which generates appropriate Taylor-series modifications to the NS PDE system, [CB95].

The original theory of the Taylor weak statement was developed based on the hyperbolic 1-dimensional scalar advection equation [BK87]

$$\frac{\partial q}{\partial t} = a\frac{\partial q}{\partial x} \tag{4.19}$$

where a is a constant scalar. Since (4.19) describes an evolutionary process, a Taylor series exists of the form

$$q^{n+1} = q^n + \Delta t \left.\frac{\partial q}{\partial t}\right|_n + \frac{\Delta t^2}{2}\left.\frac{\partial^2 q}{\partial t^2}\right|_n + \frac{\Delta t^3}{6}\left.\frac{\partial^3 q}{\partial t^3}\right|_n \tag{4.20}$$

For large Reynolds numbers and negligible source terms, the incompressible NS PDE system can be expressed as

$$\mathcal{L}(q) = \frac{\partial q}{\partial t} + \frac{\partial f_j}{\partial x_j} = \frac{\partial q}{\partial t} + A_j\frac{\partial q}{\partial x_j} = 0 \tag{4.21}$$

where A_j is the jacobian of the kinetic flux vector $\partial f_j / \partial q$. The higher order time terms in (4.20) can be replaced by the spatial derivatives of (4.21), e.g.

$$\frac{\partial^2 q}{\partial t^2} = \frac{\partial}{\partial x_j}\left(\alpha^* A_j\frac{\partial q}{\partial t} + \beta^* A_j A_k\frac{\partial q}{\partial x_k}\right) \tag{4.22}$$

with the constraint $\alpha^* - \beta^* = 1$. Using the same approach, an expression for the third derivative in time can be found and inserted into (4.20). Substituting the new Taylor series into (4.19) will lead to the Taylor modified NS PDE conservation system

$$\mathcal{L}^m(q) = \mathcal{L}(q) - \frac{\Delta t}{2}\frac{\partial}{\partial x_j}\left[\alpha^* A_j \frac{\partial q}{\partial t} + \gamma^* \frac{\Delta t}{3}\frac{\partial}{\partial x_j}\left(A_j A_k \frac{\partial q}{\partial t}\right)\right]$$
$$-\frac{\Delta t}{2}\frac{\partial}{\partial x_j}\left[\beta^* A_j A_k \frac{\partial q}{\partial x_k} + \mu^* \frac{\Delta t}{3}\frac{\partial}{\partial x_j}\left(A_j A_k A_l \frac{\partial q}{\partial x_l}\right)\right] = 0 \tag{4.23}$$

Research at the University of Tennessee CFD Laboratory, [Kol00], [Bak05], [NoB89], has examined the influence of each Taylor series term on the ability to stabilize and control various discretization error modes. The dispersion error control for the NS momentum equations is achieved through the β^* term

$$-\beta^* \frac{\Delta t}{2}\frac{\partial}{\partial x_j}\left(u_j u_k \frac{\partial u_i}{\partial x_k}\right) \tag{4.24}$$

Similarly, TWS theory dispersion error control for the energy equation results from

$$-\beta_\Theta^* \frac{\Delta t}{2}\frac{\partial}{\partial x_j}\left(u_j u_k \frac{\partial \Theta}{\partial x_k}\right) \tag{4.25}$$

Hence, the Taylor weak statement for the LES NS PDE system can be written as

$$TWS = \int_\Omega \Psi_\beta \mathcal{L}^m(u_i)\, d\tau$$
$$= \int_\Omega \Psi_\beta \mathcal{L}^m(u_i)\, d\tau - \frac{\beta \Delta t}{2}\int_\Omega \Psi_\beta \frac{\partial}{\partial x_j}\left(u_j u_k \frac{\partial u_i}{\partial x_k}\right) d\tau = 0 \tag{4.26}$$

which constitutes a Galerkin weak statement written on the TS-modified NS conservation principle PDE system.

4.3 Finite Element Flux Vector Computations

Finite element prediction of all flux vectors in the LES-CFD algorithm are readily created via Galerkin weak statements. Using the TWS beta SGS tensor FB_{ij} as the example, the parent calculus expression is

$$\mathcal{L}\left(FB_{ij}\right) = FB_{ij} - \frac{\mathrm{Re}\,h^2}{24}\left(\bar{u}_j\bar{u}_k\bar{S}_{ik} + \bar{u}_i\bar{u}_k\bar{S}_{jk}\right) = 0 \tag{4.28}$$

The Galerkin weak statement produces the following integral equation

$$\begin{aligned}&\int_\Omega \Psi_\beta \mathcal{L}\left(FB_{ij}\right) d\tau = \\ &\int_\Omega \Psi_\beta \left(FB_{ij} - \frac{\mathrm{Re}\,h^2}{24}\bar{u}_j\bar{u}_k\bar{S}_{ik} - \frac{\mathrm{Re}\,h^2}{24} + \bar{u}_i\bar{u}_k\bar{S}_{jk} \right) d\tau = 0\end{aligned} \tag{4.29}$$

Inserting the finite element expressions for the solution and noting that the measure of the mesh is related to the determinant of the Jacobian of the coordinate transformation, [Bak05], via $h^2 = 4\det\left(J\right)$, the discrete GWS^h statement on the generic FE domain is

$$\begin{aligned}GWS_e = &\int_{\Omega_e} \left\{N_1\right\}\left\{N_1\right\}^T d\tau \left\{FBIJ\right\} \\ &-\frac{\mathrm{Re}}{24}\left\{UI,UK\right\}^T \int_{\Omega_e} \left\{N_1\right\}\left\{N_1\right\}^T \left\{N_1\right\}^T 4\det\left(J\right) d\tau \left\{SIK\right\} \\ &-\frac{\mathrm{Re}}{24}\left\{UJ,UK\right\}^T \int_{\Omega_e} \left\{N_1\right\}\left\{N_1\right\}^T \left\{N_1\right\}^T 4\det\left(J\right) d\tau \left\{SJK\right\} = 0\end{aligned} \tag{4.30}$$

Separating the symmetric tensor into its components $FB11, FB12$ and $FB22$ leads to the following three uncoupled statements for a 2-dimensional problem

$$
\begin{aligned}
GWS_e &= \int_{\Omega_e} \{N_1\}\{N_1\}^T \, d\tau \{FB11\} \\
&- \frac{\mathrm{Re}}{24}\{U1,UK\}^T \int_{\Omega_e} \{N_1\}\{N_1\}^T \{N_1\}^T \, 4\det(J)\, d\tau \{S1K\} \\
&- \frac{\mathrm{Re}}{24}\{U1,UK\}^T \int_{\Omega_e} \{N_1\}\{N_1\}^T \{N_1\}^T \, 4\det(J)\, d\tau \{S1K\} = 0
\end{aligned}
\tag{4.31a}
$$

$$
\begin{aligned}
GWS_e &= \int_{\Omega_e} \{N_1\}\{N_1\}^T \, d\tau \{FB12\} \\
&- \frac{\mathrm{Re}}{24}\{U1,UK\}^T \int_{\Omega_e} \{N_1\}\{N_1\}^T \{N_1\}^T \, 4\det(J)\, d\tau \{S1K\} \\
&- \frac{\mathrm{Re}}{24}\{U2,UK\}^T \int_{\Omega_e} \{N_1\}\{N_1\}^T \{N_1\}^T \, 4\det(J)\, d\tau \{S2K\} = 0
\end{aligned}
\tag{4.31b}
$$

$$
\begin{aligned}
GWS_e &= \int_{\Omega_e} \{N_1\}\{N_1\}^T \, d\tau \{FB22\} \\
&- \frac{\mathrm{Re}}{24}\{U2,UK\}^T \int_{\Omega_e} \{N_1\}\{N_1\}^T \{N_1\}^T \, 4\det(J)\, d\tau \{S2K\} \\
&- \frac{\mathrm{Re}}{24}\{U2,UK\}^T \int_{\Omega_e} \{N_1\}\{N_1\}^T \{N_1\}^T \, 4\det(J)\, d\tau \{S2K\} = 0
\end{aligned}
\tag{4.31c}
$$

where $K = 1..2$ is a summation index. This expression can be written in the finite element template form used at the UT CFD Laboratory, where each term in Eqn. (4.31) is replaced by a line of code consisting of six entries, i.e. a global constant, an element constant, nodal distributed data, metric data resulting from the coordinate transformation, the finite element basis matrix, and the unknown variable or source data. The integrals of the basis functions are expressed via entries in the fourth and fifth placeholder of the template form, e.g. $\det(J)[B3000] = \int_{\Omega_e} \{N_1\}\{N_1\}^T \{N_1\}^T \, d\tau$

The residuals of the Galerkin weak statements (4.31) on an element are then

$$
\begin{aligned}
RES_{FB11} = &(-, FAMUL, RENO)(\ \ )(U1, U1)(0;2)(B3000)(S11) \\
&+(-, FAMUL, RENO)(\ \ )(U1, U2)(0;2)(B3000)(S12) \\
&+(-, FAMUL, RENO)(\ \ )(U1, U1)(0;2)(B3000)(S11) \\
&+(-, FAMUL, RENO)(\ \ )(U1, U2)(0;2)(B3000)(S12)
\end{aligned} \tag{4.32a}
$$

$$
\begin{aligned}
RES_{FB12} = &(-, FAMUL, RENO)(\ \ )(U2, U1)(0;2)(B3000)(S11) \\
&+(-, FAMUL, RENO)(\ \ )(U2, U2)(0;2)(B3000)(S12) \\
&+(-, FAMUL, RENO)(\ \ )(U1, U1)(0;2)(B3000)(S11) \\
&+(-, FAMUL, RENO)(\ \ )(U1, U2)(0;2)(B3000)(S22)
\end{aligned} \tag{4.32b}
$$

$$
\begin{aligned}
RES_{FB11} = &(-, FAMUL, RENO)(\ \ )(U2, U1)(0;2)(B3000)(S11) \\
&+(-, FAMUL, RENO)(\ \ )(U2, U2)(0;2)(B3000)(S22) \\
&+(-, FAMUL, RENO)(\ \ )(U2, U1)(0;2)(B3000)(S12) \\
&+(-, FAMUL, RENO)(\ \ )(U2, U2)(0;2)(B3000)(S22)
\end{aligned} \tag{4.32c}
$$

where RENO is the Reynolds number, and FAMUL stands for $\beta/6$.

The jacobians in (4.30) are expressed as

$$JAC_{FB11} = (\ \ )(\ \ )(\ \ )(0;1)(B200)(\ \ ) \tag{4.33a}$$

$$JAC_{FB12} = (\ \ )(\ \ )(\ \ )(0;1)(B200)(\ \ ) \tag{4.33b}$$

$$JAC_{FB22} = (\ \ )(\ \ )(\ \ )(0;1)(B200)(\ \ ) \tag{4.33c}$$

The code will assemble those element matrices over the sum of all elements, hence produce three global matrix statements over the domain Ω

$$\left[JAC_{FB11}\right]\{FB11\} = \{RES_{FB11}\} \tag{4.34a}$$

$$\left[JAC_{FB12}\right]\{FB12\} = \{RES_{FB12}\} \tag{4.34b}$$

$$\left[JAC_{FB22}\right]\{FB22\} = \{RES_{FB22}\} \tag{4.34c}$$

resulting in a nodal solution vector for the TWS SGS fluxes $\{FB11\}$, $\{FB12\}$ and $\{FB22\}$. The other PDE systems are transferred into template form in similar ways.

The iterative cycle used in the numerical parts of this dissertation project follows from (4.17), hence the matrix statement to be solved iteratively is approximated as

$$\begin{bmatrix} [\text{JAC_PRES}] & [0] & [0] \\ [0] & [\text{JAC_U+T+PHI}] & [0] \\ [0] & [0] & [\text{JAC_FLUXES}] \end{bmatrix} \delta \begin{Bmatrix} PRES \\ \begin{Bmatrix} U1 \\ U2 \\ TEMP \\ PHI \end{Bmatrix} \\ FLUXES \end{Bmatrix} = -\begin{Bmatrix} RES_PRES \\ \begin{bmatrix} RES_U1 \\ RES_U2 \\ RES_TEMP \\ RES_PHI \end{bmatrix} \\ RES_FLUXES \end{Bmatrix} \tag{4.35}$$

This iteration is called “quasi-Newton”, since the global Jacobian is decoupled into three major groups, namely the pressure, the velocities, temperature and constraint ϕ, and the LES theory flux vectors. The link between those groups lies through their residuals, which are functions of variables from all groups.

As organized from the pressure projection theory, the pressure at time t_n is solved first as a function of the complete LES state variable solution at time t^n, followed by the velocities, temperature and constraint, coupled with the flux vector solutions. Then the next iteration starts through the two group iteration, until the iteration converges to a

certain criteria (usually order $1x10^{-4}$). Then the next time step commences with the pressure solution.

A full Newton iterative scheme would couple all Jacobians, which would increase the degree of freedoms of the system to a level where computational memory becomes an issue. The selected quasi-Newton iteration strategy shows acceptable convergence and stability behavior, while performing the computations in a reasonable amount of time. A second approach possible would be to calculate the fluxes only once during a time step, hence the iterations would use the fluxes from the previous time step. This would certainly reduce CPU cycles and improve iterative convergence at the expense of retarding the LES flux vector influence on the flow-field solution.

4.4 Accuracy and Convergence

The semi-discrete approximation error for any finite element approximation q^h is

$$e^h\left(\boldsymbol{x},t\right)=q\left(\boldsymbol{x},t\right)-q^h\left(\boldsymbol{x},t\right) \tag{4.36}$$

where, since both q and q^h are continuous, the error is also continuous. To examine the spatial as well as temporal influences on the approximation error, it is beneficial to separate it into spatial and temporal semi-discrete components, [Bak83]. In one dimension, the resolution is

$$\sigma\left(j\Delta x,n\Delta t\right)=e^h\left(j\Delta x,t\right)+\tau\left(j\Delta x,n\Delta t\right) \tag{4.37}$$

with the spatial semi-discretization error

$$e^h\left(j\Delta x,t\right)=q\left(x,t\right)-q^h\left(j\Delta x,t\right) \tag{4.38}$$

the temporal truncation error

$$\tau\left(j\Delta x, n\Delta t\right) = q^h\left(j\Delta x, t\right) - Q_j\left(n\Delta t\right) \tag{4.39}$$

and the fully discrete error

$$\sigma\left(j\Delta x, n\Delta t\right) = q\left(x, t\right) - Q_j\left(n\Delta t\right) \tag{4.40}$$

For any choice of norm, the triangle identity yields

$$\left\|\sigma\right\| = \left\|e^h + \tau\right\| \le \left\|e^h\right\| + \left\|\tau\right\| \tag{4.41}$$

Examining the flux equation (2.67), it can be shown, [ORed76], [Kol00], that for a negligible convective flux and for the Euler explicit time integration $\theta = 0$, the semi-discrete approximation error expressed in Sobolev norm H^1, behaves as

$$\left\|e^h\left(t\right)\right\|_{H^1(\Omega)} \le C_1 h^k \left\|q\left(t\right)\right\|_{H^{k+1}(\Omega)} + C_2 \Delta t \left\|q\left(t_0\right)\right\|_{H^1(\Omega)} \tag{4.42}$$

where C_1 and C_2 are constants, h is the measure of the mesh and Δt is the time step. In the case where the diffusion flux can be neglected, the discrete approximation error is described through

$$\begin{aligned}\left\|e^h\left(t\right)\right\|_{H^1(\Omega)} &\le C_1 h^{k+1} \left\|q\left(t\right)\right\|_{H^{k+1}(\Omega)} + C_2 \Delta t \left\|q\left(t_0\right)\right\|_{H^1(\Omega)} \\ &\quad + C_3 h \int_{t_0}^{t} \left\|q\left(\tau\right)\right\|_{H^{k+1}(\Omega)} d\tau\end{aligned} \tag{4.43}$$

showing that $\left\|e^h\right\|_{H^1}$ as the measure of the mesh independent of the basis degree k.

Based on this theoretical statement, the asymptotic error estimates in *n*-dimensions for the finite element weak statement formulation can be conveniently expressed in the energy semi-norm as

$$\left\| e^h(t) \right\|_{E(\Omega)} \le C_1^2 h^{2\gamma} \left(\left\| data \right\|_{H^{k-1}(\Omega)}^2 \right) + C_2^2 \Delta t^{f(\theta)} \left\| q(t_0) \right\|_{H^1(\Omega)}^2 \qquad (4.44)$$

with $\gamma = \min(k, r-1)$ for $1/\mathrm{Re}$ non-vanishing, and where k is the order of basis degree and r characterizes the smoothness of the data. This error estimate shows that a $\{N_k\}$ finite element algorithm is $2k$ order accurate in space and first- or second order accurate in time, depending on the implicitness factor θ.

The general superiority of the finite element approach has been shown repeatedly in the past, [Bak05], especially the error control abilities of the TWS formulation [Bak97]. This can be detailed by examination of dispersion error, hence the inability of any algorithm to resolve $2\Delta x$ data on a given discretization with mesh measure Δx. Via a Fourier modal solution analysis of a simple transport equation, the amplitude factor solution can be derived, showing how much a solution is dispersed during one time step. Defining the signal propagation of the spectral distribution as the phase velocity gives a measure how accurate the solution can be propagated in one time step.

Figure 4.1 gives a comparison between currently used commercial algorithms, and how much phase velocity error occurs in the vicinity of the $2\Delta x$ cut-off. Specifically, for the $3\Delta x$ solution component, the third order finite volume QUICK algorithm, common in today's CFD packages, has a 55% error rate in its ability to propagate a solution accurate in time, while the TWS algorithm with linear basis functions and a γ correction of 0.083 only experiences 10%.

Figure 4.3 shows the amplification factor error made by these algorithms. At $3\Delta x$, the finite difference upwind algorithm produces a 75% error, while the linear TWS with $\beta = 0.063$ yields only 10%.

A very informative verification problem is the rotating cone, where a rotated Gaussian distribution is advected along a circular path until it reaches its starting location. The analytical solution (Figure 4.3a) shows that the form and amplitude of the Gaussian is unchanged after one revolution. For the numerical solution using a finite difference Crank-Nicolson algorithm, Figure 4.3b examines that the energy formerly located in the Gaussian shape has been dispersed throughout the domain. The original distribution has almost disappeared.

A much improved solution can be seen in Figure 4.3c, where the numerical experiment has been repeated using a GWS with linear finite element basis. Finally, for TWS with linear finite element basis and an optimal γ, (compare Eqn. (4.23)), the solution is accurate to within one percent.

5. Discussion and Results

To establish the viability of the developed LES theory with newly developed TWS SGS model, computational experiments were conducted comparing the closure models for three pertinent benchmark and validation test cases. First the feasibility of the TWS beta term as an SGS model is examined for a turbulent duct flow problem. Examinations are made to connect regions of spectral content with dissipation of energy via the TWS beta term in those locations, compared to the Smagorinsky model.

Second was examination of the dissipation and stabilization capabilities for a laminar flow large Re driven cavity problem, with solution dominated by extreme geometric BC singularities and using solution-adapted meshing. Finally, the LES theory is fully examined for an 8:1 thermal cavity validation problem, exhibiting a critical Ra for steady flow transition to unsteady cyclic flow with generation of a significant range of eddy scales for progressively larger Re.

5.1 Turbulent Duct Flow

The first computational assessment is for turbulent flow in a two-dimensional duct, using a non-uniform mesh of 33x25 nodes and a Reynolds number of 4.3×10^6. The objective is to examine the behavior of the Stokes, Reynolds, TWS and Smagorinsky stress tensors in a turbulent flow environment that creates false spectral content due to dispersion error

from the inflow boundary condition that has to be resolved. The main question is, how the TWS and Smagorinsky stress might stabilize the solution, hence add artificial diffusion.

The problem domain consists of a half inch high and 3 feet long duct, necessary to ensure enough distance from the entrance to allow for a fully developed steady turbulent velocity profile. The 1:72 aspect ratio of duct height to length requires the use of distorted plot styles for data interpretation. The non-uniform mesh, featuring 33x25 nodes is pushed towards the entrance of the duct, see Figure 5.1.1. The turbulent flow CFD algorithm employs the k-ε turbulence closure model, which generates an adequately accurate steady turbulent velocity profile in the downstream reach of the duct. This is show in Figure 5.1.2, which validates convergence of the turbulent velocity profile for 33x17 and 33x25 node meshing compared to turbulent boundary theory. The Y+ distribution of the first node of the wall, Figure 5.1.3, confirms that the k-ε algorithm employed is indeed accurately imposing the law of the wall boundary condition.

The inflow boundary condition for the duct is an interpolated (simulated) turbulent velocity profile, the inaccuracy of which generates dispersion error, hence significant spectral content in the immediate downstream region (Figure 5.1.4). The boundary condition for the turbulent kinetic energy is zero, resulting in significant dispersion error peaks close to the wall (Figure 5.1.5). The BC for dissipation ε is set as vanishing Neumann, i.e., floating, hence resulting in the localized sharp peak shown in Figure 5.1.6. From these data, it is obvious that singularities induced by the inflow BC require numerical dissipation to maintain stability. The k-ε turbulent model by itself cannot

handle these instabilities, created by the dispersion error, which can be deducted from the plot of the turbulent Reynolds number, Figure 5.1.7.

In this code execution, all stresses are post-processed from the computed velocity profile. A comparison of the laminar Stokes shear stress FD_{12} with the TWS SGS stress FB_{12} at the far downstream location $x_1 = 2.27\,ft$, Figure 5.1.8, shows that the TWS stress is two orders of magnitude smaller than the Stokes stress. This is due to the fact that the spectral content has already been dissipated that far down the duct, by orders of magnitude in the core flow of the duct. Figure 5.1.9 gives a comparison of the k-ε turbulent Reynolds shear stress T_{12} and the Smagorinsky SGS shear stress FS_{12}. The magnitude of the Reynolds stress is much higher than the Smagorinsky stress. The profile of T_{12} distribution clearly shows the classical turbulent content, while the Smagorinsky stress resolves the turbulent profile badly, especially close to the wall.

The TWS SGS normal stress FB_{11} is having an influence only in the core region of the dispersion error induced spectral content, Figure 5.1.11, and its magnitude is orders higher than the Stokes, Reynolds or Smagorinsky stresses (Figures 5.1.10, 5.1.12 and 5.1.13) in this local region. It clearly dominates energy dissipation in that region, hence controls the dispersion error spectral content by smoothing, therefore retaining the stability of the system. The SGS Smagorinsky normal stress FS_{11} does not have this ability (Figure 5.1.12). Its maxima are located at the inflow wall points, dissipating only a small amount of energy in the large spectral content region.

For the shear stress component of the SGS TWS stress FB_{12}, it is evident that energy dissipation again is contained to the regions of spectral content, while it is negligible

elsewhere, Figure 5.1.15. Its magnitude is comparable to the Reynolds shear stress T_{12}, which shows a turbulent profile disturbed by the influence of the dispersion error created by the inflow boundary condition, Figure 5.1.17. The laminar Stokes shear stress FD_{12} and the SGS Smagorinsky stress FS_{12} show similar behavior, Figures 5.1.14 and 5.1.16, with the magnitude of Smagorinsky two orders higher at the wall. It seems to have no influence on energy dissipation in the regions of dispersion error spectral content.

In summary, it is evident that the TWS SGS stress tensor is performing well in dissipating energy from areas of high spectral content. Since this content is unwelcome, because it was created by dispersion error, the TWS SGS model seems to do well as a stabilization mechanism. The Smagorinsky SGS model does not seem to have a major influence on stability.

5.2 Laminar Flow in Driven Cavity

The second computational simulation is for laminar flow in a two-dimensional driven cavity at Reynolds number of 2000. This problem is a benchmark in that comparable established numerical results exist in abundance, [GGS82, Eri01]. The objective of this test case is to examine the behavior of the TWS beta stress tensor versus the laminar Stokes stress tensor, especially in the areas of apparently inadequate mesh resolution and around the geometric singularities.

The problem domain is a square cavity, enclosed on three sides by stationary walls (Figure 5.2.1). The top of the cavity features a sliding lid with constant velocity to the right. This induces a clock-wise flow in the interior of the cavity. Since the upper corners experience the moving lid, as well as walls with a no-slip condition, singularities are produced by these boundary conditions, giving this benchmark problem its unique character.

To handle the singular behavior at the corners and the wall boundary layers appropriately, a non-uniform mesh is used which has progression ratios that move more meshing into the upper corners (Figure 5.2.2). The values of those mesh progression ratios are optimized based for an equi-distribution (see [Eri01]) of the energy norms of vorticity and stream-function, as summarized in Figure 5.2.3. Hence this mesh has enough resolution in both upper corners to handle the BC singularities. The associated velocity solution for this problem, created by [Eri01], is shown in Figure 5.2.4, graphed as unit vectors colored for speed. The solution features a central clock-wise circulating region, as well as two smaller secondary re-circulation bubbles in each lower corner, and a sharp localized recirculation near the upper left corner.

This dissertation project executed the test case using the energy norm equi-distribution mesh parameters, Figure 5.2.2. The resultant velocity field appears visually identical to that in [Eri01], compare Figures 5.2.4 and 5.2.5. The associated pressure distribution exhibits sharp maxima in both upper corners, due to the BC singularity of the sliding lid, which are resolved adequately on this optimized mesh, see Figure 5.2.6.

Using the developed LES template, the laminar Stokes stresses tensor distributions can be compared with the TWS beta term stress tensor. The laminar Stokes normal stress, FD11, has its maxima in the regions of the BC singularities, Figure 5.2.7, as is expected. Green represents a null level of this tensor, which dominates the lower areas of the mesh, following the outskirts of the center vortex. In comparison to the Stokes normal stress the TWS SGS normal stress has extrema two orders higher, hence dominates the laminar normal stress by far, Figure 5.2.8. It shows strong dissipation of dispersion error induced along the lid, hence the false spectral content generated by the problem definition. Furthermore it generates increased dissipation in the areas of the secondary recirculation bubbles located in the left bottom and right top of the cavity, where the mesh appears too coarse to adequately resolve the transition region at the edge of the secondary recirculation bubbles.

The Stokes shear stress FD12 exhibits large peaks of diffusion in both upper corners and along the lid, Figure 5.2.9, but its magnitude is an order smaller compared with the TWS SGS shear stress FB12, Figure 5.2.10. However, the TWS SGS shear stress dominates not at the corner singularities but along the edges of the primary vortex.

For the Stokes normal stress FD22, Figure 5.2.11, a similar distribution can be seen as for FD11, hence peaks at upper corners as well as small values around the edges of the secondary recirculation bubbles. The TWS SGS normal stress FB22 shows a magnitude two orders higher than the Stokes stress FD22, Figure 5.2.12, and contains a very complicated distribution of local extrema mainly in the regions of the secondary recirculation bubbles. This presented energy dissipation of the spectral content featured by the TWS SGS stresses acts as a control, which dominates the algorithm stability.

In summary, the Stokes stress tensor distributions are small in comparison with the TWS SGS stress tensor. Obviously, this quality benchmark solution is dominated by the dissipation mechanism due to the numerical (artificial) TWS SGS stresses, which in fact are dissipating false, dispersion error induced energy as generated by Re being quite large. Analogously, these are areas of high spectral content, comparable to eddy structures in turbulent flow. This mesh-scale dissipation effect is according to theory for LES sub-grid scale models, and proves that the TWS SGS stresses fulfill the basic requirements of a SGS model. Furthermore, the TWS SGS stress tensor absolutely stabilizes the solution process, generating a benchmark grade solution for recirculation bubbles in the lower corners of the cavity. Hence the TWS SGS stress tensor appears well suited in meeting the mathematical requirement for LES simulation embedding of the SGS mechanism.

5.3 Thermal Cavity, Laminar to Turbulent Flow

The selected validation-class simulation problem statement for the LES theory assessment is an 8:1 aspect ratio thermal cavity enclosure, which features a natural convection induced flowfield in a bounded domain. Experiments show that this problem transitions from steady to multi-scale unsteady above a critical Rayleigh number, [LeQ94]. Numerical experiments of this test case have determined the critical Rayleigh number to be in the vicinity of $Ra_{crit} \approx 3.1x10^5$, [CGS02]. The unsteady flow experiences

a vast range of features, e.g. vertical and horizontal boundary layers, corner structures, stratified core, shedding and multi-scale eddies, hence is considered a perfect “CFD laboratory” for the LES theory implementation assessment due to the enormous variety of spectral content, see Figure 5.3.1, as parameterized by Rayleigh number.

The objective of this test case is to examine the behavior of the LES theory simulation as the flow condition is changed from laminar to turbulent flow via an increase of the Rayleigh number past critical, hence also the Reynolds number. Questions to be answered are how the magnitudes of the LES theory stress tensors are changing, specifically the shift in dominance through laminar/turbulent transition. Furthermore, the efficiency of the various SGS models on the stability of the algorithm over a Rayleigh number range is facilitated, to determine if SGS models do not require an additional numerical diffusion mechanism. Last, the issue of selected bounded domain boundary condition enforcement needs to be assessed.

The 8:1 thermal cavity is a rectangular enclosure (Figure 5.3.2), eight length units tall and one length unit wide. The left wall is kept at a constant temperature T_{hot}, while the right wall is kept cool at T_{cold}. Top and bottom of the cavity are insulated. The whole enclosure experiences a gravitational force in the negative y-direction. Since the driving force of this problem is buoyancy, it is necessary to non-dimensionalize the LES theory PDE system with a reference velocity that is based on the temperature difference between the two walls. Hence U_r is defined as, [Wil93]

$$U_r = \sqrt{\beta g \Delta T_r L_r} \tag{5.1}$$

where $\Delta T_r = T_{hot} - T_{cold}$. This definition relates the Reynolds number directly to the Rayleigh number, hence the transition from laminar to turbulent flow is uniquely controlled the Rayleigh number, see Table 5.1. The Prandtl number for all numerical experiments is constant at $\Pr = 0.71$. The TWS SGS model, Eqn. (2.63) and (2.64), was implemented using a β and β_t of 0.01, which provided dissipation in a range between compared SGS models.

The boundary condition issue is handled as described in Chapter 2.9 by use of a dual-theory implementation on a partitioned domain. The interior of the domain is equipped with a uniform mesh (Figure 5.3.3), on which the complete rational LES theory system is operating. The wall regions are admitted by changing the rational Pade filter to the box filter, [Joh04]. This assumption allows a non-uniform filter scale, hence mesh distribution, wherein only the SGS stress tensor operates.

5.3.1 About Symmetries in Thermal Cavity Flow-Fields

First computational experiments in the 8:1 thermal cavity generated concern that the perceived symmetric behavior, expected for this problem statement, was not indeed occurring. Specifically, laminar flow executions in the 8:1 thermal cavity case at $Ra = 3.4x10^6$ resulted in a slightly non-symmetric flow field beyond $t = 80$ sec, as observed in the stream-function and temperature distributions in Figure 5.3.1.1. This was not the expected result, as the well established square cavity benchmark indeed produced

solutions exhibiting a symmetric behavior. Ample benchmark solutions are available for the square cavity, [Eri02].

Therefore, the benchmark square thermal cavity was recovered to quantify mathematically what had previously only been measured in the “eyeball” norm. The standard case uses a non-uniform 33x33 mesh, which was then extended to a 33x165 non-uniform mesh on a 5:1 aspect ratio vacity. The algorithm chosen for this benchmark assessment employs the same FE CFD framework developed at the UT CFD Laboratory [Bak05]. The state variables members are vorticity and stream-function, calculated directly, which has historically been proven of excellent stability and robustness.
The expected vorticity solution symmetry is quantified by the observation that nodally $\Omega(i, j) = \Omega(j, i)$, therefore the existent symmetry plane is the diagonal between the lower left and upper right corners of the domain. The symmetric assessment variable definition is thus

$$\tau_2 = \Omega(i, j) - \Omega(j, i) \tag{5.2}$$

Algorithm executions on the 33x33 mesh square cavity at Rayleigh numbers of $1\text{x}10^3$, $1\text{x}10^4$ and $1\text{x}10^5$ prove that the magnitude of τ_2 is indeed machine zero, Figures 5.3.1.2 - 5.3.1.4. Therefore, the square cavity vorticity distribution indeed is diagonal plane symmetric. The next step was to progressively elongate the laminar benchmark, finally ending up with a 5:1 aspect ratio cavity. For the same algorithm and range of Rayleigh numbers, Figures 5.3.1.5 to 5.3.1.7 summarize the results. Now, the increase in Rayleigh number progressively increases the magnitude of τ_2, which clearly confirms that

vorticity symmetry accrues only for the square thermal cavity. Comparative results among these executions for τ_2, vorticity Ω and the energy-norm of Ω, are summarized in Table 5.2.

These results clearly validate that the unsteady lack of symmetry for the selected 8:1 aspect ratio thermal cavity is not a theory, code implementation or mesh discretization error, but due to the geometric setup of the problem. The consensus explanation is that since buoyancy is uni-directional, i.e. not symmetric, hence is the equivalent of an adverse pressure gradient for flow moving downwards along the right wall, while along the left wall this gradient assists in moving the flow upwards. This could certainly destroy the apparent symmetry over time and distance of flow travel as a function of the wall length. These results fully confirm my confidence in a correct LES theory formulation and code implementation for the validation experiments on the 8:1 thermal cavity.

5.3.2 Thermal Cavity at Ra = 3.4x10^5

The first computational experiment on the 8:1 thermal cavity using the complete LES theory with the TWS SGS model was executed on a 41x281 mesh (Figure 5.3.3) at the slightly above-critical Rayleigh number of 3.4x10^6, resulting in a Reynolds number of Re = 680. This clearly defines an insipient unsteady, laminar flow ($Ra > Ra_{crit}$), which is recognizable in the temperature distributions at t = 54, 194 and 294 seconds, Figure 5.3.2.1. The distribution at t = 294 sec shows only a minor un-symmetric character. Eddy

structures are confined to the top and bottom section of the cavity, as well as to an elongated area in the center (Figure 5.3.2.2). The Stokes normal stress tensor in x-x direction shows magnitudes that are one to two orders larger than the Reynolds and TWS SGS stresses, hence the computation is dominated by the laminar physics (Figure 5.3.2.3). The influence of the filtering, hence the LES Reynolds stress is limited to the recirculation regions in the top and bottom of the cavity in the Ω_{LES} domain mesh. For the shear stress in x-y direction, Figure 5.3.2.4 confirms that the Stokes stress operates at left and right wall boundary layer regions, as expected, again surpassing both the LES Reynolds and TWS SGS shear stresses in magnitude. The TWS SGS stress experiences its maxima at the interface between non-uniform and uniform meshing, hinting at its proven stabilization capabilities in regions of spectral content, while the Reynolds stress shows small influences only in the region of the two recirculation bubbles.

In summary, the laminar insipient unsteady 8:1 thermal cavity flow is dominated by the Stokes stress tensor (laminar diffusion mechanism). The TWS SGS model performs in this Reynolds range only as algorithm stabilizer due to energy dissipation in the theory transition region. It assists in getting a smooth transition of state variable values over the interior/wall layer interface, hence enables the use of a two-model approach for boundary condition purposes. The LES theory Reynolds stresses due to filtering are obviously negligible.

5.3.3 Thermal Cavity at Ra = 3.4×10^6

The second execution of the 8:1 thermal cavity employs a Rayleigh number of 3.4×10^6, resulting in a Reynolds number of Re = 2186. This is close to the transition Re between laminar and turbulent channel flow. The temperature distribution of the truly unsteady flow shows many more eddy structures, Figure 5.3.3.1, in particular some wall shedding originating in the boundary layer. The top and bottom recirculation bubbles, which were present at the lower Reynolds number, have stagnated, and the elongated center vortex has spawned two new recirculation regions in its periphery at $t = 96.8$ sec (Figure 5.3.3.2).

The normal Reynolds stress surpasses the normal Stokes stress slightly, only in the immediate region of the eddy structures (recirculation bubbles), see Figure 5.3.3.3. The normal TWS SGS stress is at null level everywhere, showing solution participation in the momentum balance only at the upper eddy structure. For the shear stresses (Figure 5.3.3.4), the Stokes stress is dominating in the wall regions, as expected, while the Reynolds stress experiences local peaks of the same order in the central eddy regions. The shear component of the TWS SGS stress is at null level except locally fulfilling its stabilizing function in the region where the elongated vortex penetrates the two-mesh interface. Overall, the extrema of all stresses are comparable in order, and all have increased in comparison with the Ra = 3.4×10^5 execution by one to two orders.

In summary, the numerical experiment at Ra = 3.4×10^6, i.e. Re = 2186, shows the overall magnitude of all involved stresses increased over the Re=680 laminar execution. The Stokes stresses remain dominating the general flow, with principle importance in the laminar boundary layer regions at the left and right wall. The LES Reynolds stresses are showing principle impact in the regions of local eddy formation, while the TWS SGS stresses remain generally null except for stabilizing function in the two-mesh interface region.

5.3.4 Thermal Cavity at Ra = 3.4×10^7

The simulation of the 8:1 thermal cavity at Ra = 3.4×10^7 has been performed on an optimized 41x281 node mesh (Figure 5.3.3), featuring a non-uniform wall-layer part and a uniform interior domain. The Reynolds number for this execution is Re = 6850, which puts it in the beginning of what should be turbulent flow.

The temperature distributions at times t = 7.03, 49.5 and 104 seconds show a very thin thermal boundary layer (Figure 5.3.4.1), in comparison with earlier lower Rayleigh number executions. Vortex shedding is reduced to a very narrow band along both walls. A multitude of recirculation eddies have formed, Figure 5.3.4.2, which can be seen from the stream-function distributions. The core eddy structures are rather uniformly distributed; the two recirculation bubbles at the top and bottom end of the cavity appear dominant. Non-symmetric flow behavior is clearly present in the stream-function plot at time t = 104 sec.

The Stokes shear stress is mainly dominant in the boundary layers on the left and right walls (Figure 5.3.4.3). The LES Reynolds shear stress level is null generally except for sharp extrema existent in each of the areas of eddy structures. The TWS SGS shear stress again is mainly operative in the wall-layers up to the two-mesh interface. A close-up view of these shear stress distributions in the upper left corner is given in Figure 5.3.4.4, which shows clearly that the two-model approach disables the rational LES Reynolds stress in the wall region with distributions around the interface between SGS non-uniform and LES uniform mesh being relatively smooth, with no discontinuities apparent. This indicates that the two-model approach is well able to admit enforcing the no-slip Dirichlet boundary condition at the wall while generating an adequate state variable field into the uniform-mesh rational LES theory domain. The solution tensor for the momentum equation auxiliary problem, Figure 5.3.4.5, which is computed throughout both the wall layer domain and the interior rational LES model domain, reveals the inappropriateness of non-uniform meshing for the rational LES theory formulation. The extrema occur in the wall regions, hence the non-uniform mesh region, and therefore hence would over-predict the energy transfer of the LES Reynolds stresses.

A comparison of the TWS SGS shear stress, the Smagorinsky model shear stress and the SGS shear stress based on the formulation in Eqn. (2.57) is given in Figure 5.3.4.6. The Smagorinsky stress has the highest overall magnitude, which confirms its over-diffusive character as stated in [Joh04]. The SGS model based on (2.57) is two orders of magnitude smaller then the Smagorinsky model, while the TWS SGS model falls in between with a magnitude one order lower than Smagorinsky, as set by $\beta = 0.01 = \beta_t$. All SGS model

shear stresses appear to dissipate energy at the same locations, i.e., at the areas of eddy structures.

Recalling the FE CFD algorithm theory on suitability of a mesh, [Bak05], examination of the temperature energy norm shows that the maxima and minima are within one order of magnitude, Figure 5.3.4.7. This is considered firm quantization of mesh adequacy, since an equal distribution of the energy-norm indicates an optimal mesh. The graph shows that the energy norm extrema lie in the wall regions, which is understandable, since the wall-mesh has to resolve the highest gradients due to the Dirichlet boundary conditions.

In summary, the Ra=3.4×10^7 specification seems to be still in the transitional region of the flow regime, with orders of magnitude of the Stokes, Reynolds and TWS SGS stresses similar to each other. This larger Rayleigh, hence Reynolds number solution has created a vast array of different-size eddies, between which the LES Reynolds stress seems to adequately transfer energy. The SGS stresses concentrate their energy dissipation at the location of spectral content, with the TWS SGS stress performing in the median of the examined SGS models.

5.3.5 Thermal Cavity at Ra = 3.4×10^8

The Ra = 3.4×10^8 execution with Re = 19932 uses the same mesh as for Ra = 3.4×10^7. The temperature distributions at t = 1.83, 9.86 and 22.8 seconds show a very thin thermal boundary layer (Figure 5.3.5.1). Some algorithm stability issues occurred while running

at these Reynolds and Rayleigh numbers on this mesh, but were contained by the code through reduction of the time step. The TWS SGS model, Eqn. (2.63) and (2.64), was implemented using a β and β_t of 0.01. No extra artificial diffusion had to be added to stabilize this numerical experiment. The previously elongated center vortex structure at Ra = 3.4×10^7 has been replaced by two smaller bubbles, Figure 5.4.5.2. The number of smaller eddies appears reduced, as visible at time t = 22.8 sec at the left wall, as well as the top and bottom region of the domain. This would be expected as the flow-field transitions to turbulent with the associated increase in spectral content dissipation.
The laminar Stokes shear stress provides an influence only within the thin wall layer, Figure 5.3.5.3, see also the close-up view in Figure 5.3.5.4. The LES Reynolds shear stress dominates on the interior mesh, having its maxima at the locations of the most energy-rich eddies. The TWS SGS stress shows modest dissipation of energy in the regions of the vortex structures, with dominant dissipation in the wall layer, where the onset of shedding is apparent (see Figure 5.3.5.2, right plot, upper left wall region). Figure 5.3.5.5 compares the shears stresses of the TWS SGS and Smagorinsky models, as well as the SGS model based on Eqn. (2.57). Again, the Smagorinsky model extrema are almost an order larger.

Driving up the Rayleigh and Reynolds numbers, hence forcing the flow to change from laminar to turbulent, showed that the TWS based SGS model is able to keep the CFD algorithm stable. The same has to be assessed for the Smagorinsky model and SGS model based on (2.57).

From the Ra = 3.4×10^8 solution generated using the TWS SGS model, a restart was performed at t = 9.6 seconds for these two numerical experiments. Using exactly the same input, parameters and convergence criteria, the simulations were run for 500 time steps. The simulation using the Smagorinsky model progressed through 500 steps to a final time of 15.2 seconds, with the code reducing the time step to maintain stability. The temperature distributions of select time points are given in Figure 5.3.5.6. Wall shedding remains visible at both the left and right walls at t = 15.2 sec. A large vortex structure close to the center is maintained, moving slightly upwards. Not many of the original smaller eddies are visible at the end of the simulation, Figure 5.3.5.7.

The code execution of the LES theory implementation using (2.57) as SGS model reached a time of 19 seconds after 500 time steps, hence the time step was lowered slightly less than for the Smagorinsky simulation indicating better stability performance. The temperature distributions, Figure 5.3.5.8, all show wall shedding. A higher number of eddies are present, Figure 5.3.5.9, distributed throughout the domain. Four larger structures are recognizable in the right graph of Figure 5.3.5.9, with several smaller eddies located in between them.

A third SGS model, based on Eqn. (2.52) was tested, but the algorithm did not converge. The addition of artificial diffusion through a TWS beta term did not improve stability. Since the model is based on a second velocity derivative, it seems logical that a finer mesh at the wall combined with a smaller time step might generate solution convergence. But a required increase in meshing, hence substantially increased computational time, would make this model inferior to the other tested SGS models.

The stream-function distribution at t = 14.7 sec. of each of those executions is compared in Figure 5.3.5.10. It is evident that the simulation using the Smagorinsky SGS model is overly diffusive in that it dissipated most small scale structures. Those small eddies are retained well in the TWS SGS model simulation, while the SGS model based on (5.57) retains some small structures, as well as a larger, elongated vortex.

A comparison of the shear components of the SGS models at t = 14.7 seconds clearly compares their magnitude. The Smagorinsky shear stress $SMAG12$ has the highest magnitude, hence again proves its overly diffusive character as stated by [Joh04]. The smallest magnitude is experienced by the SGS model based on Eqn. (2.57), while the TWS SGS shear stress lies in between, as set by $\beta = 0.01 = \beta_t$.

In summary, the results of this section can be concluded as following. Driving the flow problem from laminar to turbulent decreased the importance of the Stokes stresses, as can be expected. The Stokes stresses are still influential in the wall layers. The LES Reynolds stresses gain importance the larger Re becomes, and are confined to the interior of the domain as implemented by the two-model simulation. The wall region flow is therefore driven solely by the SGS closure model. The TWS SGS stress takes responsibility for dissipating energy in the regions of eddy activity, as well as a stabilization mechanism. Based on comparison of magnitude, it is placed between the overly diffusive Smagorinsky model and an established SGS model used in previous rational LES theory implementations, [Joh04]. It dissipates energy, hence stabilizes the simulation, without draining to much energy, which will dampen out smaller eddy structures. All three SGS models proved stable for the largest Re cavity test, without requiring an additional

artificial diffusion mechanism. The problem of no-slip Dirichlet boundary conditions was solved by implementation of a two-theory approach. Examination of close-ups of the Reynolds stress showed that no visible discontinuities occurred at this interface, nor did they occur in the temperature and stream-function distributions.

6. Conclusions and Recommendations

6.1 Conclusions

In this dissertation project an LES theory for the 3-dimensional, incompressible, unsteady Navier-Stokes equations, focused on prediction of mixed convections flows, was developed and implemented into computable form. The rational LES theory, as developed in the literature, was extended to the heat and mass transport equation systems. Boundary conditions appropriate to analysis of flows in bounded domain for this LES theory were developed, leading to a two-theory approach successfully implemented in the computational part of this project. A candidate SGS model was developed based on TWS stability theory developments reported in the literature and its appropriateness to dissipate energy assessed. Comparisons with three other SGS models were performed and showed that the developed TWS theory SGS model is able to acceptably (according to theory) dissipate mechanical energy at the sub-grid scale of eddy structures. It also proved to have positive stabilization effects on the algorithm, without the need of additional artificial diffusion mechanisms. Computational experiments were performed for two benchmark and one validation case, confirming that the TWS SGS model is less diffusive than the Smagorinsky model. Conversely, for the thermal cavity validation case, it was set to be more diffusive than the comparable appropriate order SGS model. It appears to be a valuable addition to the current range of LES sub-grid scale models.

6.2 Recommendations

This newly developed LES theory provides ample research opportunity. For the thermal cavity experiments, the TWS SGS model was implemented using a β and β_t of 0.01. Those values were chosen arbitrarily to place the dissipation ability of the TWS SGS model in between those of the established models examined in this project. Therefore it is imperative, in the next step, to match the exact values of β and β_t for a multitude of flow problems by comparison with experimental data. A first possible flow problem to be examined could be the step-wall diffuser, for which experimental data over a wide range of Re are available. This problem is in particular interesting, since a distinct recirculation bubble downstream of the step is present. Experimental data defines this bubble in size, form and location, hence comparison with numerical simulation of the developed LES theory is simple and more appropriate than questionable comparisons of time-averaged velocity distributions.

Furthermore it is of interest to examine the thickness of the non-uniform wall-layer domain as influenced by the implemented filter width δ. It is desirable to minimize the non-uniform domain region at the walls for mesh reduction purposes, while the boundary layer profile still needs to be correct.

Bibliography

Bibliography

[AH70] Amsden, A. A., Harlow, F.H., "The SMAC Method: A Numerical Technique for Calculating Incompressible Fluid Flows," Los Alamos, New Mexico: Los Alamos Scientific Laboratory, University of California, LA-4370.

[Bak83] Baker, A.J., "Finite Element Computational Fluid Mechanics," Taylor&Francis, 1983.

[Bak05] Baker, A.J., "Fem.PSE," CFD Lab Press, 2005.

[BBP96] Balaras, E., Benocci, C, and Piomelli, U., "Two-layer approximate boundary conditions for large-eddy simulations," AIAA Journal, Vol. 34, pp. 1111-1119, 1996.

[BGO+92] Boris, J.P., Grinstein, F.F., Oran, E.S. and Kolbe, R.L., "New insights into large eddy simulation," Fluid Dynamics Research, Vol. 10, 1992, pp. 199-228.

[Bou03] Boussinesq, J., "Theorie Analytique de la Chaleur [Analytic Theory of Heat]," Vol. 2, Paris: Gauthier-Villars, 1903.

[CB95] Chaffin, D.J. and Baker, A.J., "On Taylor Weak Statement Finite Element Methods for Computational Fluid Dynamics," Int. Journal for Numerical Methods in Fluids, Vol. 21, issue 4, pp. 273-294.

[CGS02] Christon, M.A., Gresho, P.M., and Sutton, S.B., "Computational predictability of time-dependent natural convection flows in enclosures

(including a benchmark solution)," Int. Journal Numerical Methods in Fluids, Vol. 40, issue 8, pp. 953-980, 2002.

[Cha97] Chaffin, D.J., "A Taylor weak statement finite element method for computational fluid dynamics," Dissertation, University of Tennessee, 1997.

[Cut01] Cuturic, D., "Large-Eddy Simulation of Turbulent Channel Flow Significantly Affected by Buoyancy," Chalmers University of technology, Goteborg, Sweden, 2001.

[Eri01] Ericson, S.C., "A CFD Laboratory Archive supporting the academic process," Thesis, University Tennessee, 2001.

[GL00] Galdi, G.P. and Layton, W.J., "Approximation of the large eddies in fluid motion II: A model for space filtered flow," Mathematical Models and Methods, Applied Sciences, Vol 10(3), pp. 343-350, 2000.

[GPMC91] Germano, M., Piomelli, U., Moin, P., and Cabot, W., "A Dynamic subgrid-scale eddy viscosity model," Phys. Fluids A, 3:1760-1765, 1991.

[IL98] Illiescu, T., Layton, W.J., "Approximating the large eddies in fluid motion III: the Boussinesq model for turbulent fluctuations," 1998.

[IJL+03] Iliescu, T., John, V., Layton, W.J., Matthies, G., Tobiska, L., "A numerical study of a class of LES models," Int. J. Comput. Fluid Dyn., Vol.11, pp. 75-85, 2003.

[JA05] John, V. and Liakos, A., "Time-dependent flow across a step: the slip with friction boundary condition," Int. J. for Numerical Methods in Fluids, Vol. 50, pp. 713-731, 2006.

[JC02] Jian, Y. and Chen, Q., “Effect of fluctuating wind direction on cross natural ventilation in buildings from large eddy simulation,” Building and Environment, Vol 37, 2002, pp. 379-386.

[JLS04] John, V., Layton, W. and Sahin, N., “Derivation and Analysis of Near Wall Models for Channel and Recirculating Flows,” Computational Math Applications, Vol 48, pp. 1135-1151, 2004.

[Joh04] John, V., “Large Eddy Simulation of Turbulent Incompressible Flows. Analytical and Numerical Results for a Class of LES Models,” Lecture Notes in Computational Science and Engineering 34, Springer Verlag Berlin, Heidelberg, New-York, 2004.

[Kim88] Kim, J.W., “Taylor Weak Statement,” Dissertation, University Tennessee, 1988.

[Kol00] Kolesnikov, A., “Efficient Implementation of higher Order Methods in Computational Fluid Dynamics,” Dissertation, University of Tennessee, 2000.

[LeQ94] Le Quere, P., “Onset of unsteadiness, routes to chaos and simulations of chaotic flows in cavities heated from the side: a review of present status,” Proceeding of the 10th Int. Heat Transfer Conference, Brighton, UK, pp. 281-296, 1994.

[Lil92] Lilly, D.K., “A proposed modification of the Germano subrid-scale closure method,” Phys. Fluids A, 4:663-635, 1992.

[NoB89] Noronha, W.P., and Baker, A.J., "A Taylor weak statement finite element CFD algorithm for 2D incompressible Navier-Stokes equations," AIAA 27th Aerospace Sciences Meeting, January 9-12, Reno, Nevada, 1989.

[PB02] Piomelli, U. and Balaras, E., "Wall-Layer Models for Large-Eddy Simulations," Annual Review Fluid Mechanics, Vol. 34, pp. 349-374, 2002.

[Pop00] Pope, S.B., "Turbulent Flows,", Cambridge University Press, 2000.

[RF99] Roy, S. and Fleming, M., "Nonlinear Subgrid Embedded Element-free Galerkin Method for Monoton CFD Solutions," 3rd ASME/JSME Joint Fluid Engineering Conference, 1999.

[SCC01] Su, M., Chen, Q. and Chiang, C., "Comparison of Different Subgrid-Scale Models of Large Eddy Simulation for Indoor Airflow Modeling," Journal of Fluids Engineering, Vol. 123, 2001, pp/ 628-639.

[Sch75] Schumann, U., "Subgrid-scale model for finite difference simulation of turbulent flows in plane channels and annuli," Journal of Computational Physics, Vol. 18, pp. 376-404.

[Sma63] Smagorinsky, J., "General Circulation Experiments with the Primitive Equations. I. The Basic Experiments," Monthly Weather Revue, Vol. 91, 1963, pp.99-164.

[SPF+97] Spitler, J.D., Pedersen, C.O., Fisher, D.E., Menne, P.F. and Cantillo, J., "An Experimental Facility for Investigation of Interior Convective Heat Transfer," ASHRAE Transactions, NY-91-5-1, pp. 497-504.

[SRY78] Schneider, G.E., Raithby, G.D. and Yovanovich, M.M., “Finite Element Solution Procedures for Solving the Incompressible Navier-Stokes Equations Using Equal Order Variable Interpolation,” Numerical Heat Transfer, Vol. 1, pp. 433-451.

[WB96] Williams, P.T., Baker, A.J., “Incompressible computational fluid dynamics and the Continuity Constrain Method for the three-dimensional Navier-Stokes equations,” In. J. Num. Heat Transfer, Part B Fundamentals, Vol. 29, pp. 137-273, 1996.

[Wil93] Williams, P.T., “A Three-Dimensional, Time-Accurate, Incompressible, Navier-Stokes, Finite Element CFD Algorithm, Dissertation, University of Tennessee, 1993.

[Wil00] Wilcox, D.C., “Turbulence Modeling for CFD”, DCW Industries, 2000.

[ZSK93] Zang, Y., Street, R.L. and Koseff, J.R., “A dynamic mixed subgrid-scale model and its application to turbulent recirculating flows,” Physics of Fluids A, Vol. 5, pp/ 3186-3196, 1993.

Appendix

Tables

Table 2.1 Filter functions and transfer functions

Name	Filter function	Transfer function
General	$g(y)$	$\hat{g}(\kappa) \equiv \int_{-\infty}^{\infty} e^{i\kappa y} g(y)\, dy$
Box	$\frac{1}{\delta} H\left(\frac{1}{2}\delta - \lvert y \rvert\right)$	$\frac{\sin\left(\frac{1}{2}\kappa\delta\right)}{\frac{1}{2}\kappa\delta}$
Sharp spectral	$\frac{\sin\left(\pi y / \delta\right)}{\pi y}$	$H\left(\kappa_c - \lvert\kappa\rvert\right), \quad \kappa_c \equiv \pi / \delta$
Gaussian	$\left(\frac{\gamma}{\pi\delta^2}\right)^{1/2} \exp\left(-\frac{\gamma \lVert y \rVert_2^2}{\delta^2}\right)$	$\exp\left(-\frac{\delta^2}{24} \lVert \kappa \rVert_2^2\right)$

Table 5.1 Compilation of temperature difference between hot and cold wall, Rayleigh, Reynolds, Grashof and Archimedes numbers for the thermal cavity test case

Ra	**ΔT (°F)**	**Re**	**Gr**	**Ar**
$3.4x10^5$	0.21666	680	$4.78x10^5$	1
$3.4x10^6$	2.16666	2186	$4.78x10^6$	1
$3.4x10^7$	21.6666	6851	$4.69x10^7$	1
$3.4x10^8$	216.666	19932	$3.97x10^8$	1

Table 5.2 Comparison of symmetry between square cavity and 5:1 aspect ratio thermal cavity using Omega-Psi algorithm

Square cavity (33x33 nodes)

Ra	τ_2	**Omega**	**Omega E-norm**
$1x10^{3}$	0	$6x10^{-3}$	$2x10^{-4}$
$1x10^{4}$	0	$2x10^{-2}$	$2x10^{-2}$
$1x10^{5}$	$1x10^{-13}$	$9x10^{-2}$	$2x10^{0}$

5:1 aspect ratio cavity (33x165 nodes)

Ra	τ_2	**Omega**	**Omega E-norm**
$1x10^{3}$	$2x10^{-8}$	$7x10^{-3}$	-
$1x10^{4}$	$1x10^{-7}$	$4x10^{-2}$	-
$1x10^{5}$	$8x10^{-7}$	$1x10^{-1}$	-

Figures

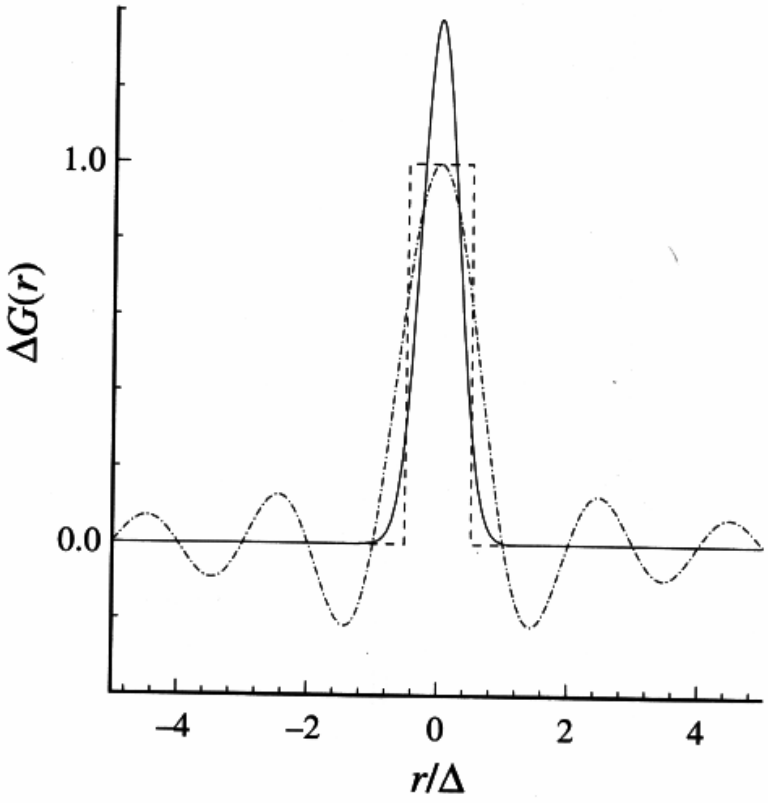

Figure 2.1 Filter functions in physical space; solid line: Gaussian filter, dashed line: box filter, dashed-dotted line: sharp spectral filter

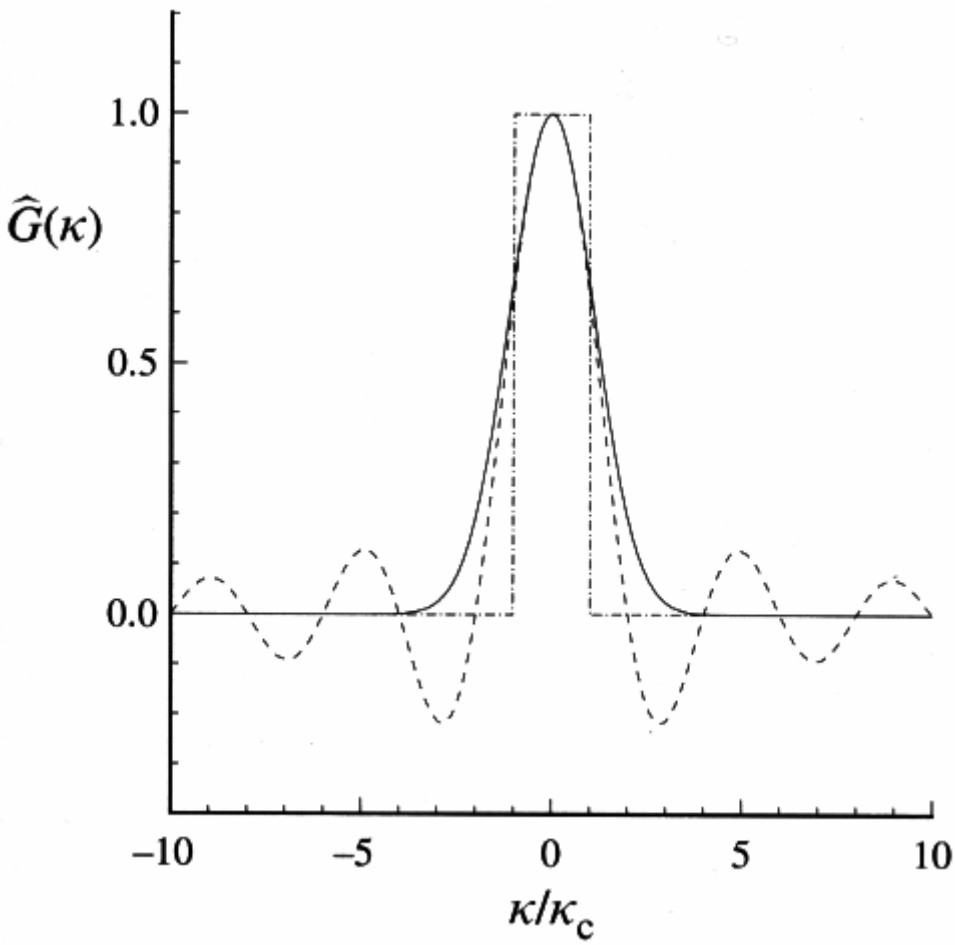

Figure 2.2 Filter functions in wave number space; solid line: Gaussian filter, dashed line: box filter, dashed-dotted line: sharp spectral filter

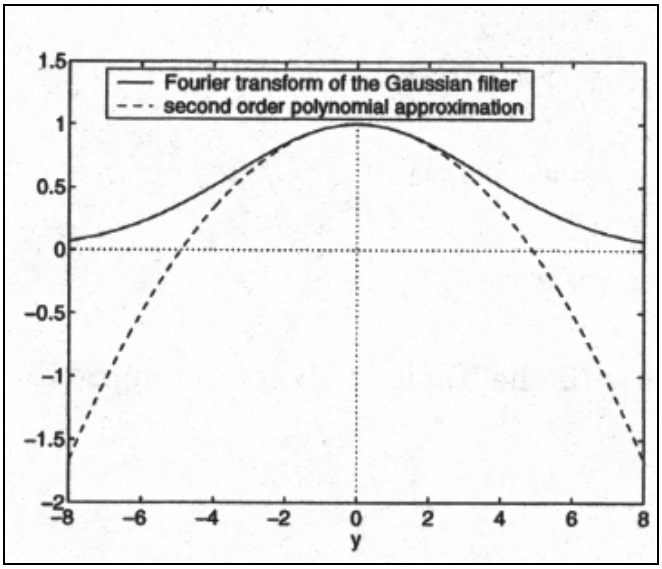

Figure 2.3. Second order Taylor series approximation for the Gaussian filter

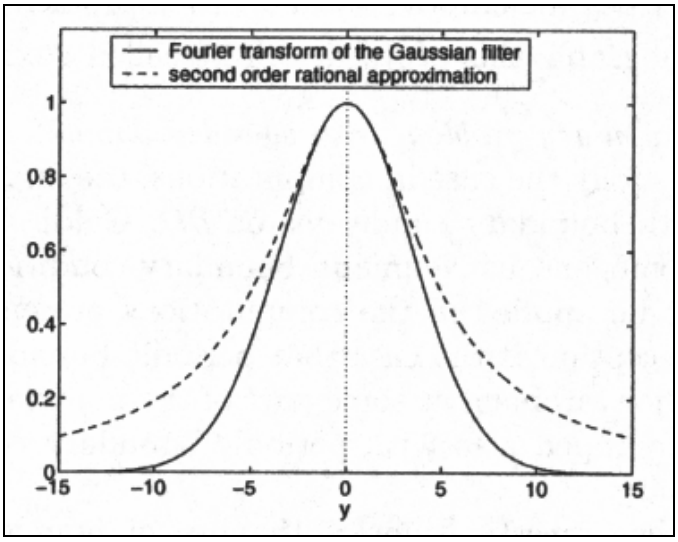

Figure 2.4. Second order Pade approximation for the Gaussian filter

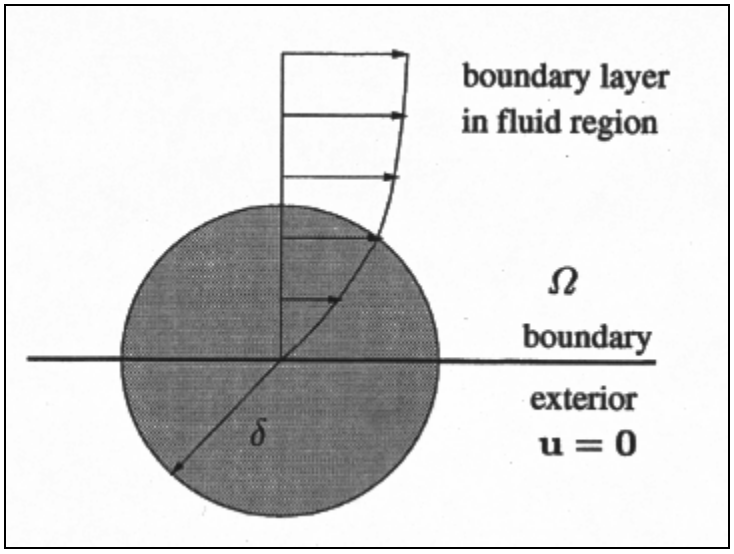

Figure 2.5 Filtering at the wall

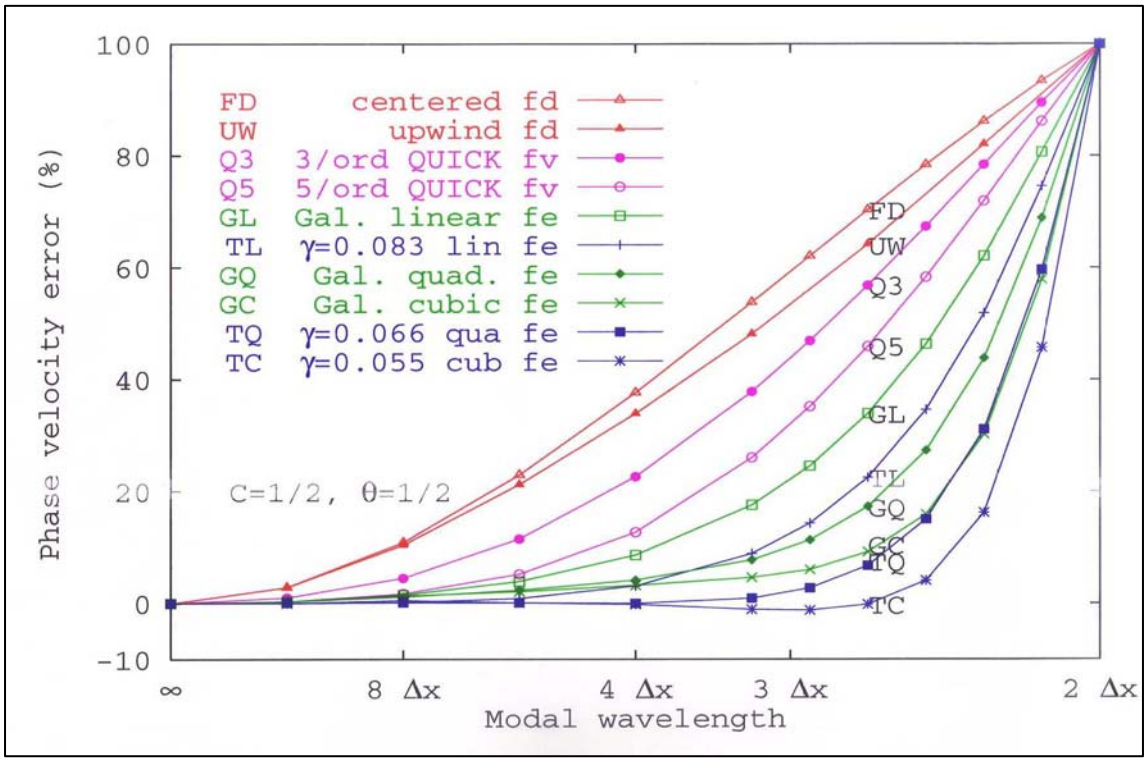

Figure 4.1 Phase velocity error distribution for a range of CFD algorithm

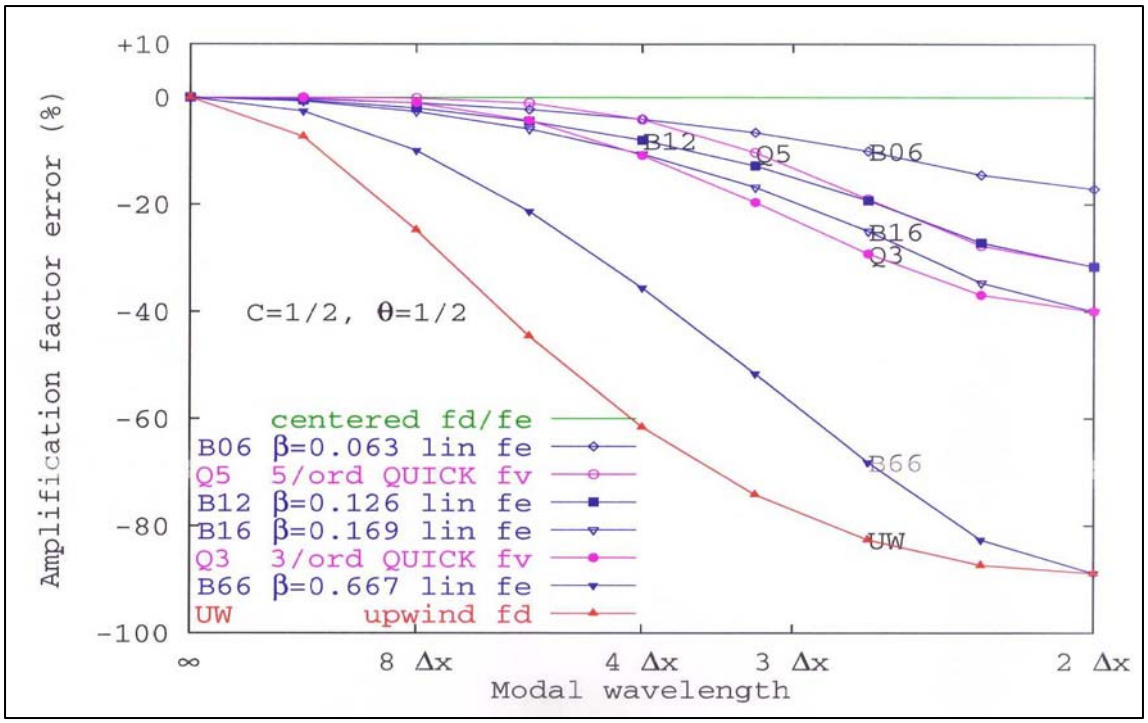

Figure 4.2 Amplification factor error distribution for a range of CFD algorithm

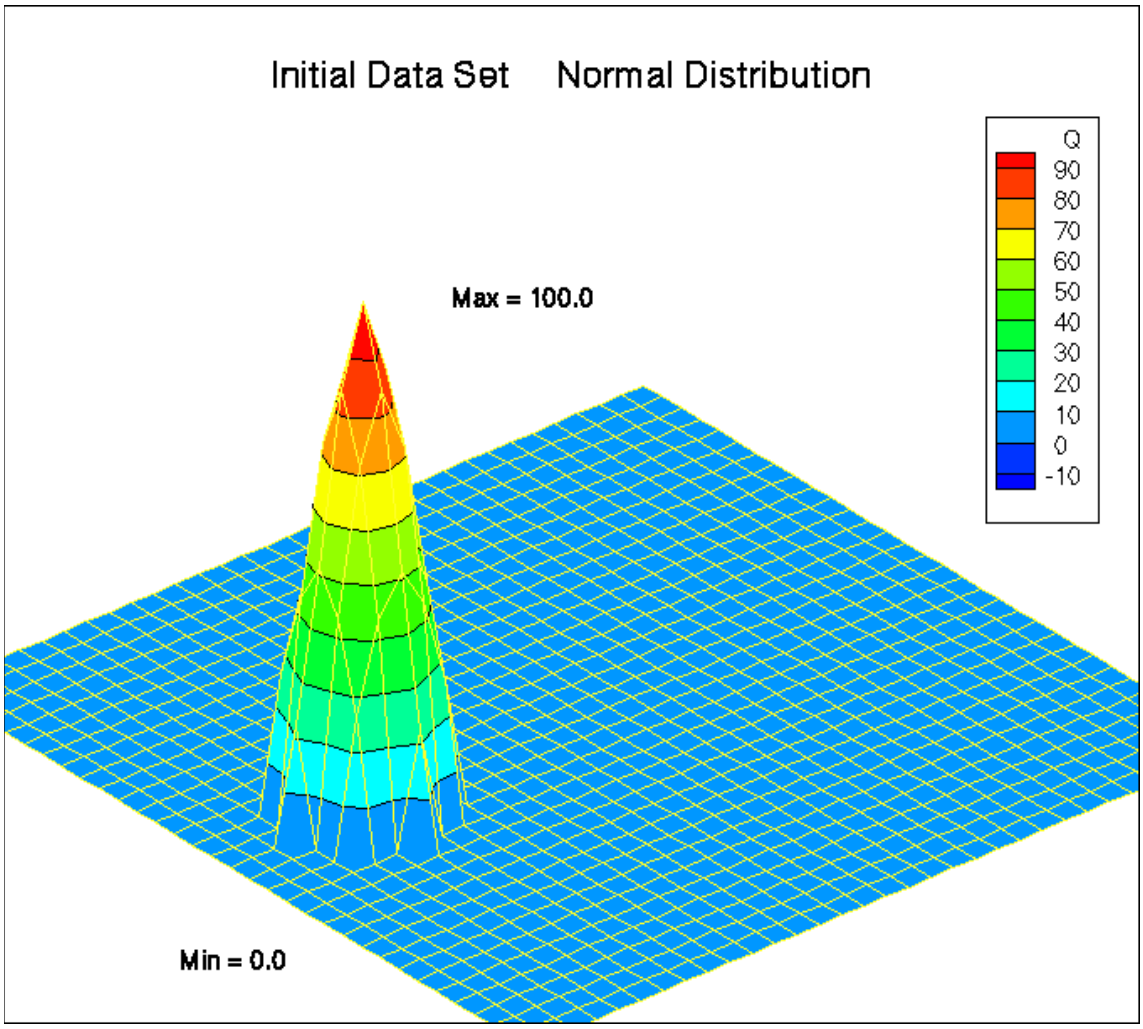

Figure 4.3a Analytical solution for rotating cone problem

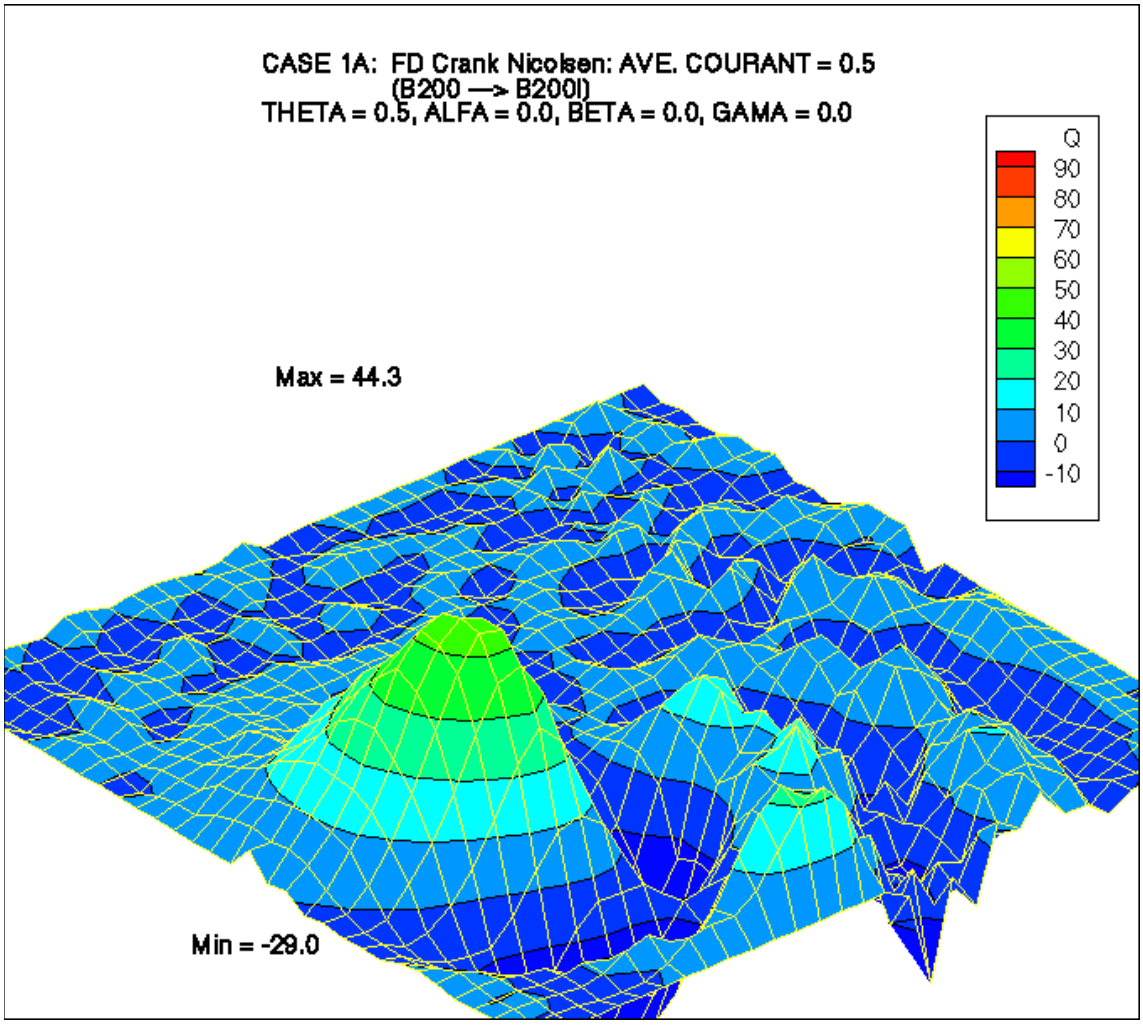

Figure 4.3b Crank-Nicolson solution for rotating cone problem

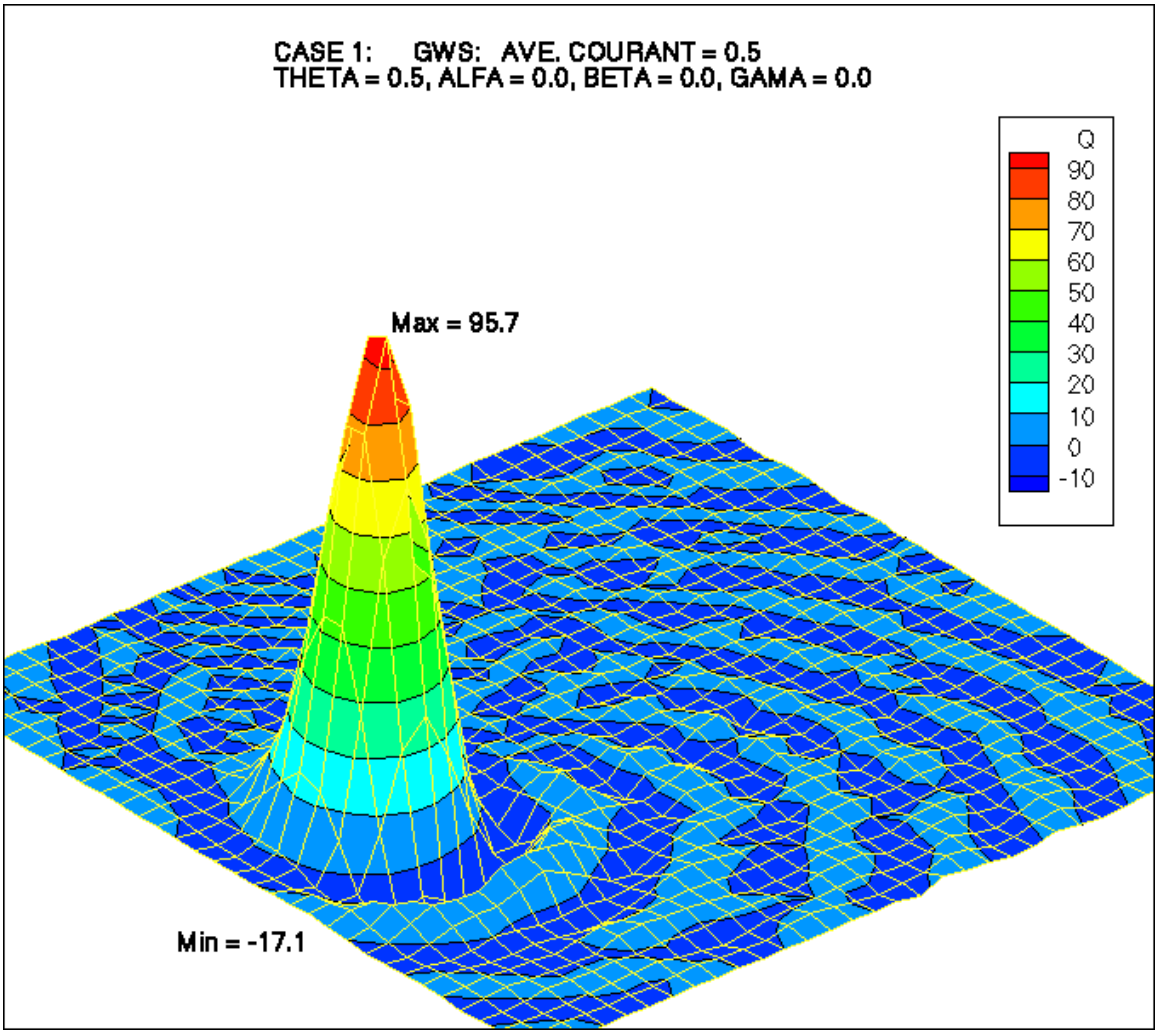

Figure 4.3c GWS solution for rotating cone problem

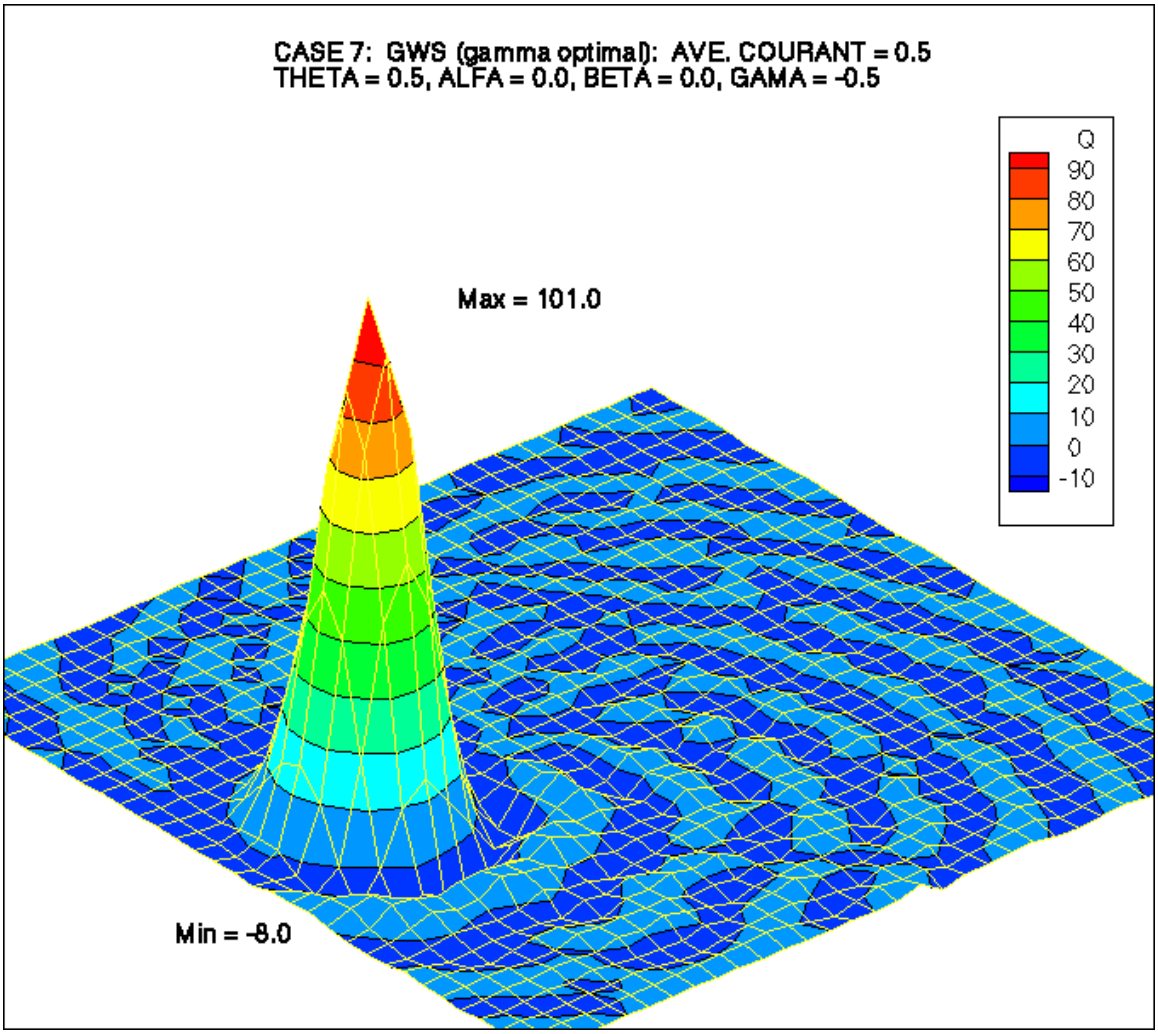

Figure 4.3d TWS solution for rotating cone problem

Turbulent Duct

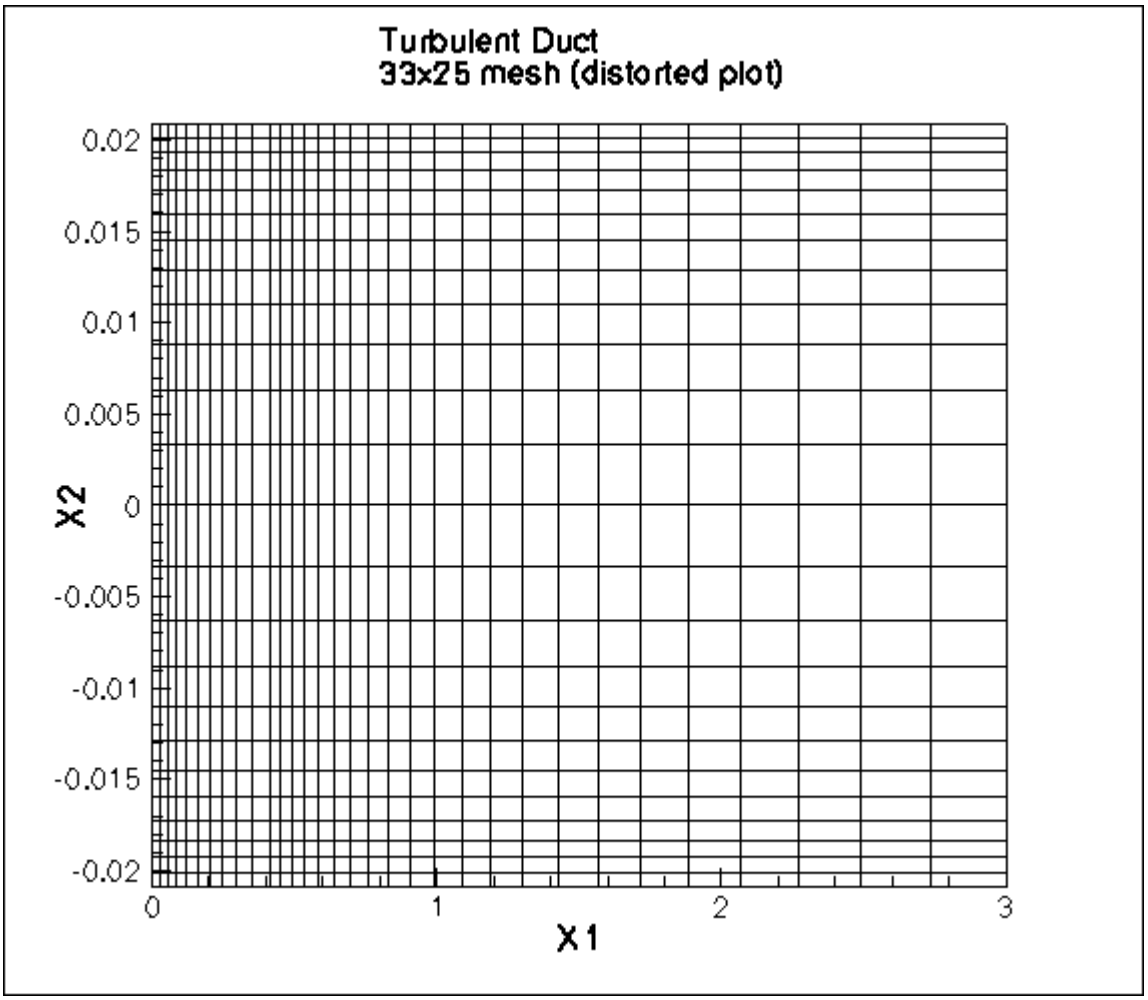

Figure 5.1.1 33x25 non-uniform meshing for turbulent duct flow case; distorted plot; original dimensions are 0.5 inch height to 3 feet length

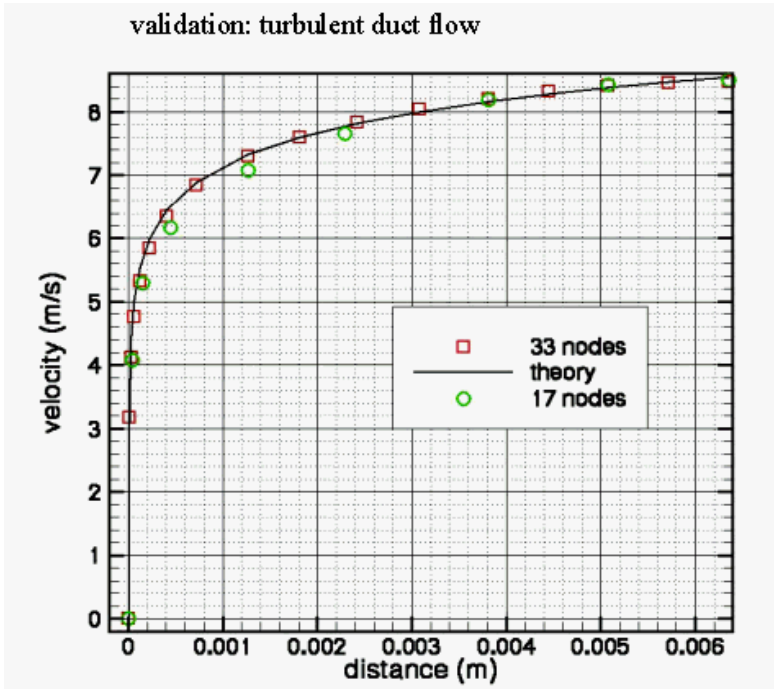

Figure 5.1.2 Validation of turbulent duct velocity profile along centerline of duct versus turbulent boundary layer theory

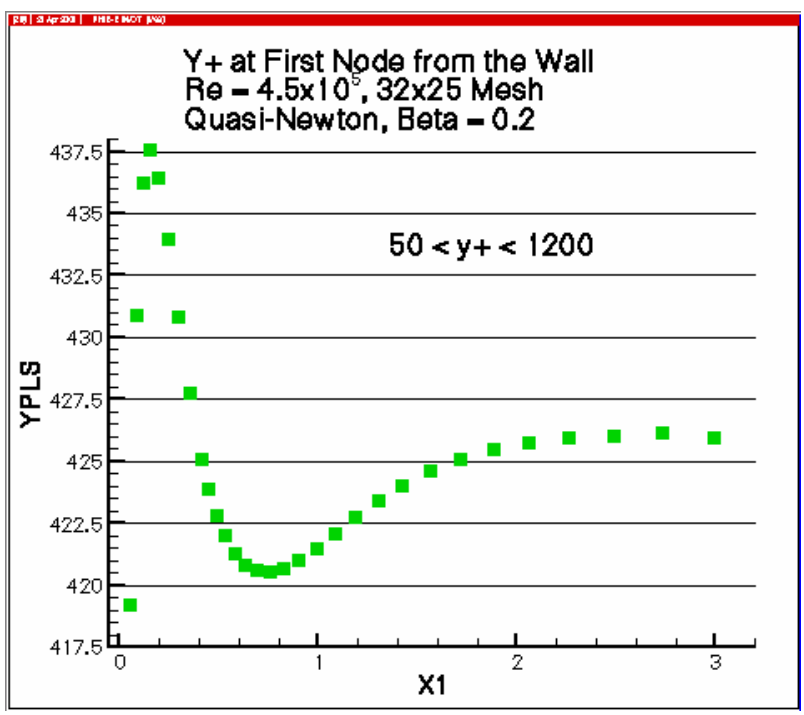

Figure 5.1.3 Y+ at first node of the wall distribution along the length of the duct

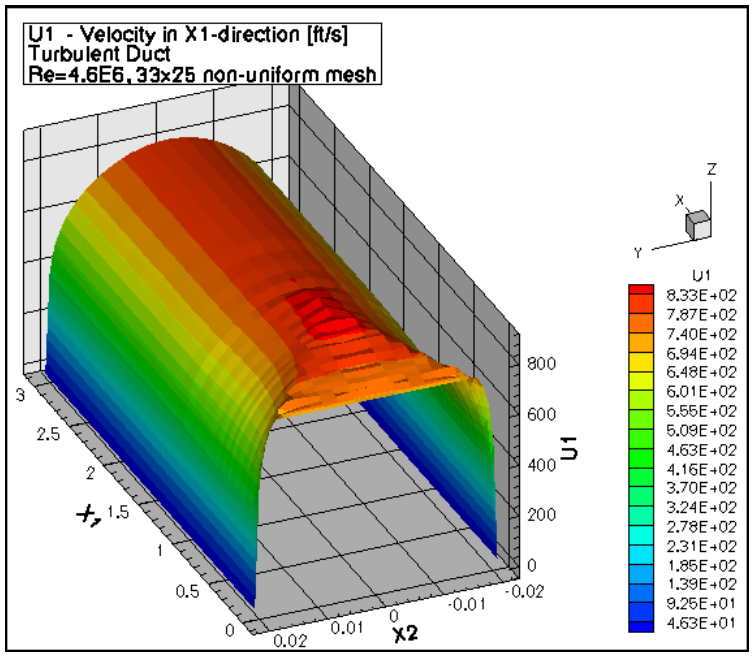

Figure 5.1.4. Axial-velocity profile for turbulent duct flow

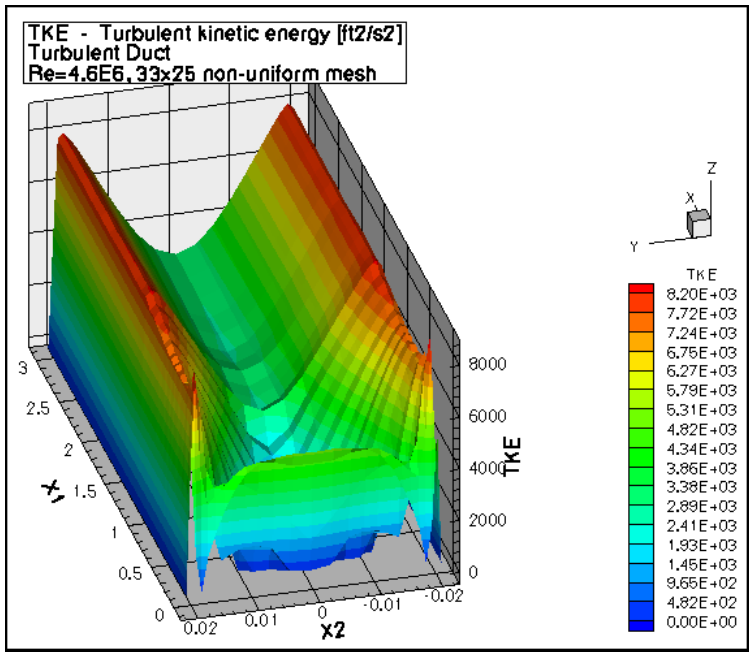

Figure 5.1.5. Turbulent duct turbulence kinetic energy

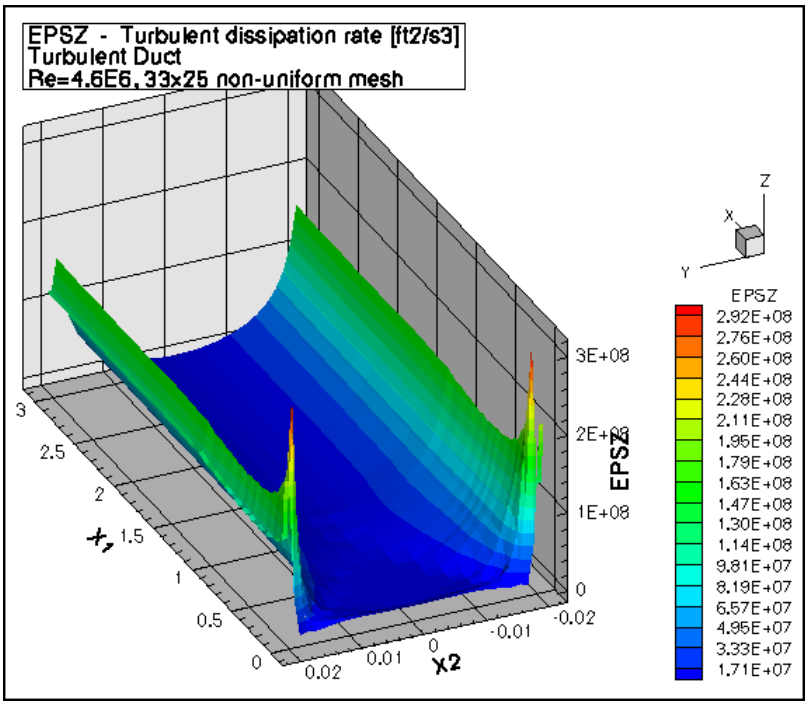

Figure 5.1.6. Turbulent duct dissipation rate

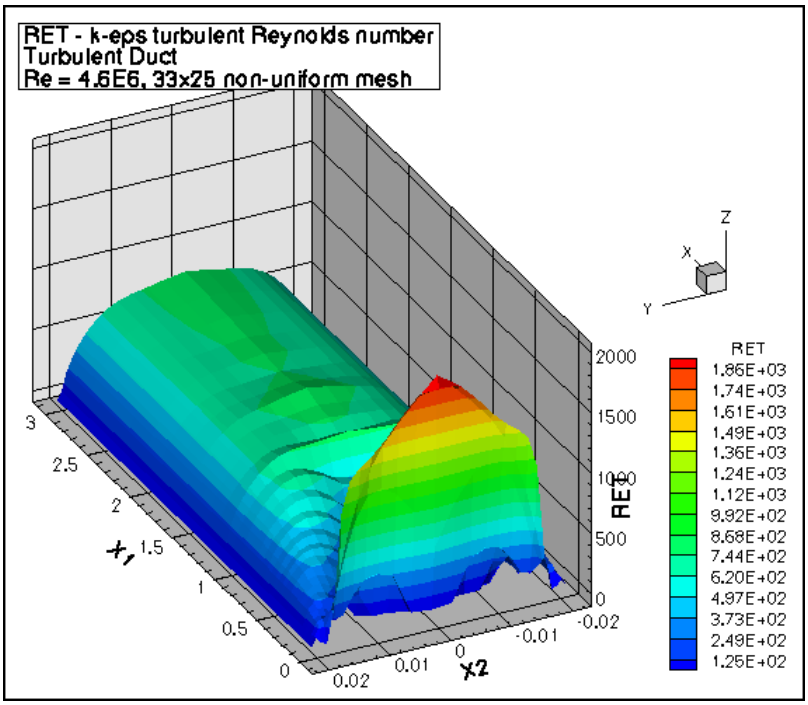

Figure 5.1.7. Turbulent duct turbulent Reynolds number

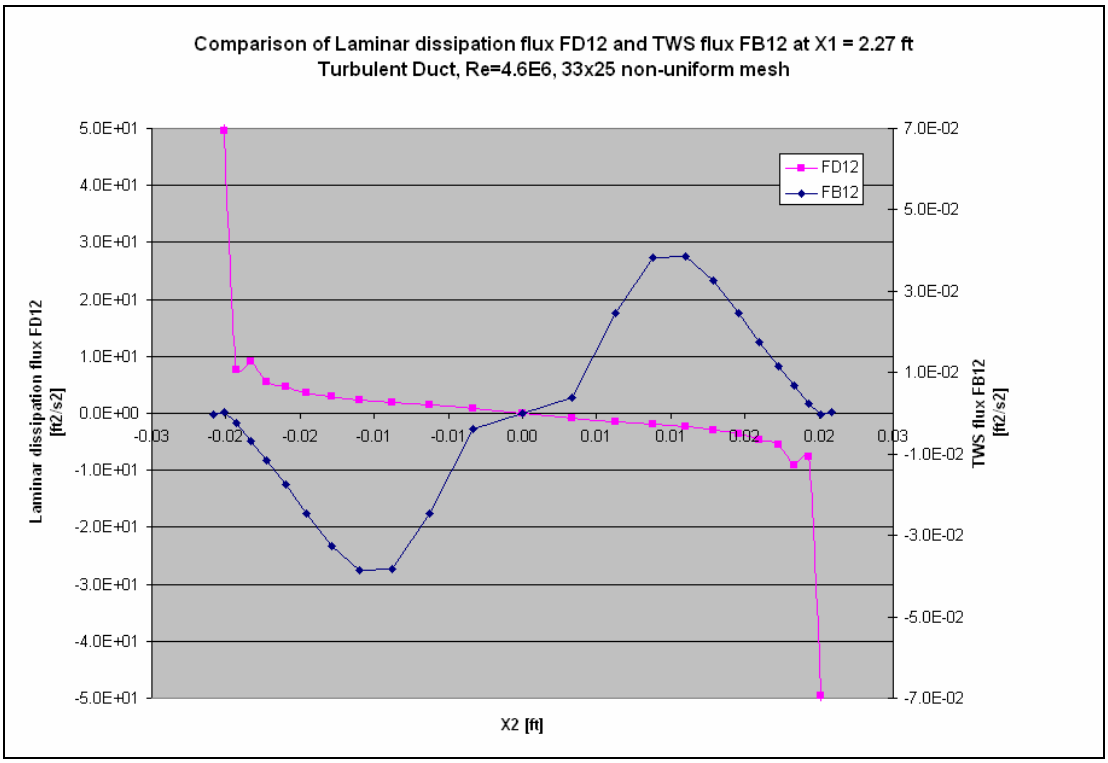

Figure 5.1.8. Comparison of Stokes shear stress FD12 and TWS shear stress FB12

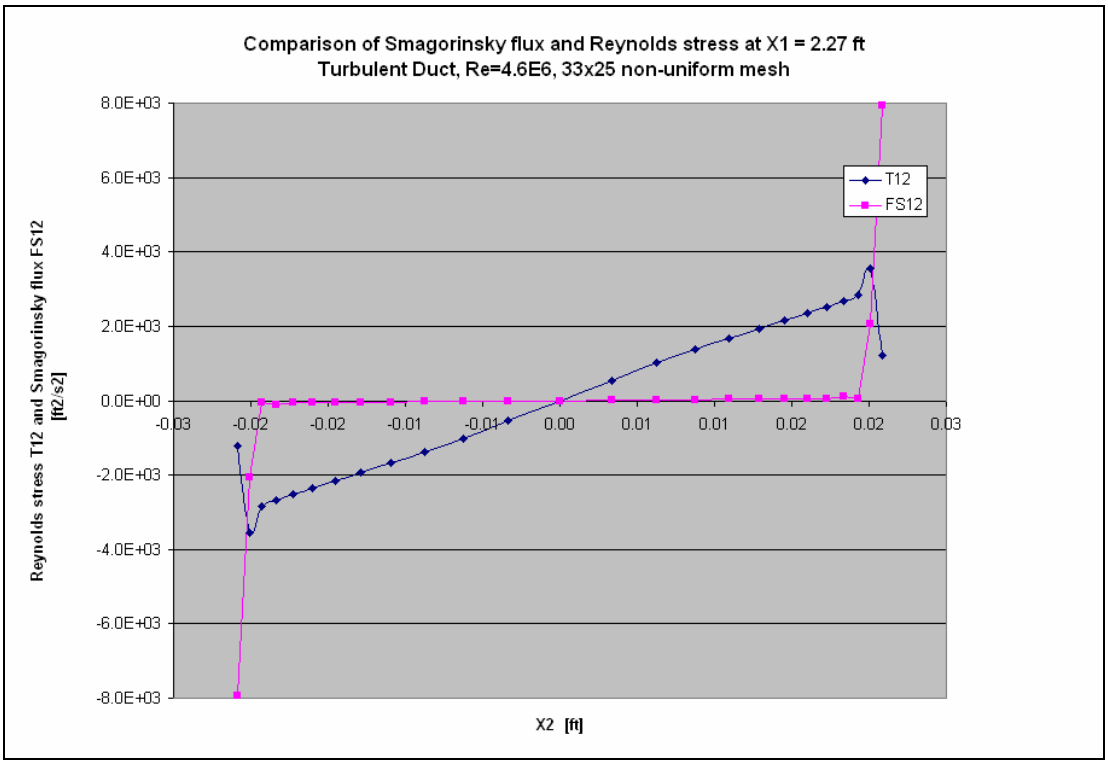

Figure 5.1.9. Comparison of Smagorinsky FS12 and Reynolds shear stresses T12

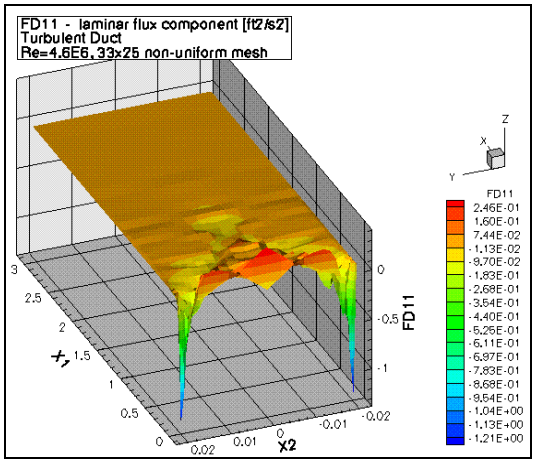

Figure 5.1.10. Laminar diffusion flux vector component FD11

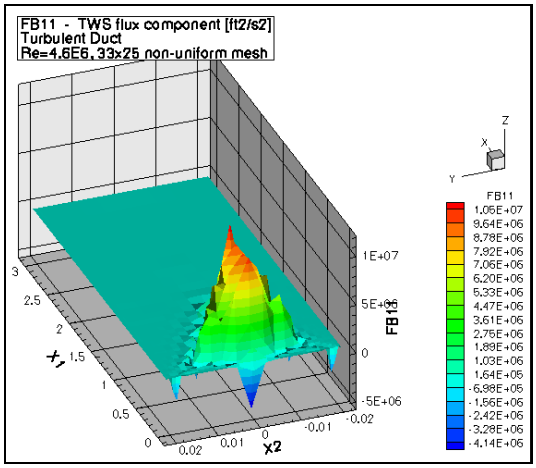

Figure 5.1.11. Modified TWS flux vector component FB11

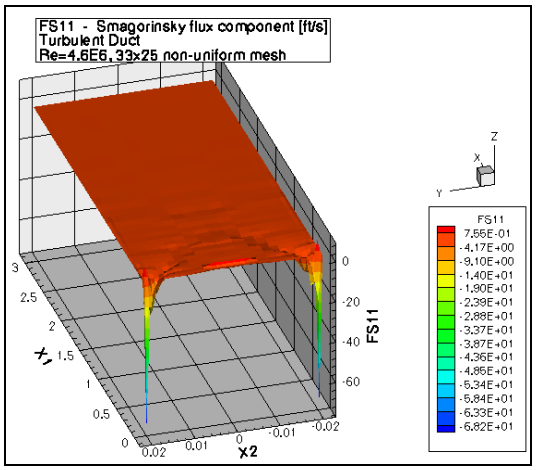

Figure 5.1.12. Smagorinsky flux vector component FS11

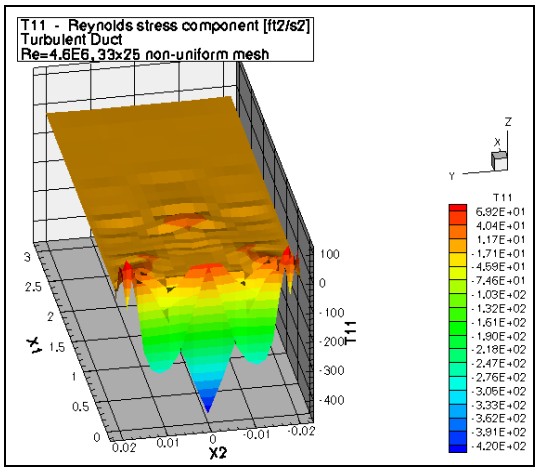

Figure 5.1.13. Reynolds stress tensor component T11

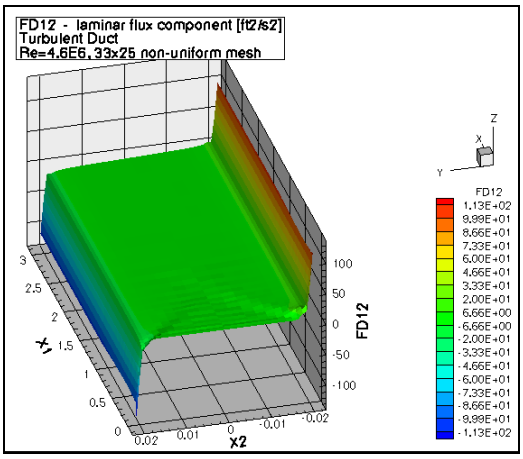

Figure 5.1.14. Laminar diffusion flux vector component FD12

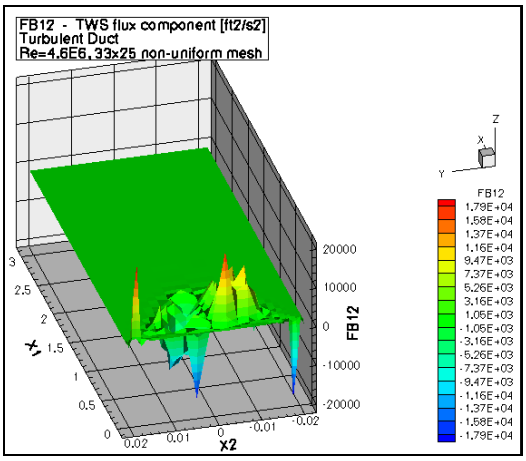

Figure 5.1.15. Modified TWS flux vector component FB12

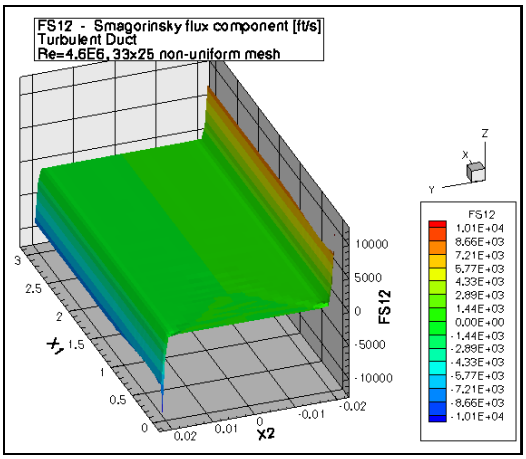

Figure 5.1.16. Smagorinsky flux vector component FS12

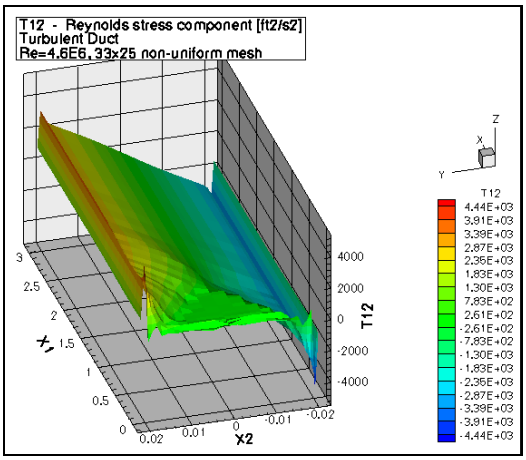

Figure 5.1.17. Reynolds stress tensor component T12

Driven Cavity

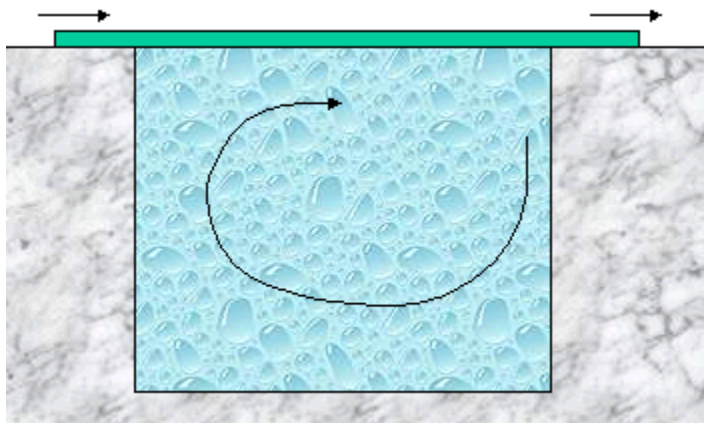

Figure 5.2.1 Driven cavity setup

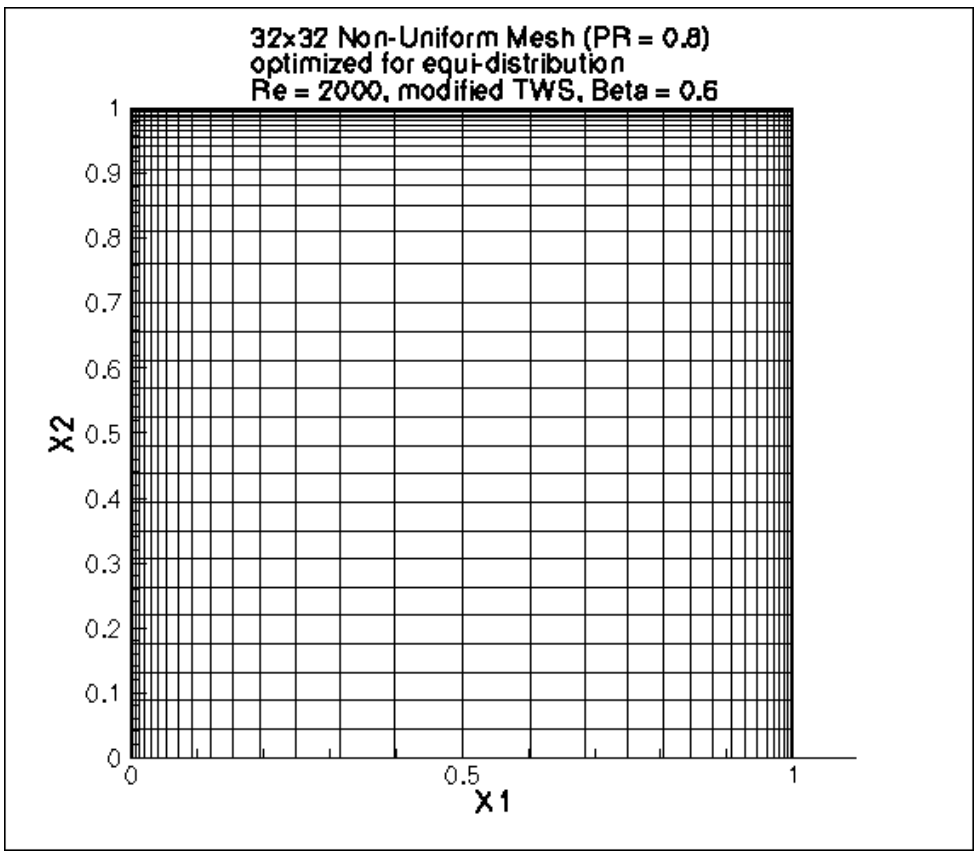

Figure 5.2.2 Optimized meshing for Re = 2000 laminar execution

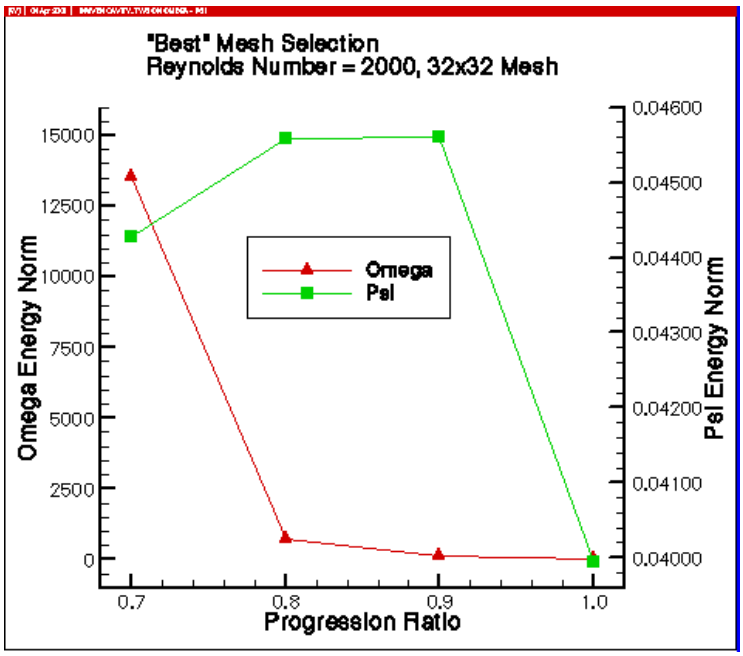

Figure 5.2.3 Energy norm comparison versus mesh progression ratio for driven cavity at Re = 2000

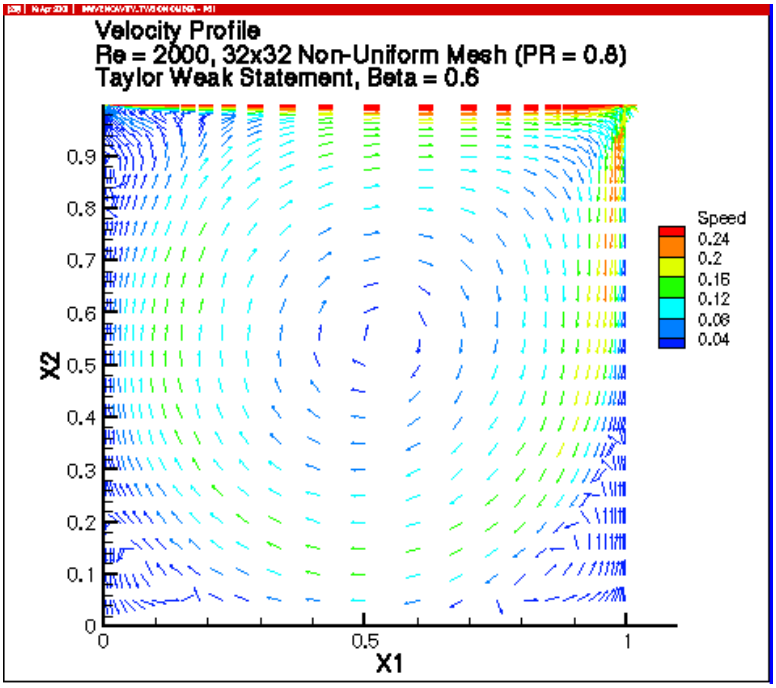

Figure 5.2.4 Reference solution by [Eri01], showing the velocity field of the laminar driven cavity for Re = 2000 on an optimized mesh, featuring TWS beta stabilization

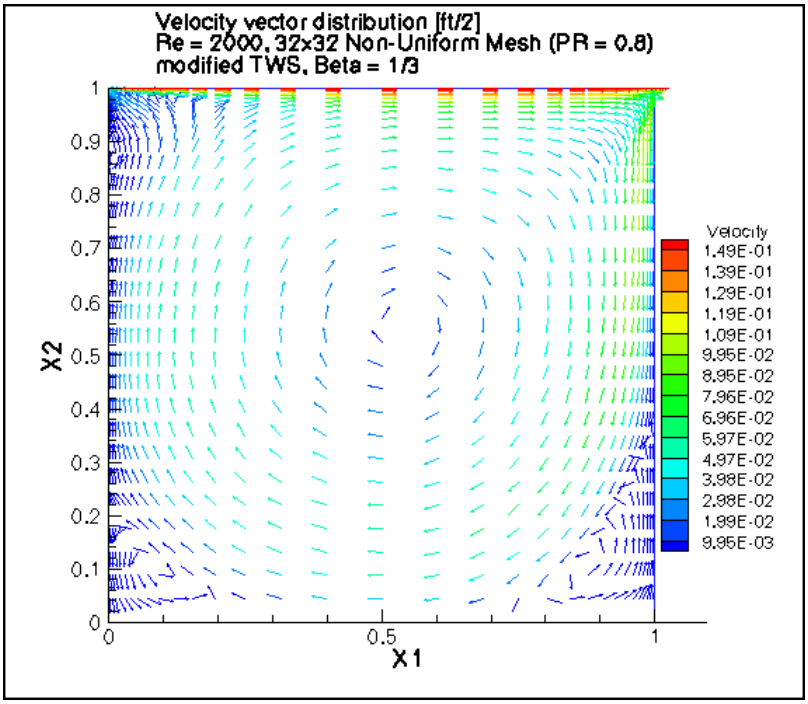

Figure 5.2.5. Velocity vector distribution

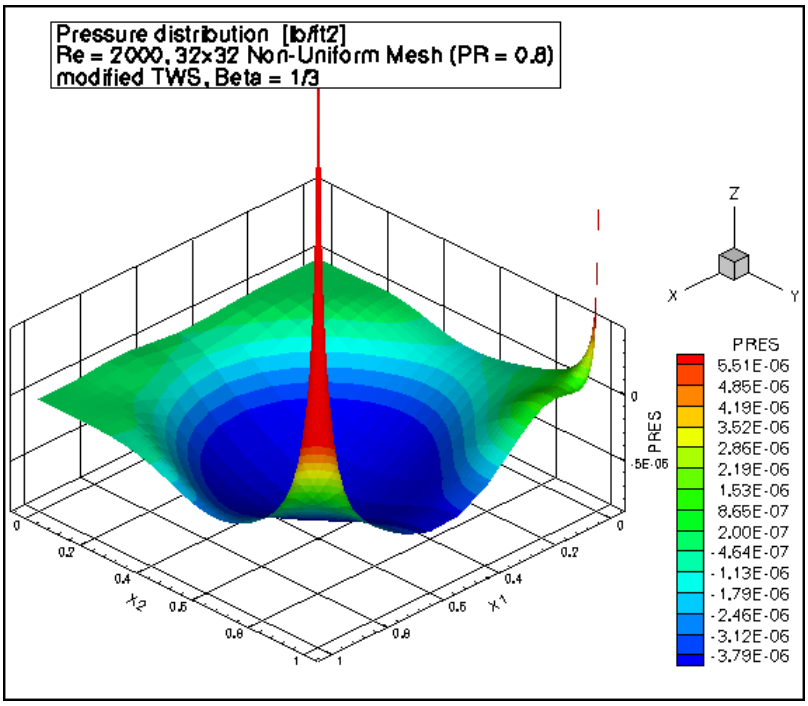

Figure 5.2.6. Pressure distribution

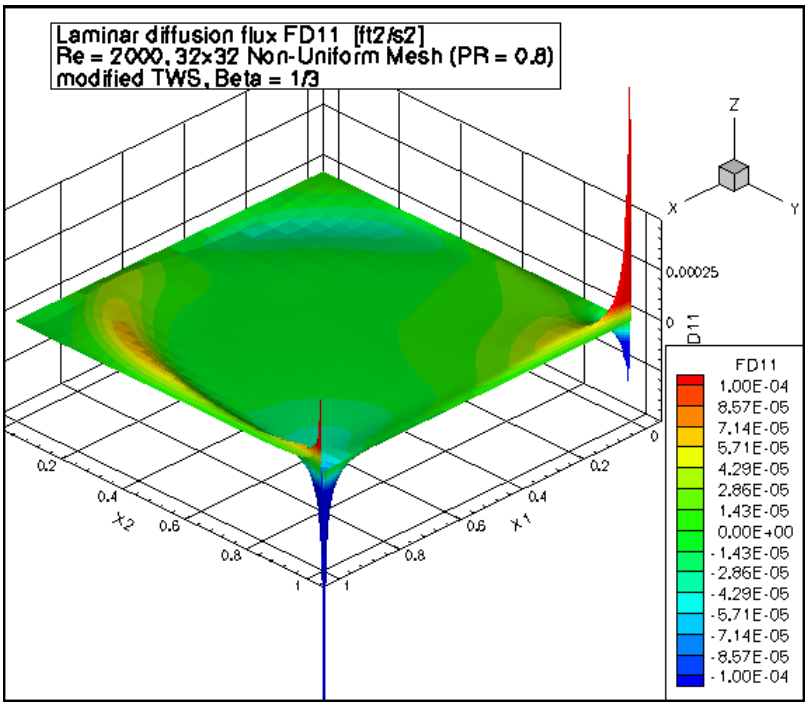

Figure 5.2.7. Laminar diffusion flux vector component FD11

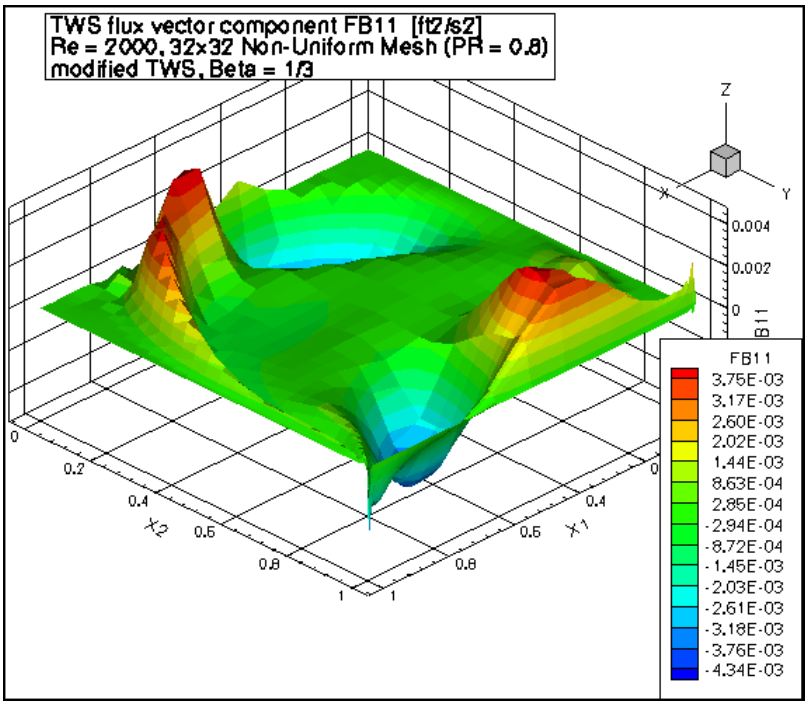

Figure 5.2.8. Modified TWS flux vector component FB11

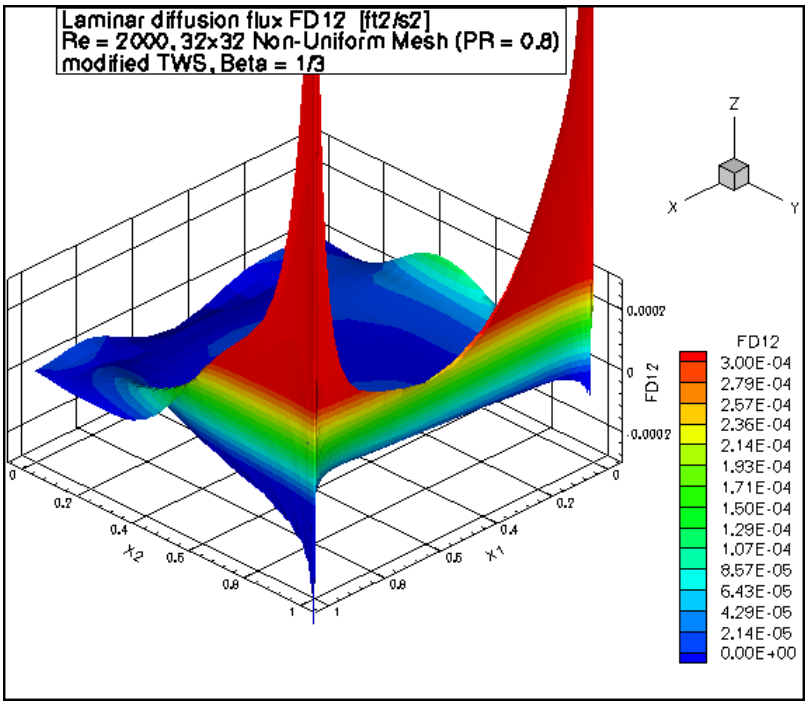

Figure 5.2.9. Laminar diffusion flux vector component FD12

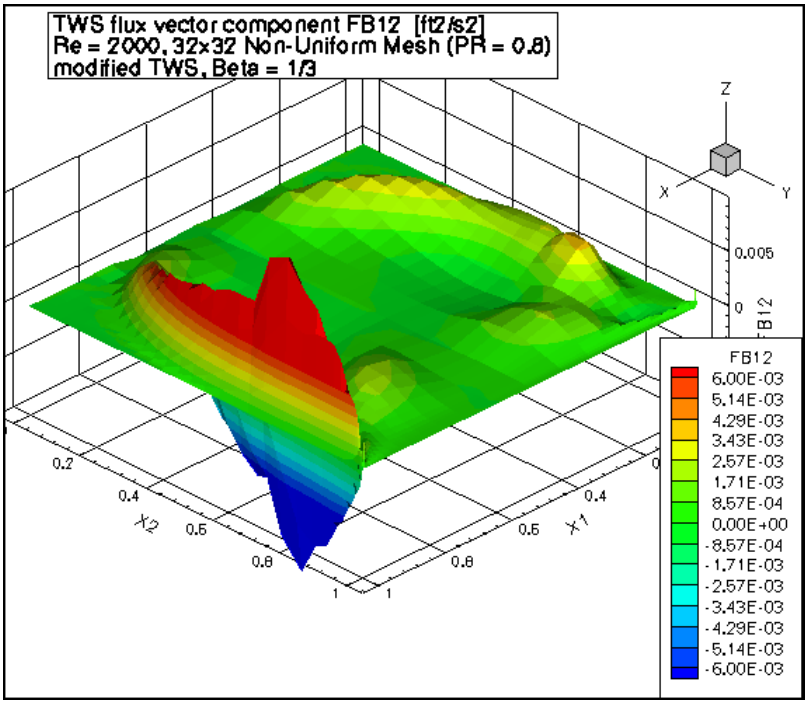

Figure 5.2.10. Modified TWS flux vector component FB12

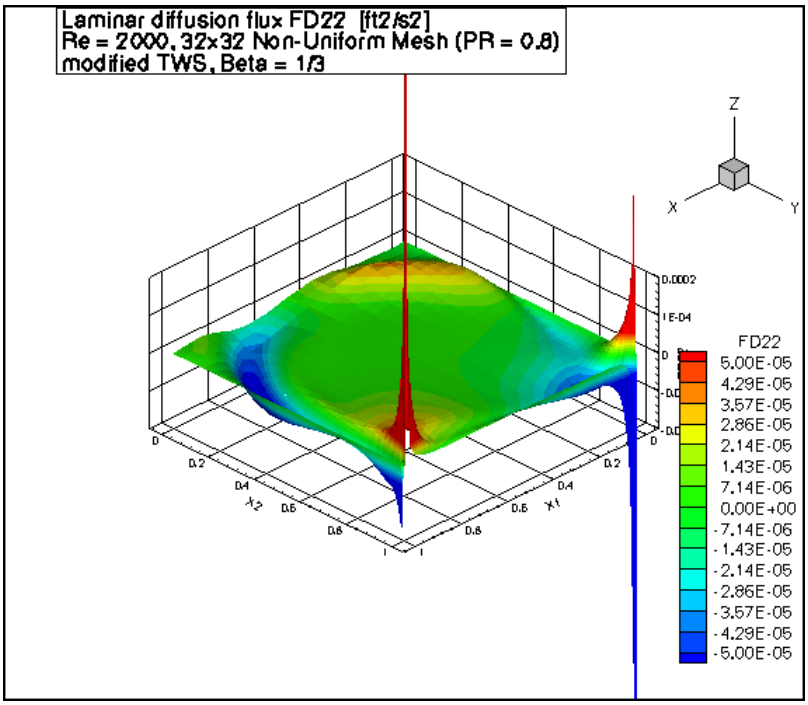

Figure 5.2.11. Laminar diffusion flux vector component FD22

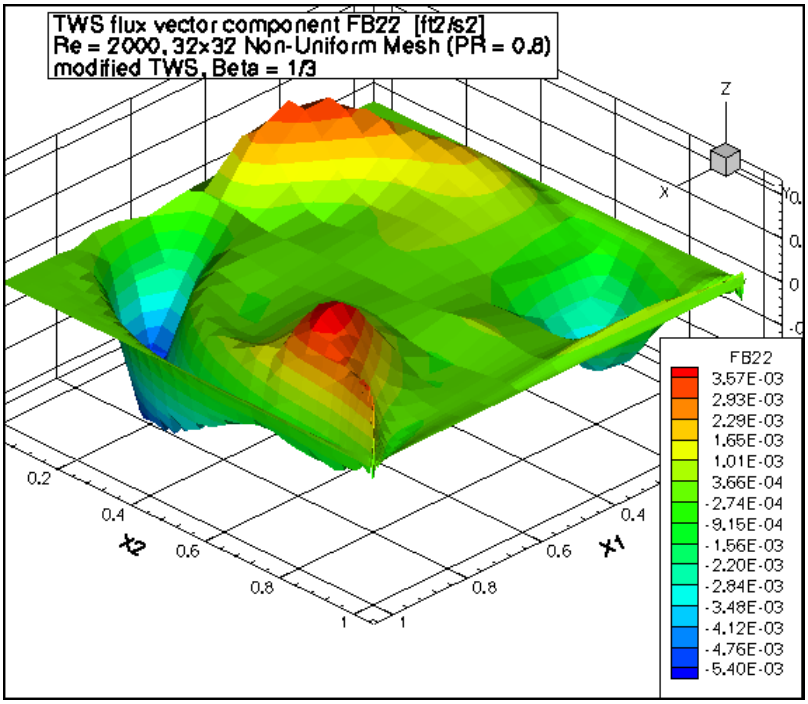

Figure 5.2.12. Modified TWS flux vector component FB22

Thermal Cavity

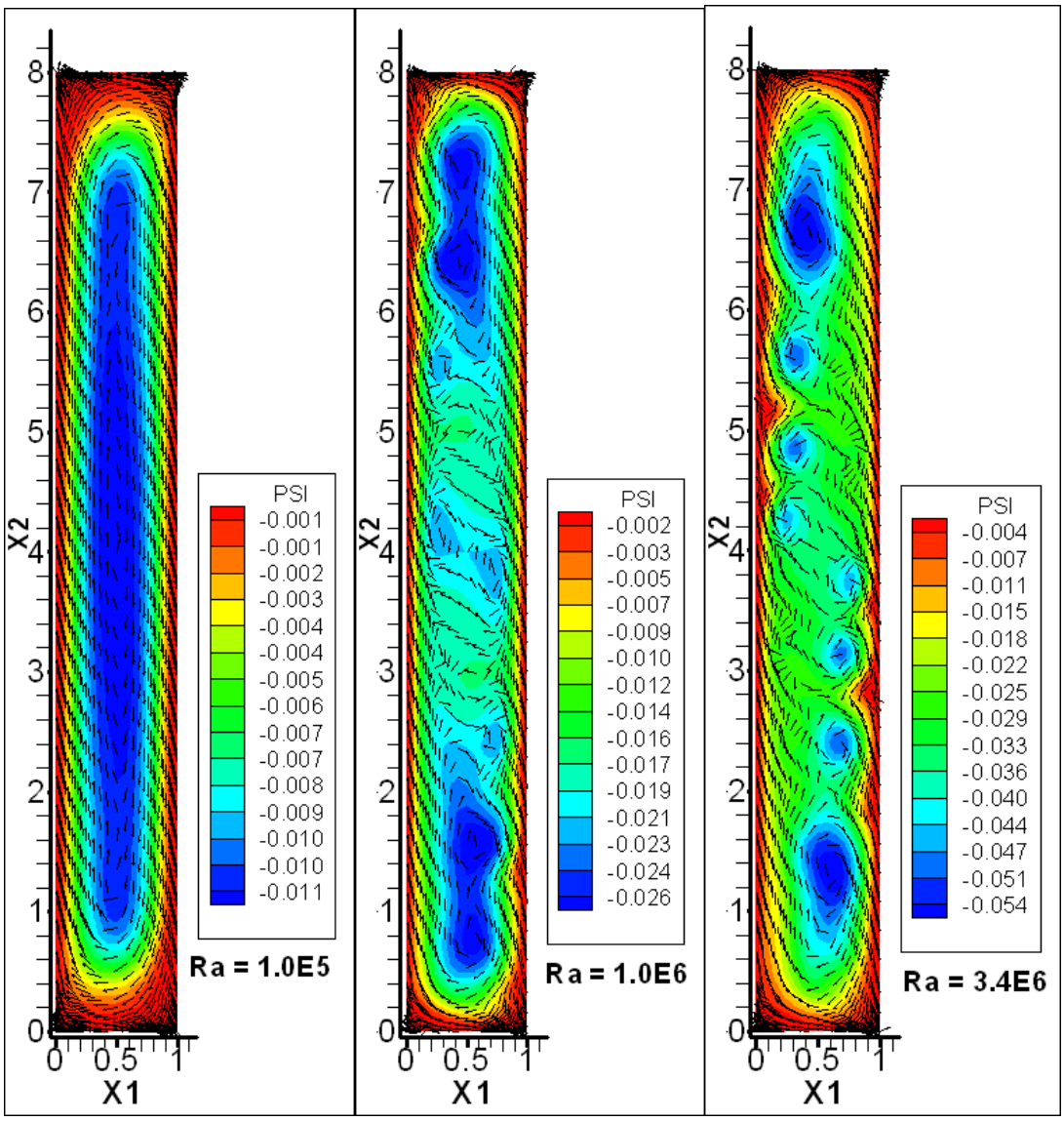

Figure 5.3.1 Comparison of stream function on an 8x1 thermal cavity at Ra = 1.0E5 (left), 1.0E6 (middle) and 3.4E6 (right)

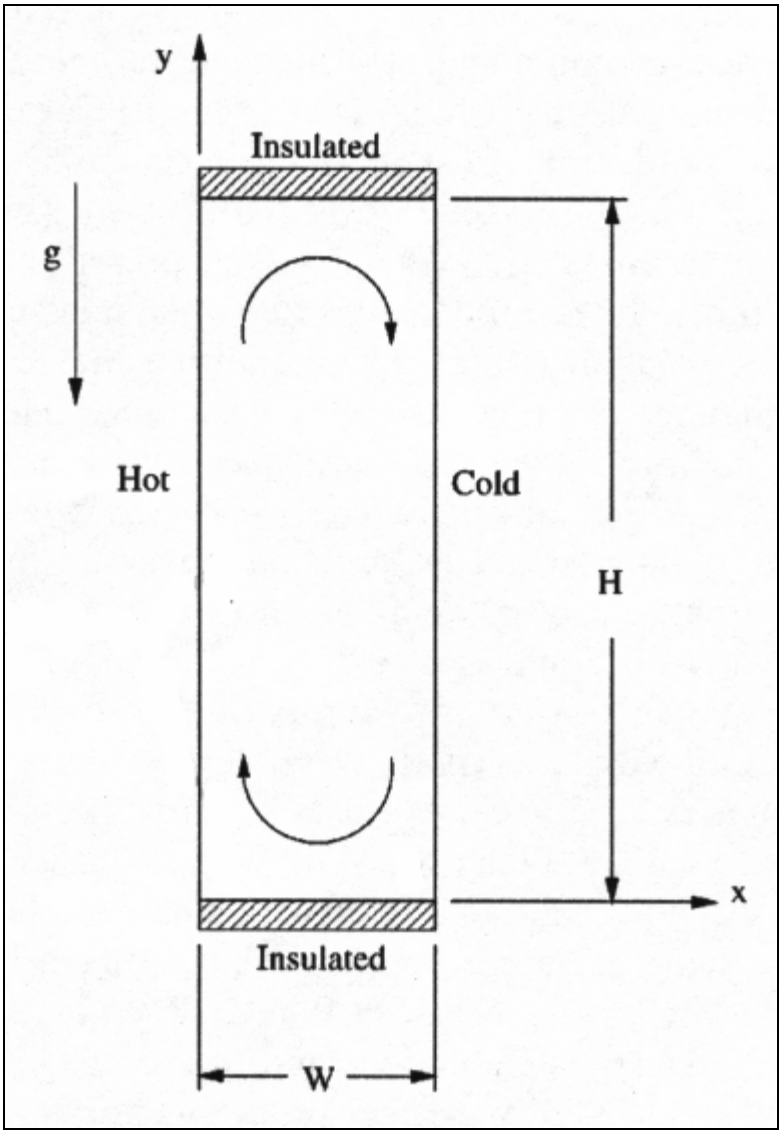

Figure 5.3.2 8:1 thermal cavity problem

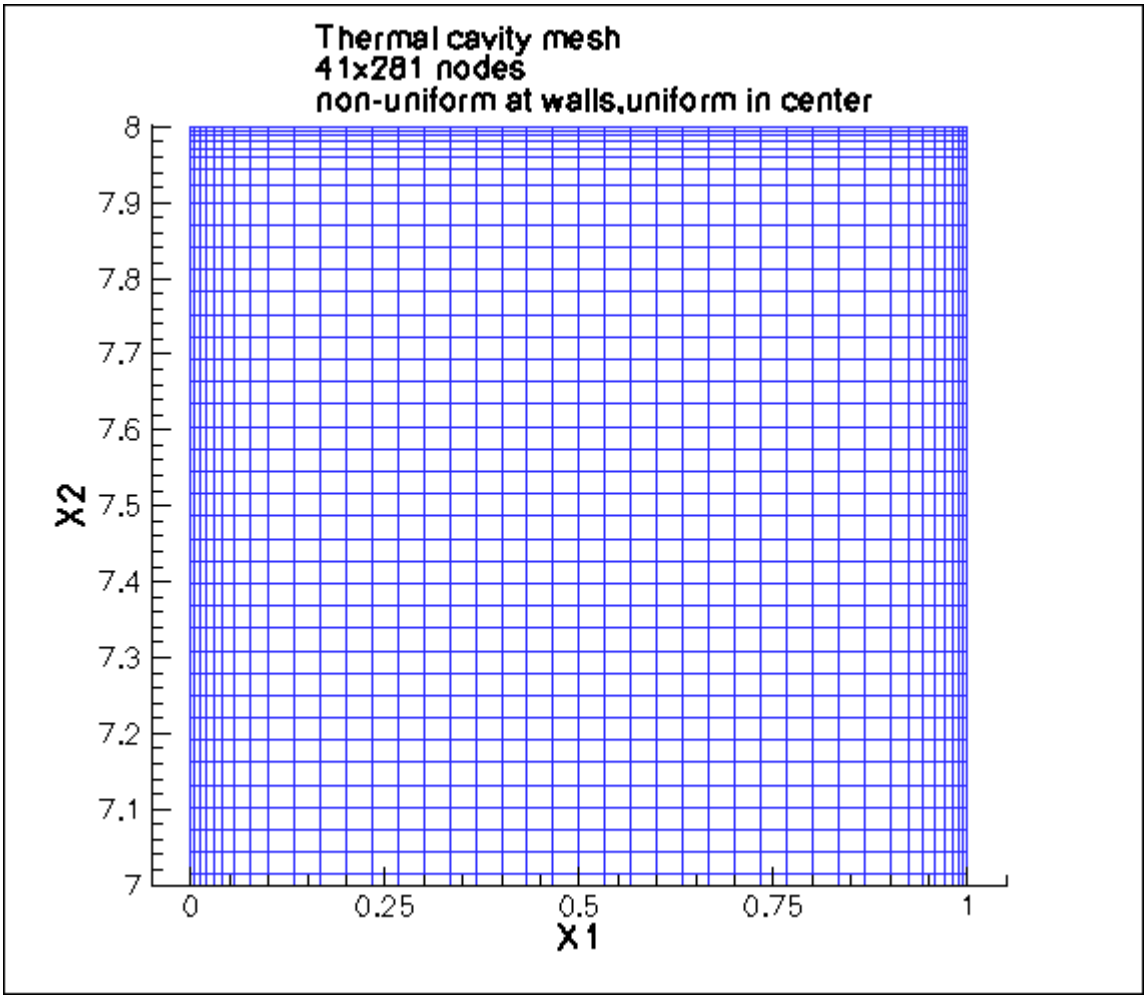

Figure 5.3.3 8:1 ration non-uniform mesh featuring 41x281 nodes. This figure shows the upper 12.5% of the mesh

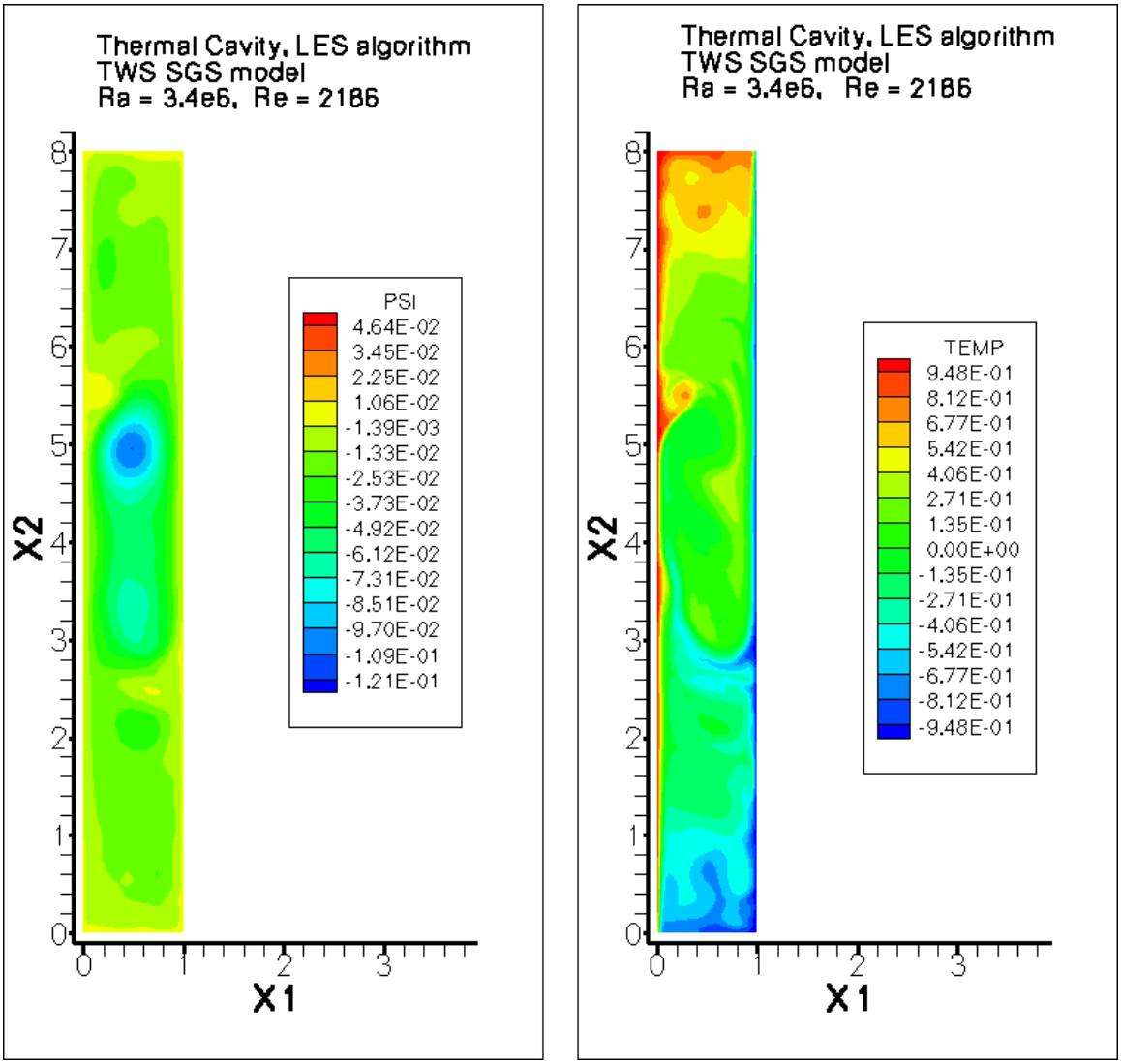

Figure 5.3.1.1 Un-symmetric stream-function (left) and temperature (right) distribution at t = 88 sec for a laminar LES algorithm computation using TWS SGS model, Re = 2186, Ra = 3.4E6

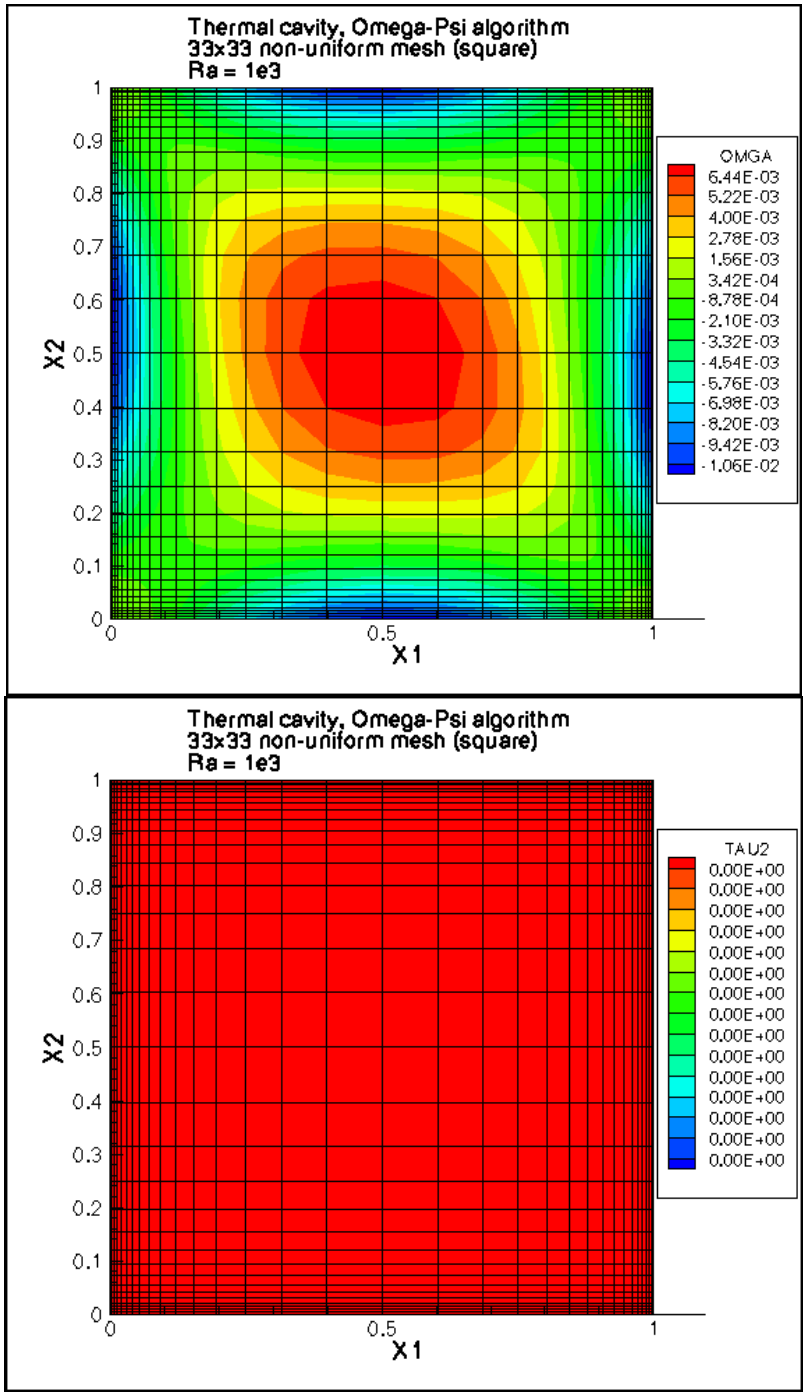

Figure 5.3.1.2 Vorticity (upper) and symmetry variable TAU2 (lower) distribution for a laminar, square thermal cavity at Ra = 1E3

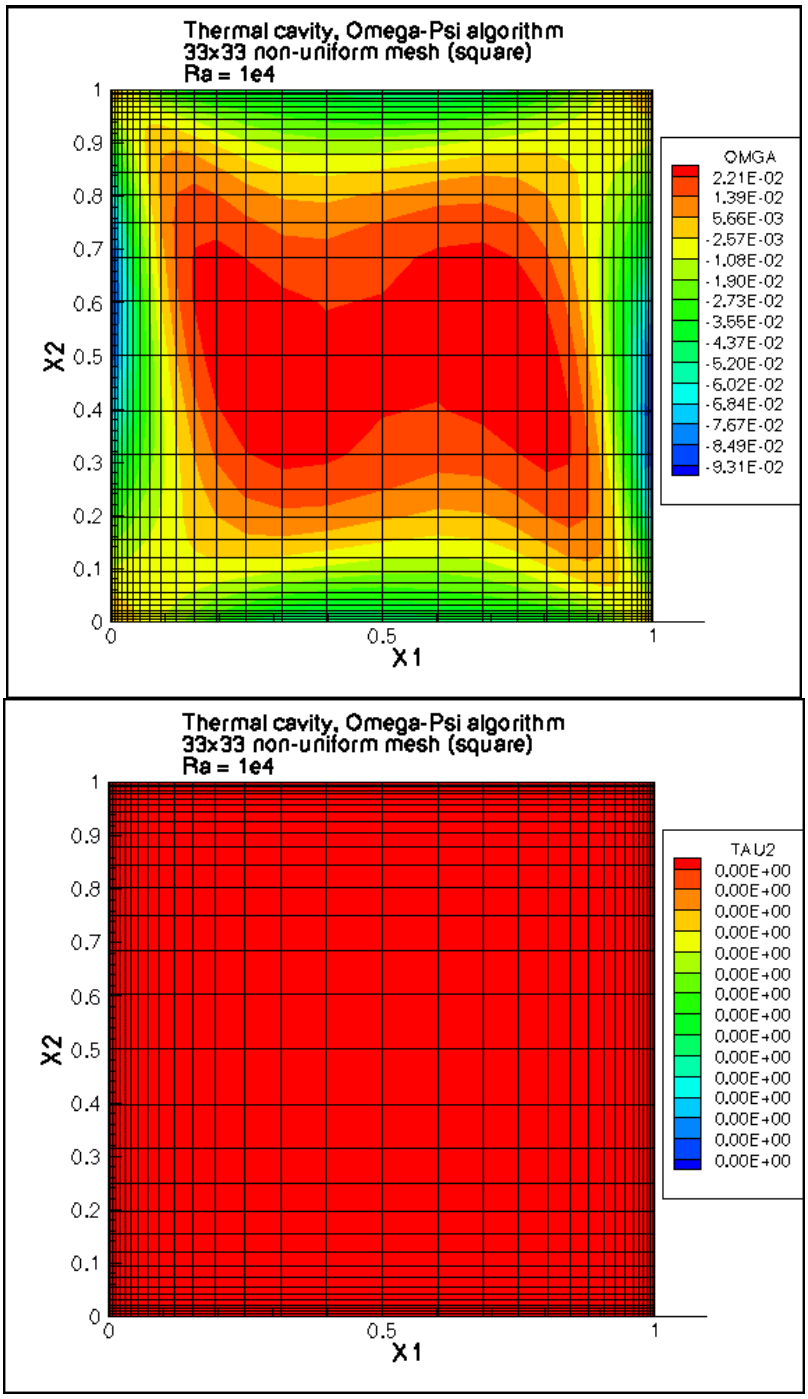

Figure 5.3.1.3 Vorticity (upper) and symmetry variable TAU2 (lower) distribution for a laminar, square thermal cavity at Ra = 1E4

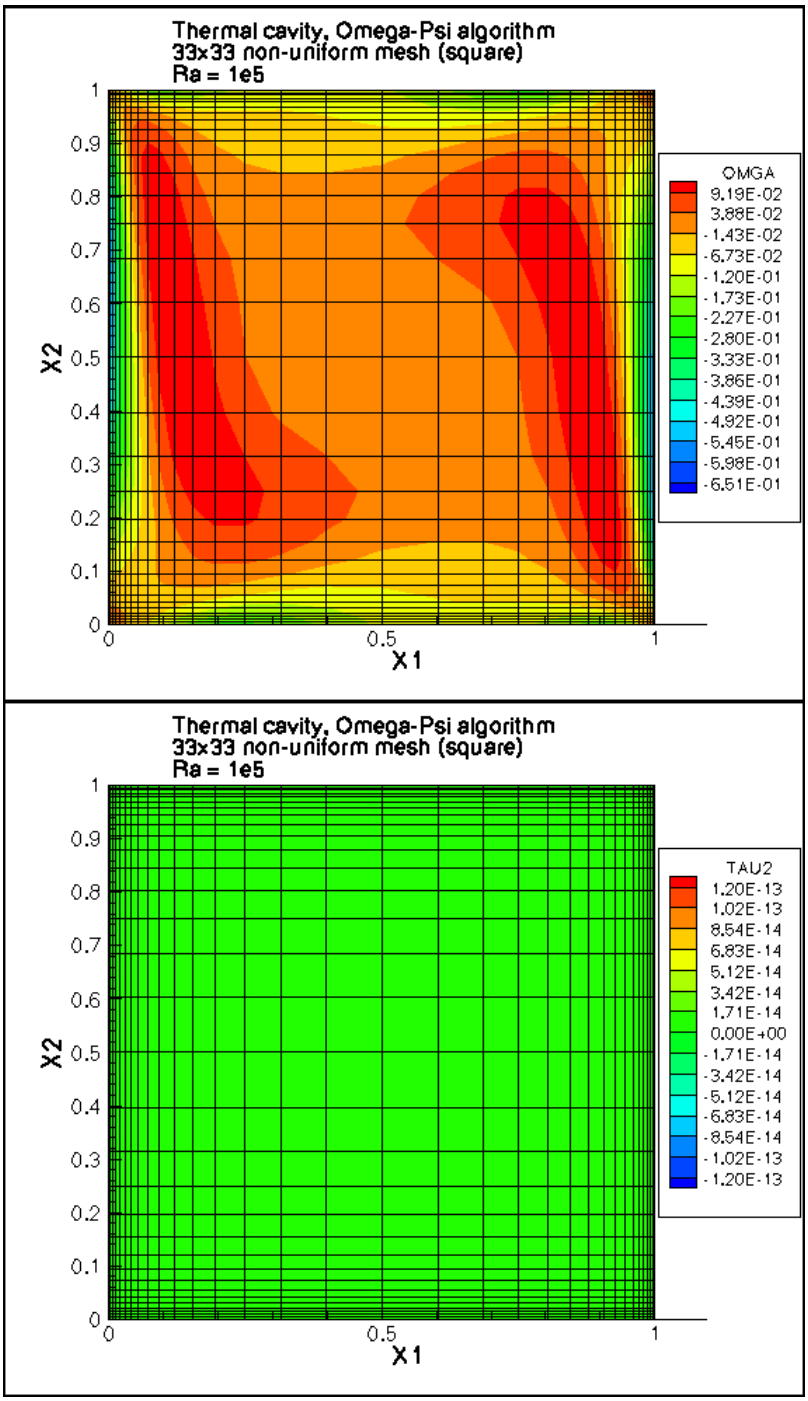

Figure 5.3.1.4 Vorticity (upper) and symmetry variable TAU2 (lower) distribution for a laminar, square thermal cavity at Ra = 1E5

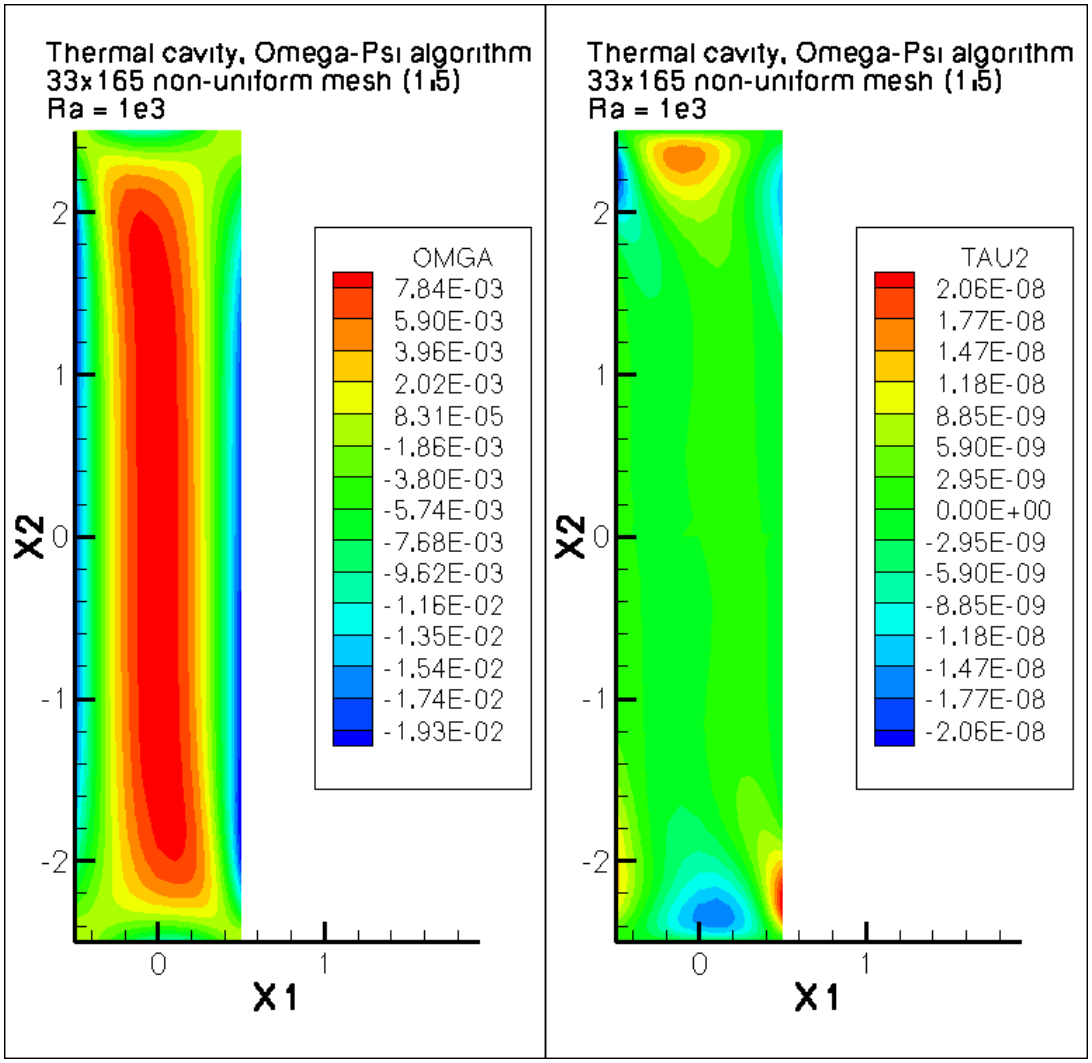

Figure 5.3.1.5 Vorticity (left) and symmetry variable TAU2 (right) distribution for a laminar, 5:1 aspect ratio, thermal cavity at Ra = 1E3

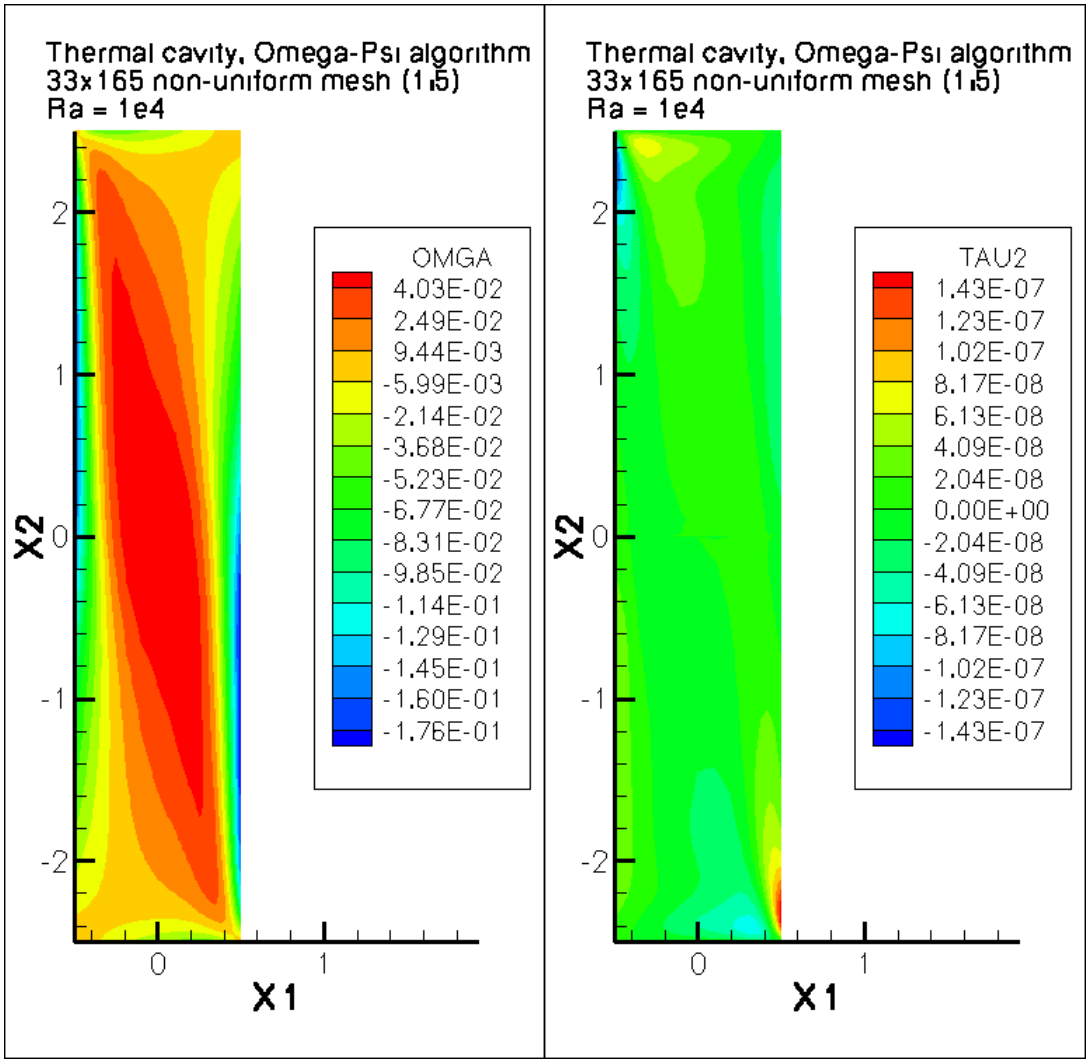

Figure 5.3.1.6 Vorticity (left) and symmetry variable TAU2 (right) distribution for a laminar, 5:1 aspect ratio, thermal cavity at Ra = 1E4

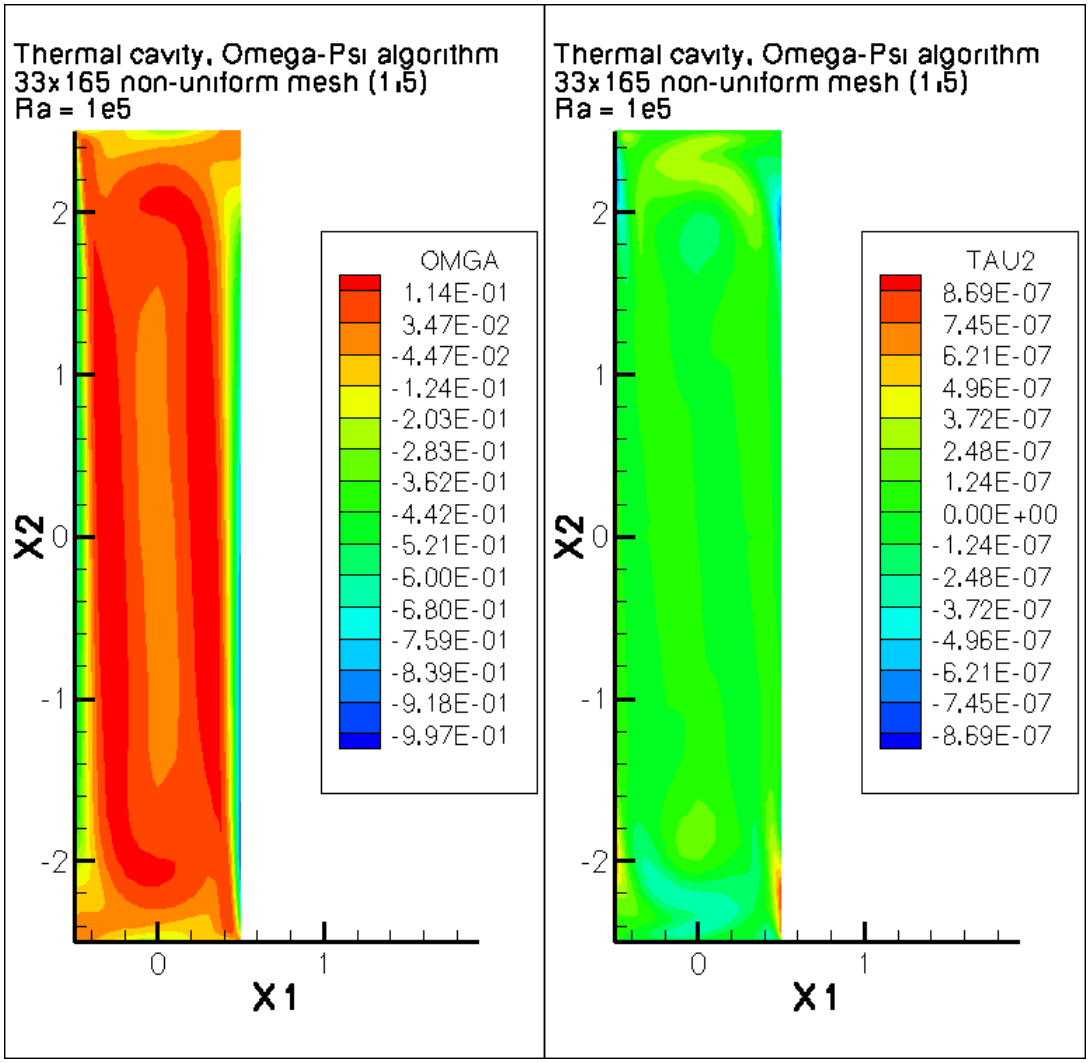

Figure 5.3.1.7 Vorticity (left) and symmetry variable TAU2 (right) distribution for a laminar, 5:1 aspect ratio, thermal cavity at Ra = 1E5

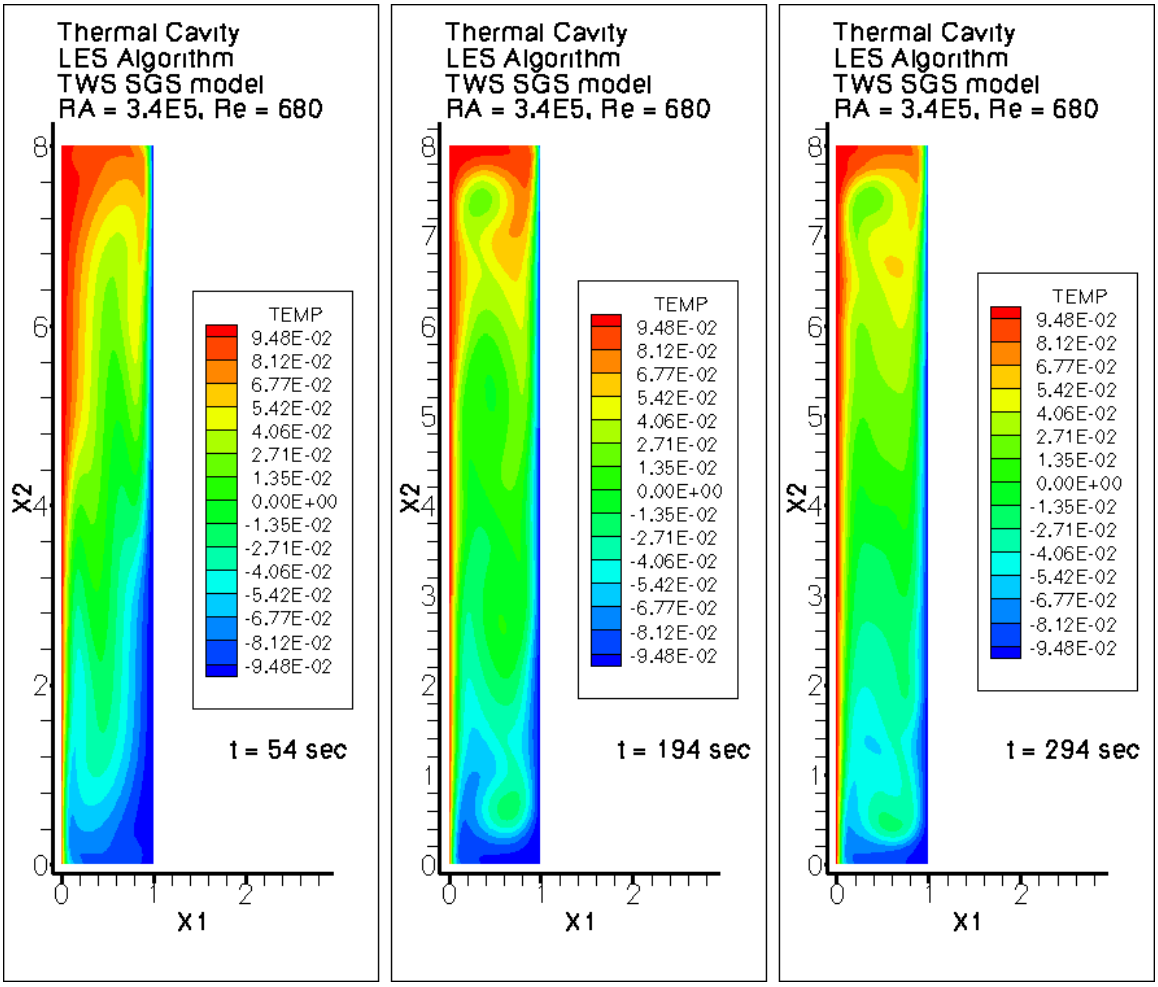

Figure 5.3.2.1 Temperature distribution at t = 54, 194 and 294 sec for a laminar flow LES algorithm computation using TWS SGS model, Ra = 3.4xE5, Re = 680

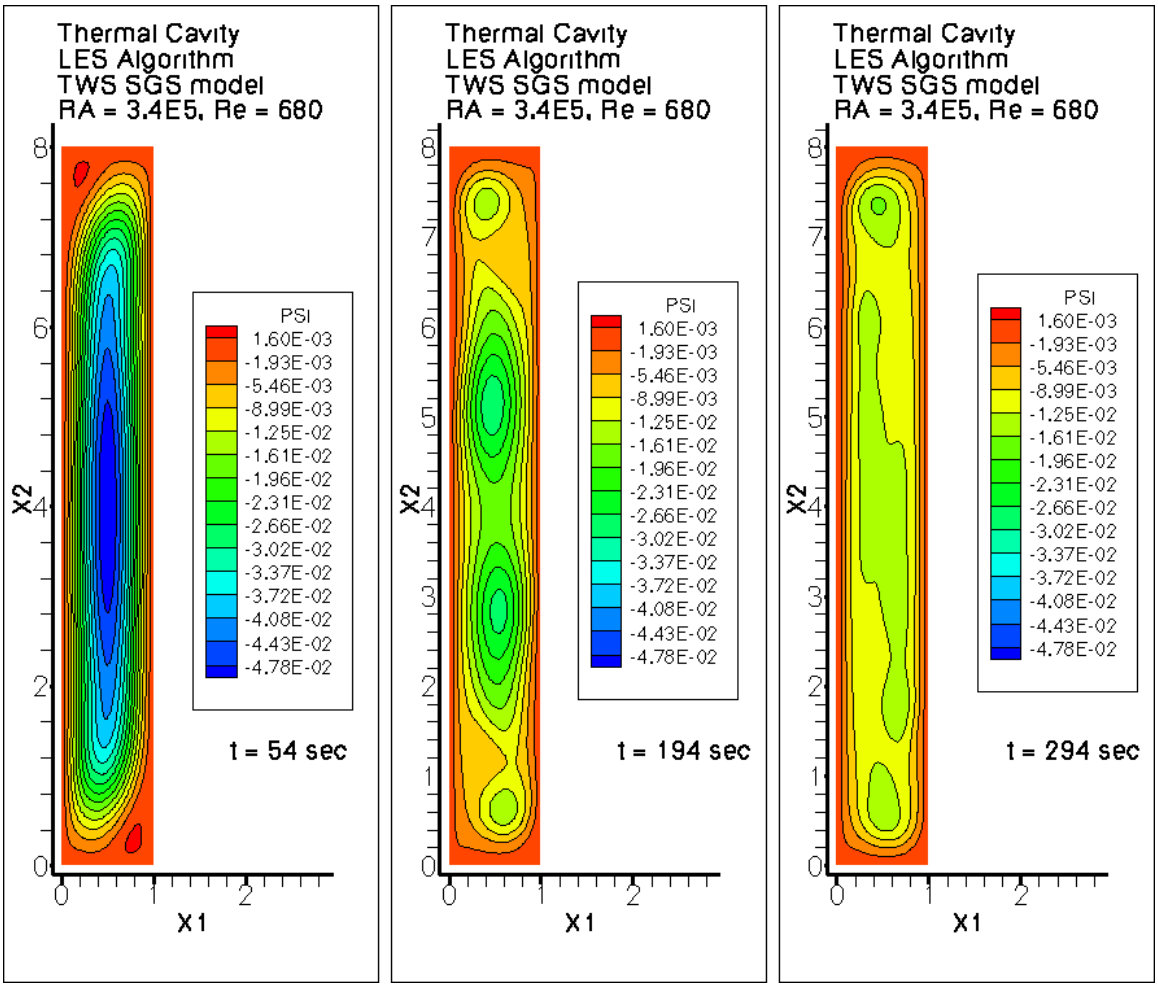

Figure 5.3.2.2 Stream-function distribution at t = 54, 194 and 294 sec for a laminar flow LES algorithm computation using TWS SGS model, Ra = 3.4xE5, Re = 680

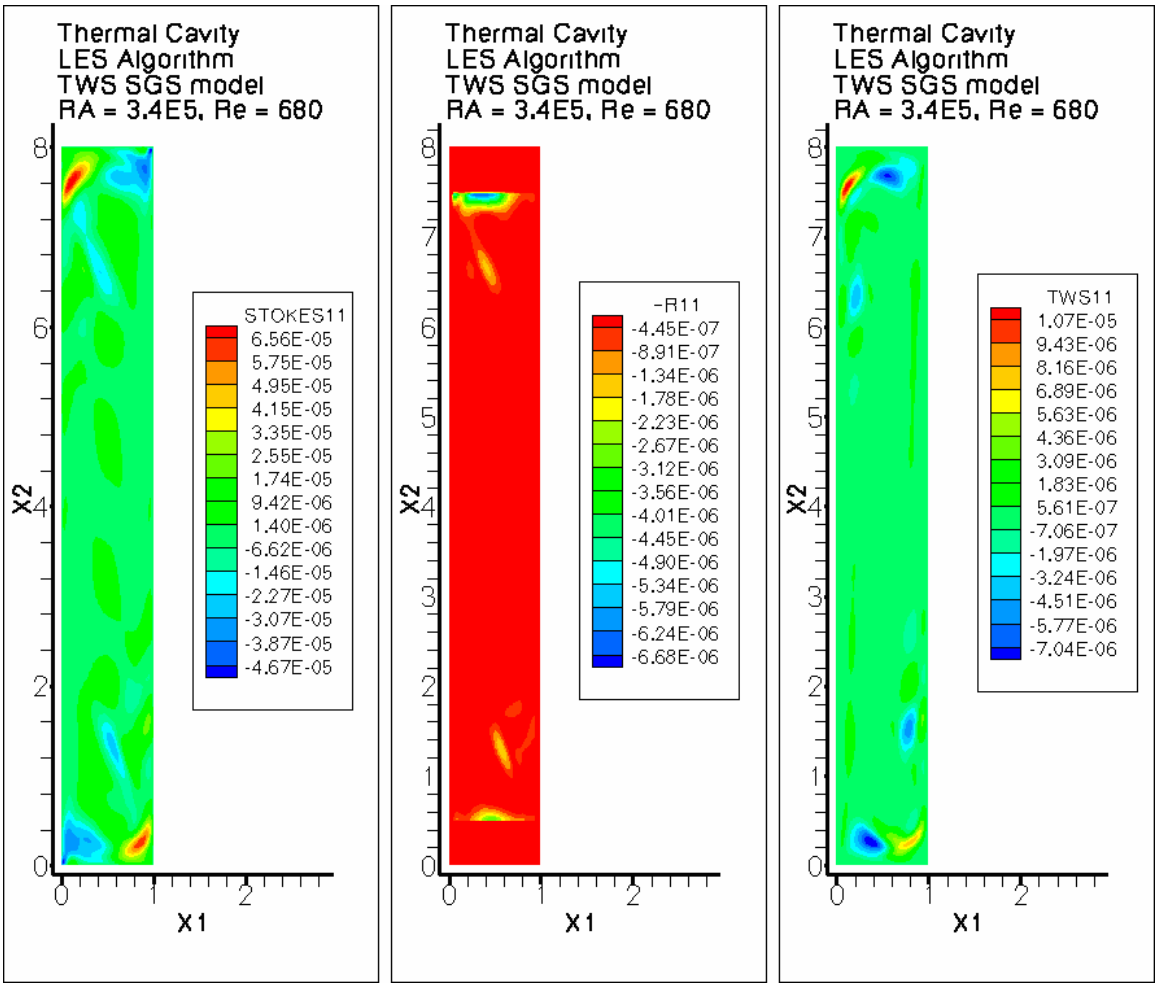

Figure 5.3.2.3 Comparison of Stokes (STOKES11), Reynolds (R11) and TWS SGS (TWS11) normal stresses for a laminar flow LES algorithm computation using TWS SGS model, Ra = 3.4xE5, Re = 680 at t = 296 sec.

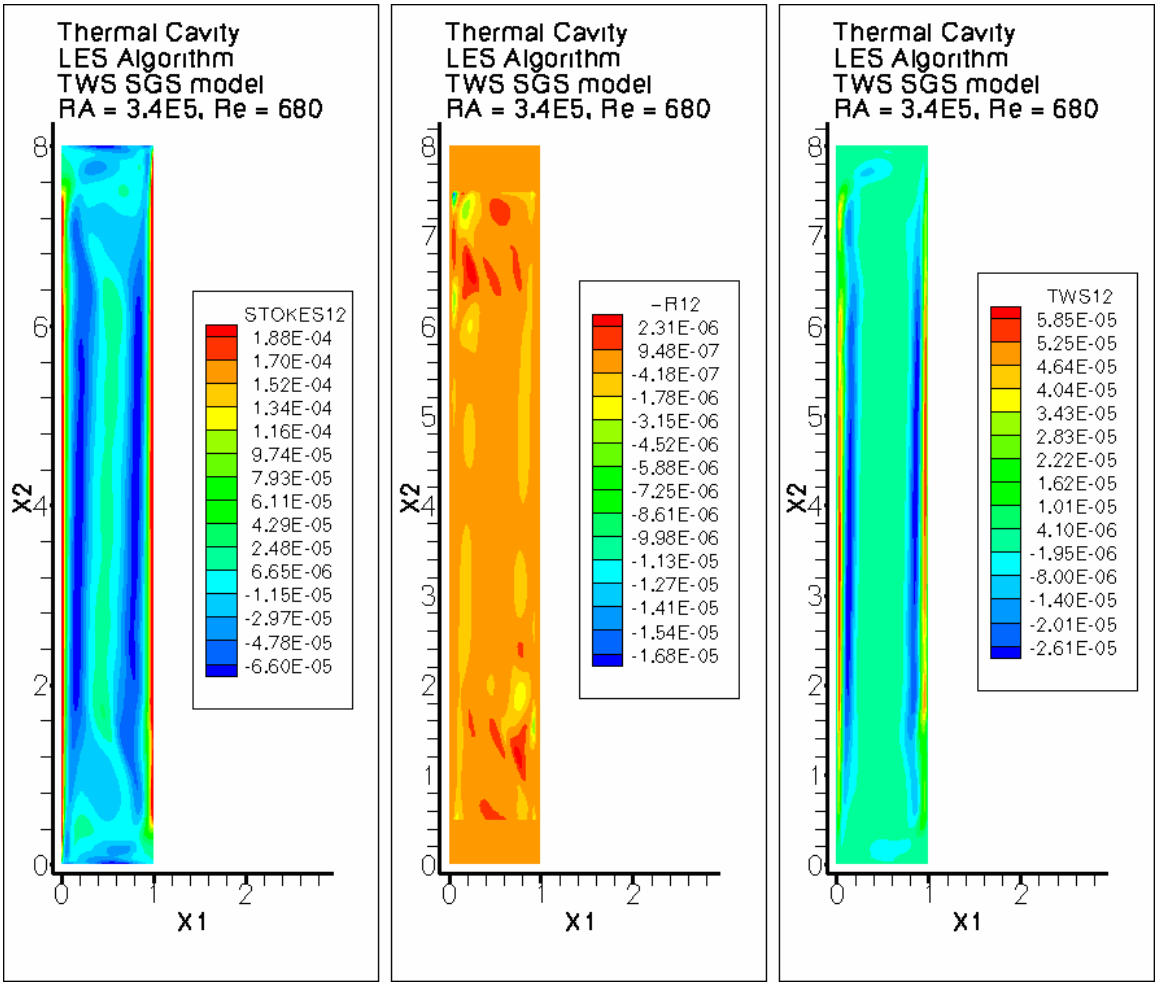

Figure 5.3.2.4 Comparison of Stokes (STOKES12), Reynolds (R12) and TWS SGS (TWS12) shear stresses for a laminar flow LES algorithm computation using TWS SGS model, Ra = 3.4xE5, Re = 680 at t = 296 sec.

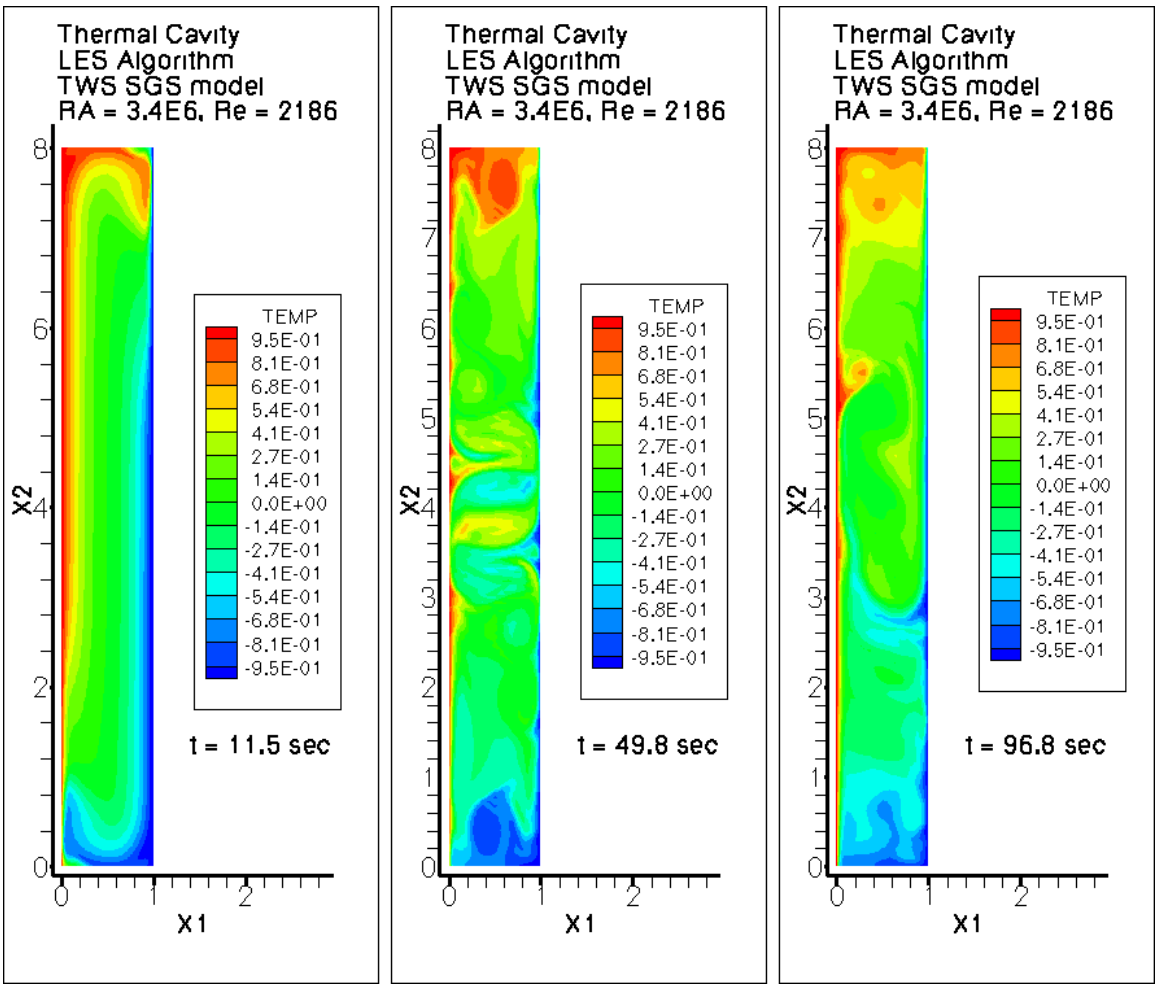

Figure 5.3.3.1 Temperature distribution at t = 11.5, 49.8 and 96.8 sec for the rational LES algorithm computation using TWS SGS model, Ra = 3.4xE6, transitional Re = 2186

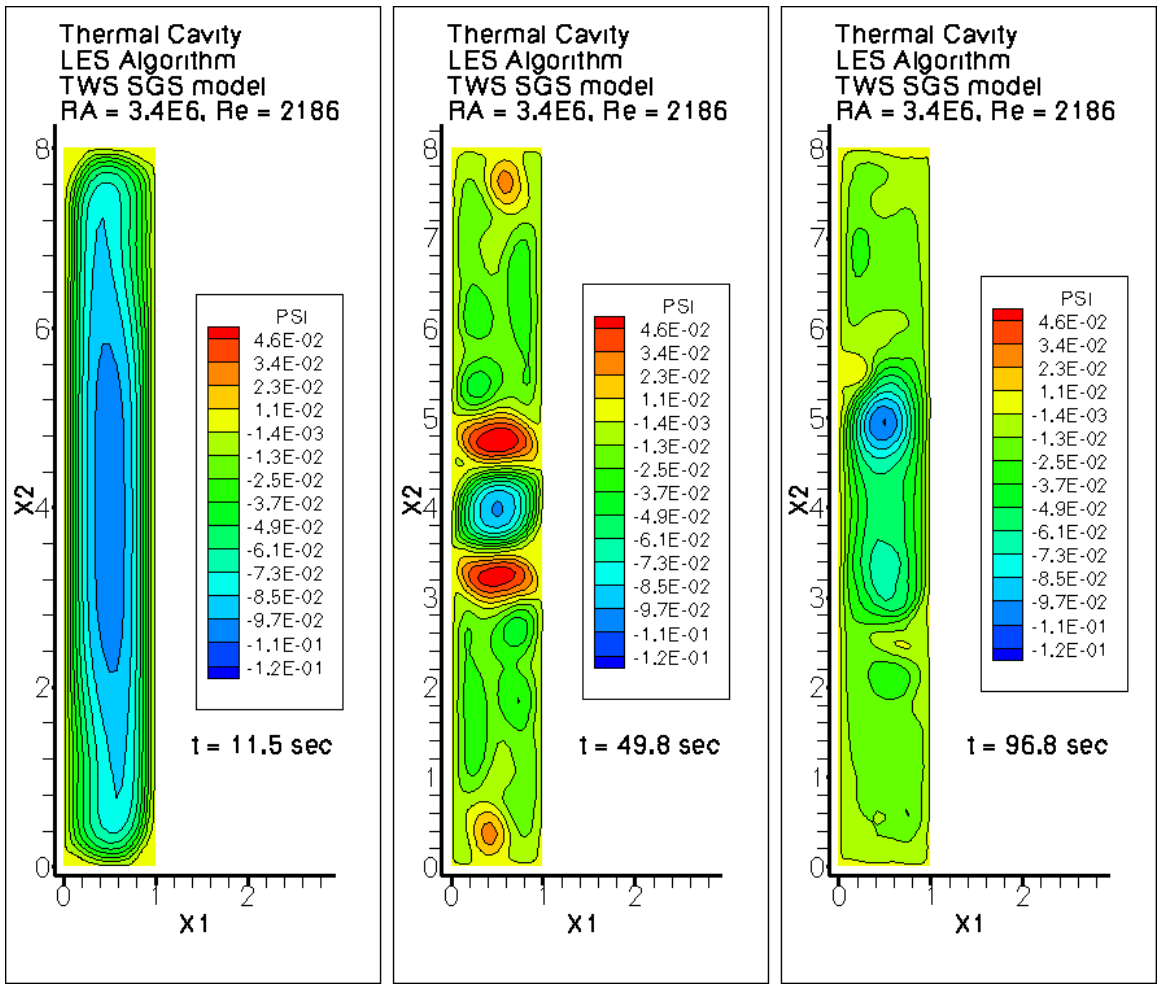

Figure 5.3.3.2 Stream-function distribution at t = 11.5, 49.8 and 96.8 sec for the rational LES algorithm computation using TWS SGS model, Ra = 3.4xE6, transitional Re = 2186

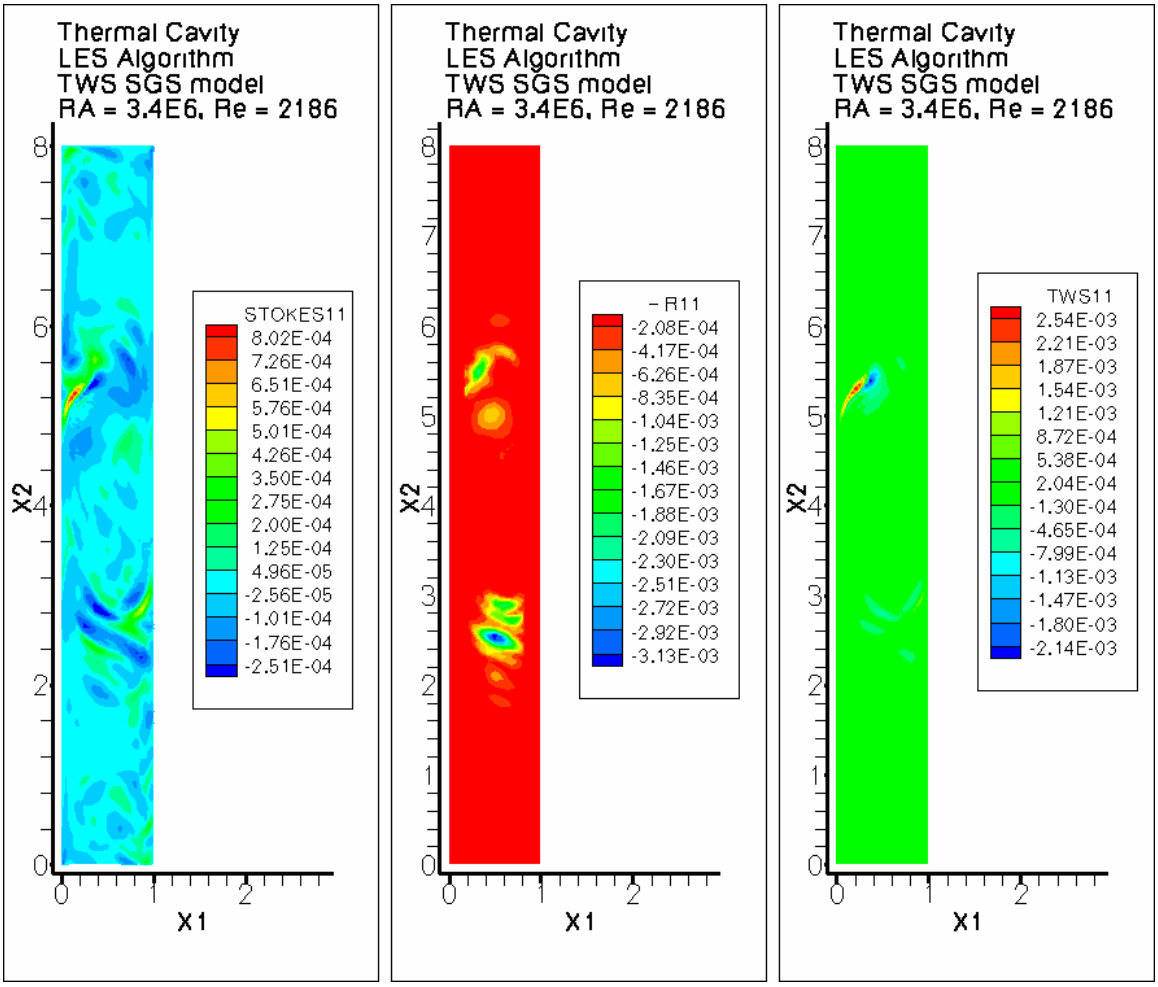

Figure 5.3.3.3 Comparison of Stokes (STOKES11), Reynolds (R11) and TWS SGS (TWS11) normal stresses for a transitional flow LES algorithm computation using TWS SGS model, Ra = 3.4xE6, Re = 2186 at t = 96.8 sec.

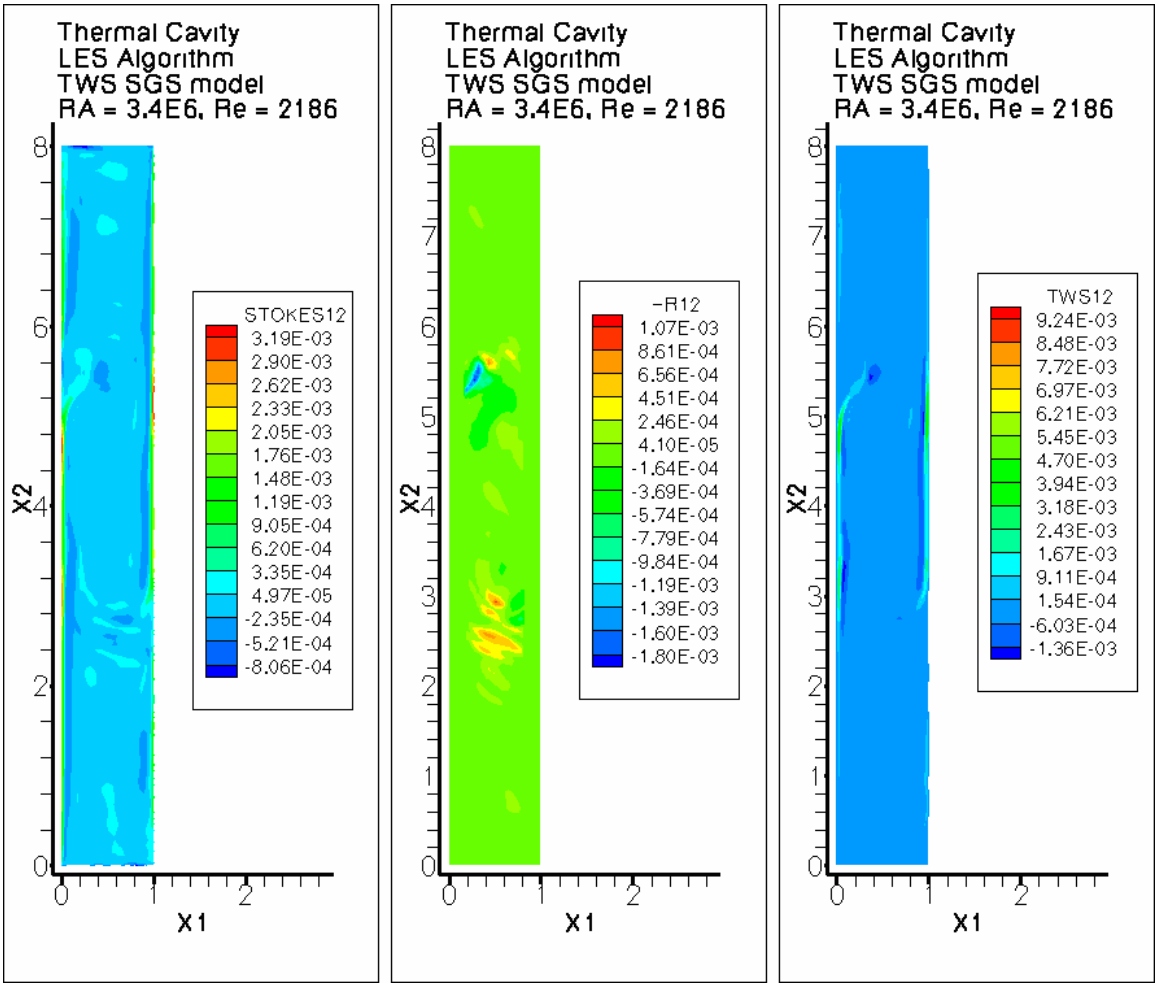

Figure 5.3.3.4 Comparison of Stokes (STOKES12), Reynolds (R12) and TWS SGS (TWS12) shear stresses for a laminar flow LES algorithm computation using TWS SGS model, Ra = 3.4xE6, Re = 2186 at t = 96.8 sec.

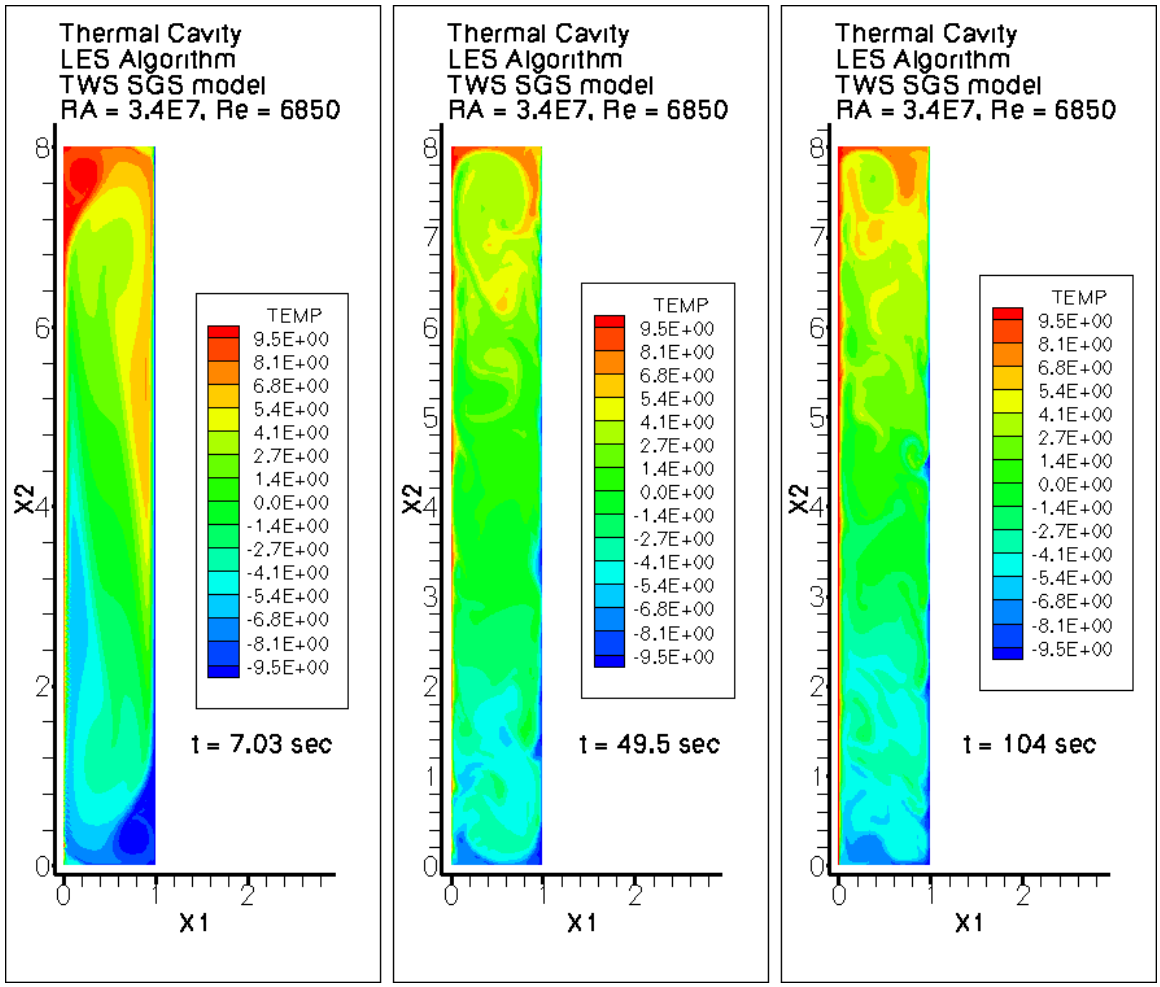

Figure 5.3.4.1 Temperature distribution at t = 7.03, 49.5 and 104 sec for a LES algorithm computation using TWS SGS model, Ra = 3.4xE7, Re = 6850.

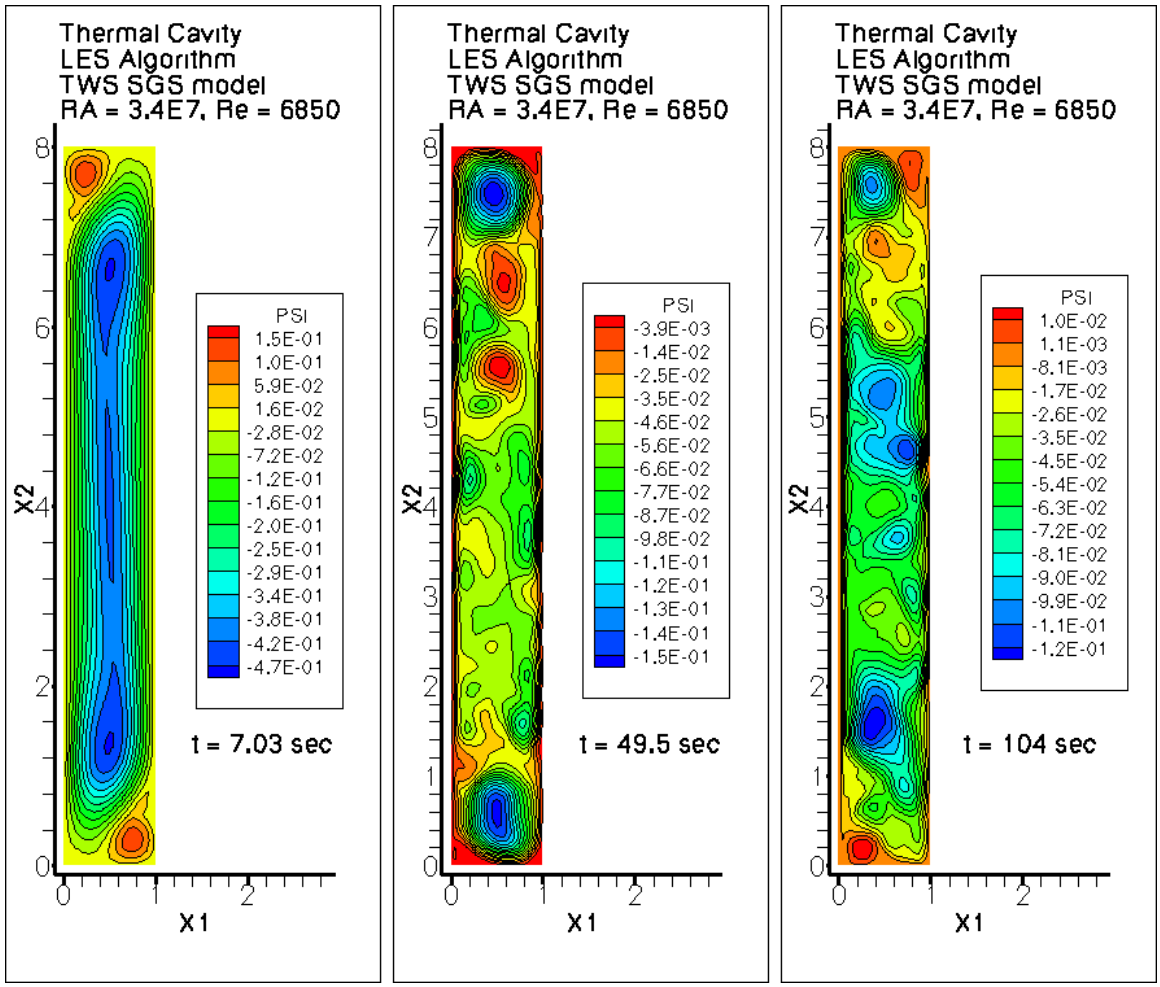

Figure 5.3.4.2 Stream-function distribution at t = 7.03, 49.5 and 104 sec for a LES algorithm computation using TWS SGS model, Ra = 3.4xE7, Re = 6850

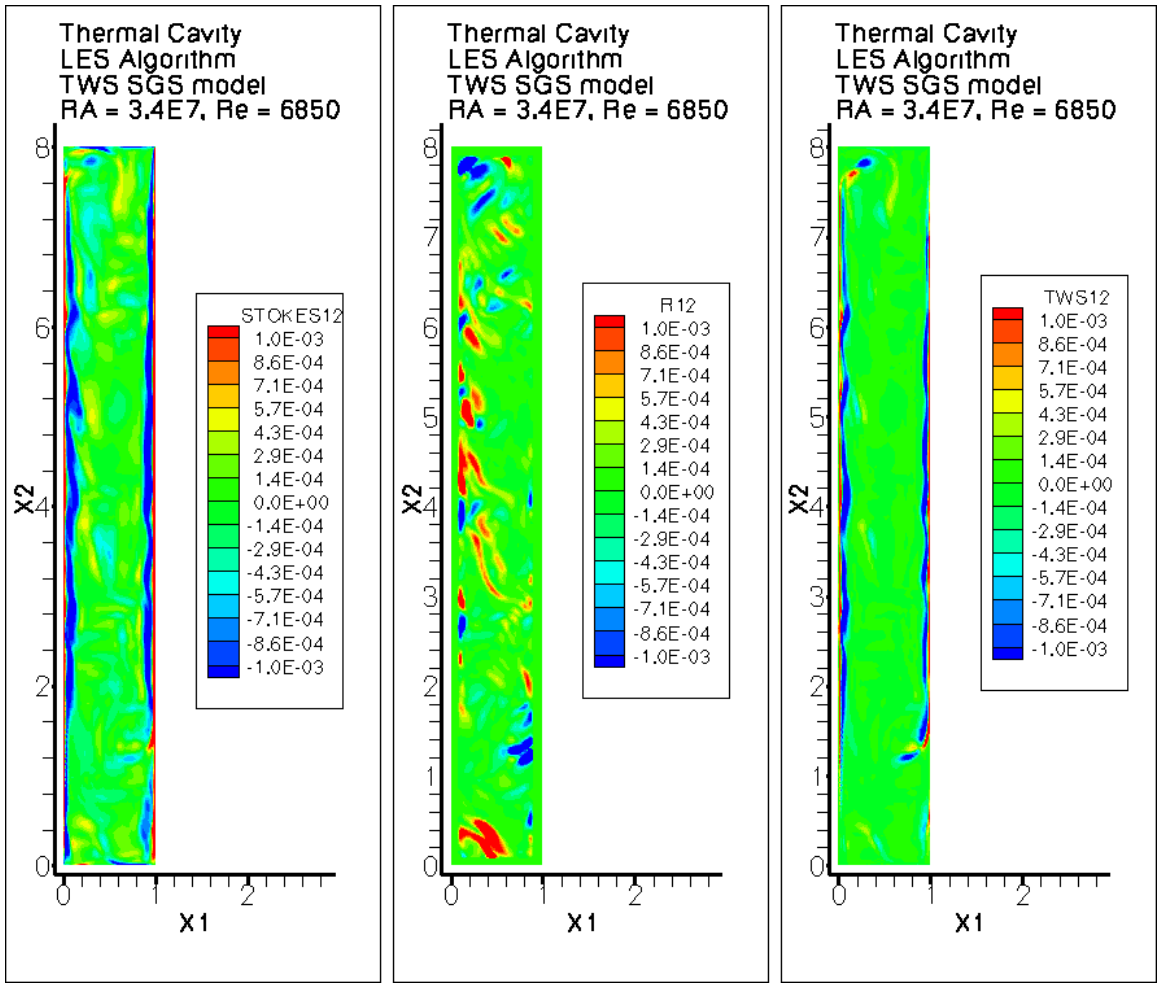

Figure 5.3.4.3 Comparison of Stokes (STOKES12), Reynolds (R12) and TWS SGS (TWS12) shear stresses for a LES algorithm computation using TWS SGS model, Ra = 3.4xE7, Re = 6850 at t = 104 sec

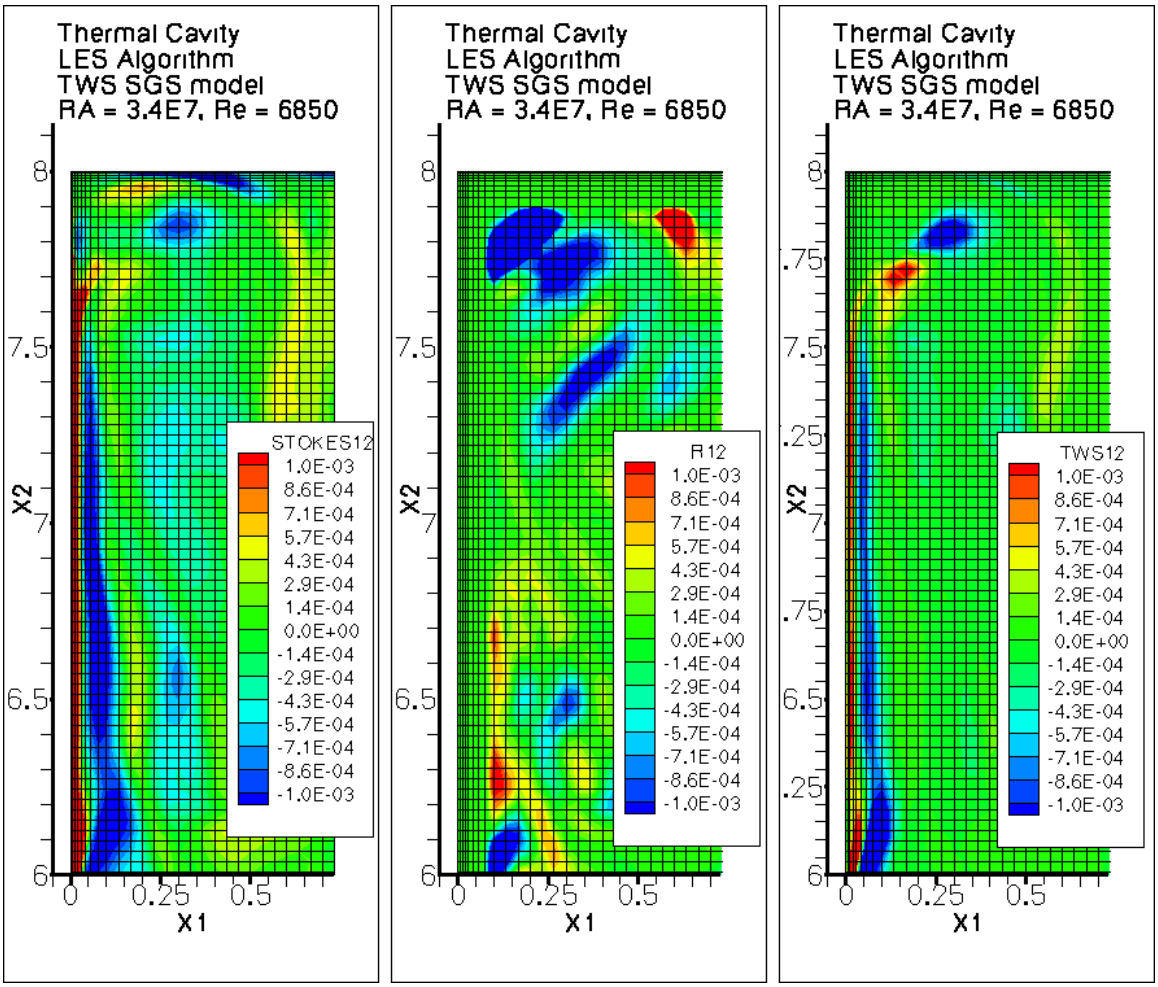

Figure 5.3.4.4 Comparison of Stokes (STOKES12), Reynolds (R12) and TWS SGS (TWS12) shear stresses for a transitional flow LES algorithm computation using TWS SGS model, Ra = 3.4xE7, Re = 6850 at t = 104 sec; close-up at upper left corner

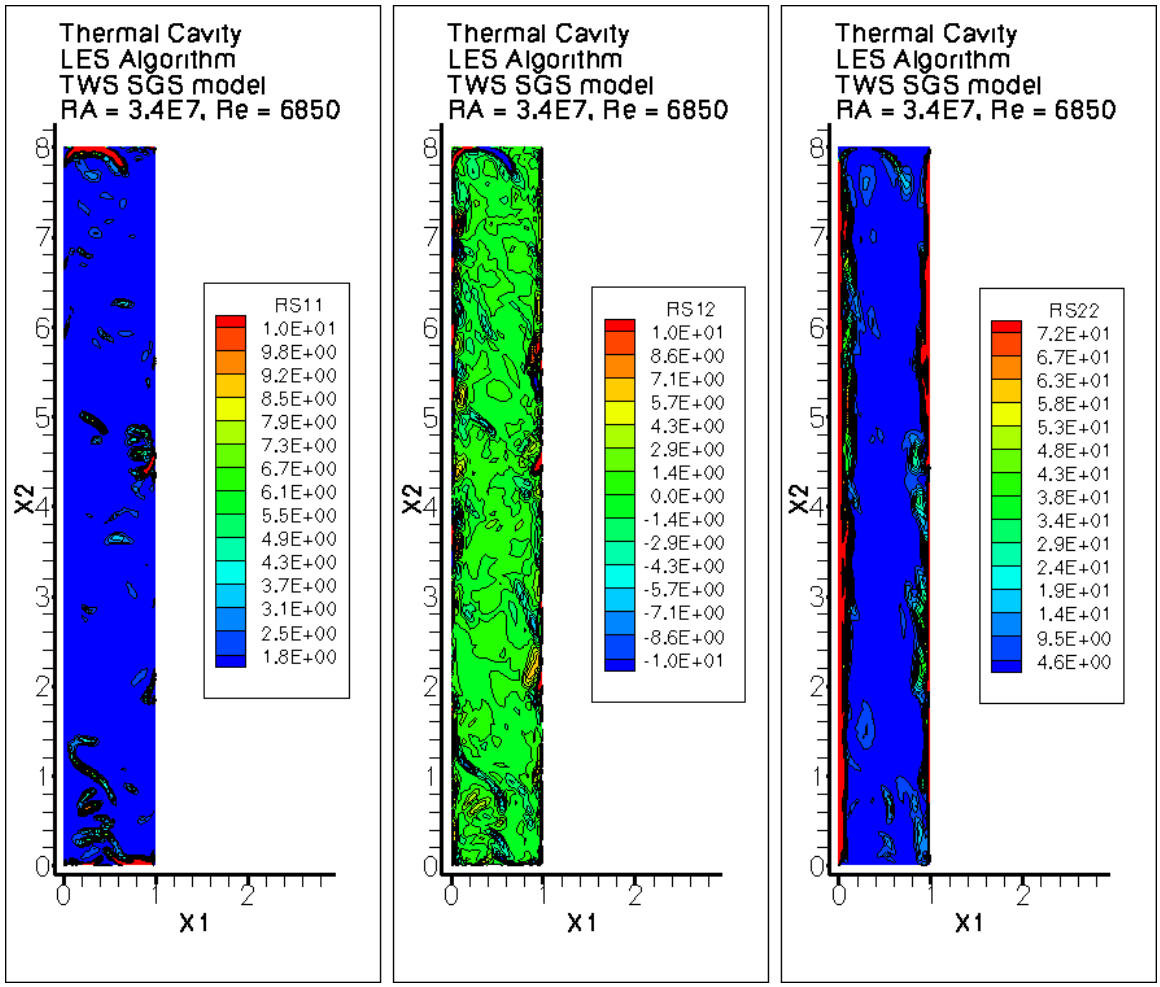

Figure 5.3.4.5 Auxiliary variable tensor of the momentum equations, RS11, RS12 and RS22 for a LES algorithm computation using TWS SGS model, Ra = 3.4xE7, Re = 6850 at t = 104 sec

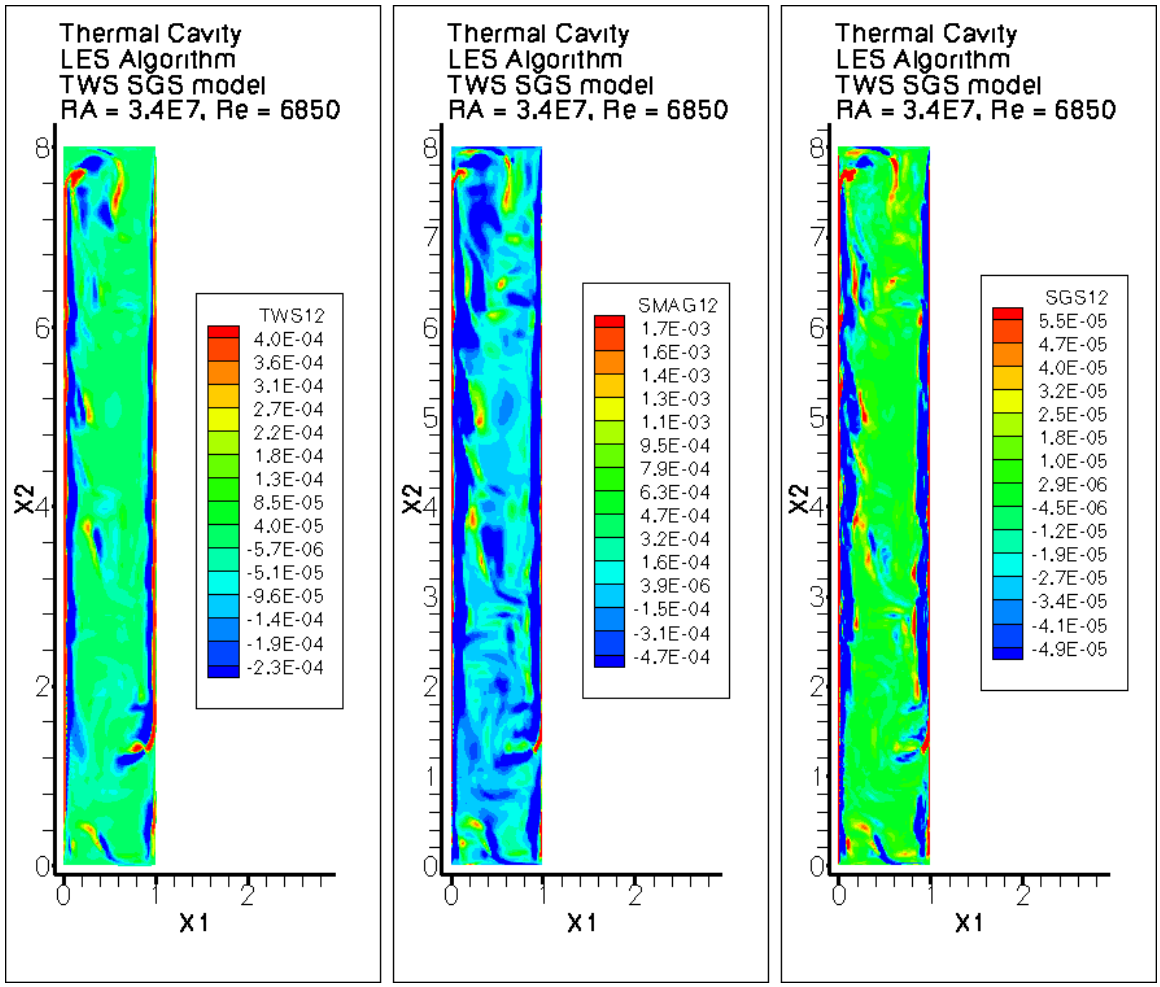

Figure 5.3.4.6 Comparison of shear TWS SGS stress (TWS12), Smagorinsky (SMAG12) and SGS stress based on Eqn. (2.57), (SGS12), for a transitional flow LES algorithm computation using TWS SGS model, Ra = 3.4xE7, Re = 6850 at t = 104 sec.

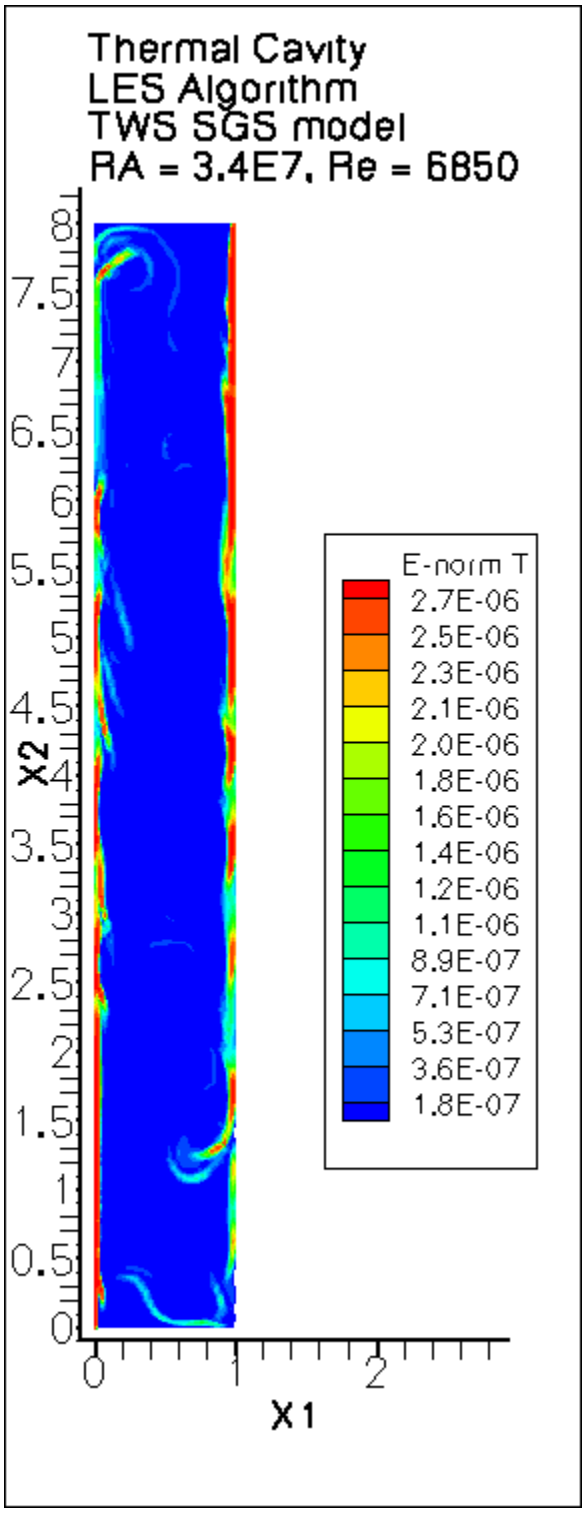

Figure 5.3.4.7 Energy norm based on temperature for a rational LES algorithm computation using TWS SGS model, Ra = 3.4xE7, Re = 6850 at t = 104 sec.

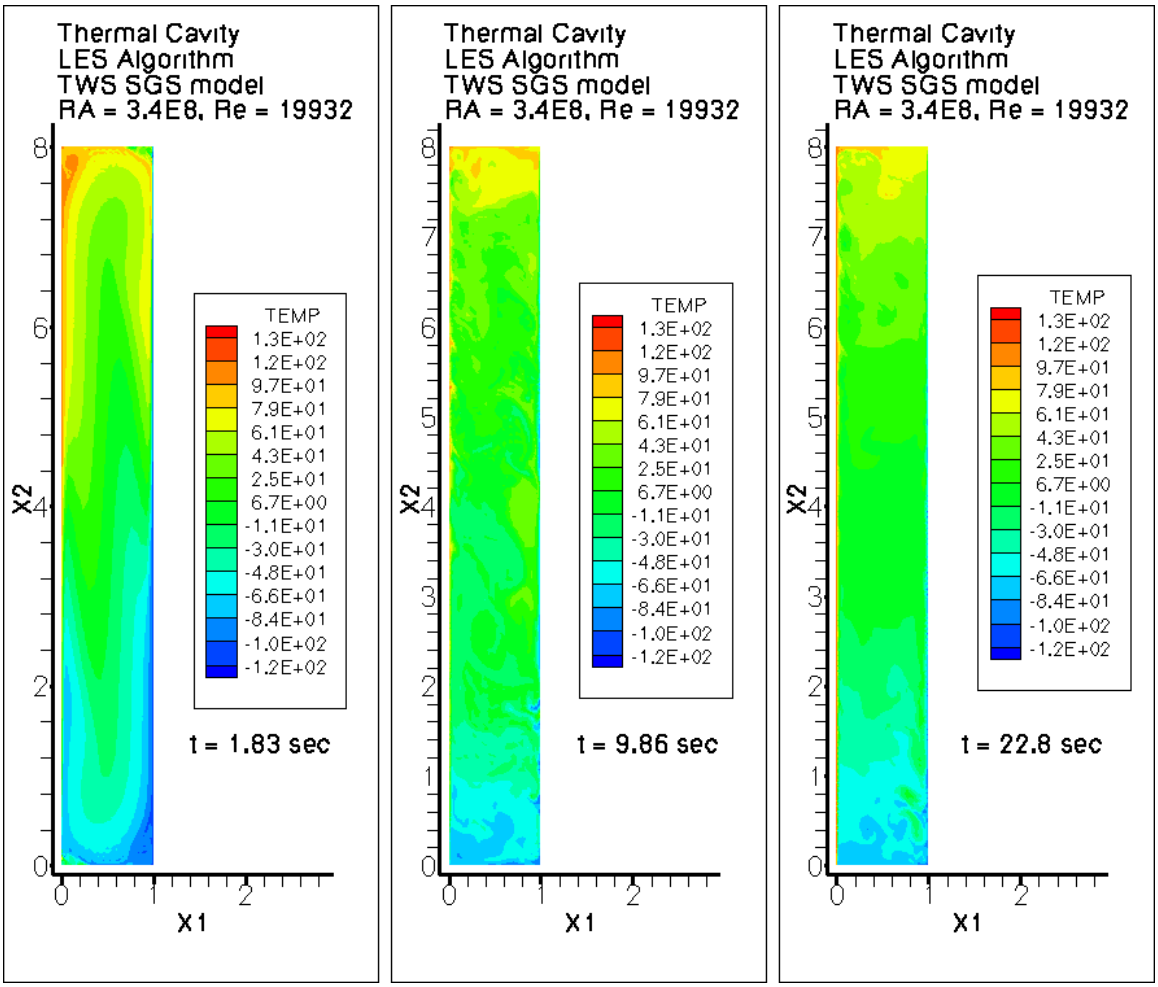

Figure 5.3.5.1 Temperature distribution at t = 1.83, 9.86 and 22.8 sec for a turbulent flow LES algorithm computation using TWS SGS model, Ra = 3.4xE8, Re = 19932.

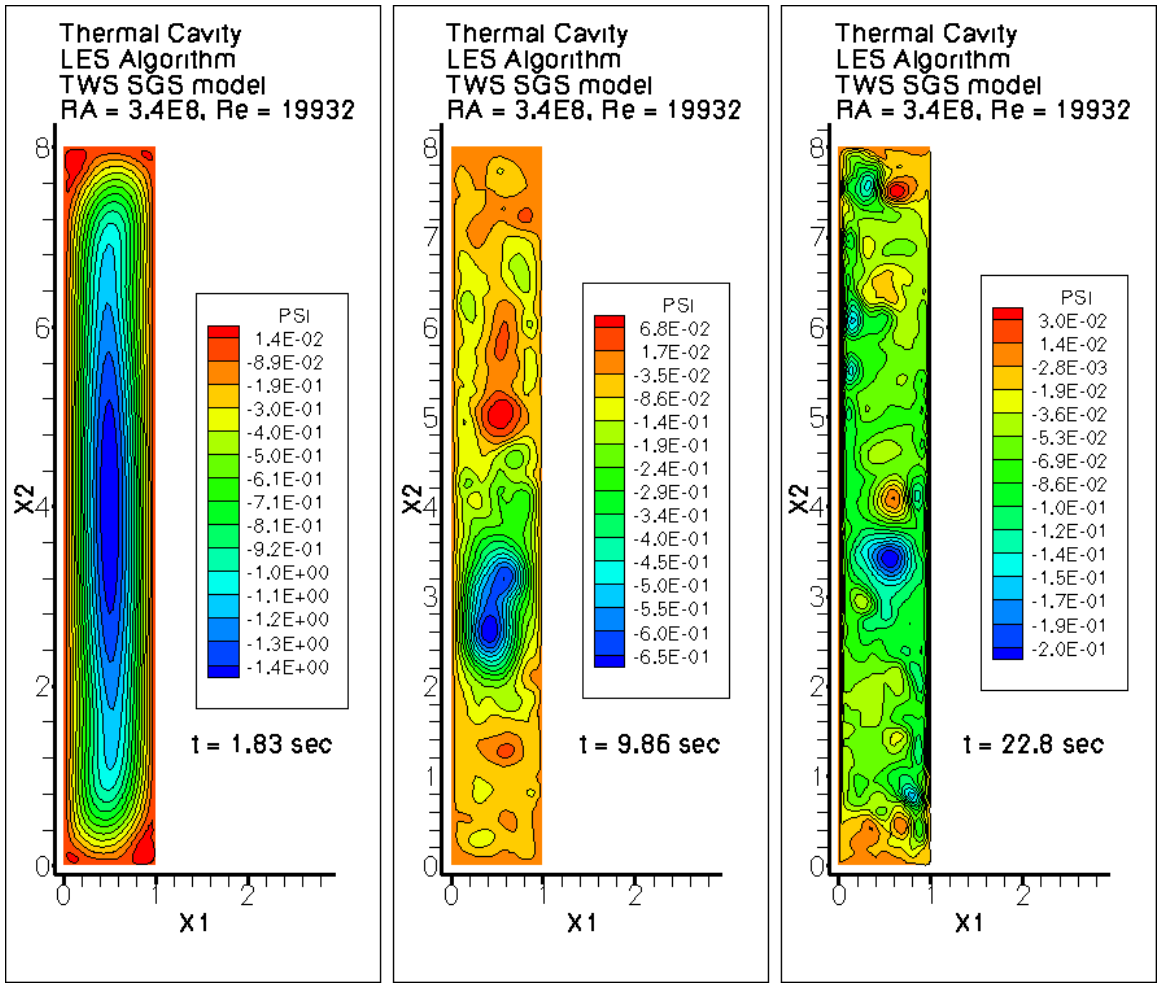

Figure 5.3.5.2 Stream-function distribution at t = 1.83, 9.86 and 22.8 sec for a rational LES algorithm computation using TWS SGS model, Ra = 3.4xE8, Re = 19932

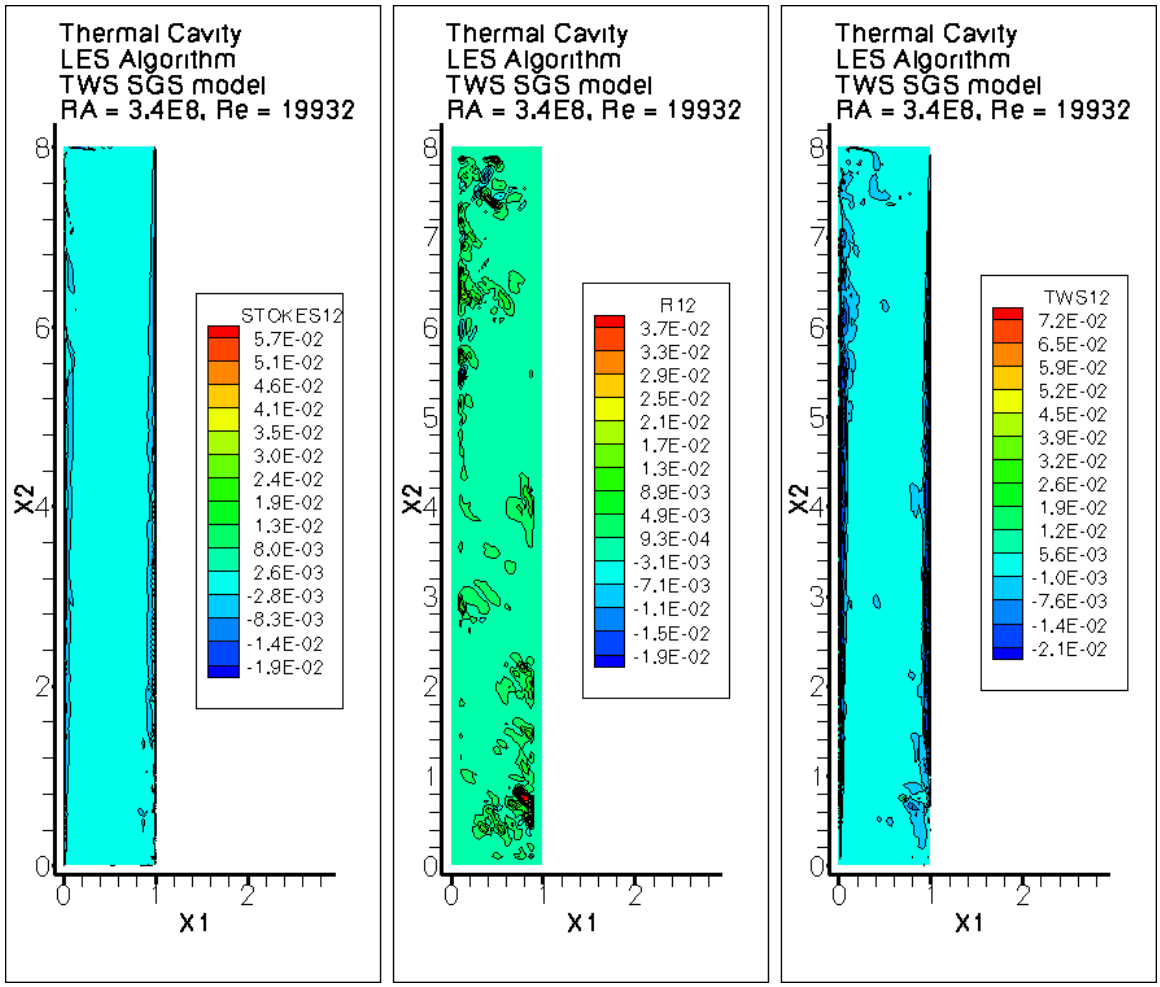

Figure 5.3.5.3 Comparison of Stokes (STOKES12), Reynolds (R12) and TWS SGS (TWS12) shear stresses for a turbulent flow LES algorithm computation using TWS SGS model, Ra = 3.4xE8, Re = 19932 at t = 22.8 sec

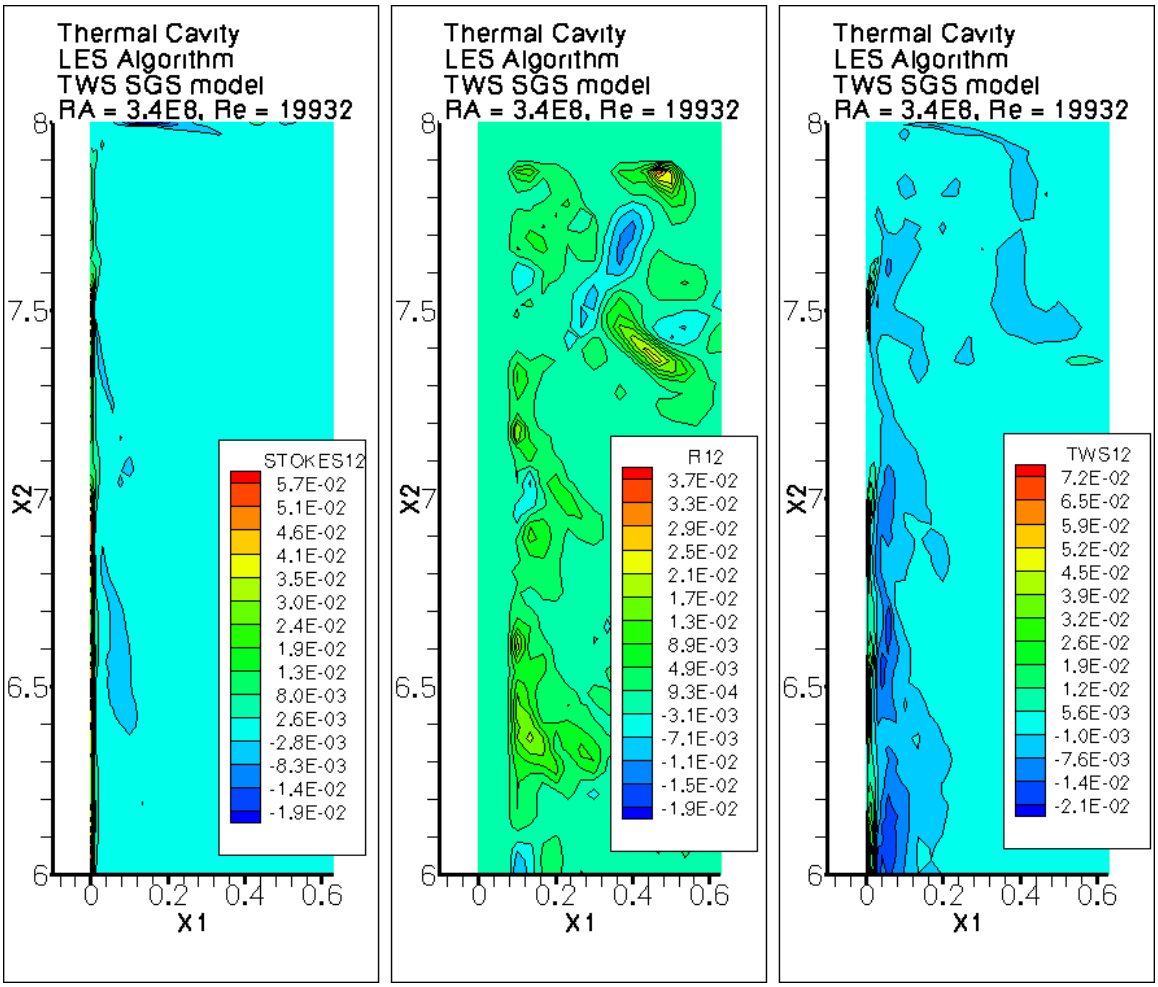

Figure 5.3.5.4 Comparison of Stokes (STOKES12), Reynolds (R12) and TWS SGS (TWS12) shear stresses for a turbulent flow LES algorithm computation using TWS SGS model, Ra = 3.4xE8, Re = 19932 at t = 22.8 sec; close-up of upper left corner of domain

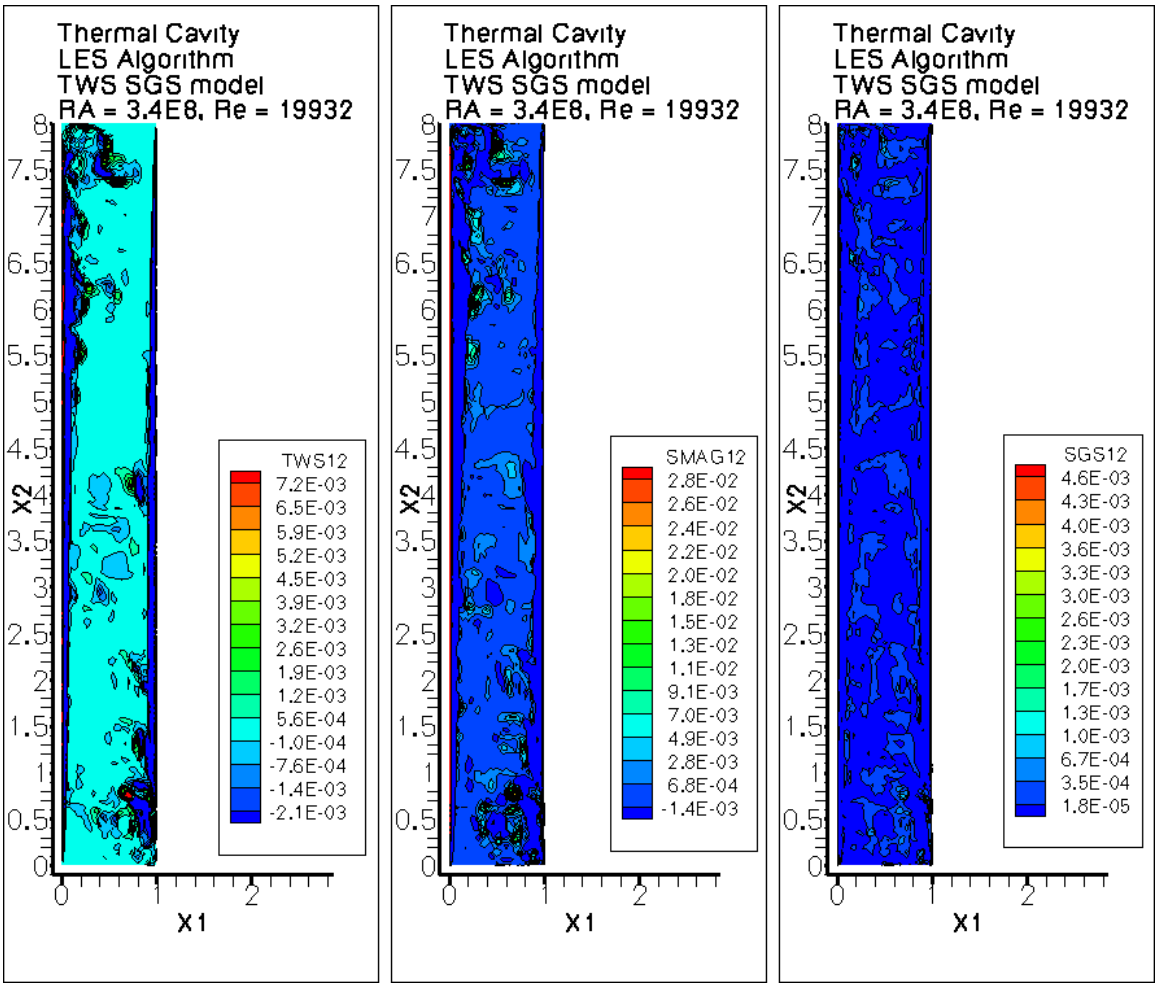

Figure 5.3.5.5 Comparison of shear TWS SGS stress (TWS12), Smagorinsky (SMAG12) and SGS stress based on Eqn. (2.57), (SGS12), for a rational LES algorithm computation using TWS SGS model, Ra = 3.4xE8, Re = 19932 at t = 22.8 sec.

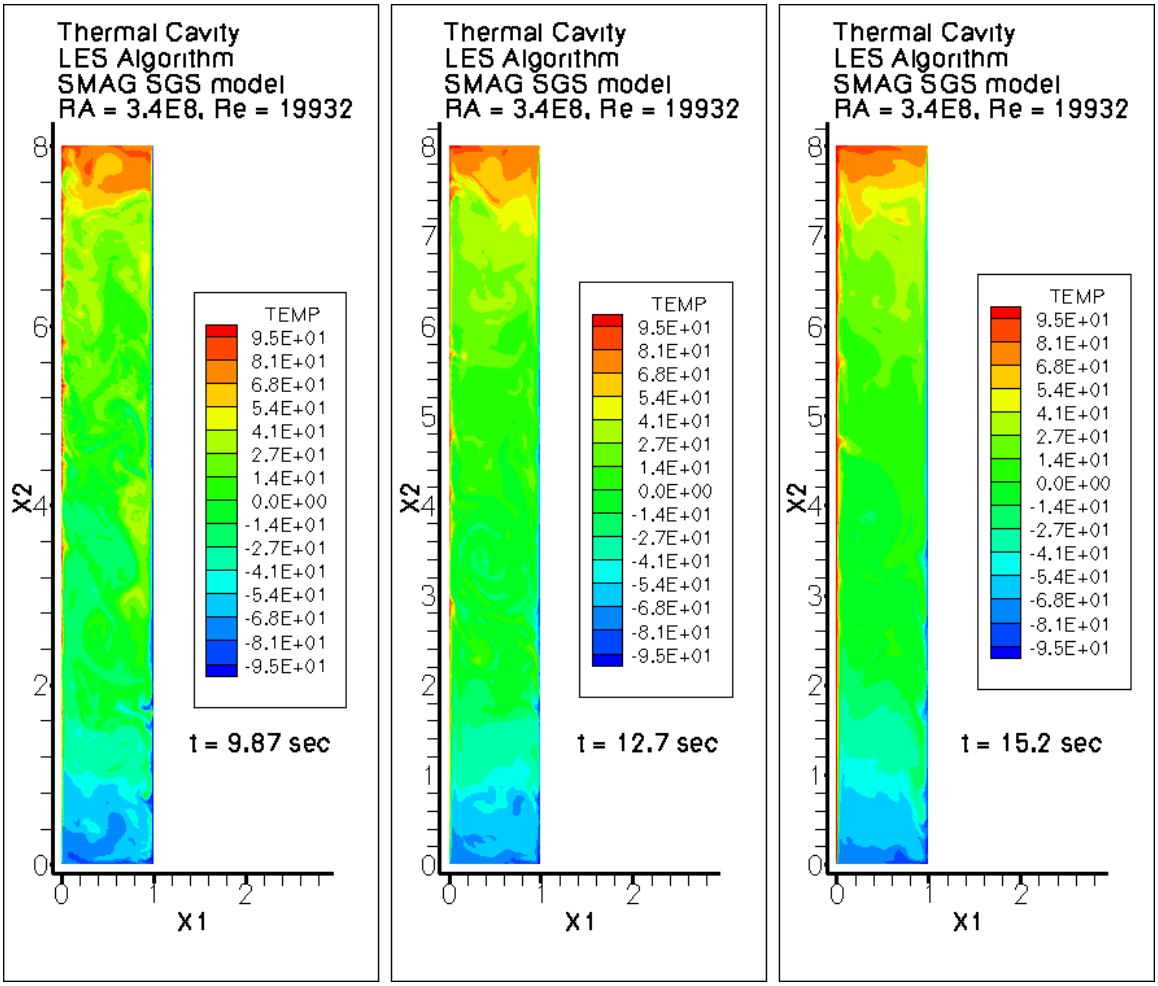

Figure 5.3.5.6 Temperature distribution at t = 9.87, 12.7 and 15.7 sec for a turbulent flow LES algorithm computation using Smagorinsky SGS model, Ra = 3.4xE8, Re = 19932. This execution is a continuation of the TWS result at t = 9.6 for the same Rayleigh number

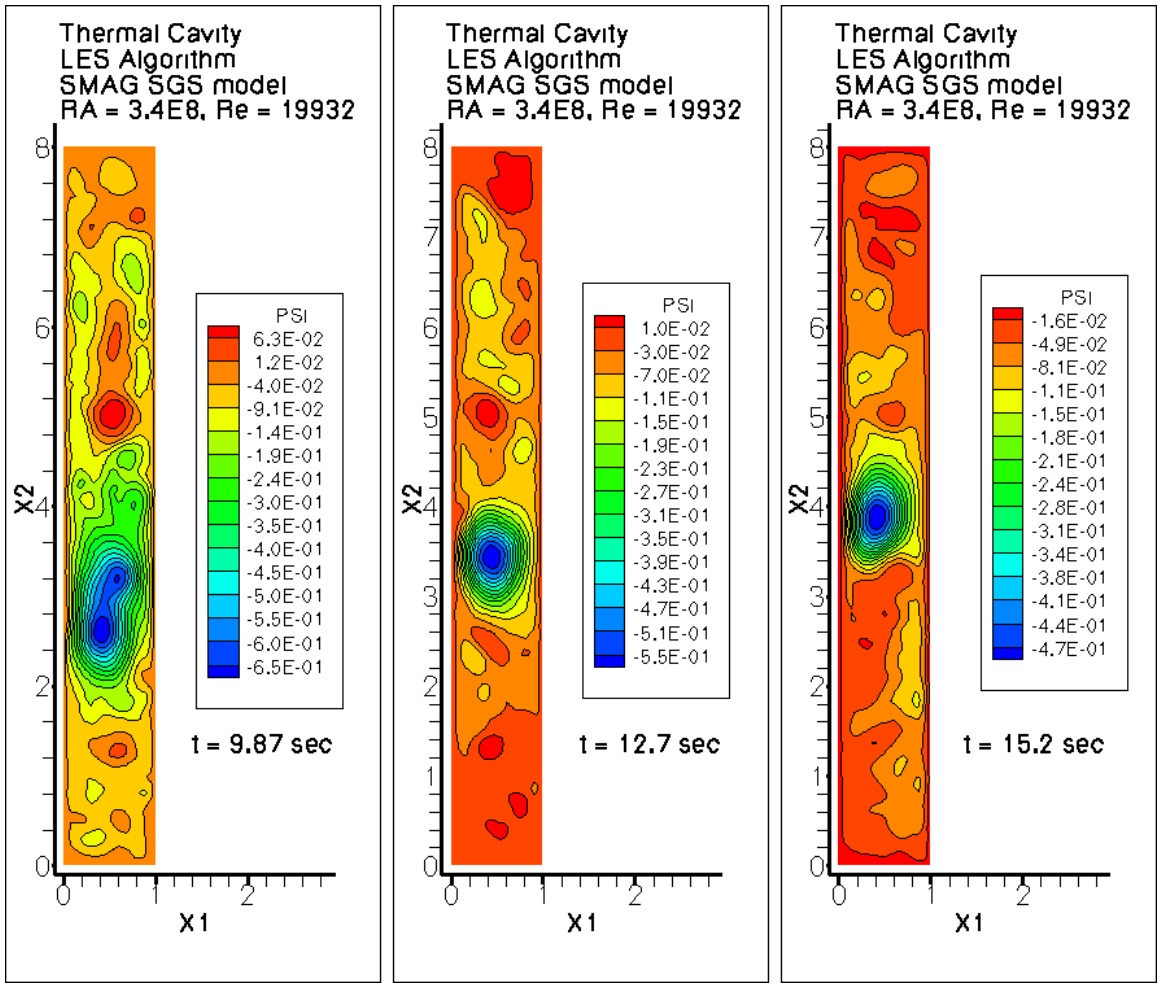

Figure 5.3.5.7 Stream-function distribution at t = 9.87, 12.7 and 15.7 sec for a turbulent flow LES algorithm computation using Smagorinsky SGS model, Ra = 3.4xE8, Re = 19932. This execution is a continuation of the TWS result at t = 9.6 for the same Rayleigh number

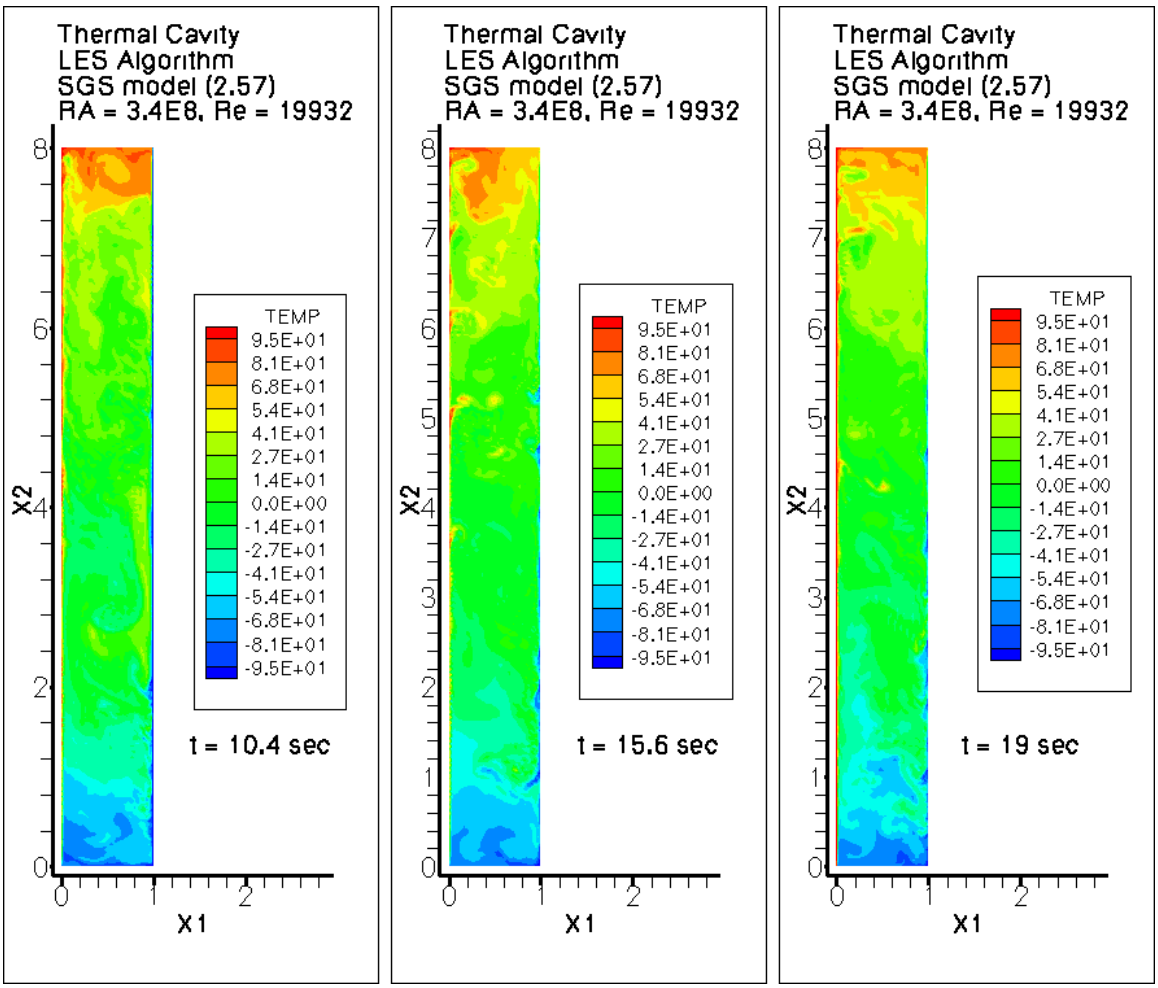

Figure 5.3.5.8 Temperature distribution at t = 10.4, 15.6 and 19 sec for a turbulent flow LES algorithm computation using SGS model based on (2.57), Ra = 3.4xE8, Re = 19932. This execution is a continuation of the TWS result at t = 9.6 for the same Rayleigh number

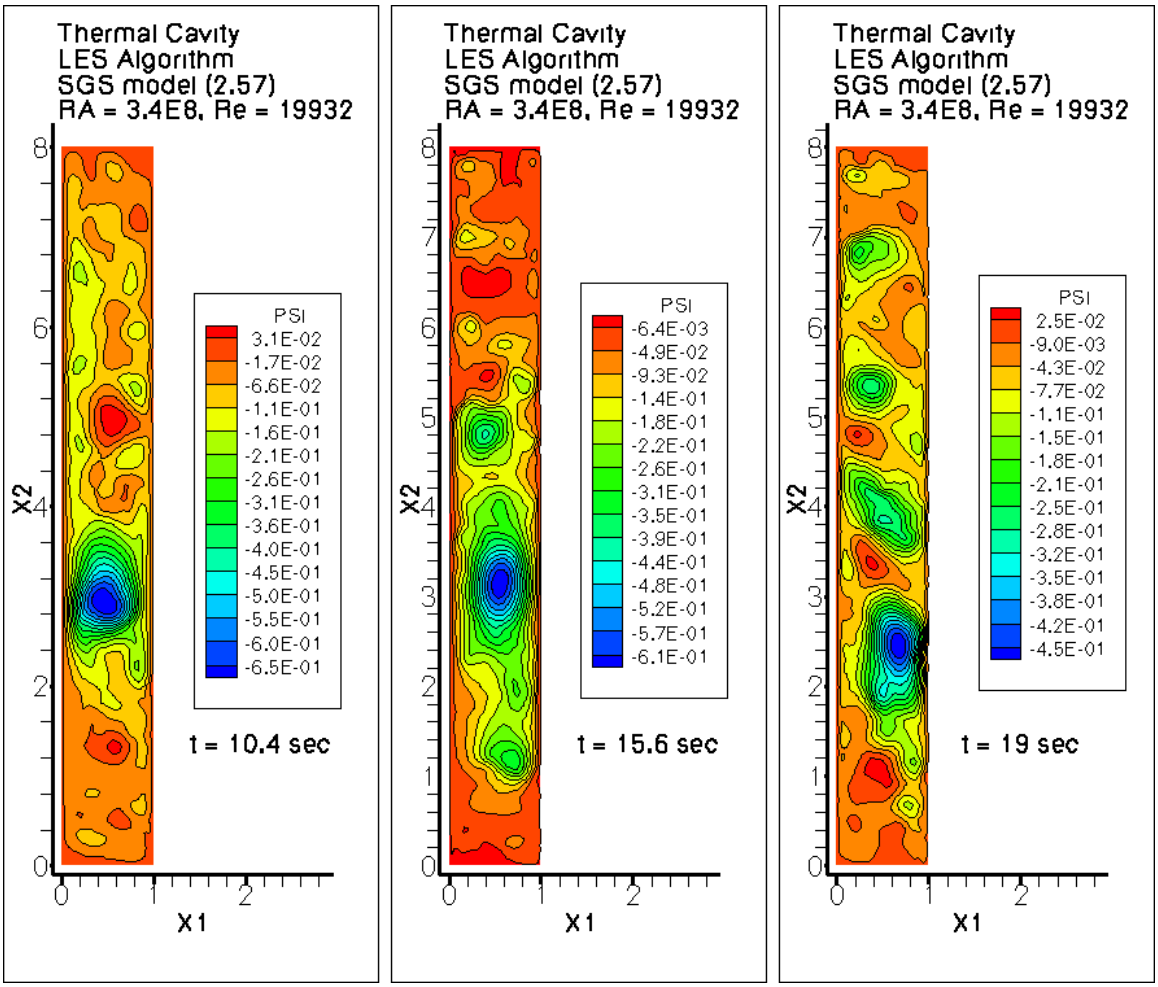

Figure 5.3.5.9 Stream-function comparison at t = 14.7, 15.6 for turbulent flow LES algorithm computations using TWS, Smagorinsky and SGS model based on (2.57), Ra = 3.4xE8, Re = 19932. This execution is a continuation of the TWS result at t = 9.6 for the same Rayleigh number

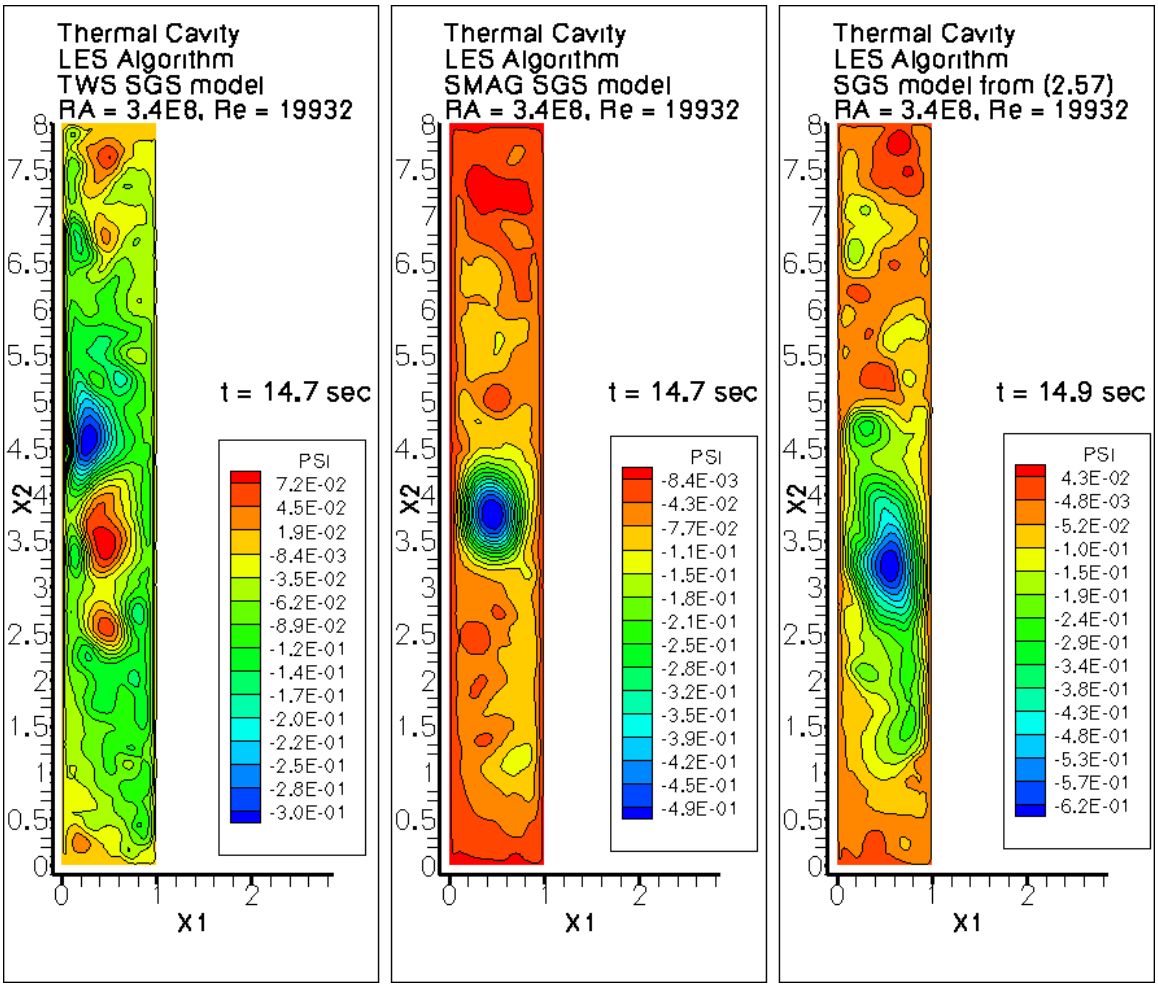

Figure 5.3.5.10 Comparison of stream-function distributions at t = 14.7 sec for turbulent flow LES algorithm computations using the TWS, Smagorinsky and SGS model based on (2.57), Ra = 3.4xE8, Re = 19932

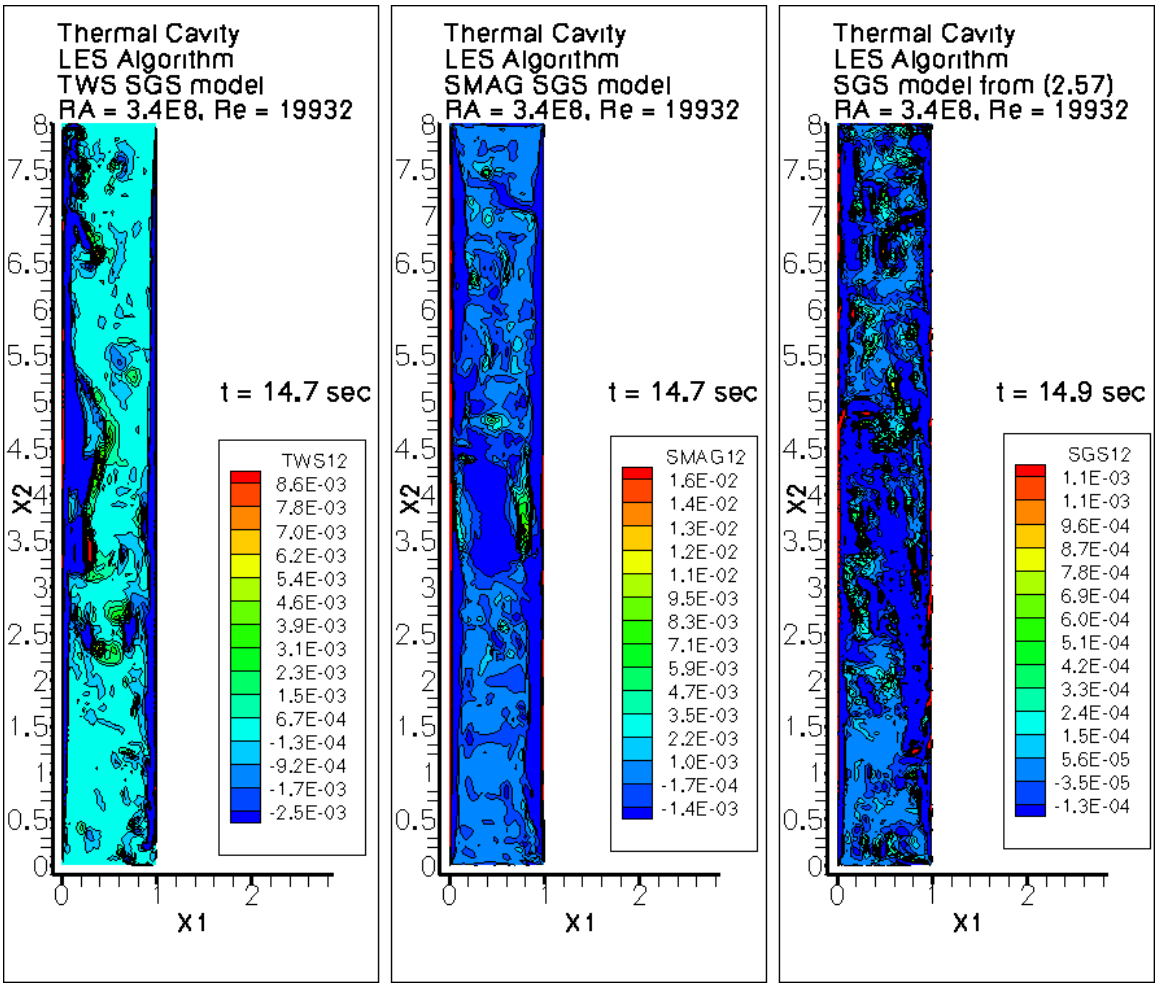

Figure 5.3.5.11 Comparison of driving SGS shear stress distribution at t = 14.7 sec for turbulent flow LES algorithm computations using the TWS, Smagorinsky and SGS model based on (2.57), Ra = 3.4xE8, Re = 19932

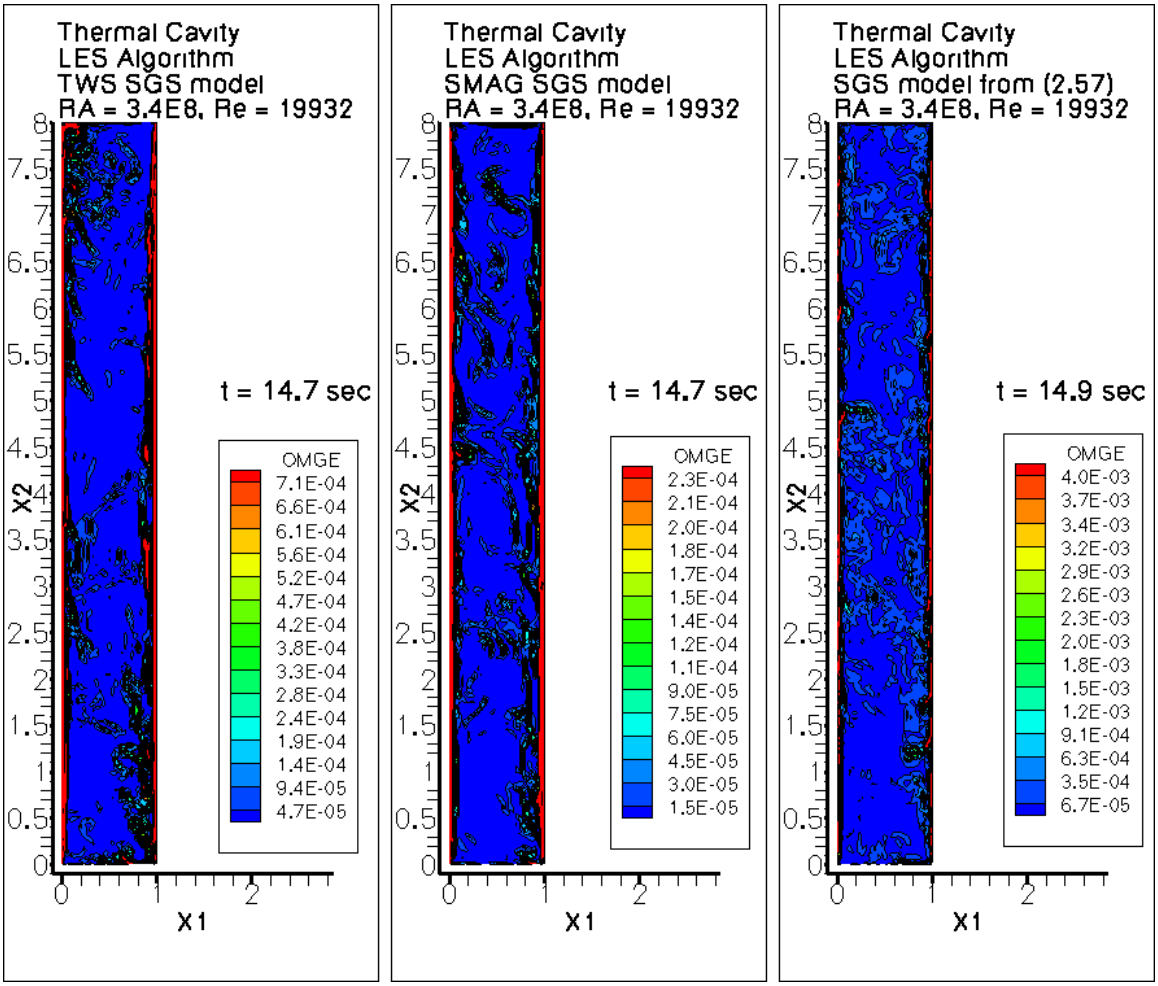

Figure 5.3.5.12 Comparison of temperature energy norm distribution at t = 14.7 sec for turbulent flow LES algorithm computations using the TWS, Smagorinsky and SGS model based on (2.57), Ra = 3.4xE8, Re = 19932

Code template

```
##### **** temp.les **** {PRES} {U1 U2 TEMP PHI} {FLUXES} {OMGA} {PSI}
{NORMS}
INTEGRATION FACTORS
   INITIAL_TIME
   FINAL_TIME
   PROBLEM_CONVERGENCE_CRITERIA
   MAXIMUM_CHANGE_IN_Q_(DQ)
   INITIAL_TIME_STEP
   TIME_STEP_MULTIPLIER
   MAXIMUM_TIME_STEP
   CRITERIA_TO_RAISE_MAX_TIME_STEP
   MAXIMUM_NUMBER_OF_STEPS
   MAXIMUM_NUMBER_OF_ITERATIONS_PER_STEP
   ITERATION_CONVERGENCE_CRITERIA
   THETA_IMPLICITNESS_FACTOR
   CONVERGENCE_VARIABLE

TRANSFORMATION ARRAYS
      ETKJ      1.
      DETJ      1
#      DETE      0.

BOUNDARY CONDITIONS
          U1 U2 TEMP PHI PRES OMGA PSI    # ORDER
  FLUX     3  0  0  0  0  0  0     # CONVECTION HEAT FLUX
  HFLUX    4  0  0  0  0  0  0     # HEAT FLUX
  RFLUX    5  0  0  0  0  0  0     # RADIATION HEAT FLUX
  HRFLX    6  0  0  0  0  0  0     # RADIATION HEAT FLUX
  INLT_P   3  0  0  0  0  0  0     # INLET
  WALL_SL  4  0  0  0  0  0  0     # SLIP WALL
  DIRI_U   D  0  0  0  0  0  0     # DIRICHLET U
  DIRI_V   0  D  0  0  0  0  0     # DIRICHLET V
  WALL_NS  D  D  0  0  0  0  D     # NO SLIP WALL
  DIRI_T   0  0  D  0  0  0  0     # WALL TEMPERATURE
  DIRI_PHI 0  0  0  D  0  0  0     # THROUGHFLOW PHI
  DIRI_P   0  0  0  0  D  0  0     # THROUGHFLOW PRESSURE
  DIRI_OMG 0  0  0  0  0  D  0     # DIRICHLET OMGA
  DIRI_PSI 0  0  0  0  0  0  D     # DIRICHLET PSI
  BLANK    D  D  D  D  D  D  D     # BLANK REGION

TITLE
   PHI ALGORITHM,  DELSQ PRESSURE SOLVE

RESIDUALS
  PRES   2   #  VARBL, SET NO.,  --- SPATIAL  SET (PRES)
 ()(U1)(EPMN)(11;-1)(B3011)(U1)
+()(U2)(EPMN)(12;-1)(B3011)(U1)
+()(U1)(EPMN)(21;-1)(B3011)(U2)
+()(U2)(EPMN)(22;-1)(B3011)(U2)
+()(U1)(EPMN)(13;-1)(B3012)(U1)
+()(U2)(EPMN)(14;-1)(B3012)(U1)
```

```
+()(U1)(EPMN)(23;-1)(B3012)(U2)
+()(U2)(EPMN)(24;-1)(B3012)(U2)
+()(U1)(EPMN)(31;-1)(B3021)(U1)
+()(U2)(EPMN)(32;-1)(B3021)(U1)
+()(U1)(EPMN)(41;-1)(B3021)(U2)
+()(U2)(EPMN)(42;-1)(B3021)(U2)
+()(U1)(EPMN)(33;-1)(B3022)(U1)
+()(U2)(EPMN)(34;-1)(B3022)(U1)
+()(U1)(EPMN)(43;-1)(B3022)(U2)
+()(U2)(EPMN)(44;-1)(B3022)(U2)
+(-)()()(11;-1)(B211)(FB11)
+(-)()()(13;-1)(B212)(FB11)
+(-)()()(31;-1)(B221)(FB11)
+(-)()()(33;-1)(B222)(FB11)
+(-)()()(12;-1)(B211)(FB12)
+(-)()()(14;-1)(B212)(FB12)
+(-)()()(32;-1)(B221)(FB12)
+(-)()()(34;-1)(B222)(FB12)
+(-)()()(21;-1)(B211)(FB12)
+(-)()()(23;-1)(B212)(FB12)
+(-)()()(41;-1)(B221)(FB12)
+(-)()()(43;-1)(B222)(FB12)
+(-)()()(22;-1)(B211)(FB22)
+(-)()()(24;-1)(B212)(FB22)
+(-)()()(42;-1)(B221)(FB22)
+(-)()()(44;-1)(B222)(FB22)
+(-,FLAG1)()()(11;-1)(B211)(FF11)
+(-,FLAG1)()()(13;-1)(B212)(FF11)
+(-,FLAG1)()()(31;-1)(B221)(FF11)
+(-,FLAG1)()()(33;-1)(B222)(FF11)
+(-,FLAG1)()()(12;-1)(B211)(FF12)
+(-,FLAG1)()()(14;-1)(B212)(FF12)
+(-,FLAG1)()()(32;-1)(B221)(FF12)
+(-,FLAG1)()()(34;-1)(B222)(FF12)
+(-,FLAG1)()()(21;-1)(B211)(FF12)
+(-,FLAG1)()()(23;-1)(B212)(FF12)
+(-,FLAG1)()()(41;-1)(B221)(FF12)
+(-,FLAG1)()()(43;-1)(B222)(FF12)
+(-,FLAG1)()()(22;-1)(B211)(FF22)
+(-,FLAG1)()()(24;-1)(B212)(FF22)
+(-,FLAG1)()()(42;-1)(B221)(FF22)
+(-,FLAG1)()()(44;-1)(B222)(FF22)
+(-,GRSH,RE2I)()()(2;0)(B210)(TEMP)
+(-,GRSH,RE2I)()()(4;0)(B220)(TEMP)
  PRES   6   #  VARBL, SET NO.,  --- BOUNDARY  SET (PRES)
 (REI)()(EPMN,RET)(0;-1)(A3011)(U1)
#()(U1)(EPMN)(11;-1)(B3011R)(U1)
  PRES   7   #  VARBL, SET NO.,  --- BOUNDARY  SET (PRES)
 (-,REI)()(EPMN,RET)(0;-1)(A3011)(U1)
  PRES   8   #  VARBL, SET NO.,  --- BOUNDARY  SET (PRES)
 (TWO,REI)()(EPMN,RET)(0;0)(A3001)(U1)
  PRES   9   #  VARBL, SET NO.,  --- BOUNDARY  SET (PRES)
 (-,TWO,REI)()(EPMN,RET)(0;0)(A3001)(U1)

JACOBIANS
```

```
  PRES PRES  2  1  #  VARBL, VARDIF, SET, ALL DIRECTIONS
 ()()(EPMN)(1122;-1)(B3011)()
+()()(EPMN)(3344;-1)(B3022)()
+()()(EPMN)(1324;-1)(B3021)()
+()()(EPMN)(1324;-1)(B3012)()

GROUP FREQUENCY
     -1
SOLUTION TYPE
  Q
  ILU_GMRES
  IMPLICIT_EULER
END

TITLE
     PHI CONSTRAINT INS GWS ALGORITHM, 2D, FULL NEWTON JACOBIAN
(12/21/99)

RESIDUALS
  U1   1    #  VARBL, SET NO.,  --- TEMPORAL SET (U1)
 ()()()(0;1)(B200)(-U1)
+()()()(1;0)(B201)(PHI)
+()()()(3;0)(B202)(PHI)
+()()()(1;0)(B201)(SPHI)
+()()()(3;0)(B202)(SPHI)
  U1   2    #  VARBL, SET NO.,  --- SPATIAL  SET (U1)
 ()()(U1+U2)(1020;0)(B3001)(U1)
+()()(U1+U2)(3040;0)(B3002)(U1)
+()()()(1;0)(B201)(PRES)
+()()()(3;0)(B202)(PRES)
+(REI)()()(1122;-1)(B211)(U1)
+(REI)()()(3344;-1)(B222)(U1)
+(REI)()()(1324;-1)(B221)(U1)
+(REI)()()(1324;-1)(B212)(U1)
+(-)()()(1;0)(B201)(FB11)
+(-)()()(3;0)(B202)(FB11)
+(-)()()(2;0)(B201)(FB12)
+(-)()()(4;0)(B202)(FB12)
#+(-)()()(1;0)(B201)(FS11)
#+(-)()()(3;0)(B202)(FS11)
#+(-)()()(2;0)(B201)(FS12)
#+(-)()()(4;0)(B202)(FS12)
#+(-)()()(1;0)(B201)(FL11)
#+(-)()()(3;0)(B202)(FL11)
#+(-)()()(2;0)(B201)(FL12)
#+(-)()()(4;0)(B202)(FL12)
#+(-)()()(1;0)(B201)(FI11)
#+(-)()()(3;0)(B202)(FI11)
#+(-)()()(2;0)(B201)(FI12)
#+(-)()()(4;0)(B202)(FI12)
+(-,FLAG1)()()(1;0)(B201)(FF11)
+(-,FLAG1)()()(3;0)(B202)(FF11)
+(-,FLAG1)()()(2;0)(B201)(FF12)
+(-,FLAG1)()()(4;0)(B202)(FF12)
+(BETA,HT)()(U1,U1)(11;-1.0)(B3011)(U1)
```

```
+(BETA,HT)()(U1,U2)(12;-1.0)(B3011)(U1)
+(BETA,HT)()(U1,U2)(21;-1.0)(B3011)(U1)
+(BETA,HT)()(U2,U2)(22;-1.0)(B3011)(U1)
+(BETA,HT)()(U1,U1)(13;-1.0)(B3012)(U1)
+(BETA,HT)()(U1,U2)(14;-1.0)(B3012)(U1)
+(BETA,HT)()(U1,U2)(23;-1.0)(B3012)(U1)
+(BETA,HT)()(U2,U2)(24;-1.0)(B3012)(U1)
+(BETA,HT)()(U1,U1)(31;-1.0)(B3021)(U1)
+(BETA,HT)()(U1,U2)(32;-1.0)(B3021)(U1)
+(BETA,HT)()(U1,U2)(41;-1.0)(B3021)(U1)
+(BETA,HT)()(U2,U2)(42;-1.0)(B3021)(U1)
+(BETA,HT)()(U1,U1)(33;-1.0)(B3022)(U1)
+(BETA,HT)()(U1,U2)(34;-1.0)(B3022)(U1)
+(BETA,HT)()(U1,U2)(43;-1.0)(B3022)(U1)
+(BETA,HT)()(U2,U2)(44;-1.0)(B3022)(U1)

  U2   1    #  VARBL, SET NO.,  --- TEMPORAL SET (U2)
 ()()()(0;1)(B200)(-U2)
+()()()(2;0)(B201)(PHI)
+()()()(4;0)(B202)(PHI)
+()()()(2;0)(B201)(SPHI)
+()()()(4;0)(B202)(SPHI)
  U2   2   #  VARBL, SET NO.,  --- SPATIAL  SET (U2)
 ()()(U1+U2)(1020;0)(B3001)(U2)
+()()(U1+U2)(3040;0)(B3002)(U2)
+()()()(2;0)(B201)(PRES)
+()()()(4;0)(B202)(PRES)
+(REI)()()(1122;-1)(B211)(U2)
+(REI)()()(3344;-1)(B222)(U2)
+(REI)()()(1324;-1)(B221)(U2)
+(REI)()()(1324;-1)(B212)(U2)
+(-)()()(1;0)(B201)(FB12)
+(-)()()(3;0)(B202)(FB12)
+(-)()()(2;0)(B201)(FB22)
+(-)()()(4;0)(B202)(FB22)
#+(-)()()(1;0)(B201)(FS12)
#+(-)()()(3;0)(B202)(FS12)
#+(-)()()(2;0)(B201)(FS22)
#+(-)()()(4;0)(B202)(FS22)
#+(-)()()(1;0)(B201)(FL12)
#+(-)()()(3;0)(B202)(FL12)
#+(-)()()(2;0)(B201)(FL22)
#+(-)()()(4;0)(B202)(FL22)
#+(-)()()(1;0)(B201)(FI12)
#+(-)()()(3;0)(B202)(FI12)
#+(-)()()(2;0)(B201)(FI22)
#+(-)()()(4;0)(B202)(FI22)
+(-,FLAG1)()()(1;0)(B201)(FF12)
+(-,FLAG1)()()(3;0)(B202)(FF12)
+(-,FLAG1)()()(2;0)(B201)(FF22)
+(-,FLAG1)()()(4;0)(B202)(FF22)
+(BETA,HT)()(U1,U1)(11;-1.0)(B3011)(U2)
+(BETA,HT)()(U1,U2)(12;-1.0)(B3011)(U2)
+(BETA,HT)()(U1,U2)(21;-1.0)(B3011)(U2)
+(BETA,HT)()(U2,U2)(22;-1.0)(B3011)(U2)
```

```
+(BETA,HT)()(U1,U1)(13;-1.0)(B3012)(U2)
+(BETA,HT)()(U1,U2)(14;-1.0)(B3012)(U2)
+(BETA,HT)()(U1,U2)(23;-1.0)(B3012)(U2)
+(BETA,HT)()(U2,U2)(24;-1.0)(B3012)(U2)
+(BETA,HT)()(U1,U1)(31;-1.0)(B3021)(U2)
+(BETA,HT)()(U1,U2)(32;-1.0)(B3021)(U2)
+(BETA,HT)()(U1,U2)(41;-1.0)(B3021)(U2)
+(BETA,HT)()(U2,U2)(42;-1.0)(B3021)(U2)
+(BETA,HT)()(U1,U1)(33;-1.0)(B3022)(U2)
+(BETA,HT)()(U1,U2)(34;-1.0)(B3022)(U2)
+(BETA,HT)()(U1,U2)(43;-1.0)(B3022)(U2)
+(BETA,HT)()(U2,U2)(44;-1.0)(B3022)(U2)
+(-,GRSH,RE2I)()()(0;1)(B200)(TEMP)

  TEMP   1    #  VARBL, SET NO.,  --- TEMPORAL SET (TEMP)
 ()()()(0;1)(B200)(-TEMP)
  TEMP   2   #  VARBL, SET NO.,  --- SPATIAL  SET (TEMP)
 ()()(U1+U2)(1020;0)(B3001)(TEMP)
+()()(U1+U2)(3040;0)(B3002)(TEMP)
+(PEI)()()(1122;-1)(B211)(TEMP)
+(PEI)()()(3344;-1)(B222)(TEMP)
+(PEI)()()(1324;-1)(B221)(TEMP)
+(PEI)()()(1324;-1)(B212)(TEMP)
#+(-)()()(0;1)(B200)(SRCT)
+(-)()()(1;0)(B201)(TB1)
+(-)()()(3;0)(B202)(TB1)
+(-)()()(2;0)(B201)(TB2)
+(-)()()(4;0)(B202)(TB2)
+(-,FLAG1)()()(1;0)(B201)(TF1)
+(-,FLAG1)()()(3;0)(B202)(TF1)
+(-,FLAG1)()()(2;0)(B201)(TF2)
+(-,FLAG1)()()(4;0)(B202)(TF2)
+(BETAT,HT)()(U1,U1)(11;-1.0)(B3011)(TEMP)
+(BETAT,HT)()(U1,U2)(12;-1.0)(B3011)(TEMP)
+(BETAT,HT)()(U1,U2)(21;-1.0)(B3011)(TEMP)
+(BETAT,HT)()(U2,U2)(22;-1.0)(B3011)(TEMP)
+(BETAT,HT)()(U1,U1)(13;-1.0)(B3012)(TEMP)
+(BETAT,HT)()(U1,U2)(14;-1.0)(B3012)(TEMP)
+(BETAT,HT)()(U1,U2)(23;-1.0)(B3012)(TEMP)
+(BETAT,HT)()(U2,U2)(24;-1.0)(B3012)(TEMP)
+(BETAT,HT)()(U1,U1)(31;-1.0)(B3021)(TEMP)
+(BETAT,HT)()(U1,U2)(32;-1.0)(B3021)(TEMP)
+(BETAT,HT)()(U1,U2)(41;-1.0)(B3021)(TEMP)
+(BETAT,HT)()(U2,U2)(42;-1.0)(B3021)(TEMP)
+(BETAT,HT)()(U1,U1)(33;-1.0)(B3022)(TEMP)
+(BETAT,HT)()(U1,U2)(34;-1.0)(B3022)(TEMP)
+(BETAT,HT)()(U1,U2)(43;-1.0)(B3022)(TEMP)
+(BETAT,HT)()(U2,U2)(44;-1.0)(B3022)(TEMP)
  TEMP   3   #  VARBL, SET NO.,  --- BOUNDARY SET (TEMP)
 ()(NUSL)()(0;1)(A200)(TEMP)
+(-)(NUSL)()(0;1)(A200)(TRBC)
  TEMP   5   #  VARBL, SET NO.,  --- BOUNDARY SET (TEMP)
 ()()()(0;1)(A200)(SRCT)

  PHI   1     #  VARBL, SET NO.,  --- SPATIAL  SET (PHI)
```

```
 ()()(EPMN)(1;0)(B3001)(U1)
+()()(EPMN)(3;0)(B3002)(U1)
+()()(EPMN)(2;0)(B3001)(U2)
+()()(EPMN)(4;0)(B3002)(U2)
+()()(EPMN)(1122;-1)(B3011)(PHI)
+()()(EPMN)(3344;-1)(B3022)(PHI)
+()()(EPMN)(1324;-1)(B3021)(PHI)
+()()(EPMN)(1324;-1)(B3012)(PHI)

  PHI   3  #  VARBL, SET NO.,-- BOUNDARY SET (PHI)
 (-)()()(1;0)(A200)(U1)
+()()()(2;0)(A200)(U2)

JACOBIANS
  U1  U1  1  1  #  VARBL, VARDIF, SET, DIRECTION 1
 ()()()(;1)(B200)()
  U1  U1  2  1  #  VARBL, VARDIF, SET, DIRECTION 1
+()()(U1+U2)(1020;0)(B3001)()
+()()(U1+U2)(3040;0)(B3002)()
+()()(U1)(1;0)(B3100)()
+()()(U1)(3;0)(B3200)()
+(REI)()()(1122;-1)(B211)()
+(REI)()()(1324;-1)(B212)()
+(REI)()()(1324;-1)(B221)()
+(REI)()()(3344;-1)(B222)()
+(BETA,HT)()(U1,U1)(11;-1.0)(B3011)()
+(BETA,HT)()(U1,U2)(12;-1.0)(B3011)()
+(BETA,HT)()(U1,U2)(21;-1.0)(B3011)()
+(BETA,HT)()(U2,U2)(22;-1.0)(B3011)()
+(BETA,HT)()(U1,U1)(13;-1.0)(B3012)()
+(BETA,HT)()(U1,U2)(14;-1.0)(B3012)()
+(BETA,HT)()(U1,U2)(23;-1.0)(B3012)()
+(BETA,HT)()(U2,U2)(24;-1.0)(B3012)()
+(BETA,HT)()(U1,U1)(31;-1.0)(B3021)()
+(BETA,HT)()(U1,U2)(32;-1.0)(B3021)()
+(BETA,HT)()(U1,U2)(41;-1.0)(B3021)()
+(BETA,HT)()(U2,U2)(42;-1.0)(B3021)()
+(BETA,HT)()(U1,U1)(33;-1.0)(B3022)()
+(BETA,HT)()(U1,U2)(34;-1.0)(B3022)()
+(BETA,HT)()(U1,U2)(43;-1.0)(B3022)()
+(BETA,HT)()(U2,U2)(44;-1.0)(B3022)()

  U1  U2  2  1  #
 ()()(U1)(2;0)(B3100)()
+()()(U1)(4;0)(B3200)()

   U1  PHI 1 1 #
 ()()()(1;0)(B201)()
+()()()(3;0)(B202)()

  U2  U1  2  1  #
 ()()(U2)(1;0)(B3100)()
+()()(U2)(3;0)(B3200)()

  U2  U2  1  1  #
```

```
 ()()()(;1)(B200)()
  U2  U2  2  1  #
+()()(U1+U2)(1020;0)(B3001)()
+()()(U1+U2)(3040;0)(B3002)()
+()()(U2)(2;0)(B3100)()
+()()(U2)(4;0)(B3200)()
+(REI)()()(1122;-1)(B211)()
+(REI)()()(1324;-1)(B212)()
+(REI)()()(1324;-1)(B221)()
+(REI)()()(3344;-1)(B222)()
+(BETA,HT)()(U1,U1)(11;-1.0)(B3011)()
+(BETA,HT)()(U1,U2)(12;-1.0)(B3011)()
+(BETA,HT)()(U1,U2)(21;-1.0)(B3011)()
+(BETA,HT)()(U2,U2)(22;-1.0)(B3011)()
+(BETA,HT)()(U1,U1)(13;-1.0)(B3012)()
+(BETA,HT)()(U1,U2)(14;-1.0)(B3012)()
+(BETA,HT)()(U1,U2)(23;-1.0)(B3012)()
+(BETA,HT)()(U2,U2)(24;-1.0)(B3012)()
+(BETA,HT)()(U1,U1)(31;-1.0)(B3021)()
+(BETA,HT)()(U1,U2)(32;-1.0)(B3021)()
+(BETA,HT)()(U1,U2)(41;-1.0)(B3021)()
+(BETA,HT)()(U2,U2)(42;-1.0)(B3021)()
+(BETA,HT)()(U1,U1)(33;-1.0)(B3022)()
+(BETA,HT)()(U1,U2)(34;-1.0)(B3022)()
+(BETA,HT)()(U1,U2)(43;-1.0)(B3022)()
+(BETA,HT)()(U2,U2)(44;-1.0)(B3022)()

  U2 TEMP 2  1 #
+(-,GRSH,RE2I)()()(;1)(B200)()

   U2  PHI  1 1 #
 ()()()(2;0)(B201)()
+()()()(4;0)(B202)()

 TEMP U1 2 1 #
()()(TEMP)(1;0)(B3100)()+()()(TEMP)(3;0)(B3200)()

 TEMP U2 2 1 #
()()(TEMP)(2;0)(B3100)()+()()(TEMP)(4;0)(B3200)()

  TEMP TEMP 1  1     #
 ()()()(0;1)(B200)()
  TEMP TEMP 2  1    #
+()()(U1+U2)(1020;0)(B3001)()
+()()(U1+U2)(3040;0)(B3002)()
+(PEI)()()(1122;-1)(B3011)()
+(PEI)()()(3344;-1)(B3022)()
+(PEI)()()(1324;-1)(B3021)()
+(PEI)()()(1324;-1)(B3012)()
+(BETAT,HT)()(U1,U1)(11;-1.0)(B3011)()
+(BETAT,HT)()(U1,U2)(12;-1.0)(B3011)()
+(BETAT,HT)()(U1,U2)(21;-1.0)(B3011)()
+(BETAT,HT)()(U2,U2)(22;-1.0)(B3011)()
+(BETAT,HT)()(U1,U1)(13;-1.0)(B3012)()
+(BETAT,HT)()(U1,U2)(14;-1.0)(B3012)()
```

```
+(BETAT,HT)()(U1,U2)(23;-1.0)(B3012)()
+(BETAT,HT)()(U2,U2)(24;-1.0)(B3012)()
+(BETAT,HT)()(U1,U1)(31;-1.0)(B3021)()
+(BETAT,HT)()(U1,U2)(32;-1.0)(B3021)()
+(BETAT,HT)()(U1,U2)(41;-1.0)(B3021)()
+(BETAT,HT)()(U2,U2)(42;-1.0)(B3021)()
+(BETAT,HT)()(U1,U1)(33;-1.0)(B3022)()
+(BETAT,HT)()(U1,U2)(34;-1.0)(B3022)()
+(BETAT,HT)()(U1,U2)(43;-1.0)(B3022)()
+(BETAT,HT)()(U2,U2)(44;-1.0)(B3022)()
 TEMP TEMP 3  1 #
 ()(NUSL)()(0;1)(A200)()

  PHI U1  1 1 #
 ()()(EPMN)(1;0)(B3001)()
+()()(EPMN)(3;0)(B3002)()
  PHI U1  3 1 #
 (-)()()(1;0)(A200)()

  PHI U2 1 1 #
 ()()(EPMN)(2;0)(B3001)()
+()()(EPMN)(4;0)(B3002)()
  PHI U2 3 1 #
 ()()()(2;0)(A200)()

  PHI PHI  1  1  #  VARBL, VARDIF, SET, ALL DIRECTIONS
 ()()(EPMN)(1122;-1)(B3011)()
+()()(EPMN)(3344;-1)(B3022)()
+()()(EPMN)(1324;-1)(B3021)()
+()()(EPMN)(1324;-1)(B3012)()

GROUP FREQUENCY
      1
SOLUTION TYPE
  DELTA_Q
  ILU_GMRES
  IMPLICIT_EULER
END

TITLE            **** TEMPLATE FILE Sij ****
  2-D  PHI ALGORITHM  Strain Tensor  (12/05)

RESIDUALS
  S11  2  # LOAD SET -{B} FOR S11
+(-)()()(1;0)(B201)(U1)
+(-)()()(3;0)(B202)(U1)

  S12  2  # LOAD SET -{B} FOR S12
+(-,HALF)()()(2;0)(B201)(U1)
+(-,HALF)()()(4;0)(B202)(U1)
+(-,HALF)()()(1;0)(B201)(U2)
+(-,HALF)()()(3;0)(B202)(U2)

  S22  2  # LOAD SET -{B} FOR S22
+(-)()()(2;0)(B201)(U2)
```

```
+(-)()()(4;0)(B202)(U2)

JACOBIANS
  S11  S11  2  1  # S11: D(S11)/D(S11)
 ()()()(0;1)(B200)()

  S12  S12  2  1  # S12: D(S12)/D(S12)
 ()()()(0;1)(B200)()

  S22  S22  2  1  # S22: D(S22)/D(S22)
 ()()()(0;1)(B200)()

GROUP FREQUENCY
    1
SOLUTION TYPE
  Q
  ILU_GMRES
  IMPLICIT_EULER
END

TITLE            **** TEMPLATE FILE S33 and S44 ****
  2-D  PHI ALGORITHM  laplacian of U  (12/05)

RESIDUALS
  S33  2  # LOAD SET -{B} FOR S33
+(-)()()(1122;-1)(B211)(U1)
+(-)()()(1324;-1)(B212)(U1)
+(-)()()(3142;-1)(B221)(U1)
+(-)()()(3344;-1)(B222)(U1)

  S44  2  # LOAD SET -{B} FOR S44
+(-)()()(1122;-1)(B211)(U2)
+(-)()()(1323;-1)(B212)(U2)
+(-)()()(3142;-1)(B221)(U2)
+(-)()()(3344;-1)(B222)(U2)

JACOBIANS
  S33  S33  2  1  # S33: D(S33)/D(S33)
+()()()(0;1)(B200)()

  S44  S44  2  1  # RMU_2: D(S44)/D(S44)
+()()()(0;1)(B200)()

GROUP FREQUENCY
    1
SOLUTION TYPE
  Q
  ILU_GMRES
  IMPLICIT_EULER
END

TITLE            **** TEMPLATE FILE FFij ****
  2-D  PHI ALGORITHM   inverse operator on velocity for Layton 2
(12/05)
```

```
RESIDUALS
  XB1  2  # LOAD SET -{B} FOR XB_1
+(-)()()(0;1)(B200)(U1)

  XB2  2  # LOAD SET -{B} FOR XB_2
+(-)()()(0;1)(B200)(U2)

JACOBIANS
  XB1  XB1  2  1  # XB_1: D(XB_1)/D(XB_1)
+()()()(0;1)(B200)()
+(SIXTH)()()(1122;0)(B211)()
+(SIXTH)()()(1324;0)(B212)()
+(SIXTH)()()(3142;0)(B221)()
+(SIXTH)()()(3344;0)(B222)()

  XB2  XB2  2  1  # XB_2: D(XB_2)/D(XB_2)
+()()()(0;1)(B200)()
+(SIXTH)()()(1122;0)(B211)()
+(SIXTH)()()(1324;0)(B212)()
+(SIXTH)()()(3142;0)(B221)()
+(SIXTH)()()(3344;0)(B222)()

GROUP FREQUENCY
    1
SOLUTION TYPE
  Q
  ILU_GMRES
  IMPLICIT_EULER
END

TITLE            **** TEMPLATE FILE RETS ****
  2-D  PHI ALGORITHM  turb. Reynolds number, Smagorinsky SGS  (12/05)

RESIDUALS
  RETS  2  # LOAD SET -{B} FOR RETS
+(-,MULS)()()(0;2)(B200)(SSQ)

JACOBIANS
  RETS  RETS  2  1  # RETS: D(RETS)/D(RETS)
+()()()(0;1)(B200)()

GROUP FREQUENCY
    1
SOLUTION TYPE
  Q
  ILU_GMRES
  IMPLICIT_EULER
END

TITLE            **** TEMPLATE FILE RETA ****
  2-D  PHI ALGORITHM  turb. Reynolds number, Layton 1 SGS  (12/05)

RESIDUALS
  RETA  2  # LOAD SET -{B} FOR RETA
+(-,MULA)()()(0;2.5)(B200)(SSQ2)
```

```
JACOBIANS
  RETA  RETA  2  1  # RETA: D(RETA)/D(RETA)
+()()()(0;1)(B200)()

GROUP FREQUENCY
    1
SOLUTION TYPE
  Q
  ILU_GMRES
  IMPLICIT_EULER
END

TITLE            **** TEMPLATE FILE RETB ****
  2-D  PHI ALGORITHM  turb. Reynolds number, Layton 2 SGS  (12/05)

RESIDUALS
  RETB  2  # LOAD SET -{B} FOR RETB
+(-,MULB)()()(0;1.5)(B200)(SBQ2)

JACOBIANS
  RETB  RETB  2  1  # RETB: D(RETB)/D(RETB)
+()()()(0;1)(B200)()

GROUP FREQUENCY
    1
SOLUTION TYPE
  Q
  ILU_GMRES
  IMPLICIT_EULER
END

TITLE            **** TEMPLATE FILE RSij ****
  2-D  PHI ALGORITHM  rational LES Reynolds stress tensor  (12/05)

RESIDUALS
  RS11  2  # LOAD SET -{B} FOR RS_11
+(-)()(U1)(1122;-1)(B3101)(U1)
+(-)()(U1)(1324;-1)(B3102)(U1)
+(-)()(U1)(3142;-1)(B3201)(U1)
+(-)()(U1)(3344;-1)(B3202)(U1)

  RS12  2  # LOAD SET -{B} FOR RS_12
+(-)()(U1)(1122;-1)(B3101)(U2)
+(-)()(U1)(1323;-1)(B3102)(U2)
+(-)()(U1)(3142;-1)(B3201)(U2)
+(-)()(U1)(3344;-1)(B3202)(U2)

  RS22  2  # LOAD SET -{B} FOR RS_22
+(-)()(U2)(1122;-1)(B3101)(U2)
+(-)()(U2)(1324;-1)(B3102)(U2)
+(-)()(U2)(3142;-1)(B3201)(U2)
+(-)()(U2)(3344;-1)(B3202)(U2)

JACOBIANS
```

```
  RS11  RS11  2  1  # RS_11: D(RS_11)/D(RS_11)
+()()()(0;1)(B200)()
+(SIXTH,CF2)()()(1122;0)(B211)()
+(SIXTH,CF2)()()(1324;0)(B212)()
+(SIXTH,CF2)()()(3142;0)(B221)()
+(SIXTH,CF2)()()(3344;0)(B222)()

  RS12  RS12  2  1  # RS_12: D(RS_12)/D(RS_12)
+()()()(0;1)(B200)()
+(SIXTH,CF2)()()(1122;0)(B211)()
+(SIXTH,CF2)()()(1324;0)(B212)()
+(SIXTH,CF2)()()(3142;0)(B221)()
+(SIXTH,CF2)()()(3344;0)(B222)()

  RS22  RS22  2  1  # RS_22: D(RS_22)/D(RS_22)
+()()()(0;1)(B200)()
+(SIXTH,CF2)()()(1122;0)(B211)()
+(SIXTH,CF2)()()(1324;0)(B212)()
+(SIXTH,CF2)()()(3142;0)(B221)()
+(SIXTH,CF2)()()(3344;0)(B222)()

GROUP FREQUENCY
    1
SOLUTION TYPE
  Q
  ILU_GMRES
  IMPLICIT_EULER
END

TITLE            **** TEMPLATE FILE FFij ****
  2-D  PHI ALGORITHM  mom. equation, rational LES  filter flux  (12/05)

RESIDUALS
  FF11  2  # LOAD SET -{B} FOR FF11
+(THIRD,CF2)()()(0;2)(B200)(RS11)

  FF12  2  # LOAD SET -{B} FOR FF12
+(THIRD,CF2)()()(0;2)(B200)(RS12)

  FF22  2  # LOAD SET -{B} FOR FF22
+(THIRD,CF2)()()(0;2)(B200)(RS22)

JACOBIANS
  FF11  FF11  2  1  # FF11: D(FF11)/D(FF11)
 ()()()(0;1)(B200)()

  FF12  FF12  2  1  # FF12: D(FF12)/D(FF12)
 ()()()(0;1)(B200)()

  FF22  FF22  2  1  # FF22: D(FF22)/D(FF22)
 ()()()(0;1)(B200)()

GROUP FREQUENCY
    1
SOLUTION TYPE
```

```
  Q
  ILU_GMRES
  IMPLICIT_EULER
END

TITLE            **** TEMPLATE FILE FBij ****
  2-D  PHI ALGORITHM   mom. equ. beta SGS tensor (12/05)

RESIDUALS
  FB11  2  # LOAD SET -{B} FOR FB_11
+(-,FAMUL,RENO)()(U1,U1)(0;2)(B3000)(S11)
+(-,FAMUL,RENO)()(U1,U2)(0;2)(B3000)(S12)
+(-,FAMUL,RENO)()(U1,U1)(0;2)(B3000)(S11)
+(-,FAMUL,RENO)()(U1,U2)(0;2)(B3000)(S12)

  FB12  2  # LOAD SET -{B} FOR FB_12
+(-,FAMUL,RENO)()(U2,U1)(0;2)(B3000)(S11)
+(-,FAMUL,RENO)()(U2,U2)(0;2)(B3000)(S12)
+(-,FAMUL,RENO)()(U1,U1)(0;2)(B3000)(S12)
+(-,FAMUL,RENO)()(U1,U2)(0;2)(B3000)(S22)

  FB21  2  # LOAD SET -{B} FOR FB_21
+(-,FAMUL,RENO)()(U1,U1)(0;2)(B3000)(S12)
+(-,FAMUL,RENO)()(U1,U2)(0;2)(B3000)(S22)
+(-,FAMUL,RENO)()(U2,U1)(0;2)(B3000)(S11)
+(-,FAMUL,RENO)()(U2,U2)(0;2)(B3000)(S12)

  FB22  2  # LOAD SET -{B} FOR FB_22
+(-,FAMUL,RENO)()(U2,U1)(0;2)(B3000)(S12)
+(-,FAMUL,RENO)()(U2,U2)(0;2)(B3000)(S22)
+(-,FAMUL,RENO)()(U2,U1)(0;2)(B3000)(S12)
+(-,FAMUL,RENO)()(U2,U2)(0;2)(B3000)(S22)

JACOBIANS
  FB11  FB11  2  1  # FB_11: D(FB_11)/D(FB_11)
 ()()()(0;1)(B200)()

  FB21  FB21  2  1  # FB_21: D(FB_21)/D(FB_21)
 ()()()(0;1)(B200)()

  FB12  FB12  2  1  # FB_12: D(FB_12)/D(FB_12)
 ()()()(0;1)(B200)()

  FB22  FB22  2  1  # FB_22: D(FB_22)/D(FB_22)
 ()()()(0;1)(B200)()

GROUP FREQUENCY
    1
SOLUTION TYPE
  Q
  ILU_GMRES
  IMPLICIT_EULER
END

TITLE            **** TEMPLATE FILE FDij ****
```

```
  2-D  PHI ALGORITHM  mom. equation laminar stress tensor (12/05)

RESIDUALS
  FD11  2  # LOAD SET -{B} FOR FD11
+(-,TWO,REI)()()(1;0)(B201)(U1)
+(-,TWO,REI)()()(3;0)(B202)(U1)

  FD12  2  # LOAD SET -{B} FOR FD12
+(-,REI)()()(2;0)(B201)(U1)
+(-,REI)()()(4;0)(B202)(U1)
+(-,REI)()()(1;0)(B201)(U2)
+(-,REI)()()(3;0)(B202)(U2)

  FD22  2  # LOAD SET -{B} FOR FD22
+(-,TWO,REI)()()(2;0)(B201)(U2)
+(-,TWO,REI)()()(4;0)(B202)(U2)

JACOBIANS
  FD11  FD11  2  1  # FD11: D(FD11)/D(FD11)
 ()()()(0;1)(B200)()

  FD12  FD12  2  1  # FD12: D(FD12)/D(FD12)
 ()()()(0;1)(B200)()

  FD22  FD22  2  1  # FD22: D(FD22)/D(FD22)
 ()()()(0;1)(B200)()

GROUP FREQUENCY
    1
SOLUTION TYPE
  Q
  ILU_GMRES
  IMPLICIT_EULER
END

TITLE            **** TEMPLATE FILE FCij ****
  2-D  PHI ALGORITHM  mom. equation convective flux  (12/05)

RESIDUALS
  FC11  2  # LOAD SET -{B} FOR FC11
+(-)()(U1)(0;1)(B200)(U1)

  FC12  2  # LOAD SET -{B} FOR FC12
+(-)()(U2)(0;1)(B200)(U1)

  FC22  2  # LOAD SET -{B} FOR FC22
+(-)()(U2)(0;1)(B200)(U2)

JACOBIANS
  FC11  FC11  2  1  # FC11: D(FC11)/D(FC11)
 ()()()(0;1)(B200)()

  FC12  FC12  2  1  # FC12: D(FC12)/D(FC12)
 ()()()(0;1)(B200)()
```

```
  FC22  FC22  2  1  # FC22: D(FC22)/D(FC22)
 ()()()(0;1)(B200)()

GROUP FREQUENCY
    1
SOLUTION TYPE
  Q
  ILU_GMRES
  IMPLICIT_EULER
END

TITLE            **** TEMPLATE FILE FSij ****
  2-D  PHI ALGORITHM  Smagorinsky SGS tensor (12/05)

RESIDUALS
  FS11  2  # LOAD SET -{B} FOR FS11
+(-,REI)()(RETS)(0;1)(B200)(S11)

  FS12  2  # LOAD SET -{B} FOR FS12
+(-,REI)()(RETS)(0;1)(B200)(S12)

  FS22  2  # LOAD SET -{B} FOR FS22
+(-,REI)()(RETS)(0;1)(B200)(S22)

JACOBIANS
  FS11  FS11  2  1  # FS11: D(FS11)/D(FS11)
 ()()()(0;1)(B200)()

  FS12  FS12  2  1  # FS12: D(FS12)/D(FS12)
 ()()()(0;1)(B200)()

  FS22  FS22  2  1  # FS22: D(FS22)/D(FS22)
 ()()()(0;1)(B200)()

GROUP FREQUENCY
    1
SOLUTION TYPE
  Q
  ILU_GMRES
  IMPLICIT_EULER
END

TITLE            **** TEMPLATE FILE FLij ****
  2-D  PHI ALGORITHM  Layton 1 SGS tensor (12/05)

RESIDUALS
  FL11  2  # LOAD SET -{B} FOR FL11
+(-,REI)()(RETA)(0;1)(B200)(S11)

  FL12  2  # LOAD SET -{B} FOR FL12
+(-,REI)()(RETA)(0;1)(B200)(S12)

  FL22  2  # LOAD SET -{B} FOR FL22
+(-,REI)()(RETA)(0;1)(B200)(S22)
```

```
JACOBIANS
  FL11  FL11  2  1  # FL11: D(FL11)/D(FL11)
 ()()()(0;1)(B200)()

  FL12  FL12  2  1  # FL12: D(FL12)/D(FL12)
 ()()()(0;1)(B200)()

  FL22  FL22  2  1  # FL22: D(FL22)/D(FL22)
 ()()()(0;1)(B200)()

GROUP FREQUENCY
    1
SOLUTION TYPE
  Q
  ILU_GMRES
  IMPLICIT_EULER
END

TITLE            **** TEMPLATE FILE FIij ****
  2-D  PHI ALGORITHM  Illiescu SGS tensor  (12/05)

RESIDUALS
  FI11  2  # LOAD SET -{B} FOR FI11
+(-,REI)()(RETB)(0;1)(B200)(S11)

  FI12  2  # LOAD SET -{B} FOR FI12
+(-,REI)()(RETB)(0;1)(B200)(S12)

  FI22  2  # LOAD SET -{B} FOR FI22
+(-,REI)()(RETB)(0;1)(B200)(S22)

JACOBIANS
  FI11  FI11  2  1  # SG11: D(FI11)/D(FI11)
 ()()()(0;1)(B200)()

  FI12  FI12  2  1  # FI12: D(FI12)/D(FI12)
 ()()()(0;1)(B200)()

  FI22  FI22  2  1  # FI22: D(FI22)/D(FI22)
 ()()()(0;1)(B200)()

GROUP FREQUENCY
    1
SOLUTION TYPE
  Q
  ILU_GMRES
  IMPLICIT_EULER
END

TITLE            **** TEMPLATE FILE TBj ****
  2-D  PHI ALGORITHM   energy equation SGS vector TBj (02/06)

RESIDUALS
  TB1  2  # LOAD SET -{B} FOR TB_1
+(-,TAMUL,PE)()(U1,U1)(1;2)(B3001)(TEMP)
```

```
+(-,TAMUL,PE)()(U1,U1)(3;2)(B3002)(TEMP)
+(-,TAMUL,PE)()(U1,U2)(2;2)(B3001)(TEMP)
+(-,TAMUL,PE)()(U1,U2)(4;2)(B3002)(TEMP)

  TB2  2  # LOAD SET -{B} FOR TB_2
+(-,TAMUL,PE)()(U1,U2)(1;2)(B3001)(TEMP)
+(-,TAMUL,PE)()(U1,U2)(3;2)(B3002)(TEMP)
+(-,TAMUL,PE)()(U2,U2)(2;2)(B3001)(TEMP)
+(-,TAMUL,PE)()(U2,U2)(4;2)(B3002)(TEMP)

JACOBIANS
  TB1  TB1  2  1  # TB_1: D(TB_1)/D(TB_1)
 ()()()(0;1)(B200)()

  TB2  TB2  2  1  # TB_2: D(TB_2)/D(TB_2)
 ()()()(0;1)(B200)()

GROUP FREQUENCY
    1
SOLUTION TYPE
  Q
  ILU_GMRES
  IMPLICIT_EULER
END

TITLE            **** TEMPLATE FILE YTj ****
  2-D  PHI ALGORITHM  rational LES temperature stress vector Yj
(02/06)

RESIDUALS
  YT1  2  # LOAD SET -{B} FOR YT_1
+(-)()(U1)(1122;-1)(B3101)(TEMP)
+(-)()(U1)(1324;-1)(B3102)(TEMP)
+(-)()(U1)(3142;-1)(B3201)(TEMP)
+(-)()(U1)(3344;-1)(B3202)(TEMP)

  YT2  2  # LOAD SET -{B} FOR YT_2
+(-)()(U2)(1122;-1)(B3101)(TEMP)
+(-)()(U2)(1324;-1)(B3102)(TEMP)
+(-)()(U2)(3142;-1)(B3201)(TEMP)
+(-)()(U2)(3344;-1)(B3202)(TEMP)

JACOBIANS
  YT1  YT1  2  1  # YT_1: D(YT_1)/D(YT_1)
+()()()(0;1)(B200)()
+(SIXTH,CF2)()()(1122;0)(B211)()
+(SIXTH,CF2)()()(1324;0)(B212)()
+(SIXTH,CF2)()()(3142;0)(B221)()
+(SIXTH,CF2)()()(3344;0)(B222)()

  YT2  YT2  2  1  # YT_2: D(YT_2)/D(YT_2)
+()()()(0;1)(B200)()
+(SIXTH,CF2)()()(1122;0)(B211)()
+(SIXTH,CF2)()()(1324;0)(B212)()
+(SIXTH,CF2)()()(3142;0)(B221)()
```

```
+(SIXTH,CF2)()()(3344;0)(B222)()

GROUP FREQUENCY
    1
SOLUTION TYPE
  Q
  ILU_GMRES
  IMPLICIT_EULER
END

TITLE            **** TEMPLATE FILE TFj ****
  2-D  PHI ALGORITHM  LES filter flux for energy equation TFj (1/06)

RESIDUALS
  TF1  2  # LOAD SET -{B} FOR TF1
+(THIRD,CF2)()()(0;2)(B200)(YT1)

  TF2  2  # LOAD SET -{B} FOR TF2
+(THIRD,CF2)()()(0;2)(B200)(YT2)

JACOBIANS
  TF1  TF1  2  1  # TF1: D(TF1)/D(TF1)
 ()()()(0;1)(B200)()

  TF2  TF2  2  1  # TF2: D(TF2)/D(TF2)
 ()()()(0;1)(B200)()

GROUP FREQUENCY
    1
SOLUTION TYPE
  Q
  ILU_GMRES
  IMPLICIT_EULER
END

TITLE            **** TEMPLATE FILE FDij ****
  2-D  PHI ALGORITHM  energy equation lam. diff. flux TDj (02/06)

RESIDUALS
  TD1  2  # LOAD SET -{B} FOR TD1
+(-,PEI)()()(1;0)(B201)(TEMP)
+(-,PEI)()()(3;0)(B202)(TEMP)

  TD2  2  # LOAD SET -{B} FOR TD2
+(-,PEI)()()(2;0)(B201)(TEMP)
+(-,PEI)()()(4;0)(B202)(TEMP)

JACOBIANS
  TD1  TD1  2  1  # TD1: D(TD1)/D(TD1)
 ()()()(0;1)(B200)()

  TD2  TD2  2  1  # TD2: D(TD2)/D(TD2)
 ()()()(0;1)(B200)()

GROUP FREQUENCY
```

```
    1
SOLUTION TYPE
  Q
  ILU_GMRES
  IMPLICIT_EULER
END

TITLE            **** TEMPLATE TEMP.PHI ****
   OMEGA - FROM DELXU  (1/99)

RESIDUALS
  OMGA   2    #  VARBL, SET NO.,  --- SPATIAL  SET (OMGA)
 ()()()(2;0)(B201)(U1)
+()()()(4;0)(B202)(U1)
+(-)()()(1;0)(B201)(U2)
+(-)()()(3;0)(B202)(U2)

JACOBIANS
  OMGA OMGA  2  1  #  VARBL, VARDIF, SET, ALL DIRECTIONS
 ()()()(0;1)(B200)()

GROUP FREQUENCY
      1
SOLUTION TYPE
  Q
  ILU_GMRES
  IMPLICIT_EULER
END

TITLE            **** TEMPLATE TEMP.PHI ****
   DELSQ PSI FROM OMEGA  (1/99)

RESIDUALS
  PSI   2  #  VARBL, SET NO.,  --- SPATIAL  SET (PSI)
 (-)()()(0;1)(B200)(OMGA)

JACOBIANS
  PSI PSI  2  1 # VARBL, VARDIF, SET, ALL DIRECTIONS
 ()()()(1122;-1)(B211)()
+()()()(3344;-1)(B222)()
+()()()(1324;-1)(B221)()
+()()()(1324;-1)(B212)()

GROUP FREQUENCY
      1
SOLUTION TYPE
  Q
  ILU_GMRES
  IMPLICIT_EULER
END

TITLE            **** TEMPLATE TEMP.PHI ****
  ENERGY NORM COMPUTATIONS, ALL VARIABLES/PARAMETERS  (1/99)

RESIDUALS
```

```
  DUNC   1   #                    TEMPORAL TERM IN {F(Q)}
 ()()()(0;1)(B200)(-DUNC)

JACOBIANS
  DUNC DUNC   1 1   #             TIME TERM IN {F(Q)}
 ()()()(0;1)(A200)()
  DUNC DUNC   1 2   #             TIME TERM IN {F(Q)}
 ()()()(0;1)(A200)()

NORMS
  OMGE  1  T                          ENERGY NORM FOR OMGA
 (HALF,REI)()(OMGA)(1122;-1)(B211)(OMGA)
 (HALF,REI)()(OMGA)(1324;-1)(B212)(OMGA)
 (HALF,REI)()(OMGA)(1324;-1)(B221)(OMGA)
 (HALF,REI)()(OMGA)(3344;-1)(B222)(OMGA)

  PSIE  1  T                          ENERGY NORM FOR PSI
 (HALF)()(PSI)(1122;-2)(B211)(PSI)
 (HALF)()(PSI)(1324;-2)(B212)(PSI)
 (HALF)()(PSI)(1324;-2)(B221)(PSI)
 (HALF)()(PSI)(3344;-2)(B222)(PSI)

  U1E  1  T                          ENERGY NORM FOR U1
 (HALF)()(U1)(1122;-1)(B211)(U1)
 (HALF)()(U1)(1324;-1)(B212)(U1)
 (HALF)()(U1)(1324;-1)(B221)(U1)
 (HALF)()(U1)(3344;-1)(B222)(U1)

  U2E  1  T                          ENERGY NORM FOR U2
 (HALF)()(U2)(1122;-1)(B211)(U2)
 (HALF)()(U2)(1324;-1)(B212)(U2)
 (HALF)()(U2)(1324;-1)(B221)(U2)
 (HALF)()(U2)(3344;-1)(B222)(U2)

  PRSE  1  T                          ENERGY NORM FOR PRES
 (HALF)()(PRES)(1122;-1)(B211)(PRES)
 (HALF)()(PRES)(1324;-1)(B212)(PRES)
 (HALF)()(PRES)(1324;-1)(B221)(PRES)
 (HALF)()(PRES)(3344;-1)(B222)(PRES)

  TMPE  1  T                          ENERGY NORM FOR TEMP
 (HALF,PEI)()(TEMP)(1122;-1)(B211)(TEMP)
 (HALF,PEI)()(TEMP)(1324;-1)(B212)(TEMP)
 (HALF,PEI)()(TEMP)(1324;-1)(B221)(TEMP)
 (HALF,PEI)()(TEMP)(3344;-1)(B222)(TEMP)

  PHIE  1  T                          ENERGY NORM FOR PHI
 (HALF)()(PHI)(1122;-1)(B211)(PHI)
 (HALF)()(PHI)(1324;-1)(B212)(PHI)
 (HALF)()(PHI)(1324;-1)(B221)(PHI)
 (HALF)()(PHI)(3344;-1)(B222)(PHI)

GROUP FREQUENCY
      1
SOLUTION TYPE
```

```
  DELTA_Q
  FACTORED_GAUSS_ELIMINATION
  IMPLICIT_EULER

END
```

Vita

Marcel Andre Grubert was born in Hilden, Germany, on July 24, 1970. After completing his university-bound high school diploma at the Geschwister Scholl Gymnasium in Duesseldorf in 1990, he enrolled at the Technical University of Aachen (RWTH), Germany, where he subsequently graduated with a Diplom Ingenieur (Master of Science), with specialization in aerospace engineering, in 1998. During his final years in this program he attended the University of Tennessee Space Institute (UTSI) in Tullahoma, TN as participant of a professional exchange agreement between RWTH and UTSI, in which time he worked on his thesis. In 1998 he joined the PhD program in Mechanical Engineering at UTSI, and later switched to the CFD Lab program at the main campus in Knoxville. He is married happily to the former Mary Rebecca Borelli.